

Flow Boiling Pressure Drop and Heat Transfer of Refrigerants in Multi-microchannel Evaporators under Steady and Transient States

THÈSE N° 7306 (2016)

PRÉSENTÉE LE 25 OCTOBRE 2016

À LA FACULTÉ DES SCIENCES ET TECHNIQUES DE L'INGÉNIEUR
LABORATOIRE DE TRANSFERT DE CHALEUR ET DE MASSE
PROGRAMME DOCTORAL EN ENERGIE

ÉCOLE POLYTECHNIQUE FÉDÉRALE DE LAUSANNE

POUR L'OBTENTION DU GRADE DE DOCTEUR ÈS SCIENCES

PAR

Houxue HUANG

acceptée sur proposition du jury:

Prof. J. A. Schiffmann, président du jury
Prof. J. R. Thome, directeur de thèse
Prof. R. Revellin, rapporteur
Prof. A. W. Mauro, rapporteur
Prof. S. Haussener, rapporteur



ÉCOLE POLYTECHNIQUE
FÉDÉRALE DE LAUSANNE

Suisse
2016

A journey of a thousand miles starts
under one's feet.
— Laozi, Tao Te Ching

To my parents...

Acknowledgements

First and foremost, I would like to sincerely thank Prof. John R. Thome for providing this precious opportunity for me to do my Ph.D. thesis under his supervision at the LTCM lab. I am very grateful for his structural, insightful discussions and suggestions on my Ph.D. work. His profound knowledge in two-phase flow, his passion in research and his patience in guiding students impress me deeply and encourage me to carry on when facing difficulties. I remember clearly that on one Monday morning, Prof. Thome came to the lab to find me with a big smile on his face, saying "Houxue, I got a new idea about the model for the subcooled flow boiling heat transfer that came to my mind on Saturday." The following discussion was really inspiring, and he said "Houxue, give me a five" when we completed this work nicely.

I express my gratitude to the first assistant Dr. Navid Borhani for his encouragement and guidance, especially in the first year of my PhD study. I also thank China Scholarship Council for providing me part of the financial support during my Ph.D. years.

Then, I would like to express my thanks to the committee members, Prof. Sophia Haussener (EPFL), Prof. Schiffmann Jürg Alexander (EPFL), Prof. Rémi Revellin (INSA-Lyon) and Prof. Mauro Alfonso William (University of Naples Federico II) for their valuable comments and suggestions on this thesis.

Cecile and Nathalie are sincerely acknowledged by their assistance in administration and accommodation affairs. I would also like to take some words to thank our technician Mr. Laurent Chavelley for his dedicated work on my facility, such as designing and installing a movable high-speed video camera.

I appreciate the initial help from a former colleague Dr. Eugene Van Rooyen when I started working on the facility, from whom I have learned LTCM's spirit of being helpful and sharing with others. My special thanks go to Dr. Nicolas Lamaison since working with him is really encouraging and enjoyable. I'd like to thank Dr. Tom Saenen for sharing his comprehensive knowledge with me on my confusions.

Of course, Luca Amalfi cannot be missed in this list because he is the person who I have shared countless unforgettable moments with during these years. Being a close friend to each other, we helped each other and exchanged our opinions from the scientific research to the life philosophy. Also, Dr. Duan Wu must be mentioned as well since he led me to explore the fun in Switzerland, i.e. cycling and skiing. Thanks all other colleagues at LTCM for the happy

Acknowledgements

moments spent together, such as dinners, BBQs, ski-weekends at Sass-Fee, etc.. The present colleagues are shortlisted here : Albert, Andrea F, Chiara, Eric, Filippo, Jackson, Jeff, Mirco ; as well as the previous ones who are : Andrea C., Brian, Fazard, Giulia, Hamideh, Marco, Nicolas A., Ricardo, Sepideh and Sylwia.

Last but not the least, thank my girlfriend for her support and accompany during these years. I gratefully thank my parents, sister and brother for their continuous love, encouragement and support.

Lausanne, 18 July 2016

Houxue Huang

Abstract

Multi-microchannel evaporators used for the cooling of high heat flux electronics have been of interest to both industry and academia for more than a decade. Such interest has sparked a large number of research studies on the flow boiling pressure drop and heat transfer in multi-microchannel evaporators. However, there are still several aspects that need to be addressed in order to better understand the complicated flow boiling process taking place in such micro-evaporators. Firstly, the mechanism governing flow boiling heat transfer in microchannels is arguable; secondly, the availability of fine-resolution local heat transfer data is very limited; thirdly, over-simplified heat conduction models are used in the literature to reduce such local heat transfer data; finally, rare attention has been taken on the thermal behavior of such micro-evaporators under transient status.

Inspired by the forgoing aspects, an extensive experimental program has been conducted to study the flow boiling pressure drop and heat transfer of refrigerants in multi-microchannel evaporators under steady and transient status. For the steady-state tests, three fluids (R245fa, R236fa and R1233zd(E)) were tested in two multi-microchannel evaporators. The silicon microchannel evaporators were 10 mm long and 10 mm wide, having 67 parallel channels, each $100 \times 100 \mu\text{m}^2$, separated by a fin with a thickness of $50 \mu\text{m}$. Two types of micro-orifices (25 and $50 \mu\text{m}^2$ in width) were placed at the entrance of each channel to stabilize the two-phase flow and to obtain good flow distribution. The test section backside temperatures were measured by a self-calibrated infrared (IR) camera. The operating conditions for stable flow boiling tests were: mass fluxes from 1250 to $2750 \text{ kg m}^{-2}\text{s}^{-1}$, heat fluxes from 20 to 64 W cm^{-2} , inlet subcoolings of 5.5 , 10 and 15 K , and nominal outlet saturation temperatures of 31.5 , 35 and 40°C . The resulting maximum exit vapor quality at the outlet manifold was 0.51 .

The steady-state experimental data were reduced by solving a 3D inverse heat conduction problem to obtain the local heat transfer coefficients on a pixel-by-pixel basis. The required fluid temperature in the subcooled region was calculated from the local energy balance, while that in the saturated flow boiling region came from the general pressure drop model proposed in this manuscript based on the present data base. According to the present data base of fine-resolution local heat transfer coefficients, a new flow pattern based prediction model was developed here starting from the subcooled region all the way through the annular flow regime. This new flow pattern based model predicted the total local heat transfer database

Acknowledgements

(1,941,538 local points) well with a MAE of 14.2% and with 90.1% of the data predicted within $\pm 30\%$. It successfully tracks the experimental trends without any jumps in predictions when changing flow patterns.

For the transient tests, an extensive experimental study was conducted to investigate the base temperature response of multi-microchannel evaporators under transient heat loads, including cold startups and periodic step variations in heat flux using two different test sections and two coolants (R236fa and R245fa) for a wide variety of test conditions. In addition, a transient flow boiling test under a heat flux disturbance was performed, and a new method of solving the transient 3D inverse heat conduction problem was proposed to obtain the local transient flow boiling heat transfer coefficients.

Key words : Flow boiling, multi-microchannel evaporators, pressure drop, heat transfer, steady and transient states

Résumé

Les évaporateurs à micro-canaux utilisés pour le refroidissement de composants électroniques à haut flux de chaleur ont suscité au cours de la dernière décennie un intérêt grandissant dans l'industrie et le monde académique. Cet attrait a mené à de nombreuses études scientifiques ayant pour but la détermination des pertes de charge et des coefficients d'échange thermique des écoulements diphasiques en micro-canaux. Cependant, de nombreux aspects doivent encore être étudiés afin de mieux comprendre les phénomènes compliqués inhérents aux écoulements diphasiques dans ces micro-évaporateurs. Premièrement, les mécanismes décrits dans la littérature qui gouvernent le transfert thermique des écoulements diphasiques sont discutables. Deuxièmement, l'accès à des données locales de coefficient de transfert thermique à haute résolution spatiale est limité. Troisièmement, les modèles de conduction de chaleur utilisés dans la littérature pour obtenir ces valeurs locales sont trop simplifiés. Finalement, peu d'intérêt a été porté à la réponse dynamique de ces micro-évaporateurs lors de changement soudain de conditions d'opérations. Motivé par ces différents aspects manquants dans la littérature, une vaste campagne expérimentale a été menée afin de caractériser avec exactitude les pertes de charge et les coefficients de transfert thermique d'écoulement diphasique de réfrigérants en micro-canaux à l'état stationnaire mais aussi au cours de régime transitoire. Pour les tests stationnaires, trois fluides (R1233zd(E), R245fa et R236fa) ont été testés dans deux micro-évaporateurs différents en silicone, tous deux longs et larges de 10 mm, avec 67 micro-canaux parallèles, chacun de hauteur et de largeur $100\ \mu\text{m}$, séparé par une ailette d'épaisseur $50\ \mu\text{m}$. Ils diffèrent par la taille de leur orifice d'entrée, soit 25 et $50\ \mu\text{m}$, dont le but est de stabiliser l'écoulement et d'obtenir une bonne distribution du débit entre tous les canaux. Les températures à la base de la section d'essai ont été mesurées par une caméra infrarouge (IR) calibrée in-situ. Les conditions opératoires pour les tests stationnaires stables ont varié entre 1250 et $2750\ \text{kg m}^{-2}\ \text{s}^{-1}$ pour le flux massique et entre 20 et $64\ \text{W cm}^{-2}$ pour le flux thermique. Trois subcooling (5.5, 10 et 15 K) et trois températures de saturation à la sortie de la section d'essai (31.5, 35 et $40\ ^\circ\text{C}$) ont été testés pour ces variations de flux thermique et massique. La qualité de vapeur maximum atteinte tout test confondu à la sortie de la section d'essai a été de 0.51. Les données expérimentales de coefficient de transfert de chaleur local ont été obtenues en résolvant un problème inverse de conduction en 3 dimensions dans le micro-évaporateur en se basant sur les mesures de températures infrarouge pixel par pixel.

Chapitre 0. Résumé

La température locale du fluide, nécessaire pour la réduction des données, a été calculée à partir d'un bilan énergétique dans la zone monophasique, alors qu'elle a été obtenue à partir de la pression locale dans la zone diphasique, laquelle est déduite d'un modèle générale de pertes de charge décrit dans le présent manuscrit. Utilisant la substantielle base de données obtenue, un nouveau modèle de prédiction de coefficient de transfert thermique basé sur le type d'écoulement diphasique a été établi depuis la zone d'ébullition sous-saturée jusqu'au régime annulaire. Ce nouveau modèle a prédit toute la base de données de coefficient de transfert thermique locale (1,941,538 points) avec une erreur moyenne absolue (MAE) de 14.2% tout en prédisant 90.1% des données avec une erreur de moins de 30%. Ce modèle permet de reproduire les tendances observées expérimentalement sans sauts lors du changement de type d'écoulement. Pour les tests dynamiques, une étude expérimentale a été réalisé afin d'examiner la variation de la température à la base du micro-évaporateur lors de changement soudain du flux thermique. Pour ce faire, des tests en démarrage à froid (de zéro à une valeur donnée) et en variations périodiques en créneau du flux thermique ont été réalisés pour deux évaporateurs différents et deux fluides (R236fa et R245fa). En outre, une nouvelle méthode de résolution dynamique du problème inverse de conduction 3D a été proposée afin d'obtenir les variations dynamiques et locales de coefficient de transfert thermique lors de tests expérimentaux.

Mots clefs : Ecoulement diphasique, Evaporateur à micro-canaux multiples, Perte de charge, Transfert thermique, Régime stationnaire et transitoire.

Contents

Acknowledgements	i
Abstract	iii
Résumé	v
List of figures	xi
List of tables	xvii
Nomenclature	xix
1 Introduction	1
2 Heat conduction models	5
2.1 Introduction	6
2.2 Case descriptions	9
2.2.1 Case I: Single-phase flow	9
2.2.2 Case II: Two-phase flow	11
2.3 Theory	12
2.3.1 Filtering techniques	12
2.3.2 3D IHCP	14
2.3.3 Current heat conduction models in literature	18
2.4 Analysis of results and discussion	21
2.4.1 Filtering techniques comparison	21
2.4.2 Comparison of heat conduction models	24
2.5 Conclusion	31
3 Steady-state pressure drop	33
3.1 Introduction	34
3.2 Experimental setup	36
3.2.1 Facility	36
3.2.2 Test section	36

Contents

3.2.3	IR camera calibration	38
3.2.4	Experimental test conditions and uncertainties	38
3.3	Data reduction	40
3.3.1	Single-phase flow	41
3.3.2	Two-phase flow	44
3.4	Analysis of results and discussion	45
3.4.1	Single-Phase flow validation	46
3.4.2	Two-Phase flow pressure drop	48
3.5	Conclusion	63
4	Steady-state heat Transfer	65
4.1	Introduction	66
4.2	Experimental setup	68
4.2.1	Experimental facility and test section	68
4.2.2	Operating conditions and measurement uncertainties	68
4.3	Data Reduction	70
4.4	Experimental results and discussions	72
4.4.1	Effect of heat flux	73
4.4.2	Effect of mass flux	73
4.4.3	Effect of inlet subcooling	73
4.4.4	Effect of saturation temperature	75
4.4.5	Effect of fluid	75
4.4.6	Effect of inlet orifice	76
4.5	Local heat transfer predictions	77
4.5.1	Comparison with existing models	77
4.5.2	New local heat transfer models development	80
4.5.3	Global prediction from the new flow pattern based model	84
4.6	Conclusions	85
5	Transient base temperature response	91
5.1	Introduction	92
5.2	Experimental Setup	94
5.2.1	Facility and test section	94
5.2.2	Operating conditions and measurement uncertainties	96
5.3	Results for cold startups	96
5.3.1	Thermal and flow visualization during a cold startup	96
5.3.2	Effect of test section	101
5.3.3	Effect of pulse magnitude	102
5.3.4	Effect of mass flux	102

5.3.5	Effect of inlet subcooling	105
5.3.6	Effect of outlet saturation temperature	107
5.3.7	Effect of fluid	108
5.3.8	Effect of surface roughness	109
5.4	Heat flux periodic variation	109
5.4.1	Effect of pulse period	110
5.4.2	Effect of mass flux	110
5.5	Conclusions	110
6	Transient heat transfer coefficient	115
6.1	Introduction	116
6.2	Experimental setup	118
6.3	Data reduction	119
6.3.1	Pressure drop	119
6.3.2	Data reduction method 1 - 3D-TDMA	121
6.3.3	Method 2 - 2D-Controlled	123
6.4	Results and discussions	127
6.4.1	Case study presentation	127
6.4.2	Pressure drop	127
6.4.3	Heat transfer	129
6.5	Conclusion	132
7	Conclusions and recommendations	135
7.1	Conclusions	135
7.2	Future recommendations	136
A	An appendix	139
A.1	Detailed data reduction	139
A.1.1	Single-phase flow	139
A.1.2	Two-phase flow	140
A.2	Analysis of results and discussion	142
A.2.1	Single-phase flow validation	142
A.2.2	Two-phase flow heat transfer	145
	Bibliography	159
	Curriculum Vitae	161

List of Figures

2.1	Test section: (a) Schematic of the multi-microchannel evaporator and (b) a photo of the microchannels with inlet orifices Szczukiewicz et al. (2013).	10
2.2	Mesh types used in the 3D-TDMA model.	14
2.3	Flow chart of the new method.	15
2.4	Mesh types used in 1D-Direct and 2D-TDMA models: (a) Mesh in 1D model and (b) Mesh in 2D model.	19
2.5	Filtering results comparison against raw IR temperature ($i = 70$).	22
2.6	Comparison of two-phase flow widthwise averaged local footprint heat flux from the three temperature filtering techniques.	23
2.7	Sensitivity of polynomial surface fitting to the noise amplitude in the base temperature data: (a) local base temperature at $i = 70$ where NA represents noise amplitude, (b) obtained widthwise averaged footprint heat flux and (c) absolute relative error of overall averaged footprint heat flux versus the absolute the noise, where $Er = \frac{ q_{ftp,av,no} - q_{ftp,av} }{q_{ftp,av}} \times 100\%$	25
2.8	Single-phase flow local footprint heat flux (a) and temperature (b) (sparse grid in the middle is used for a clearer view).	26
2.9	Single-phase flow fluid temperature along the flow direction.	26
2.10	Single-phase flow local heat transfer coefficients and fin efficiency obtained with the new 3D-TDMA model.	27
2.11	Single-phase flow local Nusselt number comparison.	28
2.12	Two-phase flow local footprint heat flux (a) and temperature (b).	28
2.13	Single- and two-phase flow thermal maps of footprint heat flux and temperature: (a) single-phase T_{ftp} , (b) single-phase q_{ftp} , (c) two-phase T_{ftp} and (d) two-phase q_{ftp}	30
2.14	Two-phase flow local heat transfer coefficients and fin efficiency at the widthwise centerline, obtained from the new 3D-TDMA model.	31
3.1	Layout of the facility: (a) schematic diagram and (b) photo.	37

List of Figures

3.2	Test section: (a) schematic of the microchannel evaporator, (b) photo of the microchannels with inlet orifices Szczukiewicz et al. (2013), (c) photo of the micro-heaters Szczukiewicz et al. (2013), (d) photo of the test section housed inside the manifold, and (e) photo of the manifold bottom.	39
3.3	Single-phase pressure drop models comparison in adiabatic flow: (a) $\Delta P_{inlet,res}$ of R1233zd(E), (b) $\Delta P_{outlet,res}$ of R1233zd(E), (c) ΔP_{ch} of R1233zd(E), (d) ΔP_{ch} of R245fa, (e) ΔP_{ch} of R245fa, (f) ΔP_{ch} of R236fa ((a) ~ (d) with the present data, (e) and (f) with the data from Szczukiewicz (2012)).	47
3.4	Single-phase channel pressure drop in adiabatic flow: (a) R245fa, and (b) R236fa. (DF: considering developing region and fully developed part; FD: ignoring developing region, i.e. fully developed region only)	48
3.5	Flow friction factor in diabatic flow (Exp.1: the first set of single-phase heat transfer experiment of R1233zd(E) at $T_{sat} = 60^\circ\text{C}$ with various $G = 500 \sim 2500 \text{ kg m}^{-2}\text{s}^{-1}$ and $q = 5 \sim 30 \text{ W cm}^{-2}$; Exp.2: the same test of R1233zd(E) as Exp.1 for confirmation; Exp.3: single-phase diabatic of test R1233zd(E) at $q = 2 \text{ W cm}^{-2}$ with various G ; Exp.236fa-TS2: tests in test section 2, and the rest are in test section 1).	49
3.6	Influence from the saturation temperature on the pressure drops: (a) R245fa and (b) R236fa.	50
3.7	Influence from the inlet subcooling on the pressure drops of (a) R245fa and (b) R236fa.	51
3.8	Influence from the fluids on the pressure drops	52
3.9	Influence from the test section inlet orifice on the pressure drops.	53
3.10	Pressure drop models comparison against stable flow boiling experimental data: (a) McAdams et al. (1942), (b) Akers et al. (1958), (c) Cicchitti et al. (1960), (d) Dukler et al. (1964), (e) Beattie and Whalley (1982) (f) Lin et al. (1991), (g) Cioncolini et al. (2009); Cioncolini and Thome (2011), (h) Lockhart and Martinelli (1949), (i) Grönnerud (1979).	60
3.11	Pressure drop models comparison against stable flow boiling experimental data: (a) Chisholm Chisholm (1973), (b) Friedel (1979), (c) Müller-Steinhagen and Heck (1986), (d) Mishima and Hibiki (1996), (e) Tran et al. (2000), (f) Qu and Mudawar (2003a), (g) Lee and Garimella (2008), (h) Kim and Mudawar (2013b) and (i) Present work.	61
3.12	Two-phase flow local pressure and temperature profiles at the centerline ($y = 5 \text{ mm}$) along the channel length for $G = 2000 \text{ kg m}^{-2}\text{s}^{-1}$, $q = 44 \text{ W cm}^{-2}$	62
3.13	Two-phase flow local pressure and temperature map at $G = 2000 \text{ kg m}^{-2}\text{s}^{-1}$, $q = 44 \text{ W cm}^{-2}$: (a) local pressure map and (b) local fluid temperature map (The flow direction is from left to right side).	63

3.14	Effect of heat flux on two-phase local fluid pressure and temperature profiles of the centerline along the channel length at $G = 2000 \text{ kg m}^{-2}\text{s}^{-1}$: (a) local pressure profile and (b) local fluid temperature profile.	64
4.1	Schematics of flow patterns and local heat transfer coefficient trend (SPL: single-phase liquid, SCFB: subcooled flow boiling and SFB: saturated flow boiling). . .	67
4.2	Single-phase local Nusselt number validation for R245fa at $G = 1500 \text{ kg m}^{-2}\text{s}^{-1}$ and $q = 4 \text{ W cm}^{-2}$ in TS1 Shah and London (1978); Muzychka and Yovanovich (2004).	72
4.3	Effect of heat flux on new widthwise averaged local heat transfer coefficients for R245fa at $G = 2000 \text{ kg m}^{-2}\text{s}^{-1}$ and $T_{sat} = 40^\circ\text{C}$ in test section 1: (a) versus local length and (b) versus local vapor quality.	73
4.4	Effect of mass flux on widthwise averaged local heat transfer coefficients for: (a) R1233zd(E) (at $q = 38 \text{ W cm}^{-2}$ and $T_{sat} = 35^\circ\text{C}$ in test section 1) Huang et al. (2016b) and (b) new R245fa (at $q = 36 \text{ W cm}^{-2}$ and $T_{sat} = 31.5^\circ\text{C}$ in test section 1).	74
4.5	Effect of inlet subcooling on new widthwise averaged local heat transfer coefficients for: (a) R245fa (at $q = 44 \text{ W cm}^{-2}$ and $T_{sat} = 31.5^\circ\text{C}$ in test section 1) and (b) R236fa (at $q = 44 \text{ W cm}^{-2}$ and $T_{sat} = 31.5^\circ\text{C}$ in test section 2).	74
4.6	Effect of outlet saturation temperature on new widthwise averaged local heat transfer coefficients for $q = 38 \text{ W cm}^{-2}$ at three different mass fluxes: (a) versus local length and (b) versus local vapor quality.	75
4.7	Effect of fluid on widthwise averaged local heat transfer coefficients for $q = 44 \text{ W cm}^{-2}$, $G = 2000 \text{ kg m}^{-2}\text{s}^{-1}$, $T_{sat} = 35^\circ\text{C}$ and $\Delta T_{sub} = 5.5 \text{ K}$ including the new data: (a) versus local length and (b) versus local vapor quality.	76
4.8	Effect of test section inlet orifice on new R236fa widthwise averaged local heat transfer coefficients for $q = 40 \text{ W cm}^{-2}$, $G = 2000 \text{ kg m}^{-2}\text{s}^{-1}$, $T_{sat} = 31.5^\circ\text{C}$ and $\Delta T_{sub} = 5.5 \text{ K}$: (a) versus local length and (b) versus local vapor quality.	77
4.9	Comparison of experimental saturated flow boiling heat transfer coefficients with two-phase heat transfer models of (a) Lazarek and Black (1982), (b) Cooper (1984), (c) Liu and Winterton (1991), (d) Bertsch et al. (2009), (e) Costa-Patry and Thome (2013) and (f) Kim and Mudawar (2013a).	78
4.10	Comparison of experimental subcooled flow boiling heat transfer data with models of (a) Papell (1963), (b) Moles and Shaw (1972), (c) Lee and Mudawar (2008) and (d) present work.	80
4.11	Validation of single-phase thermal developing heat transfer models: (a) Muzychka and Yovanovich (2004) for UWF and (b) present work.	82
4.12	Validation of saturated flow boiling heat transfer model at very low vapor quality.	83

List of Figures

4.13 Comparison of the local heat transfer coefficient versus local vapor quality between the prediction from the new flow pattern based model and the experimental data: (a) for fluid R1233zd(E) Huang et al. (2016b) in TS1 at $y = 7.5$ mm under $G = 2000 \text{ kg m}^{-2}\text{s}^{-1}$, $q = 48 \text{ W cm}^{-2}$, $T_{sat} = 35^\circ\text{C}$ and $\Delta T_{sub} = 5.5 \text{ K}$; (b) for fluid R1233zd(E) Huang et al. (2016b) in TS1 at $y = 7.5$ mm under $G = 2500 \text{ kg m}^{-2}\text{s}^{-1}$, $q = 48 \text{ W cm}^{-2}$, $T_{sat} = 35^\circ\text{C}$ and $\Delta T_{sub} = 5.5 \text{ K}$ (SPL: single-phase liquid, SCFB: subcooled flow boiling, SVLQ: saturated very low quality, TAF: transition to annular flow and AF: annular flow).	86
4.14 The new flow pattern based model validation against the total experimental data bank: (a) absolute value, (b) ratio of prediction to measured data versus local vapor quality.	87
4.15 The new model comparison with experimental data sorted into four categories: (a) flow regime, (b) fluid, (c) outlet saturation temperature and (d) inlet subcooling.	88
5.1 Schematic diagram of the facility.	95
5.2 Test section: (a) schematic of the microchannel evaporator, (b) photo of the microchannels with inlet orifices Szczukiewicz et al. (2013) and (c) photo of the micro-heaters Szczukiewicz et al. (2013).	95
5.3 Wall temperature variation versus time at $y = 5.0$ and $z = 7.5$ mm of test section 1 with heat load from 0 to 30 W cm^{-2} at an initial mass flux of $1500 \text{ kg m}^{-2}\text{s}^{-1}$. . .	97
5.4 Transient flow regime response in test section 1 after the heat load is suddenly increased from 0 to 30 W cm^{-2} at initial mass flux of $1500 \text{ kg m}^{-2}\text{s}^{-1}$, inlet subcooling of 5.5 K , and outlet saturation temperature of 31.5°C : (a) $t = 5.250 \text{ s}$ (moment A-B), superheated single-phase liquid, (b) $t = 7.350 \text{ s}$ (moment B), chaotic two-phase flow, (c) $t = 7.417 \text{ s}$ (moment B-C), pure vapor phase in channels and two-phase in inlet and outlet slits, (d) $t = 7.550 \text{ s}$ (moment C), two-phase flow followed by vapor phase, (e) $t = 7.750 \text{ s}$ (moment C-D), the vapor phase nearly replaced by the two-phase, and (f) $t = 8.117 \text{ s}$ (moment D), subcooled liquid at channel inlet followed by the two-phase flow (The time datum is 0 s, as shown in Fig. 5.3. The net flow direction is from left to right, same to all the figures in this paper.).	98
5.5 Thermal maps of test section 1 after the heat load is suddenly increased from 0 to 30 W cm^{-2} , at $G = 1500 \text{ kg m}^{-2}\text{s}^{-1}$, $\Delta T_{sub} = 5.5 \text{ K}$, and $T_{sat} = 31.5^\circ\text{C}$ for six times : (a) $t = 5.250 \text{ s}$ (moment A-B), (b) $t = 7.350 \text{ s}$ (moment B), (c) $t = 7.417 \text{ s}$ (moment B-C), (d) $t = 7.550 \text{ s}$ (moment C), (e) $t = 7.750 \text{ s}$ (moment C-D) and (f) $t = 8.117 \text{ s}$ (moment D).	99
5.6 Evolution of centerline base temperature along the flow direction at seven typical moments versus time for test section 1 with heat load from 0 to 30 W cm^{-2} at $G = 1500 \text{ kg m}^{-2}\text{s}^{-1}$	100

5.7	Effect of test section inlet orifice ratio on the thermal response of test section 2 with heat load from 0 to 30 W cm ⁻²	102
5.8	Process of triggering two-phase flow during a cold startup in test section 2 for $G = 1500 \text{ kg m}^{-2}\text{s}^{-1}$, $\Delta T_{sub} = 5.5 \text{ K}$, $T_{sat} = 31.5 \text{ }^{\circ}\text{C}$, $q = 0\text{-}30 \text{ W cm}^{-2}$: (a) $t = t_0 \text{ s}$, bubbles traveling back to the outlet plenum, (b) $t = t_0 + 0.008 \text{ s}$, small stream of vapor phase starting moving upstream from the channel exit, (c) $t = t_0 + 0.016 \text{ s}$, vapor phase arriving at the channel middle with large part of channels occupied by the liquid phase and (d) $t = t_0 + 0.030 \text{ s}$, vapor phase arriving at the channel entrance with two-phase flow between the vapor phase and the two test section boundaries moving downstream (the net flow direction is from left to right). . .	103
5.9	Effect of heat flux magnitudes on the thermal response of micro-evaporators: (a) test section 1 and (b) test section 2.	104
5.10	Effect of mass flux on the thermal response of test section 2 with heat load from 0 to 30 W cm ⁻²	104
5.11	Process of triggering two-phase flow during cold startup in test section 2 at $G = 1000 \text{ kg m}^{-2}\text{s}^{-1}$: (a) $t = t_0 \text{ s}$, onset of boiling by a vapor jet with liquid phase in microchannels, (b) $t = t_0 + 0.002 \text{ s}$, starting to explode from the channel exist upstream and downstream with still liquid phase in microchannels, (c) $t = t_0 + 0.008 \text{ s}$, liquid was pushed back by the two-phase mixture creating a vapor phase behind, and (d) $t = t_0 + 0.024 \text{ s}$, two-phase in the inlet plenum with vapor phase in channels (The net flow direction is from left to right). . . .	105
5.12	Time strips at three stream-wise locations during a cold startup at $G = 1000 \text{ kg m}^{-2}\text{s}^{-1}$ in test section 2: (a) $z = 1.0 \text{ mm}$, (b) $z = 5.0 \text{ mm}$ and (c) $z = 9.0 \text{ mm}$ (position z was marked with yellow lines in Fig. 5.11d).	106
5.13	Effect of inlet subcooling on the thermal response of test section 2 with heat load from 0 to 30 W cm ⁻²	107
5.14	Photo of slug bubbles due to flash after the inlet orifices for test section 2 at $\Delta T_{sub} = 2 \text{ K}$ for $G = 1500 \text{ kg m}^{-2}\text{s}^{-1}$, $T_{sat} = 31.5 \text{ }^{\circ}\text{C}$ under adiabatic condition. .	107
5.15	Effect of outlet saturation temperature on the thermal response of test section 2 with heat load from 0 to 30 W cm ⁻²	108
5.16	Effect of fluid property on the thermal response of test section 2 with heat load from 0 to 30 W cm ⁻²	109
5.17	Effects of heat flux pulse period and distance downstream on the base temperature response of test section 2 under periodic variations in heat flux: (a) $y = 5.0$, $z = 0.25 \text{ mm}$, (b) $y = 5.0$, $z = 2.5 \text{ mm}$, (c) $y = 5.0$, $z = 5.0 \text{ mm}$, (d) $y = 5.0$, $z = 7.5 \text{ mm}$ and (e) $y = 5.0$, $z = 9.5 \text{ mm}$	112
5.18	Effects of mass flux on the base temperature response for periodic variations in heat flux: (a) $y = 5.0$, $z = 0.25 \text{ mm}$, (b) $y = 5.0$, $z = 2.5 \text{ mm}$, (c) $y = 5.0$, $z = 5.0 \text{ mm}$, (d) $y = 5.0$, $z = 7.5 \text{ mm}$, and (e) $y = 5.0$, $z = 9.5 \text{ mm}$	113

List of Figures

6.1	Layout of the facility: (a) schematic diagram and (b) photo.	119
6.2	Test section: (a) schematic of the microchannel evaporator, (b) photo of the microchannels with inlet orifices Szczukiewicz et al. (2013), (c) photo of the micro-heaters Szczukiewicz et al. (2013), (d) photo of the manifold bottom. . .	120
6.3	Initial local pressure and temperature profile.	121
6.4	Mesh types used in the 3D-TDMA model.	122
6.5	Flow chart for obtaining transient wall heat transfer coefficients with the 3D-TDMA method.	124
6.6	System identification for K_i and K_p determination	125
6.7	Flow chart for obtaining transient wall heat transfer coefficients with the 2D-controlled method.	126
6.8	Mass flux and inlet pressure response to the sudden heat load disturbance at 0.5 s. . .	128
6.9	Transient pressure drop.	128
6.10	Transient local pressure and temperature at four locations at the widthwise centerline: (a) local pressure and (b) local fluid temperature.	129
6.11	Time evolution along the widthwise centerline after the heat flux disturbance at 0.5s for both methods.: (a) mean heat transfer coefficient, (b) maximum error on the calculated temperature compared to the experimental data.	131
6.12	Time evolution of the local wall heat transfer coefficient at four different locations along the widthwise centerline after the heat flux disturbance at 0.5s for both methods.	131
6.13	Local wall heat transfer coefficient profiles along the widthwise centerline at five different instants of time.	132
A.1	Energy loss for single-phase flow of R1233zd(E): (a) energy loss in total and to the ambience and (b) energy loss to the electrical wire.	143
A.2	Single-phase local Nusselt number validation for R1233zd(E) at $G = 1500 \text{ kg m}^{-2}\text{s}^{-1}$ and $q = 5 \text{ W cm}^{-2}$	144
A.3	Assessment of single-phase local Nusselt number correlations with experimental data of R1233zd(E) in the test section with inlet orifice of $50 \mu\text{m}$: (a) Shah and London (1978), (b) Muzychka and Yovanovich (2004) for uniform wall heat flux, and (c) Muzychka and Yovanovich (2004) for uniform wall temperature (five pixels at each lateral side were cut).	145
A.4	Energy loss for two-phase flow boiling tests of R1233zd(E).	146
A.5	Thermal maps of two-phase flow at $G = 2500 \text{ kg m}^{-2}\text{s}^{-1}$, $q = 44 \text{ W cm}^{-2}$: (a) footprint temperature T_{ftp} , (b) footprint heat flux q_{ftp} , (c) fluid temperature T_{fl} , (d) temperature difference between footprint and fluid, (e) footprint heat transfer coefficients α_{ftp} and, and (f) wall heat transfer coefficients α_{wall} (The flow direction is from left to right side).	147

List of Tables

2.1	Experimental measurement uncertainties of main parameters.	12
2.2	Results from the three temperature filtering techniques.	22
3.1	Stable flow boiling test matrix.	40
3.2	Experimental measurement uncertainties of main parameters of R1233zd(E). .	40
3.3	Correlations from literature for the coefficients of irreversible pressure loss. . .	42
3.4	Correlations for single-phase channel pressure drop.	43
3.5	Homogeneous equilibrium models for two-phase flow properties.	53
3.6	Separated flow models for the frictional pressure drop.	54
3.7	Separated flow mechanistic model for two-phase pressure drop.	57
3.8	Statistical comparison between the prediction by pressure drop models and the experimental data.	58
4.1	Properties of three fluids tested here at $T_{sat} = 35\text{ }^{\circ}\text{C}$ (the properties without notation are based on the NIST REFPROP 9.0).	69
4.2	Correlations from subcooled flow boiling heat transfer.	79
4.3	Correlations from literature for single-phase local Nusselt number in channels. .	81
4.4	A new flow pattern based model including subcooled flow.	84
4.5	Statistical comparison between new model prediction and experimental data sorted into different categories.	89
5.1	Transient tests matrix.	97
6.1	Heat flux disturbance test condition.	127
A.1	Correlations from literature for single-phase local Nusselt number in channels. .	144
A.2	Saturated flow boiling heat transfer models.	148

Nomenclature

Roman	Description
A	cross section area (mm^2)
ar	aspect ratio (-)
Bo	Boiling number (-)
C	coefficients (-)
$C_1 - C_4$	empirical coefficient (-)
Co	Confinement number (-)
c_p	heat capacity ($\text{J kg}^{-1} \text{K}^{-1}$)
D_h	hydraulic diameter (m)
E	pixel numbers
Er	mean square temperature difference (K)
e	liquid entrainment (-)
$exit$	exit (-)
F	pixel numbers and Enhance factor (-)
Fr	Froude number (-)
f	Fanning factor (-)
\tilde{f}	corrected flow friction factor
G	mass flux ($\text{kg m}^{-2} \text{s}^{-1}$)
g	gravitational accelerate (m s^{-2})
H	height (m)
H_{lv}	latent heat of vaporization (J kg^{-1})
I	grids number in widthwise (-)
i	grid index in widthwise (-)
J	grids number in lengthwise (-)
j	grid index in lengthwise (-)
K	grids number in thickness direction (-)
k	thermal conductivity ($\text{W m}^{-1} \text{K}^{-1}$)
L	length (m)
m	fin parameter (m^{-1})
\dot{m}	mass flux ($\text{kg m}^{-2} \text{s}^{-1}$)

List of Tables

N	microchannel number (-)
NA	noise amplitude (K)
Nu	Nusselt number (-)
P_R	reduced pressure (-), $P_R = P/P_{crit}$
Pe	Peclet number (-), $Pe = RePr$
Pr	Prandtl number (-), $Pr = \frac{c_p \mu}{k}$
$per t$	protuberance (°C)
Q	heat transfer rate (W)
q	heat flux ($W m^{-2}$)
R	temperature difference (°C)
Re	Reynolds number (-), $Re = \frac{GD_h}{\mu}$
R_p	surface roughness (μm)
S	smoothing factor (-)
Su	Suratman number (-)
T	temperature (K)
\tilde{T}	filtered temperature, (K)
UWH	uniform wall heat flux
UWT	uniform wall temperature
V	voltage (V)
ν	noise variance (-)
W	width (m)
We	Webber number (-), $We = \frac{G^2 D_h}{\rho \sigma}$
X_{tt}	Lockhart–Martinelli parameter of turbulent liquid–turbulent vapor flows (-)
x	dimension in thickness direction (m)
y	dimension in span wise (m)
z	dimension in length wise (m)
z^O, z^*	dimensionless length (-)
Greek	
α	heat transfer coefficient ($W m^{-2} K^{-1}$)
Δ	difference (-)
μ	mean value (-)
Ω	local neighborhood (-)
ϕ	two-phase multiplier (-)
σ	variance (-)
τ	time constant (s)
ξ	mean of temperature difference square (-)

Subscripts

<i>3Z</i>	three zone
<i>AF</i>	annular flow
<i>amb</i>	ambient
<i>axial</i>	axial heat conduction
<i>b</i>	bottom
<i>base</i>	test section base
<i>cal</i>	calculated
<i>CB – AF</i>	coalescing bubble to annular flow regime
<i>ch</i>	channel
<i>Cooper</i>	Cooper
<i>cont</i>	contraction
<i>cor</i>	correlation
<i>diff</i>	differential
<i>e</i>	east
<i>Exp</i>	experiment
<i>expa</i>	expansion
<i>eff</i>	effective
<i>exp</i>	experiment
<i>FC</i>	forced convection
<i>f</i>	fin
<i>fr</i>	frictional
<i>ftp</i>	footprint
<i>IR</i>	IR camera
<i>i</i>	index,irreversible
<i>j</i>	index
<i>L</i>	large
<i>l</i>	liquid
<i>lo</i>	liquid only
<i>loc</i>	local
<i>loss</i>	heat loss
<i>ME</i>	microchannel evaporator
<i>max</i>	maximum
<i>mf</i>	manifold
<i>mom</i>	momentum
<i>NB</i>	nucleate boiling
<i>n</i>	north
<i>no</i>	noise

List of Tables

<i>Pred</i>	prediction
<i>p</i>	predictor
<i>r</i>	reversible
<i>rest</i>	restriction
<i>S</i>	small
<i>s</i>	south
<i>sat</i>	saturation temperature
<i>short</i>	short edge
<i>sta</i>	static
<i>sp</i>	single-phase
<i>sub</i>	subcooling
<i>t</i>	top
<i>tc</i>	thermocouple
<i>total</i>	total
<i>tp</i>	two-phase
<i>v</i>	vapor
<i>vo</i>	vapor only
<i>w</i>	west
<i>wall</i>	channel wall
<i>wire</i>	electrical power wires

1 Introduction

The data center industry serves as the backbone of the world economy and now consumes approximately 2.8 percent of the global electricity consumption. This represents the total annual output of nearly 170 large (500-megawatt) coal-fired power plants and the associated emissions of greenhouse gases CO_2 . Such CO_2 emissions will increase 7% annually through 2020 predicted by a widely recognized report of the SMARTer 2020. Saving energy and reducing CO_2 emissions make it imperative to reduce the data center electricity consumption. For most of the present data centers, nearly 40% of their total energy usage is consumed by their conventional air-based cooling systems. Such high energy demand by air-cooled cooling systems is due to the poor convection heat transfer coefficient and low thermal capacity of air, thus requiring more power to provide a high mass flow rate of air in order to fulfill the cooling task. As a result, for data centers located in regions with serious air pollution, air-cooled systems elevate the energy consumption, increase the operating cost, or even fail in cooling the equipment. In this case, unpleasant investment must be made in air scrubbing of the incoming air, and thus consumes even more electricity.

As a consequence, a more energy-efficient cooling system using two-phase flow has been proposed as a promising replacement for the forgoing less energy-efficient air-cooled system. These proposed on-chip two-phase flow cooling systems usually consist of a cold-plate multi-microchannel evaporator attached on a CPU or a GPU, a micro-condenser and an active driver, i.e. a pump or a compressor, or a passive driver (gravity). The first advantage of using a two-phase flow cooling system is the efficient transfer of heat through the micro-evaporator by using the latent heat of the fluid and the big heat transfer surface per unit volume. The second one is to maintain a nearly uniform low wall temperature of the cooled devices by using a coolant with low-boiling point (i.e. low saturation pressure). The third one exists in the recovery of the heat removed from the cooled devices by connecting the micro-condenser to an external heat recovery loop.

The core of the on-chip cooling system is the micro-evaporator since its pressure drop and

heat transfer coefficient mainly determine the consumption of the system pumping power and the overall thermal performance, respectively. Therefore, for properly designing such cooling systems, it is of scientific and practical importance to investigate the flow boiling pressure drop and heat transfer in multi-microchannel evaporators under not only steady state but also transient conditions. However, the current understanding on such aspects is still limited. The literature on the heat transfer mechanism governing flow boiling in multi-microchannel evaporators is conflicting, which is probably due to the lack of fine-resolution local heat transfer measurements. Furthermore, usually an over-simplified heat conduction model has been employed to reduce the local heat transfer data, thus introducing extra errors in the output results and flattening out trends in these data. Finally, the thermal behavior of multi-microchannel evaporators under transient heat loads is of the same importance as the steady state since the heat load varies during operation. However, a high resolution experimental study on such transient behaviors is currently lacking. To fill in these gaps, the present thesis is focused on the following objectives:

1. Local heat transfer data reduction in multi-microchannel evaporators by solving the 3D inverse heat conduction problem;
2. Flow boiling pressure drop measurement and modeling under high mass flux;
3. Local fine-resolution heat transfer measurement and modeling;
4. Thermal behavior of microchannel evaporators under transient heat loads;
5. Transient local heat transfer coefficient during a heat flux disturbance.

In this manuscript, each chapter from Chapter 2 to 6 will focus on one of the forgoing topics. Each chapter is a journal paper on that topic, some published and some still in review. Chapter 7 then presents the general conclusions and recommendations.

In Chapter 2, the existing heat conduction models in the literature used to reduce the heat transfer data in multi-microchannel evaporators will be reviewed. Then, a new method for reducing the local heat transfer coefficients will be proposed. In the new method, a 3D inverse heat conduction problem is solved by a finite volume method (FVM), a Newton-Raphson optimization method and a local energy balance. The test section backside temperatures recorded by a fine-resolution IR camera will be filtered by a polynomial surface fitting technique prior to being used as a known boundary condition.

Chapter 3 mainly focuses on the stable flow boiling pressure drop in multi-microchannel evaporators. The experimental measurements are firstly presented and discussed, and then the existing two-phase flow pressure drop models including homogeneous equilibrium models and separated flow models are compared with the measurements, and finally a new general pressure drop model belonging to the later category is proposed based on the present experimental data base. This new general pressure drop model is used later in Chapter 4 on heat transfer to obtain the local fluid temperature for data reduction.

In Chapter 4, fine-resolution local flow boiling heat transfer coefficients in multi-microchannel

evaporators are measured under a wide range of test conditions including two inlet restrictions, three inlet subcoolings, three outlet saturation temperatures, three fluids, and various mass fluxes and heat fluxes. The effects of the test conditions on the local heat transfer coefficients are analyzed and discussed. The saturated flow boiling local data are used to validate the heat transfer correlations and models existing in the literature. Based on the fine-resolution local data, a new flow pattern based model starting from subcooled flow all the way through to annular flow is developed and it shows good agreement with the present large data base. Chapter 5 presents the thermal response of multi-microchannel evaporators during flow boiling under two types of transient heat loads (cold start-ups and periodic variations in heat flux) with flow visualization. For cold-startups, the effects of test conditions, such as inlet subcooling, inlet orifice width, outlet saturation temperature, etc., on the maximum base temperature and the time required to initiate boiling are experimentally studied. Chapter 6 proposes a new method for obtaining the transient local heat transfer coefficient in multi-microchannel evaporators by solving the transient 3D inverse heat conduction problem. In this method, at each time step a direct transient 3D heat conduction equation with a guessed footprint temperature boundary condition from the Newton-Raphson iteration is discretized by a finite volume method and solved by a TDMA (Tridiagonal Matrix Algorithm) solver.

2 Heat conduction models

The content of this chapter is under review by Huang et al. (2016a):

H. Huang, N. Borhani, N. Lamaison, J. R. Thome. Local experimental heat transfer in multi-microchannel evaporators, under review by *Internal Journal of Thermal Sciences*, 2016.

Abstract

Measuring the strong local variation in heat transfer coefficients in multi-microchannel evaporators is related to the inverse heat conduction problem (IHCP). As the local flow heat transfer coefficients change greatly in magnitude from single-phase liquid at the entrance to a peak in slug flow and then to a minimum at the transition to the onset of annular flow and finally a new substantial rise up to the outlet, a significant heat spreading occurs due to the heat transfer process itself, and this has to be accounted for when processing the data. Until now, IHCP has not been introduced in the experimental study of heat transfer in such evaporators when reducing local experimental data. In this paper, a new method for processing experimental local heat transfer data by solving the 3D IHCP is proposed. This method is then applied and validated using two sets of single- and two-phase flow experimental data obtained with infrared (IR) camera temperature measurements. The 14,400 raw pixel temperatures per image from the IR camera are first pre-processed by a filtering technique to remove the noise and then to smooth the data, where the IR camera has undergone a prior inhouse pixel by pixel insitu temperature calibration. Three filtering techniques (Wiener filter, spline smooth, and polynomial surface fitting) are compared. The polynomial surface fitting technique was shown to be more suitable for the current type of data set. Then the 3D IHCP is solved based on a finite volume method using the TDMA (Tridiagonal Matrix Algorithm) solver with a combination of Newton-Raphson iteration and a local energy balance method. Furthermore, the present 3D TDMA method (named as 3D TDMA) is compared with three other post-processing methods currently used in the literature, among which the present one is found to be more accurate for

reducing the local heat transfer data in multi-microchannel evaporators.

2.1 Introduction

The experiments on flow boiling in multi-microchannel evaporators aim to measure the local heat transfer coefficients at the interface between the wall and the fluid along the flow channels. However, only the heat flux and the temperature at the test section backside can be directly measured, whilst the heat spreading due to the gradient in the local saturation temperature and the significant variation in the heat transfer coefficient along the channels needs to be accounted for. In particular, as the local flow heat transfer coefficients change greatly in magnitude from single-phase liquid at the entrance to a peak in slug flow to a minimum at the transition to annular flow and then a new substantial rise up to the outlet, a significant heat spreading occurs due to the heat transfer process itself, and this has to be accounted for when processing the data. Accurate multi-microchannel evaporator data are of paramount importance to the building and validation of prediction methods used to simulate the local temperatures in a CPU or GPU, which must remain below their operating limit.

In such experiments, normally the heat flux is provided by a DC electrical microheater sputtered on the test section backside. The backside temperature traditionally is measured by thermocouples Qu and Mudawar (2002) or resistance temperature detectors (RTDs) Costapatty et al. (2012). These standard techniques provide the temperature measurements with a point value or a spatial averaged value, which is regarded to be zero-dimensional in terms of spatial resolution. Such data are usually reduced assuming that only 1D heat conduction occurs to obtain local heat transfer coefficients. Hence this technique falls short when monitoring the temperature information with high spatial variation.

Infrared cameras are able to provide “high definition” temperature measurements and are becoming more widely implemented for microscale heat transfer study Hetsroni et al. (2002); Xu et al. (2005); Krebs et al. (2010); Carlomagno and Cardone (2010); Hetsroni et al. (2011); Szczukiewicz et al. (2013). Compared to standard techniques, the IR camera tends to be superior due to several merits such as non-intrusive measurements, truly two-dimensional temperature maps, high frequency acquisition, etc. For instance, the non-intrusive technique avoids any interference on the temperature fields, the high resolution temperature map enables one to quantitatively evaluate the axial heat conduction, and the high frequency acquisition allows for transient thermal measurement. A pixel by pixel inhouse calibration also allows the IR temperature accuracy to become equivalent of those of thermocouples.

From the perspective of theoretical heat conduction models, the directly measured temperatures and heat flux on the test section backside are respectively considered to be the Dirichlet and Neumann boundary conditions while the desired heat transfer coefficients on the opposite side (on top) are the Robin boundary condition. The problem of determining the heat

transfer coefficients at the top boundary from the temperatures and heat flux measured at the bottom boundary and other boundary conditions by solving the heat conduction equation is regarded as an inverse heat conduction problem (IHCP) Beck et al. (1985). The principal difficulty in solving IHCP is due to its sensitivity to noise in the input temperature data. This noise incurs oscillations in the heat flux field since it is magnified while calculating the Laplacian term, or the second derivative of the temperature in the heat conduction equation.

To our knowledge, so far two solution strategies have been proposed in the literature to overcome such problems: (1) an iterative regularization scheme Tikhonov and Arsenin (1977); Alifanov (1994); Orlande et al. (2011); Rouizi et al. (2013, 2015), and (2) a pre-filtering of the raw temperature data Rainieri and Pagliarini (2002); Bozzoli et al. (2013); Delpueyo et al. (2013). The former iterative scheme was first implemented in Tikhonov and Arsenin (1977). This method is based on the least square error between the measured and simulated temperature data. A regularization parameter is involved in the least square formula. A proper selection of this parameter is able to cope with the noise in the input raw temperature data to further alleviate oscillations in the final solution. In this regard, the most general example is the iterative regularization scheme coupled with a conjugate gradient method Ozisik (1993). However, this method for solving IHCP is only practical for traditional temperature sensors which provide limited numbers of input and output data Beck et al. (1985). Instead, for applications with a large number of input temperatures from an IR camera, this method has shown to be cumbersome due to its expensive computational cost Bozzoli and Rainieri (2011).

As an alternative, pre-process filtering of the raw temperature data has proven to be efficient at handling such large noisy data Rainieri and Pagliarini (2002); Bozzoli et al. (2013). The pre-process filtering technique is therefore adopted in our present work. In this second approach, recently three filtering techniques (an ideal low-pass filter, a Gaussian filter, and a Wiener filter) have been compared in Bozzoli et al. (2013) with respect to an example of heat source restoration in a thin plate. They found that the consecutive implementation of the Wiener filter yielded the most suitable results. In their work, the 2D heat conduction model was built assuming a constant temperature distribution along the thickness direction due to a very low Biot number ($\ll 1$). It is worth noting that the filtering technique appears not to be suitable for the case of a limited number of measurement points obtained by thermocouples or RTDs.

Until now only a few researchers have considered the IHCP when reducing their flow boiling heat transfer data in minichannels. Poniewski and co-workers Piasecka et al. (2004); Hozejowska et al. (2009) have applied IHCP to flow boiling in single small diameter tubes when using liquid crystals to obtain high resolution external temperature fields. Luciani et al. (2008) applied the inverse method to reduce the local flow boiling heat transfer data of HEF-7100 in single minichannels under normal, hyper-, and microgravity. The boundary element method was implemented to resolve the inverse heat conduction problem in 2D and 3D models to characterize the local wall heat flux and temperature.

So far, the concept of IHCP has not been introduced into the experimental local heat transfer

data reduction in multi-microchannel evaporators. In most experimental studies, a 1D heat conduction model was employed to calculate the heat transfer coefficients using the measured temperature data at the backside of the test section without any iteration Qu and Mudawar (2002); Xu et al. (2005). The 1D model only considers the heat conduction through the thickness direction, assuming no heat spreads in the axial direction, which is only suitable for small spatial temperature variations. The axial heat conduction was evaluated in a non-uniform heat flux study using diode temperature sensors by the local 2D energy balance method Ritchey et al. (2014). That allowed a better determination of the net local base heat flux than a 1D approach. However, a 1D heat conduction model was still used to conduct the calculation up to the wall temperature using this adjusted base heat flux. Also, a full 2D model was implemented by Costa-patry et al. (2012) using an array of 35 silicon diode temperature sensors to study flow boiling of refrigerants in a multi-microchannel evaporator with a non-uniform heat flux, i.e. hot spot(s) in the imposed heat flux. However, they only considered the 2D heat conduction from the bottom to the top without any iteration. This is referred from now on as the “direct” method. Recently, a 3D heat conduction model was solved directly from observations at the back of a multi-microchannel test section to characterize the local heat transfer coefficients, without any iteration or resorting to IHCP Szczukiewicz et al. (2013).

In order to implement and validate the 2D conduction model used in their dynamic modeling of multi-microchannel evaporators Lamaison et al. (2013), the authors introduced an iterative approach to solve the 2D heat conduction problem by using a guessed heat transfer coefficient profile at the top boundary and the known base temperature profile as the investigator Lamaison (2014). However, three shortcomings remained in their work: (1) the heat transferred in the widthwise direction (perpendicular to the flow) was ignored (i.e. 2D only), (2) the local fluid temperature is needed, (3) the iteration with the guessed Robin boundary condition at the top appears to be much more time-consuming than the direct method of Szczukiewicz et al. (2013).

In the present work, we aim to provide a more practical and precise data processing method by solving the 3D IHCP for obtaining the local heat transfer data in multi-microchannels (single- and two-phase cases). This method is validated using two sets of single- and two-phase flow experimental data tests for a multi-microchannel test section. In the experiment, the IR camera was employed as the temperature sensor. Due to the high resolution of the IR temperature map, an improved way to determine the lateral boundary conditions is introduced. To remove the noise in the raw temperature data, three filtering techniques are employed: Wiener filtering, spline smoothing, and polynomial surface fitting. In the new method, the direct 3D heat conduction problem is solved firstly using a finite volume method (TDMA algorithm) with a guessed Dirichlet boundary condition at the top (instead of the time-consuming Robin boundary condition of Lamaison (2014)). Then a Newton-Raphson method is used to optimize the new footprint temperature array. Finally, the local energy balance method is employed to determine the local heat flux at the top boundary. As a final test, three heat conduction models

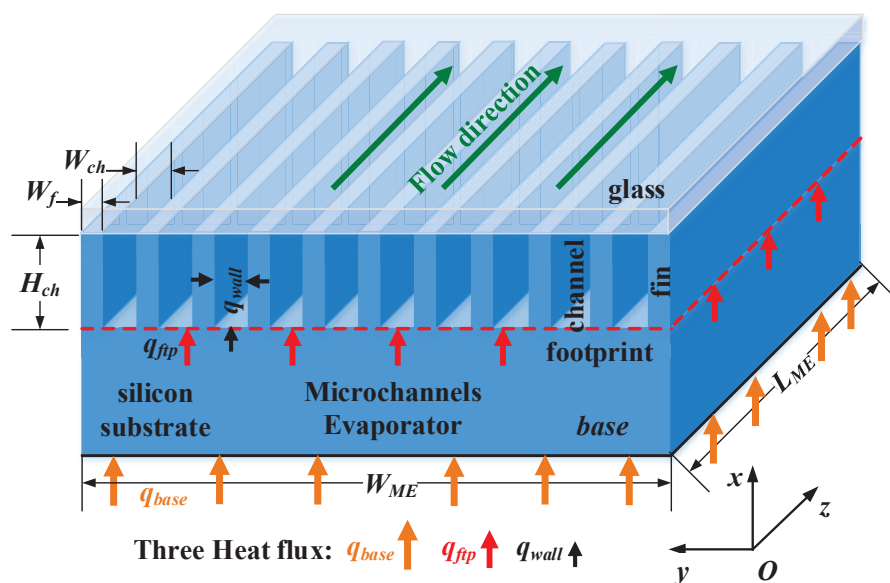
used in the current literature to reduce the experimental data are reviewed and compared with the new proposed method to demonstrate why it is important to go to this much detail to get accurate local heat transfer results.

2.2 Case descriptions

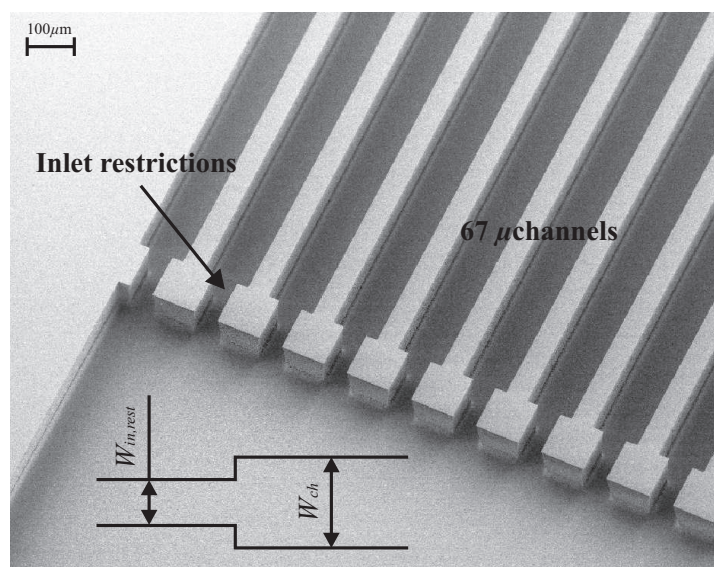
Two cases of experimental data composed of single- and two-phase flow were selected to validate the new method. The experimental facility used to acquire the data was the same as presented in Szczukiewicz et al. (2013), in which the details of the experimental setup and operation procedures were also introduced. In this part, only the experimental conditions are highlighted. As shown in Fig. 2.1, the microchannel evaporator tested during this experiment is made from silicon with 67 parallel microchannels, each $100 \times 100 \mu\text{m}^2$, with an inlet restriction ratio of 2 to stabilize the two-phase flow and obtain good flow distribution. The channels are 10 mm long and the test section is 10 mm wide. The low pressure refrigerant R245fa was used as the test fluid. The uniform heat flux was provided by two micro-heaters sputtered on the back side of the test section with a thickness of $1.5 \mu\text{m}$. The temperature map at the test section bottom covered by a high-emissivity matt tape was acquired by an IR camera (FLIR ThermaCAM SC3000) coupled with a close up lens (LW 34/80) at a frequency of 60 Hz and a resolution of 320×240 pixels. The IR camera was calibrated inhouse pixel by pixel (see Szczukiewicz et al. (2013) for calibration details) to an accuracy of 0.2 K according to the error propagation procedure, although at an isothermal condition all the pixels agreed within a band of ± 0.2 K. The pixels corresponding to the test section area of $10 \times 10 \text{ mm}^2$ gave an array of 120×120 pixels (14,400 temperatures per image), leading to a fine-resolution for the local footprint heat flux q_{ftp} and temperature T_{ftp} . This high spatial resolution however exaggerates the impact of the signal noise on the solution when solving the heat conduction equations. As a result, the original IR temperature signals need to be pre-processed by a filtering technique.

2.2.1 Case I: Single-phase flow

During the single-phase flow test, the saturation temperature was set to 60°C , allowing the subcooled fluid temperature to have enough room to increase without reaching saturation or subcooled boiling. The single-phase flow test was carried out at a mass flux of $G = 2000 \text{ kg m}^{-2}\text{s}^{-1}$ and a heat flux of $q = 20 \text{ W cm}^{-2}$ with the inlet fluid temperature of 27.4°C . The energy loss in this test to the housing of the test section and the ambient was quantified as 20.5% (based on a single-phase flow energy balance using the mass flow rate and the measured inlet and outlet temperatures). The local fluid temperature can be evaluated with the local q_{ftp} obtained from the heat conduction model presented in the latter section. The local fluid



(a)



(b)

Figure 2.1 – Test section: (a) Schematic of the multi-microchannel evaporator and (b) a photo of the microchannels with inlet orifices Szczukiewicz et al. (2013).

temperature T_{fl} can then be calculated locally based on the local energy balance:

$$q_{ftp}(y, z) = c_p \dot{m} \Delta T(y, z) \quad (2.1)$$

The local footprint heat transfer coefficients are calculated using the local values of q_{ftp} , T_{ftp} and T_{fl} , and the wall heat transfer coefficients are attained using the fin efficiency equations, where the axial heat conduction in the fins is ignored:

$$\alpha_{wall}(y, z) = \frac{\alpha_{ftp}(y, z) W_{ME} L_{ME}}{N_{ch} [W_{ch} L_{ME} + 2(L_{ME} + W_f/2) H_{ch} \eta_f(y, z)]} \quad (2.2)$$

$$\alpha_{ftp}(y, z) = \frac{q_{ftp}(y, z)}{T_{ftp}(y, z) - T_{fl}(y, z)} \quad (2.3)$$

$$\eta_f(y, z) = \frac{\tanh[m(y, z) H_{ch}]}{m(y, z) H_{ch}} \quad (2.4)$$

$$m(y, z) = \sqrt{\frac{2\alpha_{wall}(y, z)(L_{ME} + W_f)}{k_{Si}(y, z)(W_f L_{ME})}} \quad (2.5)$$

Since the local fin efficiency is unknown, Eqs. (2.2) to (2.5) need to be solved iteratively with an initially assumed fin efficiency until the convergence criterion is met. Finally, the local Nusselt number is calculated using:

$$Nu(y, z) = \frac{\alpha_{wall}(y, z) D_h}{k_{fl}(y, z)} \quad (2.6)$$

2.2.2 Case II: Two-phase flow

For the two-phase flow test, the outlet saturation temperature was set at 31.5°C. The two-phase experiment was conducted under a mass flux of $G = 2000 \text{ kg m}^{-2} \text{ s}^{-1}$ and a heat flux of $q = 20 \text{ W cm}^{-2}$ with the subcooled inlet fluid temperature at 30.4°C and an inlet subcooling of 5.4 K. The energy loss in this test was evaluated as 14%. Contrary to the single-phase flow test, the local fluid temperature in two-phase flow cannot be obtained based on an equation such as Eq. (2.1) since the flow is evaporating and the local fluid temperature is directly linked to the local pressure. The latter is generally predicted assuming a linear variation or using a two-phase pressure drop correlation. Therefore, the two-phase flow section will not exhibit any α_{wall} calculations (for which the fluid temperature profile is needed) but will rather end up with q_{ftp} and T_{ftp} calculations from the heat conduction model proposed below.

The uncertainty analysis based on the approach proposed by Kline and McClintock (1953) and the resulted uncertainty propagation were performed in this study. The obtained uncertainties of the main parameters are presented in Table 2.1. The footprint heat flux and temperature (T_{ftp} and q_{ftp}) were obtained by solving the 3D IHCP numerically. Their numerical uncertainties caused by the input measurements uncertainty (T_{IR} and q_{base}) was evaluated by the

“Brute force method” Teodosiu et al. (2003).

Table 2.1 – Experimental measurement uncertainties of main parameters.

Parameter	Unit	Uncertainty	
		SP	TP
T_{tc}	°C	± 0.1 °C	
T_{IR}	°C	± 0.2 °C	
q	W cm ⁻²	$\pm 0.16\%$	
G	kg m ⁻² s ⁻¹	$\pm 4.25\%$	
T_{ftp}	°C	$\pm 0.44\%$	$\pm 0.49\%$
q_{ftp}	kW m ⁻²	$\pm 5.9\%$	$\pm 11.6\%$
α_{ftp}	kW m ⁻² K ⁻¹	$\pm 5.7\%$	$\pm 12.1\%$
α_{wall}	kW m ⁻² K ⁻¹	$\pm 6.3\%$	$\pm 8.3\%$
Nu	–	$\pm 9.4\%$	

2.3 Theory

2.3.1 Filtering techniques

Three filtering techniques were considered and compared here. They are discussed below.

Wiener filter The Wiener filter has been shown to be an efficient tool to remove the noise in the raw data of ill-posed IHCP Rainieri et al. (2004); Bozzoli et al. (2013). The principle advantage of this filtering technique is related to its self-adaptivity by tailoring itself to the local noise level. Based on a statistical approach, the Wiener filter estimates the new data pixel by pixel from its neighborhood data points by minimizing the square of the error between the estimated data and the original one. The local mean and variance of each data point are defined as follows:

$$\mu = \frac{1}{E \cdot F} \sum_{i,j \in \Omega} T_{exp}(i, j) \quad (2.7)$$

$$\sigma^2 = \frac{1}{E \cdot F} \sum_{i,j \in \Omega} [T_{exp}(i, j) - \mu]^2 \quad (2.8)$$

where Ω , the local neighborhood, consists an array of E-by-F pixels. Then the filtered sample temperature can be estimated as:

$$\tilde{T}_{exp}(i, j) = \mu + \frac{\sigma^2 - v^2}{\sigma^2} [T_{exp}(i, j) - \mu] \quad (2.9)$$

where v is the noise variance (assumed as additive Gaussian white noise if it is unknown). This technique requires an adjustment to filter the data points close to the boundary. To overcome this problem at the boundary of the pixel field, a different window size can be used to make the statistical estimation.

Spline smoothing The spline function is another efficient tool to smooth noisy or discrete data Craven and Wahba (1979). The two-dimensional bicubic spline $s(x, y)$ is expressed in its B-spline series representation El Abbass et al. (1990) as:

$$s(x, y) = \sum_{i=1}^p \sum_{j=1}^r C_{ij} M_i(x) N_j(y) \quad (2.10)$$

where $M_i(x)$ and $N_j(y)$ are the normalized cubic B-splines, and the coefficients C_{ij} are determined by solving the following constrained minimization problem: Minimize γ with the constraint $\theta_r \leq S$, where γ is a measure of the lack of smoothness of $s(x, y)$, θ_r represents the weighted residual $\omega_r[f_r - s(x, y)]$, and S controls the extent of smoothing and is thus also named the smoothing factor Dierckx (1981).

Polynomial surface fitting Fitting data from a surface using polynomials has been used for geophysical data El Abbass et al. (1990). The value at each calculated point is determined by implementing a polynomial surface fit to the neighboring data with a least square approach:

$$\tilde{T}(x, y) = \sum_{i=0}^N \sum_{j=0}^{N-i} A_{ij} x^i y^j \quad (2.11)$$

$$R = T(x, y) - \tilde{T}(x, y) \quad (2.12)$$

where N is the polynomial degree, A_{ij} are the polynomial coefficients, and x, y denote the location of the point. Once the polynomial degree is determined, the polynomial coefficients are identified by solving the minimization problem, $\sum R^2 = \text{minimum}$, using least square method.

2.3.2 3D IHCP

Turning now to the steady state 3D heat conduction problem, the present experimental case is governed by the following expressions:

$$\frac{\partial}{\partial x} \left(k \frac{\partial T}{\partial x} \right) + \frac{\partial}{\partial y} \left(k \frac{\partial T}{\partial y} \right) + \frac{\partial}{\partial z} \left(k \frac{\partial T}{\partial z} \right) = 0; \quad (2.13)$$

$$T(0, y, z) = T_{IR}, q(0, y, z) = q_b \quad (2.14)$$

$$q(x, 0, z) = q_s, q(x, W_{ME}, z) = q_n \quad (2.15)$$

$$q(x, y, 0) = q_w, q(x, y, L_{ME}) = q_e \quad (2.16)$$

where x, y, z indicate the direction in the thickness x and the widthwise y and lengthwise z (flow) directions, as shown in Fig. 2.2, and q_w, q_e, q_n and q_s are the heat fluxes at the four lateral sides of the substrate. The thickness of the micro-heater ($1.5 \mu\text{m}$) was neglected. Currently, in most of the literature, the heat fluxes at the lateral sides are assumed to be zero (adiabatic). Due to this assumption, the local footprint heat flux at the perimeter of the evaporator would be obviously higher than in reality. This is because the heat actually lost by conduction to the surrounding base of the test section inadvertently then gets assigned to the nodes near and at the perimeter while the measured temperatures in those pixels are lower. To take this into account, a new way to approximately determine the Neumann boundary condition at the four lateral sides are proposed based on the IR temperature map. Here the Neumann boundary condition at each of the four lateral sides is assumed to be constant, and its calculation is presented in next section.

Additionally, instead of the regular way for solving IHCP using an iterative regularization

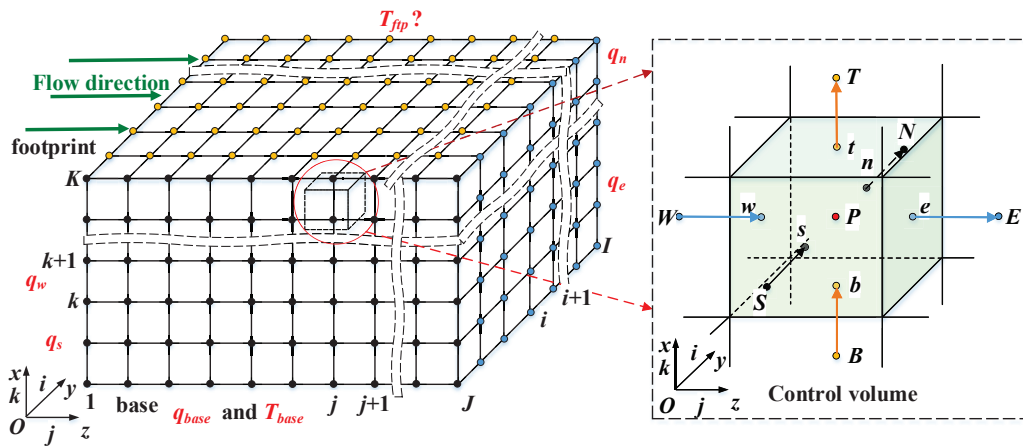


Figure 2.2 – Mesh types used in the 3D-TDMA model.

scheme, as mentioned previously, a new method based on a temperature filtering technique

is used. The main steps used in the new method to solve the 3D IHCP are as follows:

- (1) Filter the raw IR temperature data;
 - (2) Solve the direct 3D heat conduction problem based on the finite volume method using a 3D TDMA solver with an initial guessed temperature map at the footprint T_{ftp}^k (i.e. top surface in Fig. 2.2);
 - (3) Check if $\delta T_{base} = T_{base,cal} - T_{base,meas} \leq \epsilon$ to decide whether to stop or continue (ϵ being the convergence criterion);
 - (4) Use the single variable Newton-Raphson method locally to optimize the new temperature map at the footprint: $T_{ftp}^{k+1} = T_{ftp}^k - \frac{\delta T_{base}}{T_{base,per}^i}$;
 - (5) Proceed back to step 2 with T_{ftp}^{k+1} until the convergence criterion is achieved;
 - (6) Implement the local energy balance at the footprint to determine the local heat flux, q_{ftp} .
- The flow chart used in the new method is depicted in Fig. 2.3.

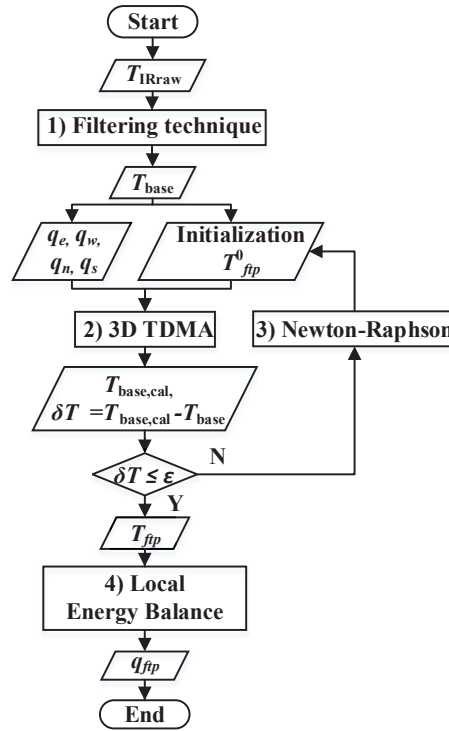


Figure 2.3 – Flow chart of the new method.

Boundary conditions

The Neumann boundary condition at the lateral sides refer to q_w , q_e , q_n and q_s in the 3D model, as shown in Fig. 2.2. So far in the open literature, these boundary conditions have been

traditionally assumed to be adiabatic, i.e. no heat loss at the lateral sides. This assumption will introduce obviously higher local heat flux at the lateral sides than the rest region ¹. Assuming adiabatic boundary condition is mainly due to the fact that there is no reference related to the boundary condition from the traditional experimental perspective. However, it is far from reality to ignore the heat conduction from the heated silicon test section to the surrounding thickness of the base of the finned cold plate evaporator and its manifold, especially for those made of copper on silicon. Thanks to the fine-resolution temperature map from the IR camera, approximate Neumann boundary conditions can be defined.

Applying the definition of the heat flux $q = -k \frac{dT}{dz}$ at the boundary, it is simple to calculate the heat flux if the temperature gradient $\frac{dT}{dz}$ is known. In this regard, the 2D temperature map from the IR camera provides sufficient information. The total lateral heat conduction $Q_{lateral}$ leaving the test section through its sides is thus evaluated by summarizing the heat loss at the four sides. Then, in order to respect the energy balance, the base heat flux q_b can be adjusted from the total heat power Q_{total} by combining the total heat loss and the lateral heat conduction as follows:

$$q_b A_b = Q_{total} - (Q_{loss} - Q_{lateral}) \quad (2.17)$$

$$Q_{lateral} = q_w A_w + q_e A_e + q_s A_s + q_n A_n \quad (2.18)$$

where w, e, s and n refer to the four directions. The above equations essentially redistribute the heat loss in a more rational way, thus allowing the base heat flux to be more accurately evaluated by accounting for the lateral heat loss in the heat conduction model. In this manner, the pixels influenced by the lateral heat conduction around the perimeter of the test section can be quantitatively identified and thus removed from the heat transfer database.

3D TDMA

The 3D heat conduction equation is a non-linear elliptical equation. Therefore, the solution is impacted by all of the boundary conditions. This means that the boundary conditions at all six boundaries should be simultaneously solved in the calculation. One might note that the boundary condition at the footprint is missing. However, there are two boundary conditions at the base, a Dirichlet and a Neumann boundary condition. Therefore, the 3D heat equation can be solved with the footprint temperature as the objective and the measured base (bottom) temperature the investigator, i.e. iterating on the T_{ftp} boundary condition in order to satisfy the condition on the measured base temperature (as already shown in Fig. 2.2).

The 3D heat conduction equation was discretized based on the finite volume method, which integrates the equation on a control volume basis Patankar (1980). One advantage of this method is to monitor the local energy balance at each control volume. The vertex-centered

1. this conclusion is based on our investigation by testing adiabatic boundary conditions and diabatic ones

grid type was implemented in the discretization of the silicon substrate, as demonstrated in Fig. 2.2, because this grid type allows the direct use of the base temperature map as the investigator. In order to maintain the energy balance at the interface of two neighboring control volumes, the harmonic average thermal conductivity between the two neighboring nodes is used. Both the Dirichlet and Neumann boundary conditions were addressed as source items. The generalized format is expressed as:

$$a_P T_P = \sum a_{nb} T_{nb} + S_u \quad (2.19)$$

$$a_P = \sum a_{nb} - S_P \quad (2.20)$$

where the subscript nb in the 3D model represents the node of W , E , N , S , T , or B (see the control volume in Fig. 2.2). The detailed process of the discretization has been well explained in Patankar (1980). Then this series of algebraic equations was solved iteratively by the TDMA (Tridiagonal Matrix Algorithm) solver. During each calculation, the temperatures at the nodes along the South-North direction are unknown, assuming the temperature at the neighboring four nodes are known. Therefore, the calculation direction proceeds from South to North, then moves to the next line from West to East, and finally from bottom to the top until the pre-defined convergence criterion is met. Then the thermal conductivity is updated globally with the newly obtained temperature of each node. After the solution converges for the initially guessed T_{ftp}^k , the Newton-Raphson method is used to optimize the next T_{ftp}^{k+1} and the TDMA solver is called again to obtain the new footprint temperature map.

Newton-Raphson iteration

The Newton-Raphson method for optimization is very efficient but not robust due to its dependence on the initial value. When referring to the silicon microchannel evaporator, however, a simple 1D heat conduction model can provide a sufficiently good initial guess of the footprint temperature. In the current experimental case, the temperature difference between the test section bottom and the footprint was evaluated to be about 0.4 K (as reported in Hetsroni et al. (2011), regarding the usual range of 0.15 ~ 0.8 K for a silicon microchannel evaporator). Therefore, the initial temperature array, T_{ftp}^0 , is guessed by subtracting 0.4 K from the measured base temperature map ($T_{ftp}^0 = T_{base} - 0.4$). The Newton-Raphson method is

described as follows:

$$\delta T_{base} = T_{base,cal} - T_{base,meas} \quad (2.21)$$

$$\delta T_{base_{pert}} = T_{base,cal_{pert}} - T_{base,meas} \quad (2.22)$$

$$T'_{base_{pert}} = \frac{\delta T_{base_{pert}} - \delta T_{base}}{pert} \quad (2.23)$$

$$T_{ftp,new} = T_{ftp,old} - \frac{\delta T_{base}}{T'_{base_{pert}}} \quad (2.24)$$

For each TDMA solver call (i.e. each T_{ftp} map), the maximum absolute temperature difference between the two consecutive calculations was used as the convergence criterion, and was set at 10^{-9} K in this case. For the Newton-Raphson iteration, the convergence criteria was set as 0.05 K based on the maximum local difference of base temperature between the calculated and the measured one. The perturbation ($per\ t$) of the Newton-Raphson iteration method was chosen to be 0.0001. Normally this method yields a converged solution within two or three steps when using the properly filtered temperature map.

Energy balance method

After convergence is reached with the 3D heat conduction equation by the TDMA solver coupled with Newton-Raphson method noted above, the local footprint heat flux q_{ftp} is obtained by a local energy balance method for all the cells at the top layer of the grid:

$$Q_N + Q_S + Q_W + Q_E + Q_T + Q_B = 0 \quad (2.25)$$

In the above equation, Q_T is calculated as $A_t q_{ftp}(y, z)$ while the other terms are obtained from the local finite volume discretized Fourier equation (taking appropriate heat transfer surfaces).

2.3.3 Current heat conduction models in literature

In the open literature, three heat conduction models have been described so far to reduce the experimental data in microchannel evaporators: 1D-Direct, 2D-TDMA, and 3D-Direct models. These models are presented and discussed below.

1D-Direct model

The popular 1D-Direct heat conduction model used in Qu and Mudawar (2002); Xu et al. (2005) simply implements the Fourier law layer by layer from the base to the footprint, as shown in

Fig. 2.4a. It is referred as a “direct” model since it uses the 2 boundary conditions at the base layer (i.e. the temperature and the heat flux) without iterating on the boundary condition at the footprint. The boundary conditions on all lateral sides of the substrate are considered to be adiabatic and the governing equation of 1D heat conduction model is thus:

$$q = -k \frac{\partial T}{\partial x}, T(z) = T_{IR}(z), q(z) = q_b(z) \quad (2.26)$$

Considering that the thermal conductivity of silicon is temperature dependent, its relation with temperature is accounted for as:

$$k = 0.0007T^2 - 0.5416T + 157.39 \quad (2.27)$$

In the 1D-Direct model, the discretization is only performed in the thickness direction x , and the proper number of layers in the grid is identified through a grid independent analysis. The number of calculation points along the evaporator lengthwise, i.e. along the flow direction, is determined by the number of temperature measurement points.

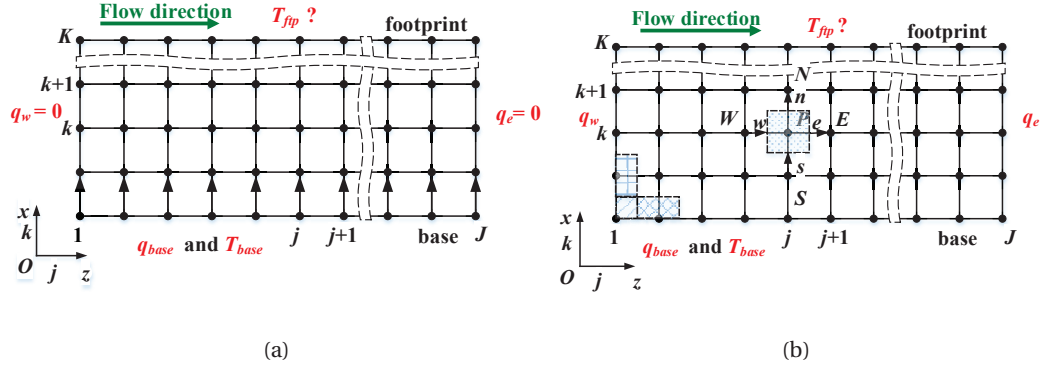


Figure 2.4 – Mesh types used in 1D-Direct and 2D-TDMA models: (a) Mesh in 1D model and (b) Mesh in 2D model.

2D-TDMA model

The 2D heat conduction model deals with both thickness and lengthwise heat transfer, i.e. the xz plane in Fig. 2.4b. The steady state 2D heat conduction equations and its boundary

conditions are expressed as follows:

$$\frac{\partial}{\partial x} \left(k \frac{\partial T}{\partial x} \right) + \frac{\partial}{\partial z} \left(k \frac{\partial T}{\partial z} \right) = 0 \quad (2.28)$$

$$T(0, z) = T_{IR}(z), q(0, z) = q_b(z) \quad (2.29)$$

$$q(x, 0) = q_w(z), q(x, L_{ME}) = q_e(x) \quad (2.30)$$

Contrary to the 1D-Direct model, the 2D-TDMA model uses only one boundary condition (i.e. temperature or heat flux) at the base and iterates on the footprint boundary condition. In Lamaison (2014) the 2D heat conduction model was solved iteratively based on the finite volume method by a TDMA solver, and a guessed Robin boundary condition at the footprint. However, this boundary condition, as mentioned previously, is time-expensive to obtain a converged solution. Therefore, this Robin condition has been modified here to evaluate this approach by guessing a Dirichlet boundary condition at the footprint. The discretized 2D heat equation is similar to Eq. (2.19) and Eq. (2.20), while the subscript nb in 2D model represents W , E , N , or S . Similar to the 3D-TDMA model, the 2D-TDMA model is solved by a TDMA solver based on the finite volume method combining the Newton-Raphson iteration. The footprint heat flux is then obtained through the local energy balance method.

3D-Direct model

The 3D direct heat conduction model is derived from the energy balance method, which is the sum of the net heat entering the central node from three dimensions being equal to zero in steady state. The 3D heat equation is solved directly from the bottom of the test section to the footprint, in the same manner as the 1D-Direct model (i.e. without iteration). For the internal nodes, the discretized equations are as follows:

$$Q_N + Q_S + Q_W + Q_E + Q_T + Q_B = 0 \quad (2.31)$$

$$Q_B = A_b k_b [T(i, j, k-1) - T(i, j, k)] / \Delta x \quad (2.32)$$

$$Q_T = A_t k_t [T(i, j, k+1) - T(i, j, k)] / \Delta x \quad (2.33)$$

$$Q_N = A_n k_n [T(i+1, j, k) - T(i, j, k)] / \Delta y \quad (2.34)$$

$$Q_S = A_s k_s [T(i-1, j, k) - T(i, j, k)] / \Delta y \quad (2.35)$$

$$Q_W = A_w k_w [T(i, j-1, k) - T(i, j, k)] / \Delta z \quad (2.36)$$

$$Q_E = A_e k_e [T(i, j+1, k) - T(i, j, k)] / \Delta z \quad (2.37)$$

For the peripheral nodes, their Q and A vary depending on the local boundary condition. For example, when this method is employed at the first layer (the test section bottom), the temperature of the upper layer can be obtained with the known $Q_B = A_b q_b$ and T_{base} . Additionally,

the thermal conductivity is updated with the new current temperature value. Then, progressively using the energy balance method from bottom to the top, the local temperature and heat flux at the footprint are obtained. Again, a grid independent analysis is used to determine the proper number of layers along the thickness direction, while the IR pixel spacings are used in the yz planar directions. This method has been used in the work of Szczukiewicz et al. (2013).

2.4 Analysis of results and discussion

2.4.1 Filtering techniques comparison

In the present section, the 3D IHCP was solved with the pre-processed temperature from the three filtering techniques previously described. The results based on the two-phase experimental data are compared in order to decide which of these techniques is better to be adopted. Prior to the comparison of the filtering methods, a grid independence analysis was performed along the x -direction, i.e. across the thickness of the substrate. The number of grid cells in the yz plane (as denoted in Fig. 2.2) are fixed according to the IR camera pixel numbers, which are 120×120 in this case and uniformly distributed. The number of grid cells in the x -direction was successively set to 5, 10 and 20 and the 3D IHCP was solved using the filtered data obtained from the polynomial surface fitting. The maximum absolute variation in q_{ftp} from 10 to 20 grid cells was only 0.2% while the computational time was increased to 2627 s from 271.9 s (a factor of 10). Hence the grid type of $10 \times 120 \times 120$ was chosen and used for all the results further presented.

The Wiener filter is applied twice as suggested in Bozzoli et al. (2013) to remove the noise and then to smooth the data. The smoothing factor used in the spline smoothing function is 8. In polynomial surface fitting, the orders of 4 and 4 are chosen respectively for the fits in the axial and perpendicular flow directions. The least absolute residual method is used as the robust linear least-squares fitting method.

Fig. 2.5 describes the filtering details with the three techniques against the raw IR temperature data of the 70th row ($i = 70$) along the flow direction. It is shown that (1) the spline smoothing technique generated the closest results to the raw data, (2) the polynomial surface fitting gave the purely smooth results with relatively higher error as a compromise, and (3) the Wiener filter yielded only moderate results. The mean of the temperature difference square between the filtered and measured ones is used to evaluate the performance of a filtering approach. This value is defined as:

$$\xi = \frac{1}{E \cdot F} \sum_{i,j \in O} [T_{exp}(i, j) - \tilde{T}_{exp}(i, j)]^2 \quad (2.38)$$

Chapter 2. Heat conduction models

When the mean of this value is below or close to the standard deviation of the raw temperature data Bozzoli et al. (2013), which is 0.07 K according to the present set from the IR camera, the filtered temperature is considered to be sufficiently accurate to be used for solving the inverse problem. Table 1 lists the difference between the three filtering approach in terms of error ξ , Newton-Raphson iteration steps and computation time to solve the entire 3D IHCP. Since each ξ of the three filtering techniques is found to be less than 0.07 K, all of them provide a sufficiently accurate temperature map for solving the IHCP.

Based on the three temperature filtering techniques, the footprint heat flux q_{ftp} was obtained

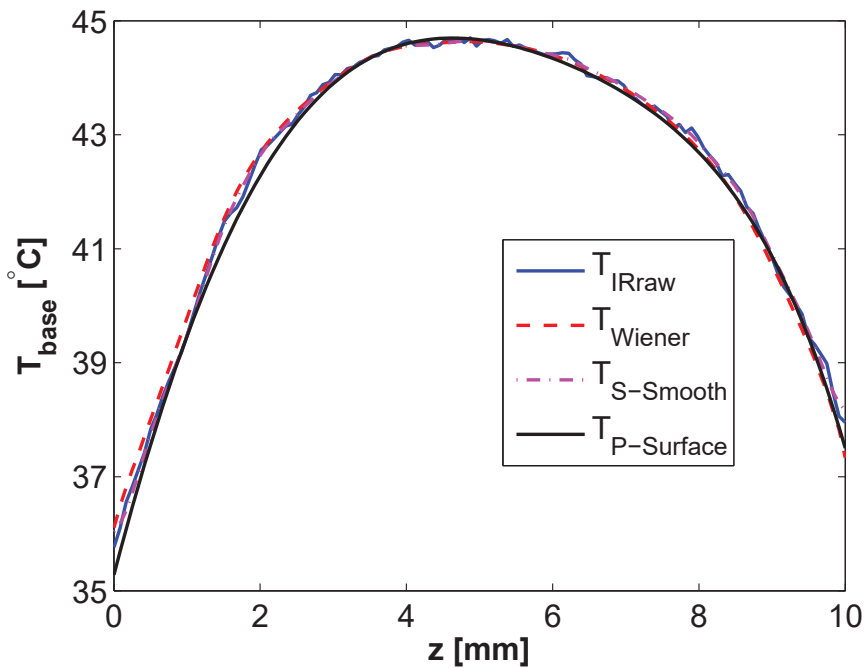


Figure 2.5 – Filtering results comparison against raw IR temperature ($i = 70$).

by solving the 3D IHCP and the results are shown in Fig. 2.6. It is found that the results based on the Wiener filter oscillated immensely, although the filtered IR temperatures appeared to be relatively smooth (see Fig. 2.5). This is because that the high-resolution temperature map (120×120 pixels in a small area of $0.01 \times 0.01 \text{ m}^2$) causes an oscillation in the second

Table 2.2 – Results from the three temperature filtering techniques.

Technique	ξ	NRsteps	Time(s)
Wiener filter	0.0403	317	6201.2
Spline smooth	0.0066	6	118.4
Polynomial surface	0.0601	2	271.9

derivative of the filtered temperature if the filter method is not appropriate. The results from the spline smoothing function fluctuated moderately around that from the polynomial surface fitting, though its corresponding ξ shown in Table 2.2 was the smallest one. This means the two filters are not robust enough to remove the impact of the signal noise on the Laplacian item, although they generated numerically converged solutions. On the other hand, the polynomial surface fitting generated smooth results with a reasonable calculation time.

In order to retain the original spatial fine resolution of temperature measurements (120×120

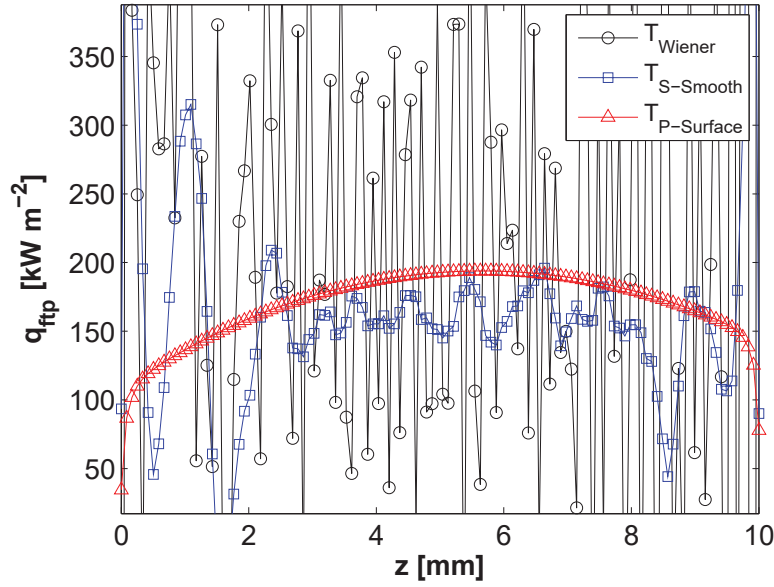


Figure 2.6 – Comparison of two-phase flow widthwise averaged local footprint heat flux from the three temperature filtering techniques.

pixels in an area of $0.01 \times 0.01 \text{ m}^2$), for our application, the success of solving the inverse heat conduction problem here to reduce the local heat transfer data comes from both the low noise level in our data and the smoothness of the data after filtering. As shown in Fig. 2.5, the Wiener filter and the spline smoothing function has generated nearly noise-free but not continuously differentiable data (ignoring the discontinuity of data), which are required by the present fine spatial resolution when calculating the second derivative item in heat equations in order to reach a physical solution of the footprint heat flux. This is also the reason why significantly non-physical oscillations in footprint heat flux obtained from the filtered data by the forgoing two methods were found in Fig. 2.6.

Regarding the link between the filter parameters and the effect of noise on an optimum inversion, the optimum inversion is not sensitive to the noise levels found in this particular application ($\pm 0.2 \text{ K}$) once an appropriate filter technique is chosen, which is referred to the polynomial surface fitting in our applications. For the polynomial surface fitting, the only filter parameters are the orders of fitting, which were chosen to be 4 and 4, as stated previously.

The reason for choosing such fitting orders is due to the trade-off between the global filtering accuracy and the boundary filtering precision which plays a very important role in boundary condition estimation.

On the other hand, if an inappropriate filtering technique is selected, such as the Wiener filter or the Spline smoothing presented in the manuscript, only changing the filtering parameters such as the cut-off frequency and the filtering window size is not enough for an optimum inversion. This is because such a filtering technique does not yield a continuously differentiable temperature profile as stated above.

In order to analyze the sensitivity of the optimum inversion towards the noise amplitude when using the polynomial surface fitting, five types of noisy base temperature data generated by adding five different noise amplitudes to a pre-filtered base temperature profile given by a previous polynomial surface fitting ($T_{P-Surface}$ in Fig. 2.5) were processed according to the procedures described in Fig. 2.3. This base (datum) temperature profile was used as it is an accurate representation of that found in the application. The noise was generated by a uniformly distributed pseudorandom function in MATLAB with a defined absolute range, which was 0.1, 0.2, 0.4, 0.6 and 1 K in the present case. The sensitivity of polynomial surface fitting to the noise amplitude in the base temperature data is presented in Fig. 2.7. Fig. 2.7a describes the accurate base temperature filtered by the polynomial surface fitting and five types of noisy base temperatures with different noise amplitudes. Fig. 2.7b presents the widthwise averaged local footprint heat fluxes obtained, which are nearly the same. This relative absolute error of the overall averaged footprint heat flux is shown in Fig. 2.7c. It can be seen that the error is negligible and increases with increasing signal noise. Therefore, the present polynomial surface fitting is able to provide an optimum inversion for the noise levels within the range tested in the present case.

Therefore, the polynomial surface fitting technique is recommended to filter the raw IR temperature and has been employed for the experimental data reduction. Additionally, it is worthwhile to mention that this polynomial surface fitting technique is suitable for high-resolution temperatures, but is not appropriate for the case with a point hot spot, since the point information will be smoothed out.

2.4.2 Comparison of heat conduction models

Based on the filtered temperatures obtained using the polynomial surface fitting technique, q_{ftp} and T_{ftp} were obtained through the various heat conduction models described previously. In order to compare with one dimensional values of q_{ftp} and T_{ftp} from the 1D-Direct and 2D-TDMA models, the results from 3D-Direct and 3D-TDMA models were averaged along the widthwise direction.

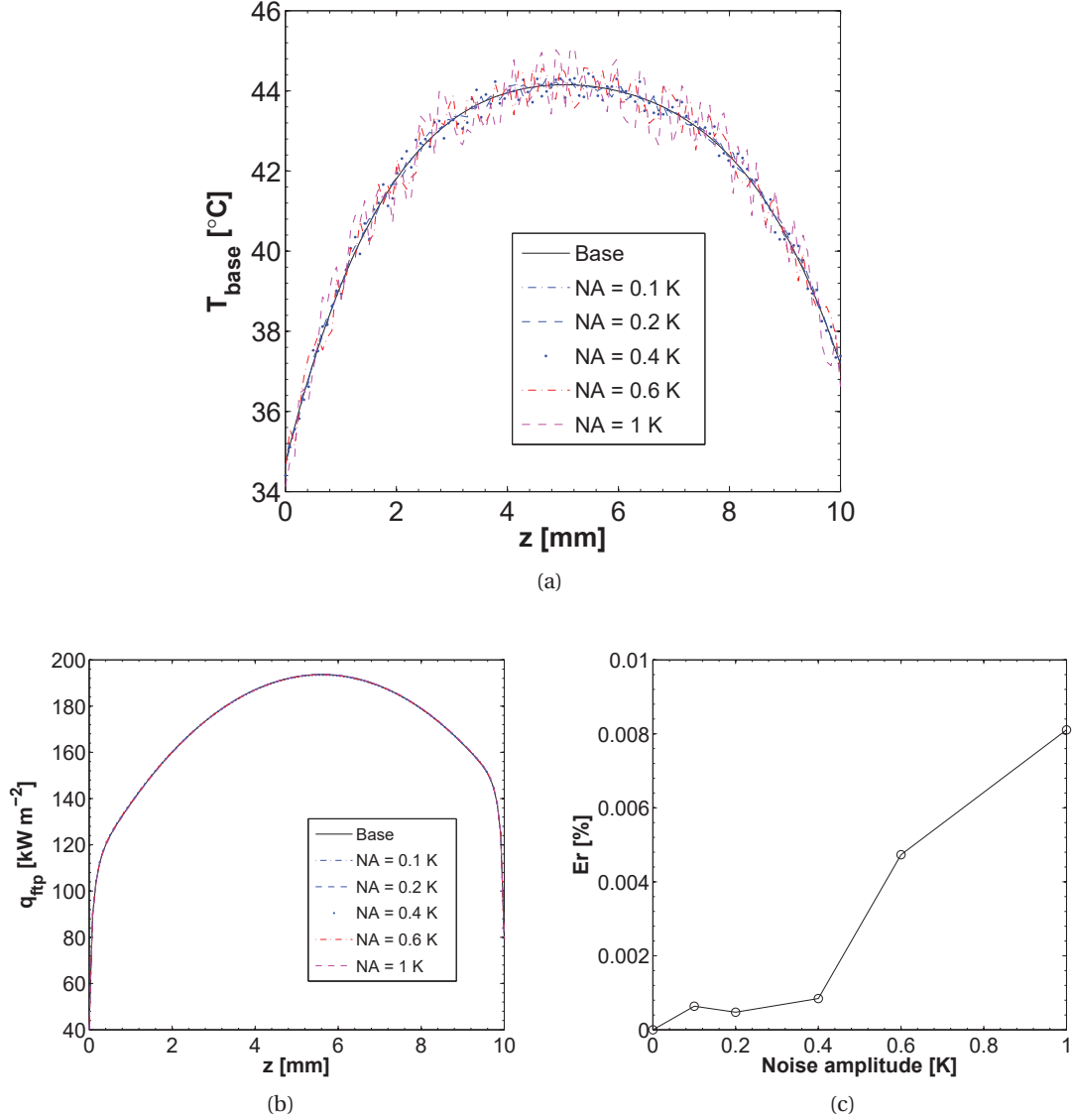


Figure 2.7 – Sensitivity of polynomial surface fitting to the noise amplitude in the base temperature data: (a) local base temperature at $i = 70$ where NA represents noise amplitude, (b) obtained widthwise averaged footprint heat flux and (c) absolute relative error of overall averaged footprint heat flux versus the absolute the noise, where $Er = \frac{|q_{ftp,av,no} - q_{ftp,av}|}{q_{ftp,av}} \times 100\%$.

Case I: Single-phase flow

Footprint heat flux and temperature Fig. 2.8a shows the different local footprint heat fluxes based on the four heat conduction models (i.e. the three found in the open literature and the new one). The first and last 20 original grid cells are kept to maintain the original trend, while in the middle a sparse grid is presented for a clearer view. The 3D-Direct model introduces a non-physical oscillation at the regions close to the boundary. The extreme values were cut from

the current plot to maintain a good viewing scale. The footprint heat flux from the 3D-Direct model in most of the regions are lower than those from the rest of the models. This discrepancy comes from the considerable amount of heat conducted to the ends when considering the total energy balance. However, the TDMA models (2D and 3D) generate reasonable results, which are close to the results from the 1D-Direct model.

Fig. 2.8b describes the trend of local footprint temperature along the flow direction. It is shown

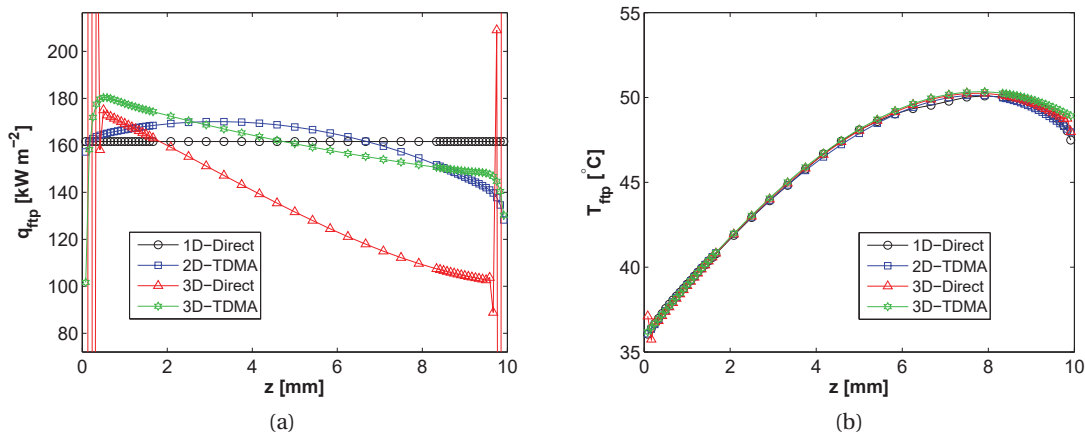


Figure 2.8 – Single-phase flow local footprint heat flux (a) and temperature (b) (sparse grid in the middle is used for a clearer view).

that the footprint temperature first increases nearly linearly versus length, then decreases when approaching the channel outlet. This decreasing trend might be due to the heat spreading from the test section to the manifold. From the results of 3D-TDMA model, the maximum temperature difference between the base and the footprint was 0.4 K.

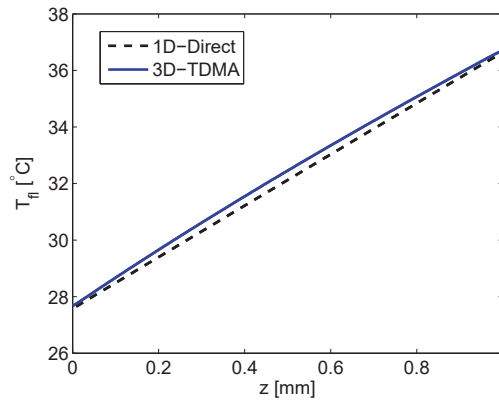


Figure 2.9 – Single-phase flow fluid temperature along the flow direction.

Local fluid temperature, heat transfer coefficients, and Nusselt number Following the analysis presented in Hetsroni et al. (2005), the axial heat conduction in the fluid needs to be taken into account in the regions where $z \leq 10 \frac{D_h}{Pe}$. For the current single-phase flow case at $G = 2000 \text{ kg m}^{-2}\text{s}^{-1}$, the corresponding length z is $0.325 \mu\text{m}$, which is negligible. The fluid temperature in single-phase flow is usually assumed to increase linearly along the flow direction based on the premise of a uniform heat flux imposed on the test section backside Qu and Mudawar (2002). However, one might note that the q_{ftp} as discussed previously is not uniform even though the base heat flux is constant. Thus the fluid temperature is unlikely to increase linearly. Fig. 2.9 represents the local fluid temperature based on the 1D-Direct model and 3D-TDMA model. The 1D-Direct model predicted a linear rise of the fluid temperature. However, the result from the 3D-TDMA model revealed that the fluid temperature increased with a parabolic trend but shared the same outlet temperature with that from the 1D model due to the total energy balance. The maximum difference in fluid temperature between the two models is 0.3 K.

The local wall and footprint heat transfer coefficients and the fin efficiency based on the

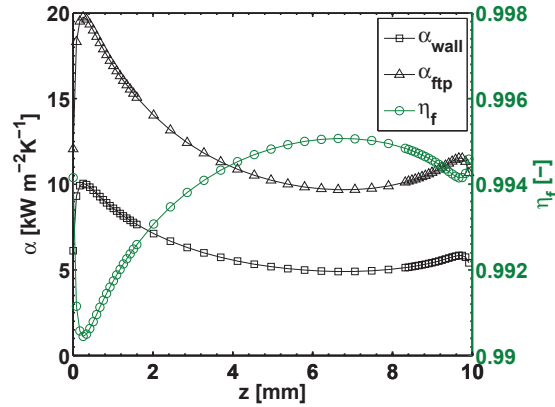


Figure 2.10 – Single-phase flow local heat transfer coefficients and fin efficiency obtained with the new 3D-TDMA model.

3D TDMA heat conduction model are plotted in Fig. 2.10. The heat transfer coefficients between the wall and the footprint are linked by the fin efficiency, which is very close to 1 in the current experimental case. For this experimental condition, the thermal entrance length, $L_{th} = 0.05 Re D_h Pr = 0.0154 \text{ m}$, is longer than the channel length of 0.01 m . Therefore, the fluid is always thermally developing. In such a case, it is known that the heat transfer coefficients continuously decreases along the channel. In our case, the slight increase towards the channel exit is considered to be related to the heat spreading to the manifold.

Fig. 2.11 compares the predicted local Nusselt number from the correlation of Shah and London (1978) with the experimental ones based on the 1D-Direct, 2D-TDMA and 3D-TDMA

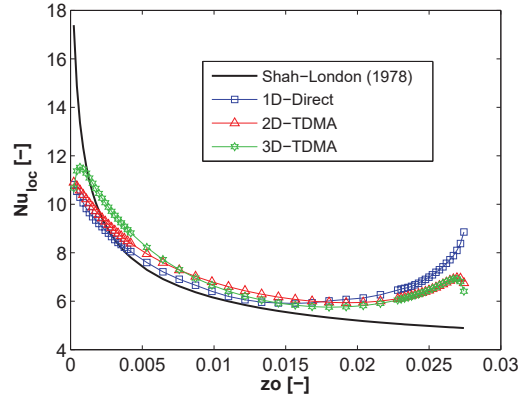


Figure 2.11 – Single-phase flow local Nusselt number comparison.

models, where zo is a dimensionless number defined as $zo = \frac{\pi z}{4RePrD_h}$. The agreement between prediction and the experimental results is good except for areas close to the channel exit, where the experimental value is higher than the predicted one. This is probably due to the exit effect at the channel end caused by a sudden expansion occurring when fluid exits the channel. This exit effect might introduce a disturbance in the thermal boundary layer, thus enhancing the local heat transfer. To further evaluate the performance of the three heat conduction models, the mean absolute errors (MAE) were obtained to be 14.47%, 13.08% and 11.81% respectively for 1D-Direct, 2D-TDMA and 3D-TDMA models. Note that the values near the inlet are influenced by the inlet orifice. Therefore, the 3D-TDMA model is proven to be more accurate for reducing the experimental data of such a multi-microchannel evaporator.

Case II: Two-phase flow

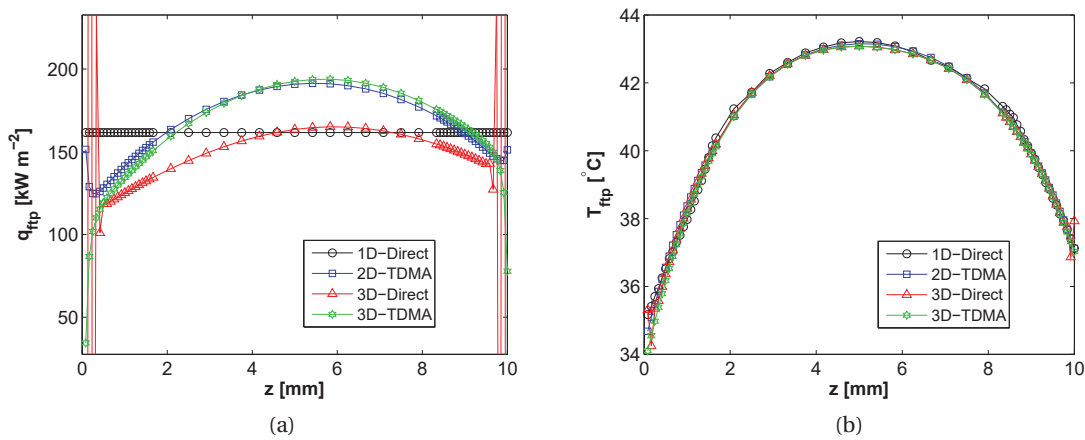


Figure 2.12 – Two-phase flow local footprint heat flux (a) and temperature (b).

Footprint heat flux and temperature Fig. 2.12 shows the local q_{ftp} and T_{ftp} at the footprint of the two-phase flow test based on the four different models. The 1D-Direct model simply predicted a constant value, which is as expected the same as q_{base} . The 2D-TDMA and 3D-TDMA models yielded similar results especially in the middle region. In the 2D-TDMA model, the unrealistic slight rise of heat flux at areas close to the two endings is resulted from ignoring the heat conduction in widthwise direction. The q_{ftp} from the 3D-Direct model strongly oscillated from -2.83 to $2.14 \times 10^3 \text{ kW m}^{-2}$ in the regions close to the boundary (extreme values were cut from the current plot to make a suitable scale). However, these non-physical fluctuations (already observed in the single-phase results) are not present in both the 2D-TDMA and 3D-TDMA models, which predicted the results smoothly in the entire region. Comparing the 3D-Direct model with the 2D- and 3D-TDMA models, these oscillations at regions close to the boundary are related to the manner of solving the heat conduction equations. As discussed previously, the 2D or 3D heat conduction model is a non-linear elliptical equation. This requires a closed set of boundary conditions to be simultaneously involved in the calculation process. However, one might notice that in the direct model the calculation proceeds from the bottom to the top without any iteration, using the boundary conditions at the bottom and lateral sides without the one at the top. In this case, the errors due to the less precise estimation of the boundary condition at the lateral sides are magnified during the calculation process. On the other hand, the 2D- or 3D-TDMA model is solved iteratively with closed boundary conditions. It assumes a Dirichlet boundary condition at the top and uses the measured Dirichlet one (base temperature from IR camera) as the investigator (i.e. to correct the footprint temperatures upon Newton-Raphson iterations). Hence, the results from the 3D-TDMA model are smooth and realistic. ,

Additionally, the 3D-TDMA model provides high-resolution thermal maps for all variables of interest. Fig. 2.13 compares q_{ftp} and T_{ftp} between single- and two-phase flow sharing the same heat flux and mass flux but different inlet and saturation temperatures. To reduce the impact of heat spreading on the scales, five pixels at each lateral side were cut off. It is shown that the q_{ftp} of two-phase flow was higher than that of single-phase flow, while the two-phase T_{ftp} was lower. For example, the maximum T_{ftp} of two-phase flow is 44.8°C , whereas that of single-phase flow is 51.9°C , considering the inlet fluid temperatures for the single- and two-phase flow were respectively 27.4 and 30.7°C . The 2D thermal map demonstrates that the two-phase flow renders the local heat flux and temperature distribution more uniform. Therefore, it is clearly shown that the thermal performance of the two-phase flow exceeds that of single-phase flow.

Fig. 2.14 presents the two-phase local wall and footprint heat transfer coefficients and the local fin efficiency at the widthwise centerline along the flow direction. According to the local vapor quality evaluated from the local energy balance method, the flow along the channel was separated into two region: the single-phase or subcooled flow boiling region and the two-phase saturated flow boiling region. The fluid temperature in the former region was calculated

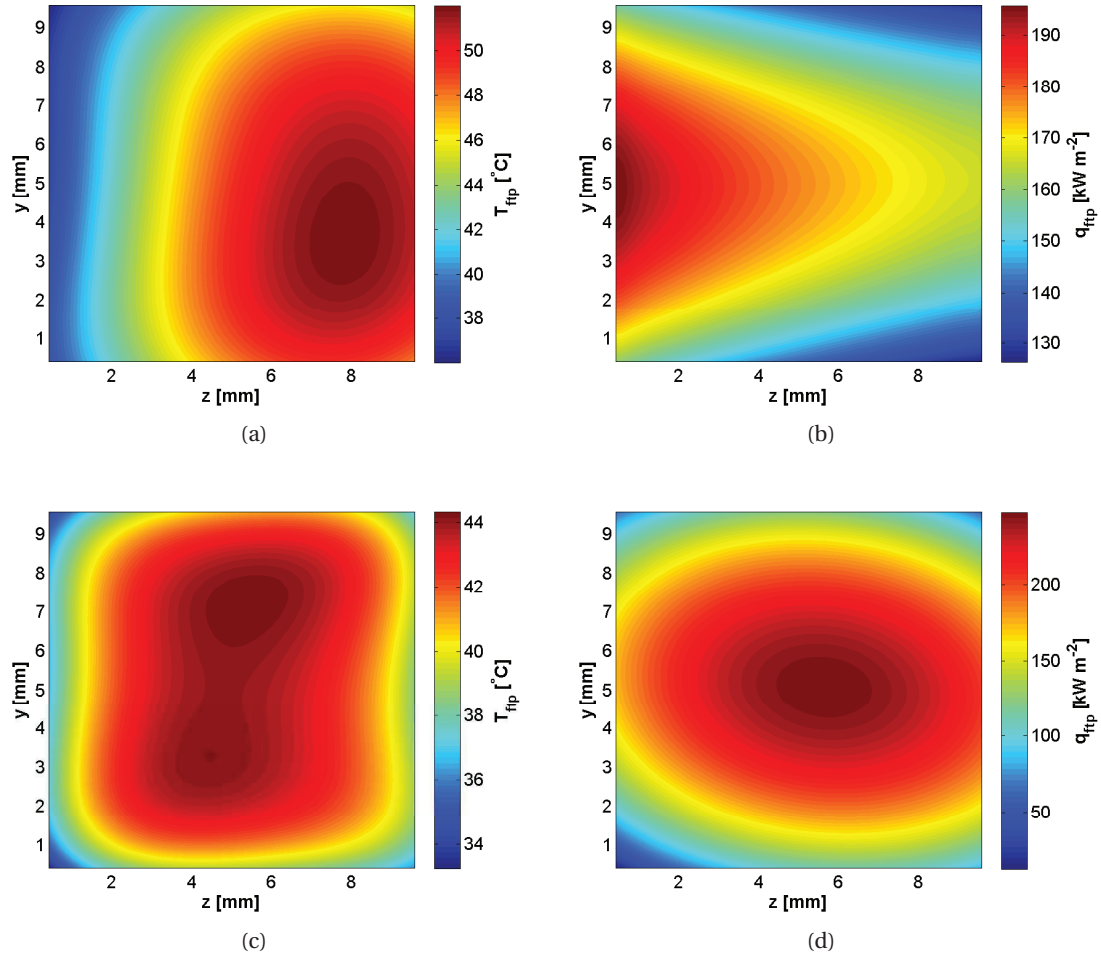


Figure 2.13 – Single- and two-phase flow thermal maps of footprint heat flux and temperature: (a) single-phase T_{ftp} , (b) single-phase q_{ftp} , (c) two-phase T_{ftp} and (d) two-phase q_{ftp} .

based on the single-phase energy balance, while the fluid temperature in the saturated flow boiling region was evaluated based on the local fluid pressure, which is normally predicted by an appropriate empirical correlation. However, a linear two-phase flow pressure drop assumption was made here due to its simplicity to obtain the local fluid temperature. It is shown that the local wall heat transfer coefficient first decreased in the single-phase thermal developing region, then it increased in the subcooled flow boiling region to a peak which is the onset of saturated flow boiling; afterwards, it experienced a very slight decrease and finally picked up after entered into annular flow regime. Therefore, the variation of two-phase local heat transfer coefficients in big magnitude emphasizes the necessity of considering the non-uniform distribution of the local footprint heat flux.

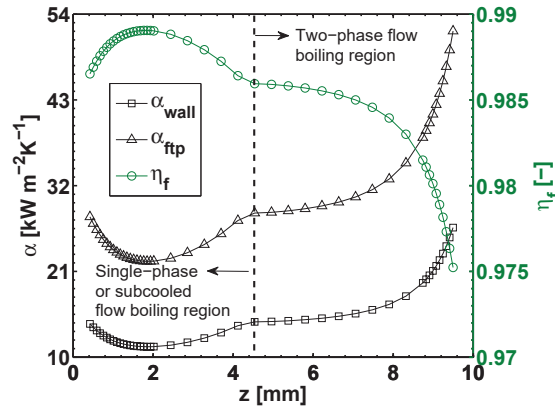


Figure 2.14 – Two-phase flow local heat transfer coefficients and fin efficiency at the widthwise centerline, obtained from the new 3D-TDMA model.

2.5 Conclusion

The problem of determining the local convective heat transfer coefficients at the interface between the fluid and channel wall in multi-microchannel evaporators using temperature measurements at the base is characterized as an inverse heat conduction problem (IHCP). In this paper, a new method of reducing the local heat transfer data in multi-microchannel evaporators by solving the 3D IHCP has been proposed. To validate this method, two sets of single- and two-phase experimental data in a multi-microchannel evaporator were used. In the experiment, the base temperature map was measured by an infrared camera, providing not only high-resolution temperature information but also a good reference to define the lateral boundary conditions. In this new method, the raw temperature map were first pre-processed by filtering techniques, including Wiener filter, spline smoothing, and polynomial surface fitting. Then the 3D IHCP was solved using the TDMA finite volume method with a combination of the Newton-Raphson and local energy balance methods. The result indicated that the polynomial surface fitting technique was more suitable to be adopted in the new method to process the present experimental data.

Based on the filtered data from surface fitting, three other heat conduction models currently used in the literature, including 1D-Direct, 2D-TDMA, and 3D-Direct models, were systematically analyzed. The results were compared with that from the 3D-TDMA model used in the present new method. The results of local footprint heat flux q_{ftp} and temperature T_{ftp} showed that the new method presented more reasonable solutions, while the direct models gave irrational oscillations in the boundary regions. These non-physical fluctuation were essentially related to the progressively magnified error, which arose from the not-so-precise estimation of the Neumann boundary condition at the lateral sides.

Furthermore, the single-phase flow local Nusselt number results indicated that the new

method provided the best agreement with the theoretical prediction with a MAE of 11.8%. Finally, the two-phase flow was proven to exhibit higher q_{ftp} and lower temperature T_{ftp} than single-phase flow, and the distributions appeared to be more uniform than those for the single-phase flow. The latter result highlights the efficiency of this 3D-TDMA model to obtain proper physical solutions for the problem of heat conduction in the frame of experimental microchannel evaporator measurements.

As a conclusion, the present 3D-TDMA method of solving the 3D IHCP using polynomial surface fitting, the 3D-TDMA model, Newton-Raphson iteration and a local energy balance method was shown to be more accurate for reducing the local heat transfer data in multi-microchannel evaporators, especially for cases using IR measurements, since such flows exhibit very large and sharp variations in the local heat transfer coefficient as a function of two-phase flow regime transitions. Extensive two-phase heat transfer coefficient data will be obtained using this new method and will be presented in future papers.

3 Steady-state pressure drop

This chapter is from the paper below by Huang and Thome (2017):

H. Huang, J.R. Thome, An experimental study on flow boiling pressure drop in multi-microchannel evaporators with different refrigerants, *Experimental Fluid and Thermal Science*, 80(2017) 391-407.

Abstract

A comparative experimental study was performed to investigate the flow boiling pressure drop of three fluids (R1233zd(E), R245fa and R236fa) in two multi-microchannel evaporators. The silicon microchannel evaporators were 10 mm long and 10 mm wide, having 67 parallel channels, each $100 \times 100 \mu\text{m}^2$, separated by a fin with a thickness of $50 \mu\text{m}$. Upstream of each channel, two types of micro-orifice was placed to stabilize the two-phase flow and to obtain good flow distribution. The test section's backside base temperatures were measured by an infrared (IR) camera. The operating conditions for stable flow boiling tests were: mass fluxes from 1250 to 2750 $\text{kg m}^{-2}\text{s}^{-1}$, heat fluxes from 20 to 64 W cm^{-2} , inlet subcooling of 5.5, 10 and 15 K, and a nominal outlet saturation temperature of 31.5, 35 and 40 °C. The resulted maximum vapor quality at the outlet manifold was 0.51. A single-phase flow validation in terms of the inlet and outlet restriction pressure drops and the channel flow friction factor was carefully done before the boiling tests. The influence from the saturation temperature, inlet subcooling, fluid and test section inlet orifice width on the flow boiling pressure drop were systematically investigated. A total of 184 points of stable flow boiling data, selected through flow visualization recorded by a high speed camera coupled with a microscope, were used to assess the applicability of seventeen existing two-phase pressure drop models. None of the current pressure drop models provided an accurate prediction with the data and therefore, a new empirical model suitable for the high mass flux operating conditions was developed.

Since the momentum pressure drop was significant at high mass flux, the impact of mass flux and vapor quality were incorporated into the new model by modifying the Chisholm parameter C as a function of the vapor and liquid only Reynolds numbers. The new pressure drop model yielded the best prediction of the experimental data with a MAE of 27.8% and it was thus implemented to predict the local pressure and temperature profiles, allowing a quantitative analysis to obtain highly accurate local heat transfer coefficients.

3.1 Introduction

To meet the increasing demand of heat dissipation from the electronics industry, cooling using microchannels with two-phase flow has been a topic of interest in both academics and industry Tuckerman and Pease (1981); Bowers and Mudawar (1994); Kandlikar (2002); Thome (2004); Thome and Kim (2015). Its main merits such as large heat transfer surface areas per unit footprint area, low amount of coolant requirement, high compactness, high heat flux dissipation capabilities and relatively uniform base temperature distribution render it attractive for such applications.

However, the implementation of two-phase cooling in microchannels is impeded by the appreciable pressure drop (consuming high pumping power), due to the small hydraulic diameters. The large pressure drop gradients (compared to conventional channels) create a corresponding significant gradient in the local saturation temperature from inlet to outlet. Therefore, since pressure drop is such a key factor, accurately predicting the two-phase pressure drop is of great importance in not only reducing test data but also for designing two-phase cooling systems Costa-Patry (2011).

The channel two-phase pressure drop consists of frictional, momentum, and static pressure drop components. The momentum and static pressure drop can be directly calculated once the void fraction is known, while frictional pressure drop due to the shear stress is generally predicted by empirical models, which can be divided into the homogeneous equilibrium (HEM) and the separated flow (SFM) models. The homogeneous flow model considers the two-phase flow to be a pseudo single-phase flow, and assumes the liquid and vapor phase move along the channel with the same velocity, i.e. the slip ratio equals to 1. The HEM is generally suitable for cases with low vapor quality, i.e. bubbly flow or slug flow. The separated flow model, as indicated by its name, addresses the two-phase flow as liquid and vapor phase with an interface in between, moving individually along the channel. A good example for this model is annular flow with the vapor phase traveling in the middle of the channel and a liquid film between the vapor core and the channel wall.

When using HEM to predict the frictional pressure drop, the two-phase flow friction factor, density and viscosity are needed. The two-phase viscosity is calculated based on a certain mixing law between the liquid and vapor phase properties according to different models

McAdams et al. (1942); Akers et al. (1958); Cicchitti et al. (1960); Dukler et al. (1964); Beattie and Whalley (1982); Lin et al. (1991). In general, the momentum component is over-predicted by the homogeneous void fraction model Kim and Mudawar (2013a), which is derived from the assumption of the slip ratio being 1.

Similar to the format of the two-phase flow friction factor in the HEM, a separated flow mechanistic model for two-phase flow friction factor correlation, based on the vapor core Weber number, was developed by Cioncolini et al. (2009); Cioncolini and Thome (2011). Their data bank contained 3908 points for eight gas-liquid combinations and 22 different tube diameters, varying from 0.571 to 31.7 mm. Their momentum pressure drop was predicted using the void fraction model of Woldesemayat and Ghajar (2007).

For the separated flow model, the frictional pressure drop of each phase is calculated the same way as that in single-phase flow. Then the frictional pressure drop is obtained by multiplying the two-phase multiplier with the pressure drop of either the liquid phase or the vapor phase. The pioneering work in this respect was performed by Lockhart and Martinelli (1949), in which the two-phase multiplier was invented and correlated with the Martinelli parameter according to four different flow regimes. More than one decade later, this correlation was simplified by Chisholm (1967) with a Chisholm parameter C .

Afterwards, the research work of developing the two-phase pressure drop model can be roughly categorized into two groups. The former one still focuses on directly correlating the two-phase multiplier, such as the correlation of Chisholm (1973), Grönnerud (1979), Friedel (1979). The later one maintains the original format of the two-phase multiplier correlation, while modifying the Chisholm parameter according to experimental results to improve the model's predictive capability.

The later methodology was first introduced for mini-scale two-phase pressure drops in a study by Lazarek and Black (1982). They studied the saturated flow boiling pressure drop of R-113 in a vertical circular tube with an inner diameter of 3.1 mm. The Chisholm parameter in two-phase multiplier correlation was modified according to an experimental data fitting. Later, Mishima and Hibiki (1996) studied adiabatic air-water two-phase flow in vertical capillary tubes with internal diameters from 1 to 4 mm. They found the frictional pressure drops were well predicted by the Chisholm equation Chisholm (1967) by modifying the Chisholm parameter as a function of tube diameter. Along this direction, Qu and Mudawar (2003a), Lee and Mudawar (2005) and Lee and Garimella (2008) developed their individual flow boiling pressure drop models empirically according to their experimental data in microchannel heat sinks. A recent version of flow boiling pressure drop model in this category was developed by Kim and Mudawar (2013b). In their model, six dimensionless parameters were included in the Chisholm parameter to correlate their collected data base containing 2378 data points.

The aforementioned studies provide valuable experimental results and discussion for understanding the two-phase flow pressure drop characteristics in microchannels. However, several weak points still remain, including: (1) no single-phase flow friction factor validation tests

prior to the two-phase flow boiling tests were done, (2) the stable and unstable flow boiling data were blended together to develop the two-phase flow pressure drop model, and (3) most of the work focused on relatively low mass flux conditions.

In a recent work by Huang et al. (2016b), the flow boiling pressure drop of a new environmentally friendly R1233zd(E) was reported. According to their experimental data, a new flow boiling pressure drop model suitable for high mass flux was developed by incorporating the impact of mass flux and vapor quality.

Followed by our recent work Huang et al. (2016b), the main purposes of this study are (1) to conduct a comparative investigation on saturated flow boiling pressure drop of three refrigerants in two silicon multi-microchannel evaporators (2) to evaluate the current two-phase pressure drop models using only stable flow boiling data, (3) to develop a new empirical two-phase pressure drop model suitable for high mass fluxes, and (4) to predict the local two-phase flow pressure and temperature using the present new model to enable better evaluation of the local heat transfer.

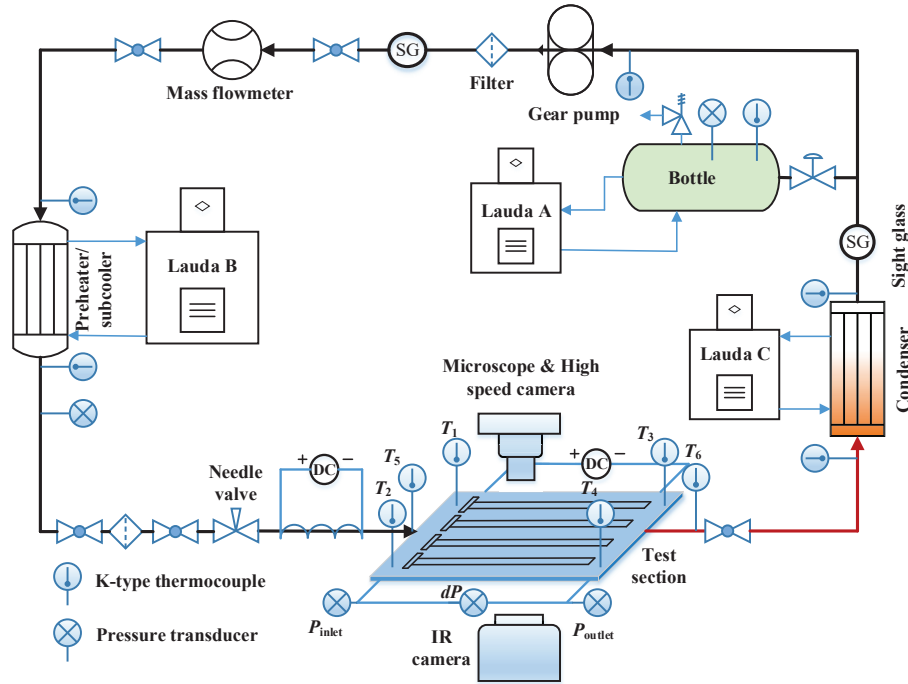
3.2 Experimental setup

3.2.1 Facility

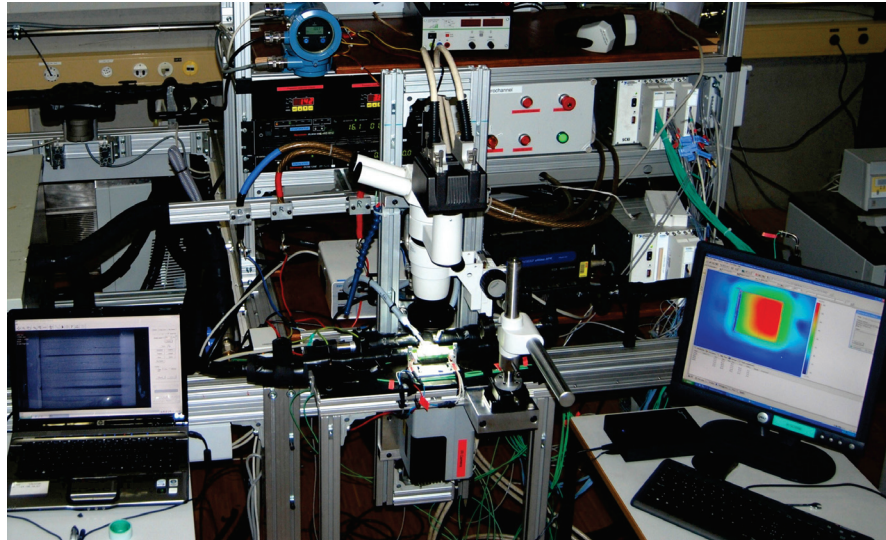
The facility used for the two-phase flow boiling study is shown in Fig. 6.1. This facility was also utilized in our previous work Szczukiewicz et al. (2013). The facility was comprised of a closed fluid flow loop, an external cooling or heating system, and a data acquisition system. In the main fluid flow loop, the refrigerant was driven by a gear pump through a Coriolis mass flowmeter, preheater or subcooler, needle valve, test section, and eventually a condenser. A temperature controllable stainless steel bottle was placed before the pump to stabilize the system. During tests, the valve between the pipe loop and the bottle was fully open to maintain the loop saturation pressure. In the data acquisition system, the fluid temperature and pressure signals were acquired by the NI-DAQ instrument, the test section base temperature was recorded by a FLIR SC3000 IR camera, and the two-phase flow was observed and recorded by a Photron Fastcam-Ultima APX high speed camera coupled with a Nikon 800 microscope. A LabVIEW program was used to simultaneously acquire and save the data. The external cooling or heating system was used to precisely control the saturation temperature and the inlet subcooling.

3.2.2 Test section

The parallel microchannels evaporator, depicted in Fig. 3.2, was micro-fabricated from silicon, and bonded to a transparent pyrex cover for flow visualization. The test section was 10×10



(a)



(b)

Figure 3.1 – Layout of the facility: (a) schematic diagram and (b) photo.

mm². There were 67 parallel channels, and each channel had a cross-section area of $100 \times 100 \mu\text{m}^2$. In order to stabilize the flow and obtain good flow distribution, a micro-orifice was inserted ahead of each channel, as shown in Fig. 3.2b. Two micro-heaters made of aluminum with a thickness of $1.5 \mu\text{m}$ were sputtered on the backside of the test section to mimic the

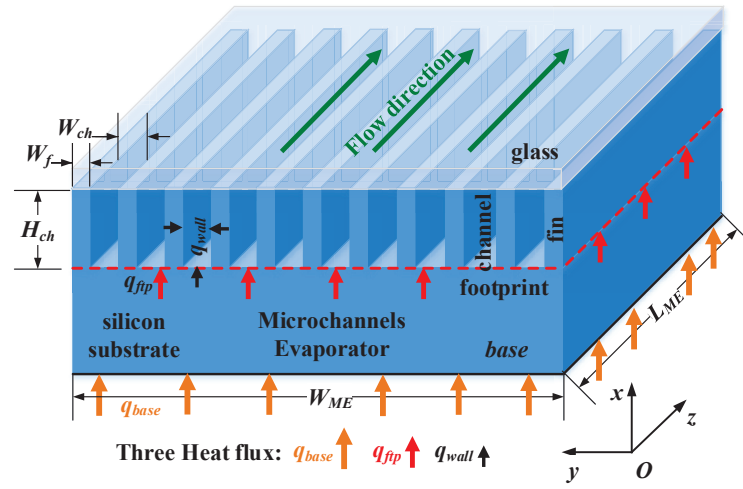
computer chip, as shown in Fig. 3.2c. The two micro-heaters were connected in parallel to a Sorensen DLM32–95E DC power supply. Through the two micro-heaters, both uniform and non-uniform heat flux boundary conditions can be realized. The test section was housed inside a cooper manifold, as demonstrated in Fig. 3.2d. Four thermocouples and two pressure taps were placed at the manifold inlet and outlet plenums to measure the fluid temperature and pressure, as depicted in Fig. 3.2e.

3.2.3 IR camera calibration

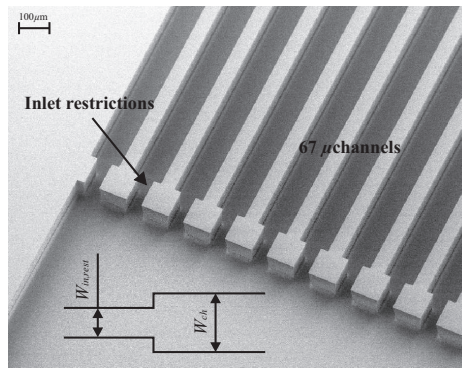
The IR camera was calibrated in-situ pixel by pixel over the range of 20 to 60 °C, which covered the temperature range of the flow boiling tests. As described in Szczukiewicz (2012), the flow loop operated at its maximum mass flux created a quasi-isothermal condition in the test section, where the mean value between the inlet and outlet temperature was used as the reference for calibration. It shows a good linear relationship between the IR raw temperature and the reference temperature. After calibration, the accuracy of IR camera is improved to $\pm 0.2^\circ\text{C}$ from the manufacturer's value of $\pm 2^\circ\text{C}$.

3.2.4 Experimental test conditions and uncertainties

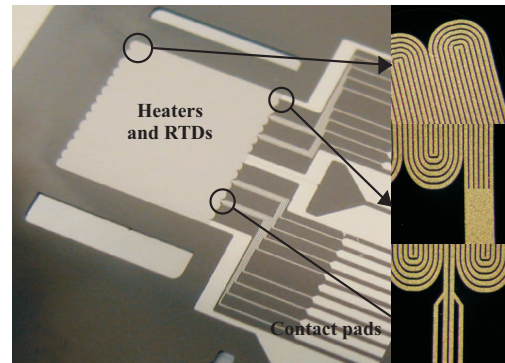
Three refrigerants (R1233zd(E), R245fa and R236fa) were tested in two multi-microchannel evaporators under three outlet saturation temperatures (31.5, 35 and 40 °C) and three inlet subcoolings (5.5, 10 and 15 K). The outlet saturation temperature was maintained within $\pm 1.5^\circ\text{C}$ and the inlet subcooling was controlled within $\pm 1.1\text{ K}$. The flow boiling tests were conducted by fixing the mass flux and increasing the heat flux. The ranges of mass flux and heat flux tested were 500 to $2750\text{ kg m}^{-2}\text{s}^{-1}$ and 20 to 64 W cm^{-2} (with a step of 2 to 4) respectively. Prior to data recording for each test condition, the facility was allowed a sufficient time to stabilize, and the stabilization was confirmed by analyzing the measurements statistically. The stable flow boiling results with mass flux ranging from 1250 to $2750\text{ kg m}^{-2}\text{s}^{-1}$ were separated from the rest of the total data base. By stable flow boiling, this means here that the temperatures of the back surface fluctuated less than 0.3 K , as witnessed by the IR camera, The pressure fluctuations are about or less than 1% of the actual absolute pressure during a test sequence, and no obvious back flow causing flow excursion was observed by the high speed camera. The test conditions are summarized in Table 3.1. An uncertainty analysis using the technique proposed in Kline and McClintock (1953) was implemented in this study. The uncertainty propagation was taken into account during data reduction. Table 3.2 lists the measurement uncertainties of the main parameters.



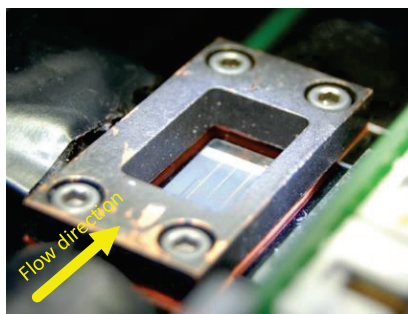
(a)



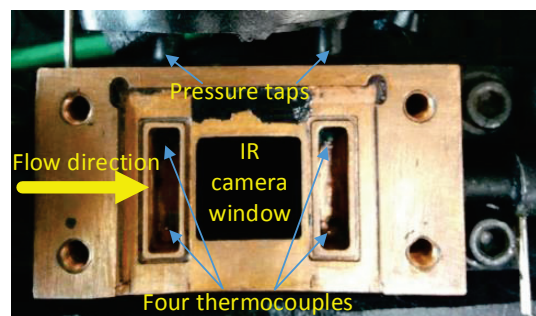
(b)



(c)



(d)



(e)

Figure 3.2 – Test section: (a) schematic of the microchannel evaporator, (b) photo of the microchannels with inlet orifices Szczukiewicz et al. (2013), (c) photo of the micro-heaters Szczukiewicz et al. (2013), (d) photo of the test section housed inside the manifold, and (e) photo of the manifold bottom.

Chapter 3. Steady-state pressure drop

Table 3.1 – Stable flow boiling test matrix.

Condition	R1233zd(E)	R245fa	R236fa
q (W cm ⁻²)	24 ~ 50	24 ~ 64	20 ~ 60
G (kg m ⁻² s ⁻¹)	1750 ~ 2750	2000 ~ 2500	1250 ~ 2500
T_{sat} (°C)	35	31.5, 35 and 40	31.5, 35 and 40
ΔT_{sub} (K)	5.5	5.5, 10 and 15	5.5, 10 and 15
Test section (TS)	TS1 ^a	TS1	TS1 and TS2 ^a

a: TS1 has an inlet orifice width of 50 μ m and TS2 has that of 25 μ m.

Table 3.2 – Experimental measurement uncertainties of main parameters of R1233zd(E).

Parameter	Unit	Test range	Uncertainty
T_{tc}	°C	–	± 0.1 °C
T_{IR}	°C	–	± 0.2 °C
P_{abs}	kPa	–	± 0.3 kPa
P_{diff}	kPa	–	± 0.25 kPa
q	W cm ⁻²	4 ~ 50	$\pm 0.16\%$
G	kg m ⁻² s ⁻¹	500 ~ 2750	$\pm 4.25\%$
Single-phase tests			
$\Delta P_{inlet,rest}$	kPa	0.17 ~ 26.1	$\pm 10.8\%$
$\Delta P_{outlet,rest}$	kPa	-2.97 ~ -0.02	$\pm 8.44\%$
ΔP_{ch}	kPa	1.63 ~ 27.1	$\pm 18.3\%$
Re	–	72 ~ 911	$\pm 7.74\%$
f	–	0.011 ~ 0.16	$\pm 6.33\%$
Two-phase tests ^b			
$\Delta P_{inlet,rest}$	kPa	6.00 ~ 22.31	$\pm 10.8\%$
$\Delta P_{outlet,rest}$	kPa	0.95 ~ 42.14	$\pm 7.36\%$
ΔP_{ch}	kPa	6.60 ~ 68.97	$\pm 19.5\%$
$x_{ch,outlet}$	–	0.031 ~ 0.49	$\pm 12.0\%$
x_{outlet}	–	0.034 ~ 0.51	$\pm 12.0\%$

b: only stable flow boiling cases were analyzed.

3.3 Data reduction

The microchannel test section is housed inside a manifold, as shown in Fig. 3.2d and 3.2e. The fluid first flows into the manifold inlet plenum. In the manifold before entering the channel,

the fluid goes through a sudden contraction into the test section inlet slit, then another sudden contraction and expansion as enters the channel through the inlet orifice. Thus, since there is a pressure tap in the manifold, the local pressure drop in the inlet manifold is composed of the flow and its contraction and expansion into the channel. The pressure drop at the outlet manifold is mainly due to the sudden expansion at the outlet of the channels. Here only the local pressure drop is taken into account, ignoring the frictional pressure drop due to the relatively short length of each component Idel'chik (2007). The total pressure drop including inlet restriction, channel pressure drop and outlet restriction, was measured by a differential pressure transducer, where:

$$\Delta P_{total} = \Delta P_{inlet,rest} + \Delta P_{ch} + \Delta P_{outlet,rest} \quad (3.1)$$

$$\Delta P_{ch} = \Delta P_{total} - \Delta P_{inlet,rest} - \Delta P_{outlet,rest} \quad (3.2)$$

3.3.1 Single-phase flow

Inlet and outlet restriction pressure drops In our current experimental set up, the inlet restriction pressure drop is composed of the following components: (1) a sudden contraction from the inlet manifold plenum to the inlet slit, ΔP_{cont1} ; (2) a sudden contraction and 90 ° bend from the inlet slit to the test section inlet plenum, ΔP_{cont2} and ΔP_{bend1} ; (3) a sudden contraction from the inlet plenum to the inlet micro-orifice, ΔP_{cont3} ; and (4) a sudden expansion from the micro-orifice to the microchannel, ΔP_{expa1} :

$$\Delta P_{inlet,rest} = \Delta P_{cont1} + \Delta P_{cont2} + \Delta P_{bend1} + \Delta P_{cont3} + \Delta P_{expa1} \quad (3.3)$$

The outlet restriction pressure drop is primarily composed of: (1) a sudden expansion from the microchannel to the test section outlet plenum, ΔP_{expa2} ; (2) a sudden expansion and the 90 ° bend from the test section outlet plenum to the outlet slit, ΔP_{expa3} and ΔP_{bend2} ; and (3) a sudden expansion from the outlet slit to the outlet manifold plenum, ΔP_{expa4} :

$$\Delta P_{outlet,rest} = \Delta P_{expa2} + \Delta P_{expa3} + \Delta P_{bend2} + \Delta P_{expa4} \quad (3.4)$$

When the fluid flows through a passage with a sudden variation in cross-sectional area, the corresponding pressure drop, named minor pressure loss or local pressure loss, can be divided into two parts, a reversible component and an irreversible one:

$$\Delta P_m = \Delta P_{m,r} + \Delta P_{m,i} \quad (3.5)$$

The reversible pressure drop, either positive or negative depending on contraction or expansion, can be calculated based on the Bernoulli equation assuming ideal flow. For a sudden

Chapter 3. Steady-state pressure drop

contraction, this is:

$$\Delta P_{cont,r} = \frac{G_s^2}{2\rho} \left[1 - \left(\frac{A_{small}}{A_{large}} \right)^2 \right] \quad (3.6)$$

For a sudden expansion, this is:

$$\Delta P_{expa,r} = -\frac{G_s^2}{2\rho} \left[1 - \left(\frac{A_{small}}{A_{large}} \right)^2 \right] \quad (3.7)$$

where G_s is the mass flux in the small cross-sectional area.

The irreversible one is always positive and is given by:

$$\Delta P_{m,i} = K \frac{G_s^2}{2\rho} \quad (3.8)$$

where K is the irreversible pressure loss coefficient. It can be evaluated by either correlations based on experimental results Idel'chik (2007) or theoretical derivation Kays (1950); Lee and Garimella (2008). Since the channel pressure drop was obtained by subtracting the inlet and outlet restriction pressure drop from the measured total pressure drop, the proper prediction model for the restriction pressure drop (as listed in Table 3.3) is very important. To obtain a suitable model, in this paper three commonly used models to predict single-phase inlet and outlet restriction pressure drops were implemented.

Table 3.3 – Correlations from literature for the coefficients of irreversible pressure loss.

Kays (1950) expansion
$K_e = 1 - 2K_{d,small}\sigma_e + (2K_{d,small} - 1)\sigma_e^2$, $\sigma_e = \frac{A_{small}}{A_{large}}$
$K_d = 1.2(1 + 0.2976ar + 0.1158ar^2 - 0.6868ar^3 + 0.5699ar^4 - 0.1479ar^5)$
Kays (1950) contraction
$K_c = \frac{1 - K_{e,large}\sigma_c^2 C_c - 2C_c + 2K_{d,small}C_c^2}{C_c^2} - (1 - \sigma_c^2)$, $\sigma_c = \frac{A_{small}}{A_{large}}$
$K_e = 1.5429(1 + 0.6914ar + 0.56ar^2 - 1.882ar^3 + 1.252ar^4 - 0.2248ar^5)$
$C_c = \frac{1 - \sigma_c}{2.08(1 - \sigma_c) + 0.5371}$, contraction coefficient from Geiger Geiger (1964)
Blevins used in Lee and Garimella (2008) expansion and contraction
$K_e = -2 \times 1.33\sigma_e(1 - \sigma_e)$
$K_c = 0.0088ar^2 - 0.1785ar + 1.6027$
Idel'chik (2007) expansion

Continued on next page

Table 3.3 – Continued from previous page

$K_e = -8.44556 - 26.163(1 - \sigma_e)^2 - 5.38086(1 - \sigma_e)^4$ $+ \log Re [6.007 + 18.5372(1 - \sigma_e)^2 + 3.9978(1 - \sigma_e)^4]$ $+ (\log Re)^2 [-1.02318 - 3.09169(1 - \sigma_e)^2 - 0.680943(1 - \sigma_e)^4], (500 \leq Re < 3300)$
$K_e = 3.62536 + 10.744(1 - \sigma_e)^2 - 4.41041(1 - \sigma_e)^4$ $+ (\log Re)^{-1} [-18.13 + -56.77855(1 - \sigma_e)^2 + 33.40344(1 - \sigma_e)^4]$ $+ (\log Re)^{-2} [30.8558 - 99.9542(1 - \sigma_e)^2 - 62.78(1 - \sigma_e)^4]$ $+ (\log Re)^{-3} [-13.217 - 53.9555(1 - \sigma_e)^2 - 33.8053(1 - \sigma_e)^4], (10 \leq Re < 500)$
$K_e = \frac{30}{Re}, (Re < 10)$
Idel'chik (2007) contraction
$K_c = AB(1 - \sigma_c), A = \sum_{i=0}^7 a_i (\log Re)^i$
$a_0 = -25.12458, a_1 = 118.5076, a_2 = -170.4147, a_3 = 118.1949;$
$a_4 = -44.42141, a_5 = 9.09524, a_6 = -0.9244027, a_7 = 0.03408265$
$B = \sum_{i=0}^2 \left\{ \left[\sum_{j=0}^2 a_{ij} \sigma_c^j \right] (\log Re)^i \right\}, a_{ij} = \begin{pmatrix} 1.07 & 1.22 & 2.9333 \\ 0.05 & -0.51668 & 0.8333 \\ 0 & 0 & 0 \end{pmatrix}, 10 \leq Re \leq 2000$

Channel pressure drop When considering the single-phase pressure drop along the channel, the channel is divided into two parts: the developing region and the developed one. In the developing region, the pressure drop is due to both fluid acceleration and the shear stress between wall and fluid. And this coupled effect is usually described by the so-called apparent flow friction factor, f_{app} . The pressure drop in the fully developed region is only related to the wall shear stress, and can be characterized by the fully developed flow friction factor, or Fanning factor, f . The demarcation between the developing and developed flow is defined by the hydraulic entrance length, L_h . For the single-phase flow tests, the inlet restriction pressure drop, $\Delta P_{inlet,rest}$, and the outlet restriction pressure drop, $\Delta P_{outlet,rest}$, are evaluated based on the model of Blevins used in Lee and Garimella (2008).

To evaluate the apparent flow friction factor f_{app} , the fully developed flow friction factor f , and the hydraulic entrance length, L_h , in this paper two models are implemented. One is from Shah and London (1978), and the other is from Muzychka and Yovanovich (2009), as listed in Table 3.4. In the model of Muzychka and Yovanovich (2009), one point should be highlighted is that the characteristic length used is the square root of the cross-sectional area, and the other one is that the hydraulic entrance length is related to the channel aspect ratio.

Table 3.4 – Correlations for single-phase channel pressure drop.

Shah and London (1978) fully developed flow:
$f_{fd} = \frac{24}{Re} (1 - 1.3553ar + 1.9467ar^2 - 1.7012ar^3 + 0.9564ar^4 - 0.2537ar^5)$

Continued on next page

Table 3.4 – Continued from previous page

$Re = \frac{GD_h}{\mu_{sp,l}}$
Developing flow:
$f_{app} = \frac{1}{Re} \left[3.44(L_{sp}^+)^{-0.5} + \frac{1.089/(4L_{sp}^+) + f_{fd}Re - 3.44(L_{sp}^+)^{-0.5}}{1 + 1.31 \times 10^{-4}(L_{sp}^+)^{-2}} \right]$
$L_{sp}^+ = \frac{L_{sp}}{ReD_h}$
$L_h = 0.05ReD_h; f_{sp} = \begin{cases} f_{app}, & \text{if } L_{sp} < L_h \\ f_{fd}, & \text{if } L_{sp} \geq L_h \end{cases}$
Muzychka and Yovanovich (2009) fully developed flow:
$f_{fd}Re\sqrt{A} = \frac{12}{\sqrt{ar}(1+ar) \left[1 - \frac{192ar}{\pi^5} \tanh\left(\frac{\pi}{2ar}\right) \right]}$
$Re_{\sqrt{A}} = \frac{G\sqrt{A}}{\mu_{sp,l}}$
Developing flow:
$f_{app}Re\sqrt{A} = \left[\left(\frac{3.44}{\sqrt{L_h^+}} \right)^2 + \left(\frac{12}{\sqrt{ar}(1+ar) \left[1 - \frac{192ar}{\pi^5} \tanh\left(\frac{\pi}{2ar}\right) \right]} \right)^2 \right]^{1/2}$
$L_h^+ = 0.0822ar(1+ar)^2 \left[1 - \frac{192ar}{\pi^5} \tanh\left(\frac{\pi}{2ar}\right) \right]^2$
$L_h = L_h^+ \sqrt{A} Re_{\sqrt{A}}$

3.3.2 Two-phase flow

Inlet and outlet restriction pressure drops During the two-phase flow tests, a subcooling of 5.8 ± 0.8 K is maintained for the fluid entering the inlet manifold. As a result, the fluid flows through the inlet restriction with purely liquid flow. Therefore, the inlet restriction pressure drop, $\Delta P_{inlet,rest}$, can still be evaluated in the same way as that used in the single-phase flow tests. On the other hand, the outlet manifold has two-phase flow. In this paper the two-phase outlet restriction pressure drop, $\Delta P_{outlet,rest}$, is extrapolated from the measurement under the half heating tests, which generates an adiabatic condition at the channel outlet. As a consequence, the wall temperature (measured by the IR camera) at the channel end during the half heating tests can be considered as the fluid temperature, from which the fluid saturation pressure at the channel end can be calculated. Therefore, the outlet restriction pressure drop, $\Delta P_{outlet,rest}$, was obtained by subtracting the calculated fluid pressure at the channel end from the measured fluid pressure at the manifold outlet, indirectly from the respective saturation temperature at the end of the channel. Then, the outlet restriction pressure drop for the half heating tests was extrapolated to the full heating tests.

Channel pressure drops Since the fluid enters the inlet manifold with a subcooling of 5.8 ± 0.8 K, the channel is normally occupied by a small length of single-phase flow and a large

length of two-phase flow. Therefore, the channel pressure drop comprised of the single-phase pressure drop due to friction and the two-phase pressure drop related to friction and acceleration:

$$\Delta P_{ch} = \Delta P_{ch,sp} + \Delta P_{ch,tp} \quad (3.9)$$

$$\Delta P_{ch,sp} = 2f_{sp} \frac{G^2 L_{sp}}{\rho D_h} \quad (3.10)$$

In this study, the transition point where $z = L_{sp}$ between the single- and two-phase region is considered to be the point of saturation ($x = 0$), which can be identified as:

$$P(z = L_{sp}) = P_{ch,inlet} - \Delta P_{ch,sp} \quad (3.11)$$

$$x(z = L_{sp}) = \frac{\frac{Q_{ftp,sp}}{\dot{m}} + H_{inlet} - H_l(P(z = L_{sp}))}{H_{lv}(P(z = L_{sp}))} \quad (3.12)$$

$$x(z = L_{sp}) = 0 \quad (3.13)$$

where $Q_{ftp,sp}$ is the sum of the local footprint heat flux, which is obtained by solving the 3D inverse heat conduction problem, as presented in the work of Huang et al. Huang et al. (2016a). By solving Eqs. (3.10) to (3.13) together, the single-phase length, L_{sp} can be identified. A Newton-Raphson iteration was implemented here to accelerate the calculation. The channel two-phase flow pressure drop can be written as:

$$\Delta P_{ch,tp} = \Delta P_{fr} + \Delta P_{mom} + \Delta P_{sta} \quad (3.14)$$

Rewritten in derivative form with a null ΔP_{sta} for the horizontal test section Collier and Thome (1994), it becomes:

$$-\left(\frac{dP}{dz}\right)_{total} = -\left(\frac{dP}{dz}\right)_{fr} - \left(\frac{dP}{dz}\right)_{mom} \quad (3.15)$$

$$= -\left(\frac{dP}{dz}\right)_{fr} + G^2 \frac{d}{dz} \left(\frac{x^2 v_v}{\epsilon} + \frac{(1-x)^2 v_l}{1-\epsilon} \right) \quad (3.16)$$

3.4 Analysis of results and discussion

In this section, the experimental results of pressure drops for single- and two-phase flow are presented and discussed. Besides the experimental results of the new fluid of R1233zd(E), previous experimental data (from the work of Szczukiewicz et al. Szczukiewicz (2012)) were also used to validate the single-phase pressure drop correlations: for diabatic flow, three fluids of R236fa, R245fa, and R1233zd(E) were tested. The fluid R245fa was commonly studied to

check the experimental repeatability. In the two-phase flow part below, only the new results for the fluid R1233zd(E) are described.

3.4.1 Single-Phase flow validation

In this part, the pressure drop results for the inlet and outlet restrictions, and channel component in adiabatic and diabatic flow conditions are reported.

Adiabatic flow The pressure drop results of adiabatic flow are presented in Fig. 3.3. The three models of inlet and outlet restrictions listed in Table 3.3 were compared to determine their suitability for calculating the inlet and outlet restriction pressure drops to further obtain the channel pressure drop. It is shown that the models of Kays (1950) and Idel'chik (2007) largely overpredict the inlet and outlet restriction pressure drops irrespective of the fluid. This over prediction leads to a small or even negative channel pressure drop, which is not realistic. However, the model of Blevins used in Lee and Garimella (2008) yielded the most reasonable restriction pressure drop results because this model provided a channel pressure drop presenting the best agreement with the predictions from the two correlations of Shah and London (1978) and Muzychka and Yovanovich (2009), covering developing and fully developed flow regions. Therefore, the model of Blevins used in Lee and Garimella (2008) was employed to reduce the experimental data. For the channel pressure drops, the experimental results based on the model of Blevins used in Lee and Garimella (2008) are slightly lower than the predictions except for the case of the new fluid of R1233ze(E).

The fluid R245fa was again tested in the present work to check the experimental repeatability by comparing the adiabatic pressure drop with our previous work by Szczukiewicz (2012). The comparison is shown in Fig. 3.4a. The agreement between the two sets of data is good. The slight difference is associated with the different fluid temperatures, which in the present work was 30.1 °C, while 32.1 °C in the previous work Szczukiewicz (2012).

To understand the effect of developing region on the channel pressure drop, the channel pressure drops predicted by the correlations with (developing and fully developed flow) and without developing region (fully developed flow only) was compared with the experimental results in Fig. 3.4. The results without considering the developing region appears to be much closer to the experimental data than that with the developing region. Apparently, this is because the developing region effect has been already taken into account when deriving the pressure loss coefficients in the model of Blevins used in Lee and Garimella (2008). Therefore, the channel pressure drop should be predicted by the correlation for fully developed flow when considering the inlet restriction pressure drop.

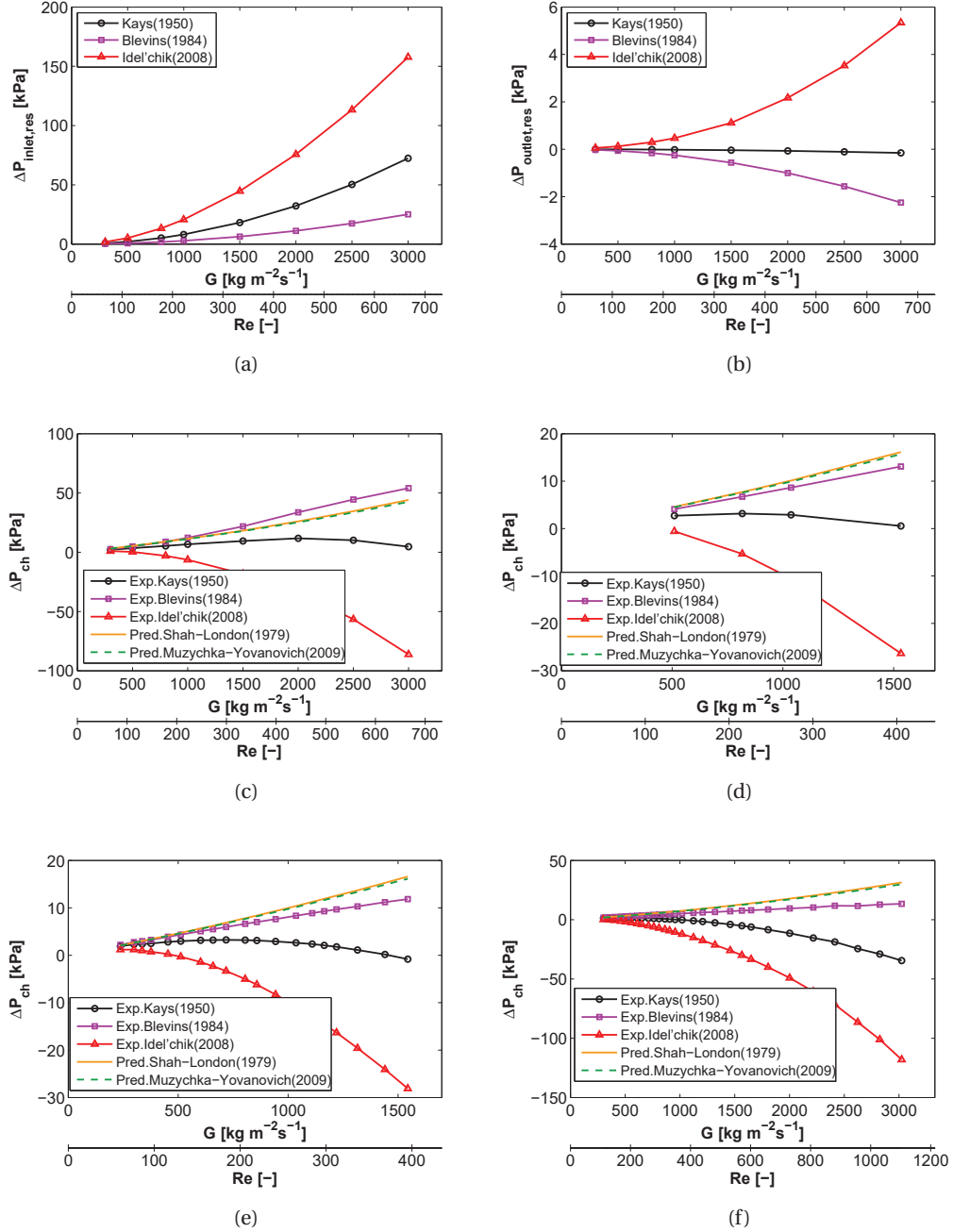


Figure 3.3 – Single-phase pressure drop models comparison in adiabatic flow: (a) $\Delta P_{inlet,res}$ of R1233zd(E), (b) $\Delta P_{outlet,res}$ of R1233zd(E), (c) ΔP_{ch} of R1233zd(E), (d) ΔP_{ch} of R245fa, (e) ΔP_{ch} of R245fa, (f) ΔP_{ch} of R236fa ((a) ~ (d) with the present data, (e) and (f) with the data from Szczukiewicz (2012)).

Diabatic flow The flow friction factor is dependent on the fluid density and viscosity. Hence, it varies with a change in the fluid temperature. In diabatic single-phase flow, the fluid tem-

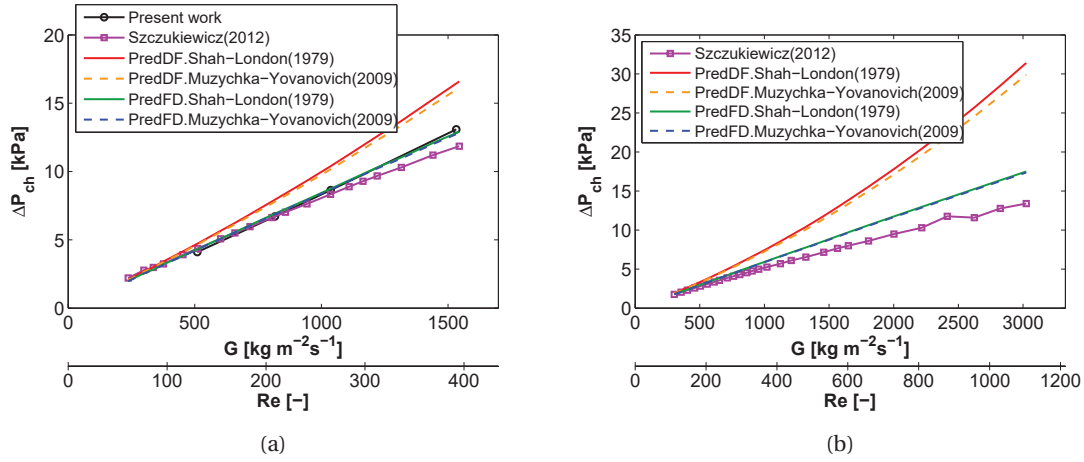


Figure 3.4 – Single-phase channel pressure drop in adiabatic flow: (a) R245fa, and (b) R236fa. (DF: considering developing region and fully developed part; FD: ignoring developing region, i.e. fully developed region only)

perature changes along the flow direction due to the imposed heat flux. In order to provide a reliable reference for the identification of two-phase flow pressure drop, in this work the flow friction factor under single-phase diabatic flow was measured and validated with the correlation. The results of flow friction factor versus Reynolds number for three fluids in two test sections are shown in Fig. 3.5. The experimental friction factors of R245fa and R236fa agreed well with the correlation of Shah and London (1978) for the fully developed flow. Therefore, this correlation will be reliable to predict the liquid phase pressure drop for two-phase flow tests. However, the measured flow friction factor of R1233zd(E) was obviously lower than the prediction from the correlation of Shah and London (1978). Hence, a new correlation for this new fluid was proposed in our previous work Huang et al. (2016b). One reason for this discrepancy is related to the decrease in fluid viscosity with the increase in fluid temperature, and the viscosity of the new fluid R1233zd(E) was most subject to the variation in fluid temperature. Apparently, the classical correlation of Shah and London (1978) failed to address this influence. After the single-phase flow friction factor validation, it is reliable to use the Shah and London (1978) to predict the flow friction factor for fluids of R245fa and R236fa, while for the new fluid R1233zd(E) it is proper to use the new model of $f = \frac{8.058}{Re}$ proposed in Huang et al. (2016b). These validation results will be used in the two-phase flow pressure drop calculation.

3.4.2 Two-Phase flow pressure drop

In this section, the experimental results are first reported, then followed by the validations of the existing two-phase pressure drop models and a new pressure drop model development in

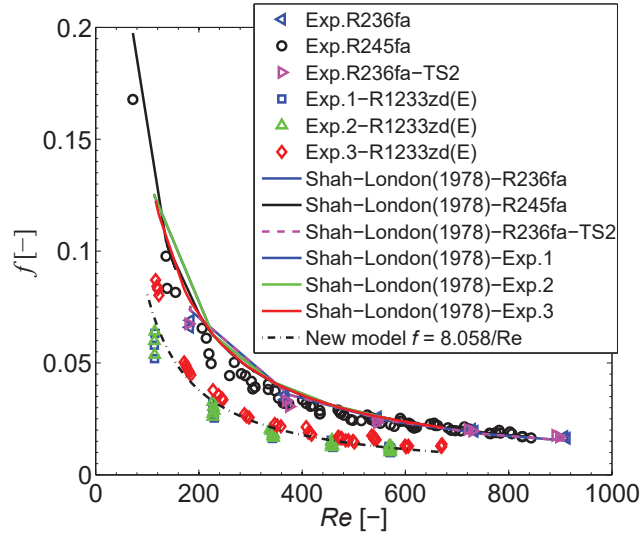


Figure 3.5 – Flow friction factor in diabatic flow (Exp.1: the first set of single-phase heat transfer experiment of R1233zd(E) at $T_{sat} = 60^\circ\text{C}$ with various $G = 500 \sim 2500 \text{ kg m}^{-2}\text{s}^{-1}$ and $q = 5 \sim 30 \text{ W cm}^{-2}$; Exp.2: the same test of R1233zd(E) as Exp.1 for confirmation; Exp.3: single-phase didiabatic of test R1233zd(E) at $q = 2 \text{ W cm}^{-2}$ with various G ; Exp.236fa-TS2: tests in test section 2, and the rest are in test section 1).

this study, and finally the local pressure and temperature predictions by the new model.

Experimental results

In our recent study Huang et al. (2016b), the two-phase pressure drops of the new fluid R1233zd(E), including the total, channel, inlet and outlet restriction, have been discussed in details. In general, the two-phase flow pressure drop increases with mass flux and vapor quality. This section is focused on the comparative study of the total and channel pressure drops considering the influence from the saturation temperature, inlet subcooling, fluids and test section inlet orifice.

Influence from saturation temperature Fig. 3.6 describes the influence from the saturation temperature on the total and channel pressure drops for two fluids: R245fa and R236fa. The total pressure drop decreased slightly with the increase in the saturation temperature or pressure. The same trend can be found in the channel pressure drop of R245fa, as shown in Fig. 3.6a. This trend was caused by the decrease in the shear stress at the two interfaces of liquid-wall and vapor-liquid. The decrease in the wall shear stress was due to the reduction of liquid viscosity when increasing the saturation temperature. The drop of shear stress at the liquid vapor interface resulted from the decrease in the slip ratio, which was due to the

decreasing liquid to vapor density ratio when elevating the saturation temperature. A slightly different result can be found for the channel pressure drop of R236fa at $T_{sat} = 40^\circ\text{C}$, which appeared to be a bit higher than that of $T_{sat} = 35^\circ\text{C}$. This slight difference must be due to the experimental measurement error.

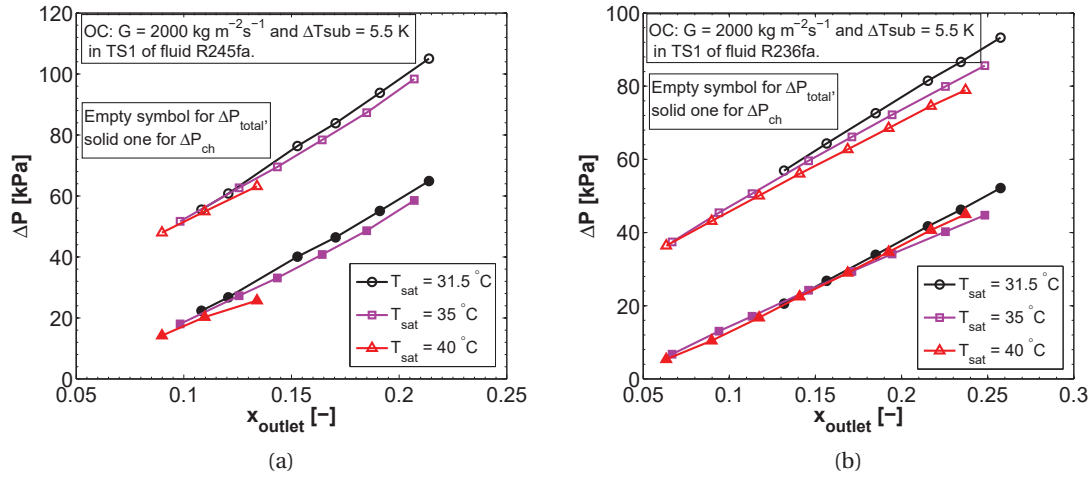


Figure 3.6 – Influence from the saturation temperature on the pressure drops: (a) R245fa and (b) R236fa.

Influence from inlet subcooling Three inlet subcoolings were tested to investigate their influence on the total and channel pressure drops. The results of two fluids of R245fa and R236fa in test section 1 are plotted in Fig. 3.7. The total pressure drop decreased slightly when increasing the inlet subcooling from 5.5 to 10 K but it appeared to be constant for the further increase from 10 to 15 K. Compared to the total pressure drop, the channel pressure drop was shown to be more subjected to the inlet subcooling for the very low outlet vapor quality (< 0.15). This is because at very low outlet vapor quality the liquid phase pressure drop, dominating the channel pressure drop, increased due to the decrease in liquid viscosity caused by the drop of fluid temperature when increasing the inlet subcooling. Besides, the low fluid temperature at high inlet subcooling induced a low outlet restriction pressure drop which was extrapolated here from the half test section heating tests Huang et al. (2016b).

Influence from fluid Fig. 3.8 presents the influence from the fluids on the total and channel pressure drops. The results of R1233zd(E) and R245fa were similar to each other due to their similar properties at the same saturation temperature. For R236fa, its total and channel pressure drop were obviously lower than the others. This phenomena is mainly due to the smallest liquid to vapor density ratio and liquid viscosity of R236fa among the three fluids

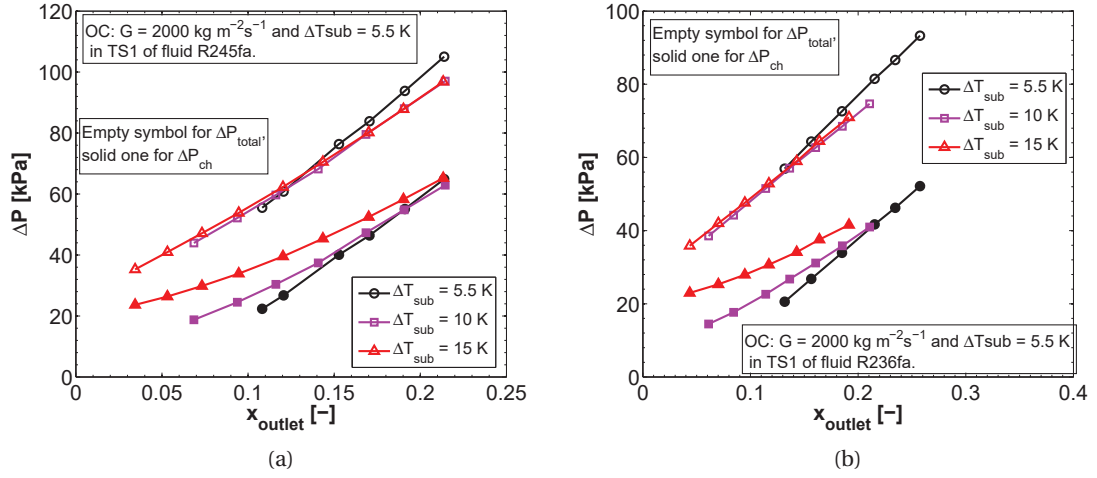


Figure 3.7 – Influence from the inlet subcooling on the pressure drops of (a) R245fa and (b) R236fa.

tested. For example, at $T_{sat} = 35^\circ\text{C}$ the liquid to vapor density ratios of R1233zd(E), R245fa and R236fa were 129.1, 109.1 and 52.6, individually. As discussed previously, low liquid to vapor density ratio and liquid viscosity render a low channel pressure drop.

Influence from test section inlet orifice Two test sections with different inlet orifices were tested here to analyze the influence from the inlet orifice width on the pressure drops as demonstrated in Fig. 3.9. The total pressure drop of TS2 was higher than that of TS1 due to the smaller orifice width. In other words, the total pressure drop increased by approximately 11 kPa when reducing the inlet orifice width from 50 to 25 μm . A flat trend of the inlet restriction pressure drop versus the outlet quality confirmed that only the pure liquid phase flowed through the inlet restriction. However, the channel pressure drop of TS2 was less than that of the TS1. The narrower inlet orifice in TS2 generated a jet with higher velocity when entering into the channel. This high-velocity jet increased the liquid phase velocity, thus reducing its difference from the vapor velocity. Hence, the shear stress at the liquid-vapor interface decreased, which led to a lower pressure drop.

Two-Phase pressure drop model validation

The reduction of Eq. (3.16) depends on two different two-phase pressure drop models: the homogeneous equilibrium model (HEM) and the separated flow model (SFM). In the case of

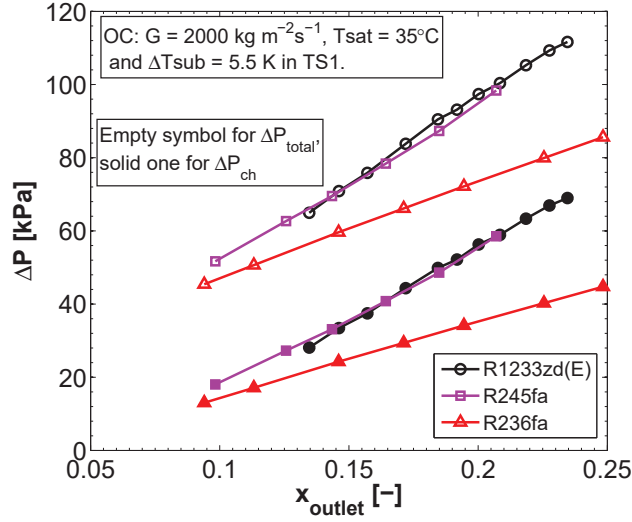


Figure 3.8 – Influence from the fluids on the pressure drops

HEM, the void fraction ϵ can be expressed as:

$$\epsilon = \frac{1}{1 + \frac{v_l}{v_v} \frac{1-x}{x}} \quad (3.17)$$

Then Eq. (3.16) can be further reduced as follows Collier and Thome (1994):

$$-\left(\frac{dP}{dz}\right)_{total} = \frac{\frac{2f_{tp}G^2}{D_h}(v_l + xv_{lv}) + G^2v_{lv}\frac{dx}{dz}}{1 + G^2x\left(\frac{dv_v}{dP}\right)} \quad (3.18)$$

Instead, with the separated flow model, Eq. (3.16) becomes Collier and Thome (1994)

$$-\left(\frac{dP}{dz}\right)_{total} = \frac{-\left(\frac{dP}{dz}\right)_{fr} + G^2\left(\frac{dx}{dz}\right)\left\{\left[\frac{2xv_v}{\epsilon} - \frac{2(1-x)v_l}{1-\epsilon}\right] + \left(\frac{\partial\epsilon}{\partial x}\right)_P\left[\frac{(1-x)^2v_l}{(1-\epsilon)^2} - \frac{x^2v_v}{\epsilon^2}\right]\right\}}{1 + G^2\left\{\frac{x^2}{\epsilon}\left(\frac{dv_v}{dP}\right) + \left(\frac{\partial\epsilon}{\partial P}\right)_x\left[\frac{(1-x)^2v_l}{(1-\epsilon)^2} - \frac{x^2v_v}{\epsilon^2}\right]\right\}} \quad (3.19)$$

The homogeneous model expresses the frictional pressure drop item with a two-phase flow friction factor, while in the separated flow model it is described by the product of the two-phase multiplier and the single-phase frictional pressure drop. The second difference is related to the void fraction. The homogeneous model assumes the liquid and vapor phase share the same velocity, which generates the homogeneous void fraction (see Eq. (3.17)). However, the void fraction in the separated model is uncertain due to the unknown slip ratio. As a result, a void fraction model, i.e. empirical correlation, based on experimental data, was necessary to obtain the momentum pressure drop. Therefore, the channel frictional pressure drop evaluated by the separated flow model also depends on the void fraction model used. Currently, this is the only way for separating the frictional pressure drop from the momentum one by using the

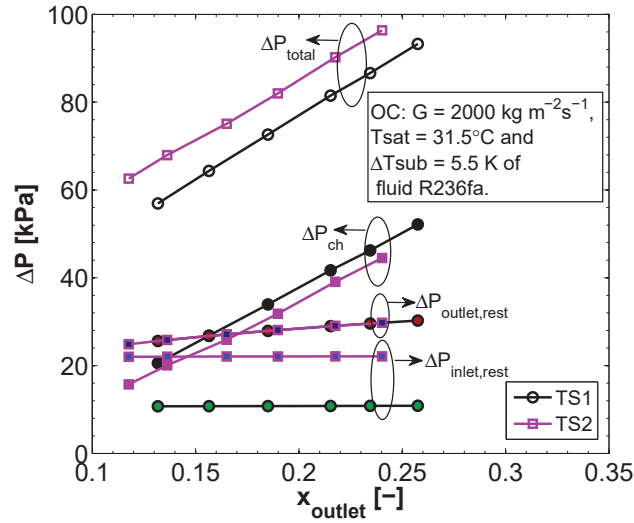


Figure 3.9 – Influence from the test section inlet orifice on the pressure drops.

SFM Qu and Mudawar (2003a); Lee and Garimella (2008); Kim and Mudawar (2013b).

In this arrangement, the homogeneous and separated flow models were implemented to predict the frictional pressure drop. Then the prediction results were compared against the stable flow boiling experimental data.

Homogeneous equilibrium model (HEM) In homogeneous flow models, the frictional pressure drop is calculated in a similar way to the single-phase flow case but with a two-phase flow friction factor and a two-phase viscosity. A piecewise function was used to determine the two-phase flow friction factor according to the different flow regimes present:

$$f_l = \begin{cases} \frac{8.058}{Re_l} & \text{(for R1233zd(E)) and} \\ \text{Shah and London (1978) (for others),} & Re_{tp} \leq 2000, \\ \frac{0.079}{Re_l^{-0.25}}, & Re_{tp} > 2000 \end{cases} \quad (3.20)$$

The homogeneous two-phase viscosity is weighted by the mixing law assumed for liquid and vapor phases. Table 3.5 lists the several of the prominent ones.

Table 3.5 – Homogeneous equilibrium models for two-phase flow properties.

Reference	Correlation
McAdams et al. (1942)	$\frac{1}{\mu_{tp}} = \frac{x}{\mu_v} + \frac{1-x}{\mu_l}$

Continued on next page

Table 3.5 – Continued from previous page

Reference	Correlation
Akers et al. (1958)	$\mu_{tp} = \frac{\mu_f}{(1-x) + x(\frac{\rho_l}{\rho_v})^{0.5}}$
Cicchitti et al. (1960)	$\mu_{tp} = x\mu_v + (1-x)\mu_l$
Dukler et al. (1964)	$\mu_{tp} = \epsilon\mu_v + (1-\epsilon)\mu_l$ $\rho_{tp} = \epsilon\rho_v + (1-\epsilon)\rho_l$
Beattie and Whalley (1982)	$\mu_{tp} = \omega\mu_v + (1-\omega)(1+2.5\omega)\mu_l$ $\omega = \frac{x\mu_v}{\mu_l + x\mu_{lv}}$
Lin et al. (1991)	$\mu_{tp} = \frac{\mu_l\mu_v}{\mu_v + x^{1.4}(\mu_l - \mu_v)}$

Separated flow model (SFM) Here, the two-phase multiplier is introduced to link the liquid or vapor phase pressure drop with the two-phase pressure drop. The liquid or vapor phase pressure drop is sorted into two different types: liquid or vapor phase only, and liquid or vapor phase alone. The former one means only liquid or vapor phase exists and flows in the channel, resulting in the liquid or vapor phase only two-phase multiplier. While the later one denotes that the liquid and vapor phase exist simultaneously and flow alone or separately in the channel, producing liquid or vapor alone two-phase multiplier.

Table 3.6 – Separated flow models for the frictional pressure drop.

Reference	Correlation
Lockhart and Martinelli (1949)	$-\left(\frac{dP}{dz}\right)_{fr} = \frac{2f_l G^2 (1-x)^2 v_l}{D_h} \phi_l^2$ $f_l = \frac{8.058}{Re_l}; Re_l = \frac{G(1-x)D_h}{\mu_l}$ $\phi_l = 1 + \frac{C}{X} + \frac{1}{X^2}; X = \sqrt{\frac{(dP/dz)_l}{(dP/dz)_v}}$ $C = 5(vv), 10(tv), 12(vt), 20(tt)$
Chisholm (1973)	$-\left(\frac{dP}{dz}\right)_{fr} = \frac{2f_{lo} G^2 v_l}{D_h} \phi_{lo}^2$ $\phi_{lo} = 1 + (Y^2 - 1)[Bx^{(2-n)/2}(1-x)^{(2-n)/2} + x^{2-n}]$ $Y^2 = \frac{(dP/dz)_v}{(dP/dz)_l}, n = 0.25$ when $0 < Y \leq 9.5$: $B = 55/\sqrt{G}$ for $G \geq 1900 \text{ kg m}^{-2} \text{ s}^{-1}$; $B = 2400/G$ for $500 \leq G < 1900 \text{ kg m}^{-2} \text{ s}^{-1}$;

Continued on next page

Table 3.6 – Continued from previous page

Reference	Correlation
	$B = 4.8 \text{ for } G < 500 \text{ kg m}^{-2} \text{ s}^{-1};$ when $9.5 < Y \leq 28$: $B = 520/(Y\sqrt{G}) \text{ for } G \leq 600 \text{ kg m}^{-2} \text{ s}^{-1};$ $B = 21/Y \text{ for } G > 600 \text{ kg m}^{-2} \text{ s}^{-1};$ when $Y > 28$: $B = 15000/(Y^2\sqrt{G})$
Grönnerud (1979)	$-\left(\frac{dP}{dz}\right)_{fr} = \frac{2f_{lo}G^2v_l}{D_h}\phi_{lo}^2$ $\phi_{lo} = 1 + \left(\frac{dP}{dz}\right)_{FR} \left[\frac{\left(\frac{v_v}{v_l}\right)}{\left(\frac{\mu_l}{\mu_v}\right)^{0.25}} - 1 \right]$ $\left(\frac{dP}{dz}\right)_{FR} = f_{FR}[x + 4(x^{1.8} - x^{10}f_{FR}^{0.5})]$ $f_{FR} = 1 \text{ if } Fr_l \geq 1$ $f_{FR} = Fr_l^{0.3} + 0.0055(\ln \frac{1}{Fr_l})^2 \text{ if } Fr_l < 1$ $Fr_l = \frac{G^2}{gD_h\rho_l^2}$
Friedel (1979)	$-\left(\frac{dP}{dz}\right)_{fr} = \frac{2f_{lo}G^2v_l}{D_h}\phi_{lo}^2$ $\phi_{lo} = E + \frac{3.24FH}{Fr_H^{0.045}We_l^{0.035}}$ $Fr_H = \frac{G^2}{gD_h\rho_H^2}, We_H = \frac{G^2D_h}{\sigma\rho_H}, \rho_H = \frac{1}{\frac{1-x}{\rho_l} + \frac{x}{\rho_v}}$ $E = (1-x)^2 + x^2 \frac{\rho_l f_{vo}}{\rho_v f_{lo}}$ $F = x^{0.78}(1-x)^{0.224}$ $H = \left(\frac{\rho_l}{\rho_v}\right)^{0.91} \left(\frac{\mu_v}{\mu_l}\right)^{0.19} \left(1 - \frac{\mu_v}{\mu_l}\right)^{0.7}$
Müller-Steinhagen and Heck (1986)	$-\left(\frac{dP}{dz}\right)_{fr} = C(1-x)^{1/3} + Bx^3$ $C = A + 2(B-A)x$ $A = -\left(\frac{dP}{dz}\right)_{lo}, -\left(\frac{dP}{dz}\right)_{lo} = \frac{2f_{lo}G^2v_l}{D_h}$ $B = -\left(\frac{dP}{dz}\right)_{vo}, -\left(\frac{dP}{dz}\right)_{vo} = \frac{2f_{vo}G^2v_v}{D_h}$
Mishima and Hibiki (1996)	$-\left(\frac{dP}{dz}\right)_{fr} = \frac{2f_l G^2(1-x)^2 v_l}{D_h} \phi_l^2$ $\phi_l^2 = 1 + \frac{C}{X} + \frac{1}{X^2}$ $C = 21(1 - e^{-319D_h})$
Qu and Mudawar (2003a)	$-\left(\frac{dP}{dz}\right)_{fr} = \frac{2f_l G^2(1-x)^2 v_l}{D_h} \phi_l^2$

Continued on next page

Table 3.6 – Continued from previous page

Reference	Correlation
Lee and Garimella (2008)	$\phi_l^2 = 1 + \frac{C}{X} + \frac{1}{X^2}$
	$C = 21(1 - e^{-319D_h})(0.00418G + 0.0613)$
	$-\left(\frac{dP}{dz}\right)_{fr} = \frac{2f_l G^2 (1-x)^2 v_l}{D_h} \phi_l^2$
Kim and Mudawar (2013b)	$\phi_l^2 = 1 + \frac{C}{X} + \frac{1}{X^2}$
	$C = 2566G^{0.5466}D_h^{0.8819}(1 - e^{-319D_h})$
	$-\left(\frac{dP}{dz}\right)_{fr} = \frac{2f_l G^2 (1-x)^2 v_l}{D_h} \phi_l^2$
Present work	$\phi_l^2 = 1 + \frac{C}{X} + \frac{1}{X^2}$
	$C = \begin{cases} C_{non-boiling} \left[1 + 60We_{lo}^{0.32} \left(Bo \frac{P_H}{P_F} \right)^{0.78} \right], & Re_l \geq 2000 \\ C_{non-boiling} \left[1 + 530We_{lo}^{0.52} \left(Bo \frac{P_H}{P_F} \right)^{1.09} \right], & Re_l < 2000 \end{cases}$
	$C_{non-boiling} =$
	$\begin{cases} 3.5 \times 10^{-5} Re_{lo}^{0.44} Su_{vo}^{0.50} \left(\frac{\rho_l}{\rho_v} \right)^{0.48}, & (vv) \\ 0.0015 Re_{lo}^{0.59} Su_{vo}^{0.19} \left(\frac{\rho_l}{\rho_v} \right)^{0.36}, & (vt) \\ 8.7 \times 10^{-4} Re_{lo}^{0.17} Su_{vo}^{0.50} \left(\frac{\rho_l}{\rho_v} \right)^{0.14}, & (tv) \\ 0.39 Re_{lo}^{0.03} Su_{vo}^{0.10} \left(\frac{\rho_l}{\rho_v} \right)^{0.35}, & (tt) \end{cases}$
	$Re_{lo} = \frac{GD_h}{\mu_l}, Su_{vo} = \frac{\rho_v \sigma D_h}{\mu_v^2}, We_{lo} = \frac{G^2 D_h}{\rho_l \sigma}, Bo = \frac{q_w}{Gh_{lv}}$
	$-\left(\frac{dP}{dz}\right)_{fr} = \frac{2f_l G^2 (1-x)^2 v_l}{D_h} \phi_l^2$
	$\phi_l^2 = 1 + \frac{C}{X} + \frac{1}{X^2}, X = \sqrt{\frac{(dP/dz)_l}{(dP/dz)_v}}$
	$f_l = \begin{cases} \frac{8.058}{Re_l} \text{ (for R1233zd(E)) and} \\ \text{Shah and London (1978) (for others),} & Re_l \leq 2000, \\ \frac{0.079}{Re_l^{0.25}}, & Re_l > 2000 \end{cases}$
	$C = \begin{cases} 0.0037 Re_v^{1.70} Re_{lo}^{-0.83}, & Re_l \leq 2000, Re_v \leq 2000 \\ 0.9 Re_v^{0.034} Re_{lo}^{0.20}, & Re_l \leq 2000, Re_v > 2000 \end{cases}$
	$Re_v = \frac{Gx D_h}{\mu_v}, Re_l = \frac{G(1-x) D_h}{\mu_l}, Re_{lo} = \frac{GD_h}{\mu_l}$

In this aspect, since the pioneering work of Lockhart and Martinelli (1949), a large number of separated flow models have been developed. The most commonly used models of macro (the first six models) and mini/micro-scale (the rest ones) are listed in Table 3.6. As can be seen, the micro-scale models were mainly developed by modifying the Chisholm parameter C based on

experimental results. However, in some previous studies Mishima and Hibiki (1996); Qu and Mudawar (2003a); Lee and Garimella (2008), some dimensional parameters (e.g. mass flux G , hydraulic diameter D_h) were included in the C expression, which should be dimensionless. In the recent model of Kim and Mudawar (2013b), a dimensionless C has been correlated with a group of non-dimensional parameters, such as the liquid only Reynolds number Re_{lo} , liquid only Weber number We_{lo} , boiling number Bo , and the density ratio $\frac{\rho_l}{\rho_v}$. When seeking the frictional pressure drop from the total measured one, the accelerational or momentum pressure drop must be properly evaluated. As expressed in Eq. (3.19), the momentum pressure drop depends on the void fraction model used. Therefore, a considerable number of void fraction models have been proposed, which could be mainly sorted into three types: homogeneous, slip ratio, and drift flux Xu and Fang (2014). The homogeneous void fraction model (see Eq. (3.17)), tends to overpredict the momentum pressure drop especially for high mass flux Kim and Mudawar (2013b). The Zivi (1964) void fraction, belonging to the type of slip ratio, as used in Qu and Mudawar (2003a); Lee and Mudawar (2005); Lee and Garimella (2008); Kim and Mudawar (2013b); Huang et al. (2016b) was also employed in the present work to obtain the momentum pressure drop¹ when validating the pressure drop models. It is worthwhile to note that the void fraction model used in the separated flow mechanistic model of Cioncolini et al. (2009) (see Table 3.7), is from Woldesemayat and Ghajar (2007).

Table 3.7 – Separated flow mechanistic model for two-phase pressure drop.

Reference	Correlation
Cioncolini et al. (2009); Cioncolini and Thome (2011)	<p>Frictional pressure gradient</p> $-\left(\frac{dP}{dz}\right)_{fr} = \frac{2f_{tp}G_c^2}{\rho_c D_c}$ $f_{tp} = 0.0196We_c^{-0.372}Re_l^{0.318}$ $We_c = \frac{G_c^2 D_c}{\rho_c \sigma}, G_c = \frac{4}{\pi} \frac{[x+e(1-x)]G}{D_c^2}$ $Re_l = (1-e)(1-x) \frac{GD_h}{\mu_l}$ $D_c \approx D_h \sqrt{\epsilon + \gamma + \epsilon\gamma}, \rho_c = (1-\epsilon_c)\rho_l + \epsilon_c\rho_v$ $\mu_c = (1-\epsilon_c)\mu_l + \epsilon_c\mu_v$ $\epsilon_c = \frac{\epsilon}{\epsilon + \gamma(1-\epsilon)}, \gamma = e \frac{\epsilon}{1-\epsilon} \frac{1-x}{x} \frac{\rho_v}{\rho_l}$ <p>Predictor-corrector methods to determine e</p> <p>1st step, predictor:</p> $\rho_c \approx \rho_v \Rightarrow We_c^P = \frac{G_c^2 D_c}{\rho_c \sigma}, e^P = [1 + 279.6(We_c^P)^{-0.8395}]^{-2.2209}$ <p>2nd step, corrector:</p> $\rho_c = \frac{x + e^P(1-x)}{x/\rho_v + e^P(1-x)/\rho_l}, We_c = \frac{G_c^2 D_c}{\rho_c \sigma}$ $e = (1 + 279.6We_c^{-0.8395})^{-2.2209}$ <p>Momentum pressure gradient</p>

Continued on next page

1. After comparing a group of void fraction models, it is found that Zivi model gives a moderate value resulting in a reasonable momentum pressure drop under high mass flux.

Chapter 3. Steady-state pressure drop

Table 3.7 – Continued from previous page

Reference	Correlation
	$-\left(\frac{dP}{dz}\right)_{mom} = G^2 \frac{d}{dz} \left[\frac{x^2}{\rho_v \epsilon} + \frac{e^2(1-x)^2}{\rho_l \gamma(1-\epsilon)} + \frac{(1-e)^2(1-x)^2}{\rho_l(1-\gamma)(1-\epsilon)} \right]$
	ϵ based on void fraction model of Woldesemayat and Ghajar (2007)

Table 3.8 – Statistical comparison between the prediction by pressure drop models and the experimental data.

Correlations	MAE (%)	within 30%	within 50%
McAdams et al. (1942)	49.9	50.0	70.7
Akers et al. (1958)	86.4	35.3	50.5
Cicchitti et al. (1960)	152.6	6.5	12.0
Dukler et al. (1964)	55.3	48.4	71.2
Beattie and Whalley (1982)	188.4	3.3	9.2
Lin et al. (1991)	82.7	40.8	54.9
Cioncolini et al. (2009)	81.5	33.2	49.5
Lockhart and Martinelli (1949)	80.1	42.9	54.9
Grønnerud (1979)	97.1	8.7	31.0
Chisholm (1973)	101.8	18.5	36.4
Friedel (1979)	183.4	4.3	8.7
Müller-Steinhagen and Heck (1986)	113.1	14.7	30.4
Mishima and Hibiki (1996)	49.9	25.0	50.5
Tran et al. (2000)	4124.3	0	0
Qu and Mudawar (2003a)	77.4	46.2	56.5
Lee and Garimella (2008)	47.5	31.0	64.1
Kim and Mudawar (2013b)	46.2	53.8	75.5
Present work	27.8	64.1	81.0

The comparison in frictional pressure drop between the prediction and the experimental results are presented in Table 3.8 and Figs. 3.10 and 3.11. It can be seen that the mini/micro-scale based models generally predicted the results better than the macro-scale based methods. The best prediction was found from the correlation of Kim and Mudawar (2013b) with a MAE of 46.2%, followed by Lee and Garimella (2008) with a MAE of 47.5%, while the correlation of McAdams et al. (1942), based on the vapor quality averaged homogeneous viscosity, yielded the best prediction with a MAE of 49.9% among the macro-scale models. However, most of the current macro-scale based models tend to over-predict the experimental data. Instead,

the mini/micro-scale based prediction methods such as Mishima and Hibiki (1996), Lee and Garimella (2008), and Kim and Mudawar (2012a) tend to under-predict the data when the frictional pressure drop was higher than 15 kPa. Such poor predictions indicated that the existing models can not be used to evaluate the two-phase frictional pressure drops at high mass flux where both the frictional and momentum pressure drops played important roles. In our recent work Huang et al. (2016b), a new pressure drop model for high mass fluxes based on the experimental results of R1233zd(E) was developed by fitting the Chisholm parameter C with the vapor Reynolds number Re_v and liquid only Reynolds number Re_{lo} . Then, the coefficients in the expression of C parameter in Huang et al. (2016b) were re-fitted according to the present data base (184 points) to propose a new frictional pressure drop method covering more operating conditions, as shown below:

$$-\left(\frac{dp}{dz}\right)_{fr} = \frac{2f_l G^2 (1-x)^2 v_l}{D_h} \phi_l^2 \quad (3.21)$$

$$\phi_l^2 = 1 + \frac{C}{X} + \frac{1}{X^2}, \quad X = \sqrt{\frac{(dP/dz)_l}{(dP/dz)_v}} \quad (3.22)$$

$$f_l = \begin{cases} \frac{8.058}{Re_l} & \text{(for R1233zd(E)) and} \\ \text{Shah and London (1978) (for others),} & Re_l \leq 2000, \\ \frac{0.079}{Re_l^{0.25}}, & Re_l > 2000 \end{cases} \quad (3.23)$$

$$C = \begin{cases} 0.0037 Re_v^{1.70} Re_{lo}^{-0.83}, & Re_l \leq 2000, Re_v \leq 2000 \\ 0.9 Re_v^{0.034} Re_{lo}^{0.20}, & Re_l \leq 2000, Re_v > 2000 \end{cases} \quad (3.24)$$

$$Re_v = \frac{Gx D_h}{\mu_v}, \quad Re_l = \frac{G(1-x) D_h}{\mu_l}, \quad Re_{lo} = \frac{G D_h}{\mu_l} \quad (3.25)$$

The comparison between the present model and the experimental results is demonstrated in Fig. 3.11i, which rendered the best agreement to a MAE of 27.8%. This new method will be implemented for the two-phase local pressure and temperature profiles prediction (as presented in the following section) to obtain the local heat transfer coefficients.

Two-phase flow local pressure and temperature predictions

The present two-phase pressure drop model expressed in Eqs. (3.21) to (3.25), were implemented to predict the local pressure for obtaining the local fluid temperature profile at saturation conditions along the microchannels. Since the two-phase flow local pressure at the channel end was indirectly measured based on the half heating tests, the predicted local pressure profile was corrected locally according to the difference in pressure value at the channel end between the predicted value and the measured one.

Fig. 3.12 shows the two-phase flow local pressure and temperature profile at the test section's centerline along the channel length. The red dashed line is the demarcation between the

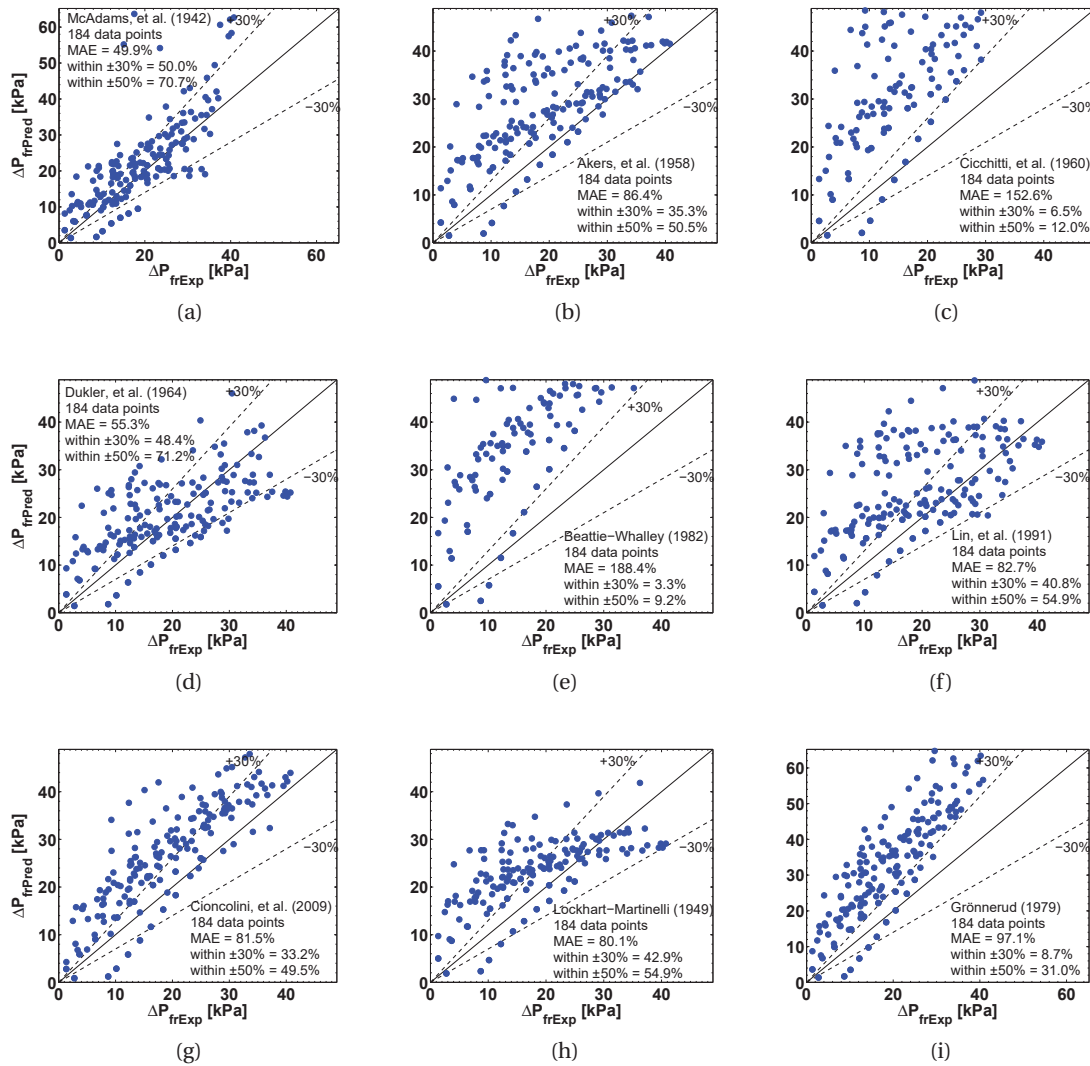


Figure 3.10 – Pressure drop models comparison against stable flow boiling experimental data: (a) McAdams et al. (1942), (b) Akers et al. (1958), (c) Cicchitti et al. (1960), (d) Dukler et al. (1964), (e) Beattie and Whalley (1982) (f) Lin et al. (1991), (g) Cioncolini et al. (2009); Cioncolini and Thome (2011), (h) Lockhart and Martinelli (1949), (i) Grönnerud (1979).

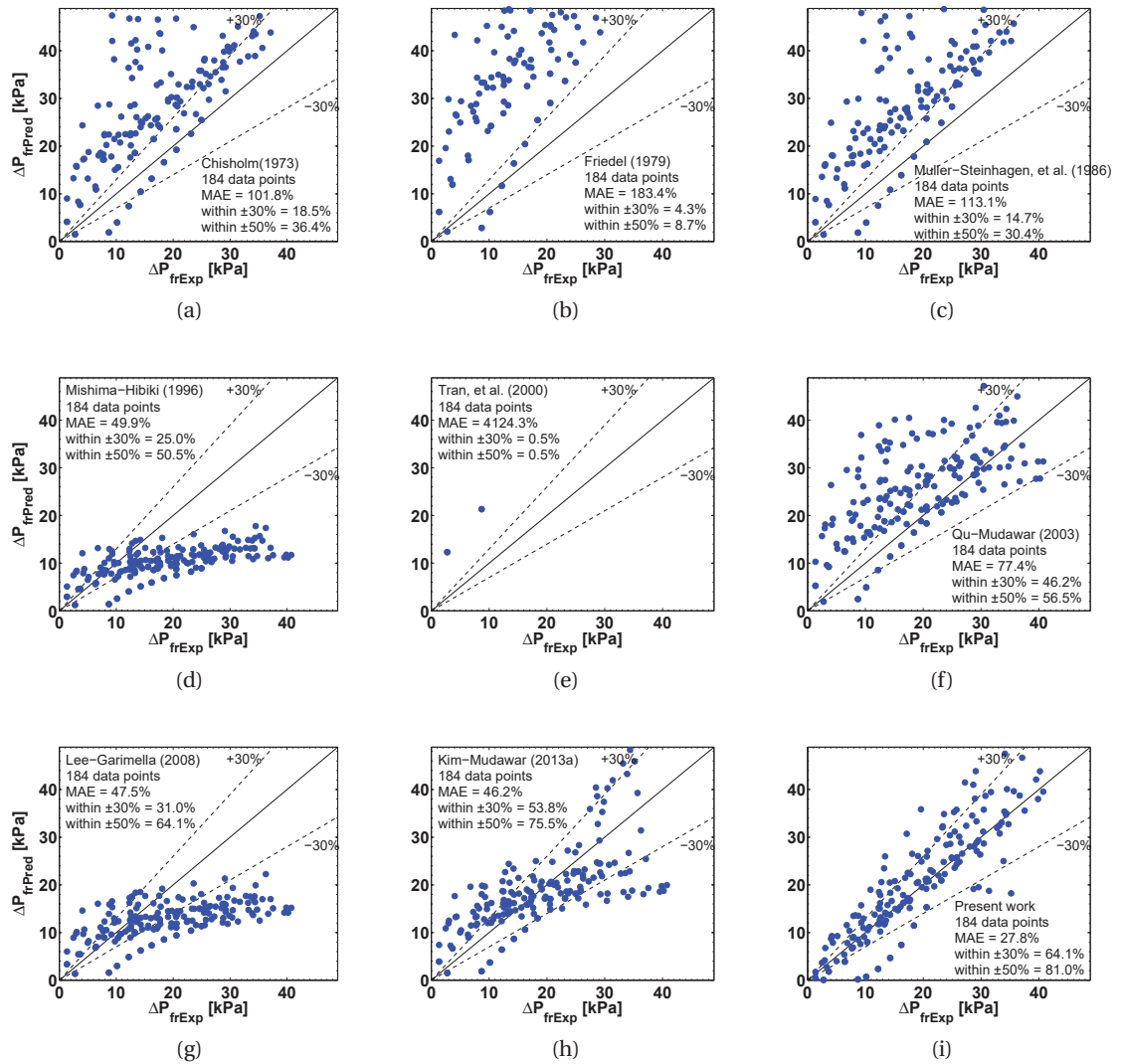


Figure 3.11 – Pressure drop models comparison against stable flow boiling experimental data: (a) Chisholm Chisholm (1973), (b) Friedel (1979), (c) Müller-Steinhagen and Heck (1986), (d) Mishima and Hibiki (1996), (e) Tran et al. (2000), (f) Qu and Mudawar (2003a), (g) Lee and Garimella (2008), (h) Kim and Mudawar (2013b) and (i) Present work.

single-phase and/or subcooled flow boiling region and the saturated flow boiling region. In the single-phase and/or subcooled flow boiling region, the local pressure profile was obtained using the single-phase flow friction factor, thus it decreases linearly versus the channel length; since the local temperature profile was calculated based on the single-phase local energy balance, it increases linearly until the maximum value, where the onset of saturation flow boiling occurs. In the saturated flow boiling region, the local pressure profile was obtained based on the present two-phase frictional pressure drop model and Zivi void fraction model for momentum pressure drop. The local pressure tends to decrease with a 'parabolic' curve rather than a linear one, which is the traditional assumption when dealing with the two-phase local pressure profiles in macrochannels where the pressure drops are small but as can be seen is not appropriate here. Correspondingly, the local fluid temperature exhibits a non-linear decreasing trend determined by the local pressure curve.

Fig. 3.13 shows the two-phase flow local pressure and temperature maps. Both of them indi-

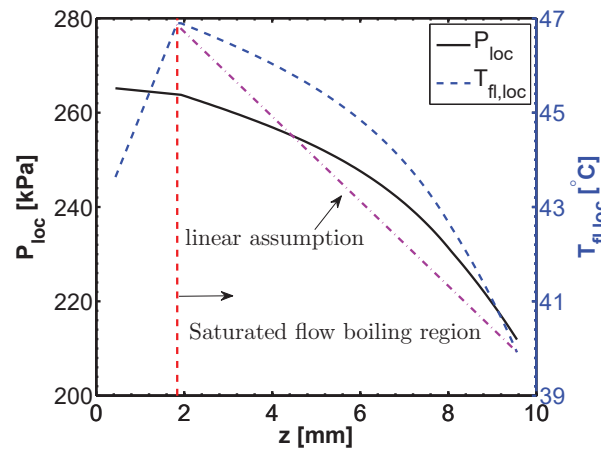


Figure 3.12 – Two-phase flow local pressure and temperature profiles at the centerline ($y = 5$ mm) along the channel length for $G = 2000 \text{ kg m}^{-2}\text{s}^{-1}$, $q = 44 \text{ W cm}^{-2}$.

cate obvious variations along the channel length due to the high mass flux, while they exhibit a nearly uniform distribution in the widthwise direction, which is related to the main assumption that channels have the same mass flux and pressure drop (small widthwise variation is due to heat flux from heat spreading accounted for in the data reduction process).

Examining Fig. 3.12 and Fig. 3.13b, one can deduce that the difference between the predicted variation in the local saturation temperature with respect to the linear assumption reaches up to 1~1.5 K. Applying Newton's law of cooling with the fluid temperature equal to the local saturation temperature, it is quite evident that an accurate prediction of the local saturation pressure is of paramount importance in obtaining the local wall superheats (especially those in very small channels with significant pressure drops) to determine local heat transfer coeffi-

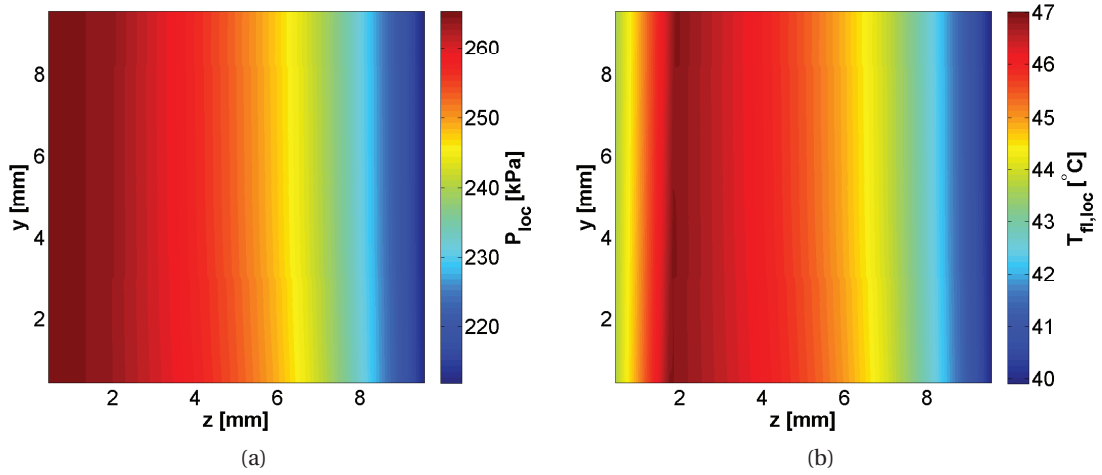


Figure 3.13 – Two-phase flow local pressure and temperature map at $G = 2000 \text{ kg m}^{-2}\text{s}^{-1}$, $q = 44 \text{ W cm}^{-2}$: (a) local pressure map and (b) local fluid temperature map (The flow direction is from left to right side).

cients. Secondly, this local saturation temperature profile also influences the heat spreading process and thus the effective value of the local heat flux, even for uniformly applied heat fluxes, since its fall in the saturated zone reaches up to 7 K in Fig. 3.13b. As a third influence, this heat spreading has to be taken into account in the energy balance to back out the local vapor qualities at which the local heat transfer coefficients are reported. Thus, the present paper has highlighted this issue and proposed an accurate approach to deal with it.

Fig. 3.14 presents the local fluid pressure and temperature profiles at the centerline along the channel length for one mass flux and different heat fluxes ($G = 2000 \text{ kg m}^{-2}\text{s}^{-1}$, $q = 34, 36, 40$ and 44 W cm^{-2}). The fluid pressure and temperature at the channel inlet increased with the heat flux experimentally in order to maintain the same inlet subcooling. Additionally, the channel pressure drop and the fluid temperature decrease with the increase in heat flux due to the increase in vapor quality. In Fig. 3.14b it is shown that the onset of saturated flow boiling moves towards the channel inlet with the increase in heat flux.

3.5 Conclusion

This paper presents a comparative investigation on flow boiling of three refrigerants (R1233zd(E), R245fa and R236fa) in two multi-microchannel evaporators under various operating conditions. The influence from the outlet saturation temperature, inlet subcooling, fluid and inlet orifice width on the channel and total pressure drop during flow boiling were systematically analyzed. The main conclusions are summarized as follows:

- (1) Single-phase flow validations, including adiabatic and diabatic flow, were carried out prior

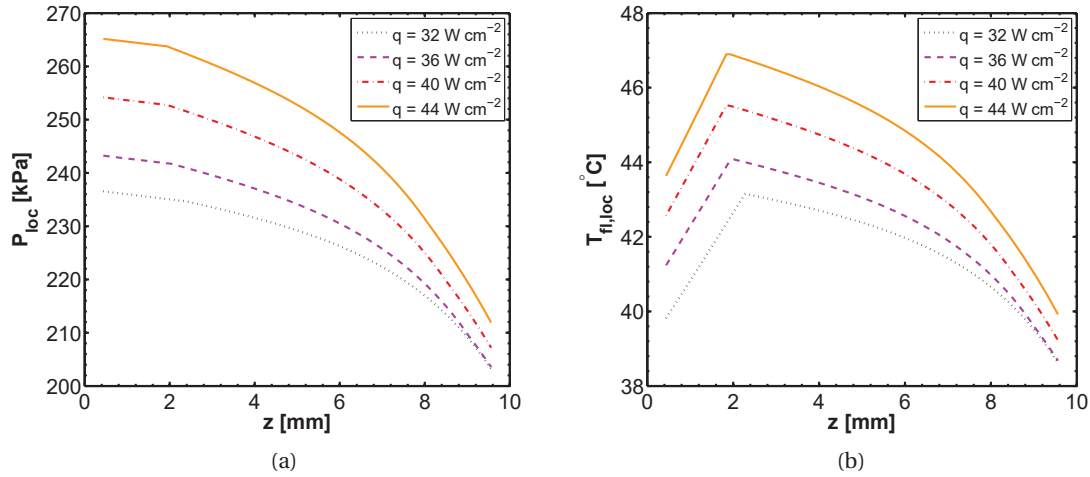


Figure 3.14 – Effect of heat flux on two-phase local fluid pressure and temperature profiles of the centerline along the channel length at $G = 2000 \text{ kg m}^{-2}\text{s}^{-1}$: (a) local pressure profile and (b) local fluid temperature profile.

to the two-phase flow tests. It is found that the correlation of Blevins for inlet and outlet restriction pressure drops yielded a channel pressure drop that agreed well with the prediction from the channel pressure drop correlations of Shah and London (1978) and Muzychka and Yovanovich (2009). Additionally, the correlation of Shah and London (1978) was proven to be reliable for predicting the flow friction factor for the fluids of R245fa and R236fa, while for that of the new fluid R1233zd(E) a new correlation based on the present experimental data was proposed. These results were used in the two-phase pressure drop calculation.

(2) Increasing the saturation temperature decreased the two-phase total and channel pressure drops. Increasing the inlet subcooling increased the channel pressure drop. The fluid R236fa exhibited the lowest total and channel pressure drops. The test section 2 (TS2) with inlet orifice width of $25 \text{ }\mu\text{m}$ introduced higher total pressure drop but lower channel pressure drop compared to TS1 whose inlet orifice width was $50 \text{ }\mu\text{m}$.

(3) Seventeen existing two-phase pressure drop models covering macro- and micro-scale were accessed against the present micro-scale data base (184 data points), and none of them was able to predict well the experimental results. Therefore, we developed a new empirical frictional pressure drop model by fitting the Chisholm parameter C with the vapor and liquid only Reynolds numbers. The new frictional pressure drop model provided agreement with the experimental data to a MAE of 27.8%.

(4) The new proposed frictional pressure drop model then was used to predict local non-linear two-phase flow pressure and temperature profiles for rendering accurate fine-resolution local heat transfer coefficients, illustrating its important influence on the data reduction process.

4 Steady-state heat Transfer

This chapter is from the paper below by Huang and Thome (2016):

H. Huang, J.R. Thome, Local measurements and a new flow pattern based model for subcooled and saturated flow boiling heat transfer in multi-microchannel evaporators, *International Journal of Heat and Mass Transfer*, 103(2016) 701-714.

The detailed data reduction methods (the single- and two-phase energy balance, and the local Nusselt number validation) and the six leading saturated flow boiling heat transfer models omitted in this chapter were presented in Appendix A.

Abstract

A comprehensive experimental campaign has been conducted to measure the local heat transfer coefficients during flow boiling of refrigerants in multi-microchannel evaporators. Three refrigerants (R1233zd(E), R245fa and R236fa) were tested in two silicon evaporators at three inlet subcoolings and at three outlet saturation temperatures. The test section back-side temperatures were measured by a fine-resolution infrared (IR) camera providing a two-dimensional thermal map, which was used by solving the three-dimensional inverse heat conduction problem to obtain the local heat transfer coefficients on a pixel-by-pixel basis. The experimental results revealed different trends along the flow direction. The decreasing trend (when existing) at the beginning of the channel was attributable to the single-phase thermal developing flow, then heat transfer increased from the onset of subcooled flow boiling up until the onset of saturated flow boiling, and afterwards it decreased again until entering the annular flow regime where it started to pick up and rose significantly. Combining our new data together with our recent experimental work of Huang et al. (2016b), a new flow pattern based model has been proposed for local heat transfer prediction, starting from single-phase flow all the way through to annular flow. This new model also included a new local heat transfer method for the subcooled flow boiling region since no truly local subcooled heat transfer

prediction method can be found in the literature for microchannels. This new flow pattern based model predicted the total local heat transfer database (1,941,538 local points) well with a MAE of 14.2% and with 90.1% of the data predicted within $\pm 30\%$. It successfully tracks the experimental trends without any jumps in predictions when changing flow patterns.

4.1 Introduction

Flow boiling heat transfer in multi-microchannel evaporators has been of interest to both industry and academia for more than a decade Thome and Kim (2015); Thome (2004); Qu and Mudawar (2003b); Kandlikar (2002); Thome et al. (2004). However, the dominating heat transfer mechanisms with respect to governing flow boiling in multi-microchannel evaporators has been debatable over the role of nucleate boiling in the low vapor quality region Thome et al. (2004); Cioncolini and Thome (2011); Kim and Mudawar (2013a); Costa-Patry and Thome (2013); Huang et al. (2016b). With respect to flow boiling in macrochannels, the numerous small bubbles growing at the wall in the low quality region are not confined by the channel wall, and hence it is generally thought that nucleate boiling plays an important role, while in the high vapor quality region convective flow boiling takes over. However, when the channel size is reduced to the micro-scale ($Co > 0.5$), the bubbles are subject to the confinement of the channel wall Thome (2004). In this case, directly extrapolating the heat transfer mechanisms occurring in macrochannels to explain what is happening in microchannels is questionable. A recent study by Huang et al. Huang et al. (2016b) has shed a little more light on these pertinent heat transfer mechanisms. In that study, a new environmentally friendly refrigerant R1233zd(E) was tested as the working fluid while in the present study new data are obtained for R245fa and R236fa. Their fine-resolution local heat transfer coefficients were obtained through solving the 3D inverse heat conduction problem with a 2D temperature map recorded by an infrared (IR) camera as the input condition Huang et al. (2016a). The fine-resolution local heat transfer data in the saturated flow boiling region were compared with existing heat transfer models. The mechanistic flow pattern based model by Costa-Patry and Thome (2013) combining the three-zone model of Thome et al. (2004) for low vapor qualities and the annular flow model of Cioncolini and Thome (2011) for medium and high vapor qualities showed the best agreement with the experimental data. Therefore, the liquid thin film evaporation process of the three-zone model was concluded to be the dominant mechanism controlling saturated flow boiling heat transfer in slug flow in microchannels rather than nucleate boiling.

In two-phase cooling of electronics, the fluid is preferred to enter the microchannel evaporators with an inlet subcooling to reduce the inlet restriction pressure drop and to avoid flow boiling instabilities. When a subcooled fluid flows through a sufficiently heated channel, it usually first experiences a single-phase liquid region and/or a subcooled flow boiling region, and finally a saturated flow boiling region, as schematically demonstrated in Fig. 4.1. The

length of each segment depends on the specific experimental conditions, such as the inlet subcooling, mass flux, heat flux and wall superheat, etc.

However, compared to saturated flow boiling, the number of studies on the subcooled flow boiling in microchannel evaporators is limited Qu and Mudawar (2002); Li and Cheng (2004); Liu et al. (2005); Liu and Garimella (2007); Lee and Garimella (2008), and thereby there are few local subcooled flow boiling heat transfer data available.

Liu and Garimella (2007) studied the flow boiling heat transfer of water in two microchan-

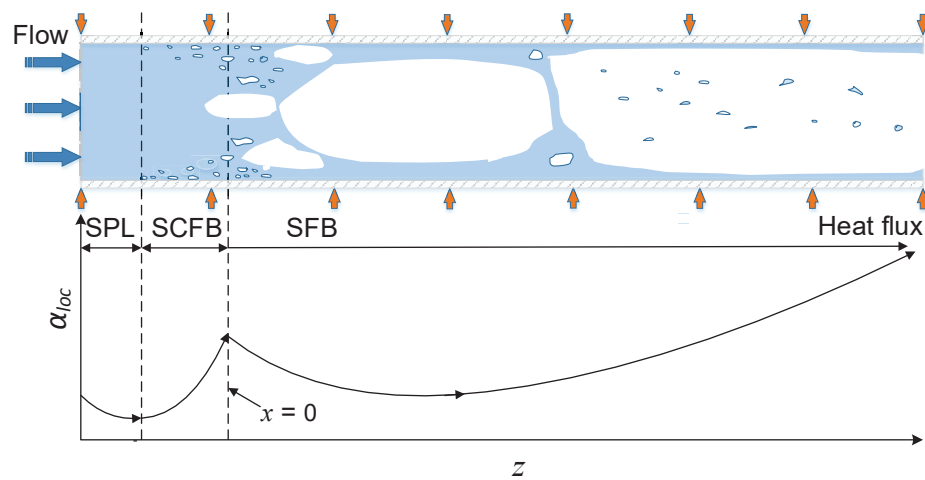


Figure 4.1 – Schematics of flow patterns and local heat transfer coefficient trend (SPL: single-phase liquid, SCFB: subcooled flow boiling and SFB: saturated flow boiling).

nel evaporators considering the heat transfer in single-phase, subcooled and saturated flow boiling regions. The length of the subcooled flow boiling region was identified by using their own model for the onset of nucleate boiling (ONB) developed in Liu et al. (2005). The local wall temperature was extrapolated based on three thermocouples (with an interval of 1.02 cm) placed at a distance of 3.17 mm to the microchannel base. A length averaged heat transfer coefficient between the single-phase and subcooled flow boiling region was compared with conventional correlations, where the Shah correlation Shah (1977) was shown to be accurate for the prediction.

Lee and Garimella (2008) investigated subcooled flow boiling heat transfer of HFE7100 in microchannel heat sinks. The subcooled flow boiling heat transfer methods developed for macrochannels were proven to be unsuitable to predict their microchannel data. Therefore, new empirical models for the incipient heat flux and the mean subcooled flow boiling heat transfer were proposed, which provided good agreement with their experimental data. Later, this model was used by Kim and Mudawar (2012b) for the heat transfer prediction in the subcooled flow boiling region. Thereby, averaged heat transfer coefficients versus the vapor quality at the channel outlet were reported.

Apparently, none of the existing studies in literature on subcooled flow boiling have reported truly local subcooled flow boiling heat transfer data, which are of particular importance for predicting and simulating the local thermal performance of microchannel evaporators Sannen (2013); Lamaison (2014).

The present study provides a comprehensive local heat transfer data base for flow boiling of refrigerants in multi-microchannel evaporators covering single-phase heat transfer and the subcooled and saturated flow boiling regions. A local “proration” heat transfer model for subcooled flow boiling will be suggested. The saturated flow boiling heat transfer data were used to confirm the mechanism governing flow boiling heat transfer in multi-microchannel evaporators. Overall, a new flow pattern based model starting from the subcooled region all the way into annular flow will be proposed.

4.2 Experimental setup

4.2.1 Experimental facility and test section

The experimental facility used here for the flow boiling study is depicted in Fig. 3.1. The fluid circulation in the system was driven by an oil-free gear pump. The mass flow rate was measured with a Coriolis mass flowmeter. Two test sections (i.e. see Fig. 3.2) were tested in the experiment. They had the same finned base area of $10 \times 10 \text{ mm}^2$ on the silicon base plate with 67 channels. Each etched channel was $100 \mu\text{m}$ in height, $100 \mu\text{m}$ in width, and separated by a fin with a thickness of $50 \mu\text{m}$. The two test sections had different inlet orifice widths: $50 \mu\text{m}$ for test section 1 (TS1) and $25 \mu\text{m}$ for test section 2 (TS2). A high speed camera (Photron Fastcam-Ultima APX) coupled with a microscope (Nikon 800) was used to visualize the flow regime through the transparent pyrex cover bonded on top of the silicon channels. A uniform heat flux was imposed by a DC power supply (Sorensen DLM32–95E) through two micro-heaters sputtered on the bottom of the test section. An IR camera (FLIR ThermoCAM SC3000) was employed to record the temperature on the backside of the test section. K-type thermocouples and pressure transducers were inserted into the inlet and outlet manifolds to measure their fluid temperatures and pressures individually, as shown in Fig. 3.2e. The facility control and the data acquisition were managed by a LabView program.

4.2.2 Operating conditions and measurement uncertainties

Six types of variables influencing the local heat transfer were investigated: heat flux (from 20 to 64 W cm^{-2}), mass flux (from 1250 to $2750 \text{ kg m}^{-2}\text{s}^{-1}$), inlet subcooling (5.5, 10 and 15 K), outlet saturation temperature (31.5, 35 and 40°C), fluid (R1233zd(E), R245fa and R236fa), and inlet orifice width (50 and $25 \mu\text{m}$). The main properties of the three fluids tested are listed in Table.

4.1. The new fluid R1233zd(E) tested in Huang et al. (2016b) has similar thermal properties as R245fa but with an excellent Global Warming Potential ($GWP < 5$) and atmospheric life time duration (26 days), so it is a promising working fluid from an environmental standpoint. The inlet subcooling was set within ± 1.1 K and the outlet saturation temperature was maintained within ± 1.5 °C of the respective targets in the various tests. The test conditions were very stable during the tests. The pressure transducer, thermocouples and the IR camera were calibrated individually Szczukiewicz et al. (2013). After calibration, the IR camera was sufficient to measure the test section's backside temperature with an accuracy of ± 0.2 °C. The approach proposed by Kline and McClintock (1953) was used for the uncertainty analysis. Through the error propagation analysis the accuracy of the wall heat transfer coefficients was evaluated to be within $\pm 9.9\%$. Precise data reduction methodology is critically important to

Table 4.1 – Properties of three fluids tested here at $T_{sat} = 35$ °C (the properties without notation are based on the NIST REFPROP 9.0).

Property	Unit	R1233zd(E)	R245fa	R236fa
Pressure	(bar)	1.80	2.12	3.76
Liquid density	(kg m ⁻³)	1273.80	1310.90	1325.40
Vapor density		9.87	12.02	25.20
Density ratio (ρ_v/ρ_l)		0.0077	0.0092	0.019
Liquid enthalpy	(kJ kg ⁻¹)	240.23	245.81	243.71
Vapor enthalpy		426.45	430.08	383.59
Latent heat	(kJ kg ⁻¹)	186.22	184.27	139.88
Liquid thermal conductivity	(W m ⁻¹ K ⁻¹)	0.090	0.085	0.070
Vapor thermal conductivity		0.015	0.014	0.014
Liquid viscosity	(μ Pa s)	400.41	359.22	252.08
Vapor viscosity		11.55	10.59	11.23
Surface tension	(N/m)	0.011	0.012	0.0089
GWP Hulse et al. (2012)		< 5	950	9810
Haynes (2010)				
Atmospheric life time Haynes (2010)		26 days	7.9 years	240 years
Hulse et al. (2012)				

obtain the final experimental results here. In this part, the data processing procedure covering single- and two-phase flow is elaborated in detail. In the current literature, two main

assumptions are usually made for processing the flow boiling data in multi-microchannels evaporators: uniform heat flux and mass flux distribution. In this work, the non-uniform heat flux distribution are carefully considered by solving a 3D inverse heat conduction problem while the uniform mass flux distribution is still assumed.

4.3 Data Reduction

The data reduction process assumes the inlet micro-orifices have created uniform flow to all channels. Hence, the local heat transfer coefficient of each pixel is determined applying Newton's law of cooling using the local values of heat flux, wall temperature and saturation temperature. The detailed steps for the data reduction were documented in our recent work Huang et al. (2016b). Therefore, only the core part was introduced in this section.

The local channel wall heat transfer coefficients were calculated through the local footprint heat transfer coefficients based on the fin equation Incropera (2006) as follows:

$$\alpha_{wall}(y, z) = \frac{\alpha_{ftp}(y, z) W_{ME} L_{ME}}{N_{ch} [W_{ch} L_{ME} + 2(L_{ME} + W_f/2) H_{ch} \eta_f(y, z)]} \quad (4.1)$$

$$\alpha_{ftp}(y, z) = \frac{q_{ftp}(y, z)}{T_{ftp}(y, z) - T_{fl}(y, z)} \quad (4.2)$$

$$\eta_f(y, z) = \frac{\tanh[m(y, z) H_{ch}]}{m(y, z) H_{ch}} \quad (4.3)$$

$$m(y, z) = \sqrt{\frac{2\alpha_{wall}(y, z)(L_{ME} + W_f)}{k_{Si}(W_f L_{ME})}} \quad (4.4)$$

where k_{Si} is the thermal conductivity of silicon, depending on its temperature Costa-Patry (2011) as:

$$k_{Si} = 0.0007T^2 - 0.5416T + 157.39 \quad (4.5)$$

The local footprint heat flux $q_{ftp}(y, z)$ and temperature $T_{ftp}(y, z)$ were obtained by solving a steady state 3D inverse heat conduction problem. The main steps for solving the steady state 3D inverse heat conduction problem are: (1) solving direct steady state 3D heat conduction equations with a guessed footprint temperature; (2) using the Newton-Raphson method to optimize the new footprint temperature; (3) employing the local energy balance method to get the footprint heat flux. The detailed procedure for doing this has been described in our

previous work Huang et al. (2016a), where the equations to solve are:

$$\frac{\partial}{\partial x}(k \frac{\partial T}{\partial x}) + \frac{\partial}{\partial y}(k \frac{\partial T}{\partial y}) + \frac{\partial}{\partial z}(k \frac{\partial T}{\partial z}) = 0; \quad (4.6)$$

$$T(0, y, z) = T_{IR}, q(0, y, z) = q_b \quad (4.7)$$

$$q(x, 0, z) = q_s, q(x, W_{ME}, z) = q_n \quad (4.8)$$

$$q(x, y, 0) = q_w, q(x, y, L_{ME}) = q_e \quad (4.9)$$

where x , y , and z indicate the thickness, the widthwise and the lengthwise directions of the microchannel evaporator, individually. q_w , q_e , q_n and q_s are the heat flux at the four lateral sides of the substrate. Currently, in most of the literature, the lateral side heat fluxes are assumed to be zero, i.e. no heat loss through the lateral sides of the test section finned area. In this case, the local footprint heat flux at the beginning and ending of the microchannels would be incorrectly higher than the rest, which is not true in reality. Therefore, a new method to determine the boundary condition at the lateral sides was proposed based on the test section base IR temperature map. Here we have assumed each of the four heat fluxes were constant, while q_b is the heat flux at the base of the substrate, which is adjusted from the nominal base heat flux q_{base} combining the total heat loss and that at the lateral sides:

$$q_b A_b = Q_{total} - (Q_{loss} - Q_{axial}) \quad (4.10)$$

$$Q_{axial} = q_w A_w + q_e A_e + q_s A_s + q_n A_n \quad (4.11)$$

After the local footprint heat flux is obtained, the local vapor quality can be calculated (i.e. not assuming a linear variation) from the local energy balance in each control volume ignoring the negligible kinetic energy variation:

$$x(y, z) = \frac{\int_0^z q_{ftp}(y, z) \Delta y dz}{\dot{m}_0} + H_{inlet} - H_l(P(y, z)) \quad (4.12)$$

The two-phase local fluid temperature is predicted by the general frictional pressure drop model proposed in our recent study on pressure drops Huang and Thome (2017), where the

Zivi (1964) void fraction model was used for obtaining the momentum pressure drop:

$$-\left(\frac{dp}{dz}\right)_{fr} = \frac{2f_l G^2 (1-x)^2 v_l}{D_h} \phi_l^2 \quad (4.13)$$

$$\phi_l^2 = 1 + \frac{C}{X} + \frac{1}{X^2}, \quad X = \sqrt{\frac{(dP/dz)_l}{(dP/dz)_v}} \quad (4.14)$$

$$f_l = \begin{cases} \frac{8.058}{Re_l} & \text{(for R1233zd(E)) and} \\ \frac{24}{Re_l} F_{ar} & \text{Shah and London (1978) (for R236fa and R245fa), } Re_l \leq 2000, \\ \frac{0.079}{Re_l^{0.25}}, & Re_l > 2000 \end{cases} \quad (4.15)$$

$$F_{ar} = 1 - 1.3553ar + 1.9467ar^2 - 1.7012ar^3 + 0.9564ar^4 - 0.2537ar^5 \quad (4.16)$$

$$C = \begin{cases} 0.0037 Re_v^{1.70} Re_{lo}^{-0.83}, & Re_l \leq 2000, Re_v \leq 2000 \\ 0.9 Re_v^{0.034} Re_{lo}^{0.20}, & Re_l \leq 2000, Re_v > 2000 \end{cases} \quad (4.17)$$

$$Re_v = \frac{Gx D_h}{\mu_v}, \quad Re_l = \frac{G(1-x) D_h}{\mu_l}, \quad Re_{lo} = \frac{G D_h}{\mu_l} \quad (4.18)$$

4.4 Experimental results and discussions

The single-phase flow validation in terms of the local Nusselt number is presented in Fig. 4.2. The detailed methods and explanation were documented in our previous work Huang et al.

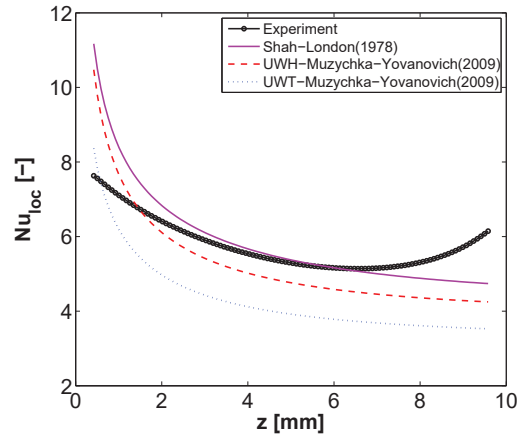


Figure 4.2 – Single-phase local Nusselt number validation for R245fa at $G = 1500 \text{ kg m}^{-2} \text{ s}^{-1}$ and $q = 4 \text{ W cm}^{-2}$ in TS1 Shah and London (1978); Muzychka and Yovanovich (2004).

(2016b). Therefore, this section mainly focuses on the analysis and discussion of the local two-phase heat transfer coefficients.

4.4.1 Effect of heat flux

The local heat transfer coefficient increased with the heat flux and the onset of saturated flow boiling occurred earlier along the test section at higher heat flux as expected. This can be seen from the new results of R245fa at saturation temperature of 40 °C, as shown in Fig. 4.3. The effect of heat flux on the local heat transfer coefficients is the same as in our previous work Huang et al. (2016b).

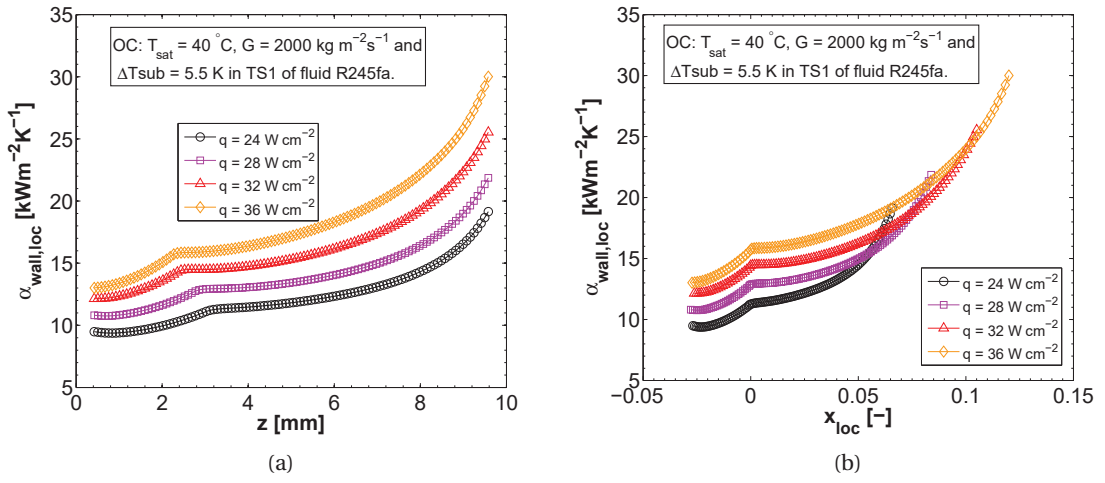


Figure 4.3 – Effect of heat flux on new widthwise averaged local heat transfer coefficients for R245fa at $G = 2000$ kg m⁻²s⁻¹ and $T_{sat} = 40$ °C in test section 1: (a) versus local length and (b) versus local vapor quality.

4.4.2 Effect of mass flux

The effect of mass flux on the local heat transfer coefficient for R245fa is described in Fig. 4.4b. Along the flow direction, the length of the subcooled region increased with mass flux and a small portion of single-phase thermal developing region was found at higher mass flux, witnessed by a decreasing trend at the beginning of the channel. Similar results were also found for the R1233zd(E) in our recent work Huang et al. (2016b), as described in Fig. 4.4a.

4.4.3 Effect of inlet subcooling

The influence from the inlet subcooling on the local heat transfer coefficients is demonstrated in Fig. 4.5. These new results reveal that the length of the subcooled region increased with inlet subcooling as one would expect from Eq. (4.12). As a result this, the local heat transfer coefficient decreased when increasing the inlet subcooling. Therefore, the inlet subcooling

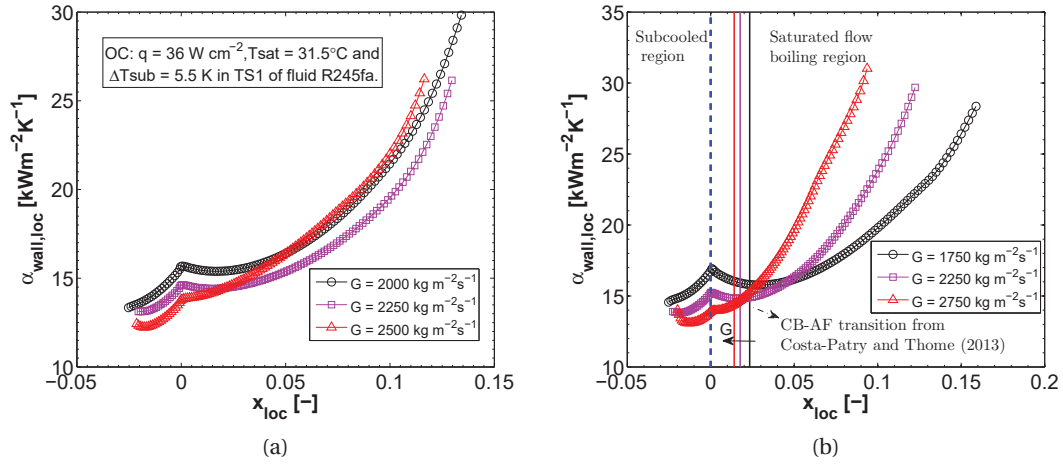


Figure 4.4 – Effect of mass flux on widthwise averaged local heat transfer coefficients for: (a) R1233zd(E) (at $q = 38 \text{ W cm}^{-2}$ and $T_{sat} = 35^\circ\text{C}$ in test section 1) Huang et al. (2016b) and (b) new R245fa (at $q = 36 \text{ W cm}^{-2}$ and $T_{sat} = 31.5^\circ\text{C}$ in test section 1).

must be chosen wisely during design of such cooling systems in order to balance its merit of prohibiting flow boiling instability and its disadvantage of degrading local heat transfer.

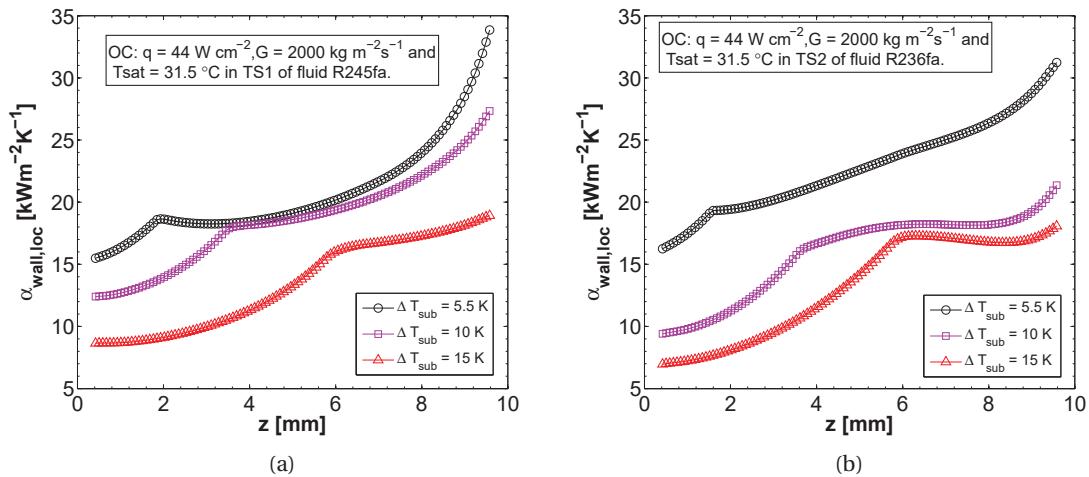


Figure 4.5 – Effect of inlet subcooling on new widthwise averaged local heat transfer coefficients for: (a) R245fa (at $q = 44 \text{ W cm}^{-2}$ and $T_{sat} = 31.5^\circ\text{C}$ in test section 1) and (b) R236fa (at $q = 44 \text{ W cm}^{-2}$ and $T_{sat} = 31.5^\circ\text{C}$ in test section 2).

4.4.4 Effect of saturation temperature

Fig. 4.6 presents new local heat transfer data at three different saturation temperatures. It is shown that the local heat transfer coefficient increased slightly with the saturation temperature. For example, the local heat transfer coefficient at $x = 0.05$ increased by 8.9% when increasing T_{sat} from 31.5 to 40 °C. The heat transfer mechanism governing flow boiling in microchannels has proven to be governed by the thin liquid film evaporation in our previous work Huang et al. (2016b). As a result, one reason for this slight increase is probably related to the thinner liquid film caused by the lower latent heat at the higher saturation temperature (i.e. for same heat flux, more liquid film is evaporated to transfer away the heat).

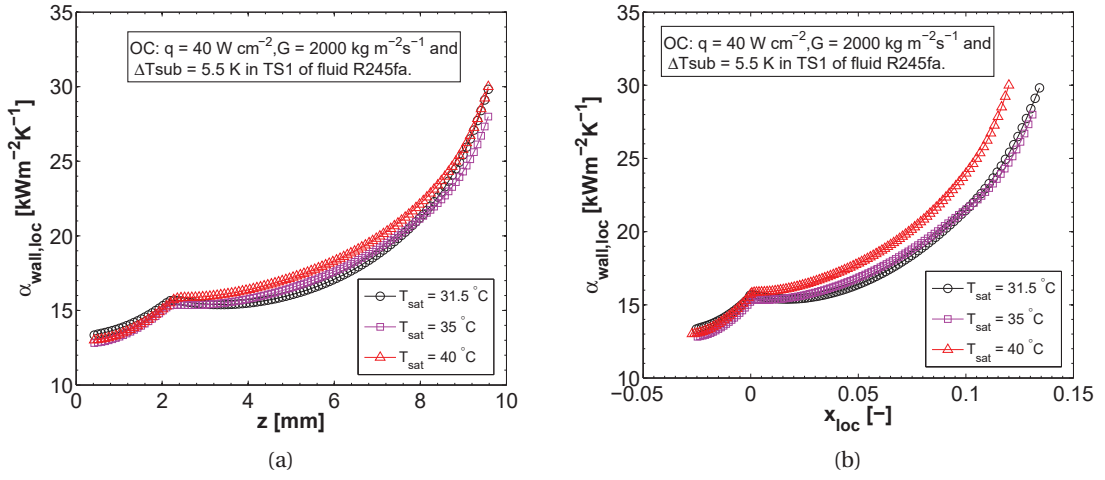


Figure 4.6 – Effect of outlet saturation temperature on new widthwise averaged local heat transfer coefficients for $q = 38 \text{ W cm}^{-2}$ at three different mass fluxes: (a) versus local length and (b) versus local vapor quality.

4.4.5 Effect of fluid

The local heat transfer coefficients of the three fluids in test section 1 are compared in Fig. 4.7. R1233zd(E) from Huang et al. (2016b) exhibited the lowest local heat transfer coefficient followed by a slight increase for R245fa, and R236fa yielded the highest value. For example, the local heat transfer coefficient of R236fa at $x_{loc} = 0.05$ increased by 39.3% over that of R1233zd(E). This increase might be mainly attributed to the lowest surface tension of R236fa among the three fluids tested (as seen in Table 4.1). The surface tension tends to hold the liquid film to the channel wall. Hence, a lower surface tension renders the liquid at the liquid-vapor interface more susceptible to being sheared off by the incoming vapor stream in terms of liquid droplet entrainment. This may have resulted in a thinner liquid film for R236fa compared to

the other two fluids, thus enhancing the local heat transfer.

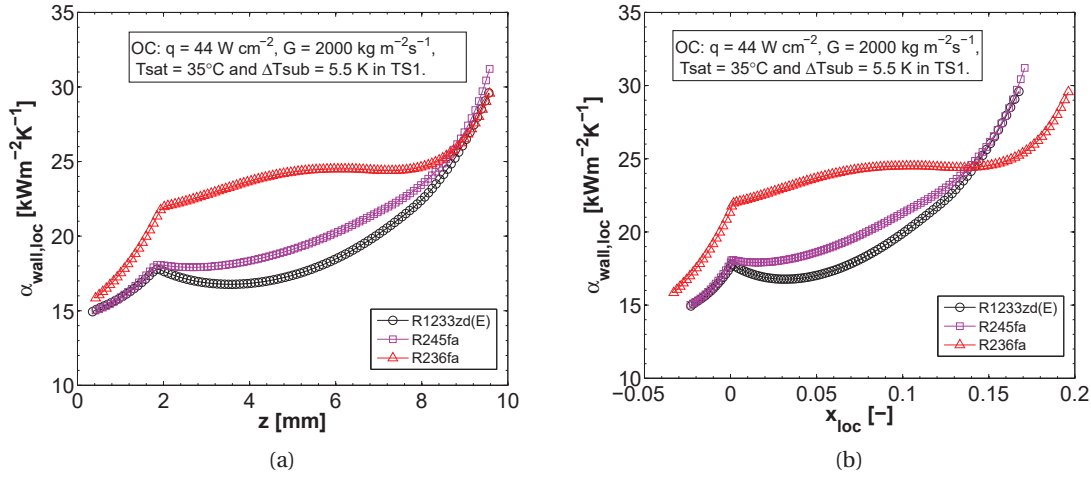


Figure 4.7 – Effect of fluid on widthwise averaged local heat transfer coefficients for $q = 44 \text{ W cm}^{-2}$, $G = 2000 \text{ kg m}^{-2} \text{s}^{-1}$, $T_{sat} = 35^\circ\text{C}$ and $\Delta T_{sub} = 5.5 \text{ K}$ including the new data: (a) versus local length and (b) versus local vapor quality.

4.4.6 Effect of inlet orifice

Fig. 4.8 compares the local heat transfer coefficient of R236fa in two test sections with different inlet orifices. It is found that the local heat transfer coefficient in test section 1 with an inlet orifice width of $50 \mu\text{m}$ was higher than that in test section 2 having the inlet orifice width of $25 \mu\text{m}$. The similar results were also reported in Szczukiewicz et al. (2013). Considering the same averaged mass flux in two test sections with the same channel size and number, the inlet orifice with the smaller width tends to generate a stronger liquid jet at the channel entrance which increases the mid-stream liquid phase velocity. Such a high liquid velocity, as explained in Szczukiewicz et al. (2013), may have created a thicker liquid film, which resulted in a lower heat transfer. Other possible influences may come from the bubble frequencies impacted by the two micro-orifices, which were not able to be discerned from the high speed videos. However, no method, not even the new prediction method to be presented here, is able to explain and predict this effect. At the channel outlet of the two test sections, the local heat transfer coefficients approach each other since they have very similar channel outlet pressure due to the similar outlet restriction pressure drop under the same test conditions.

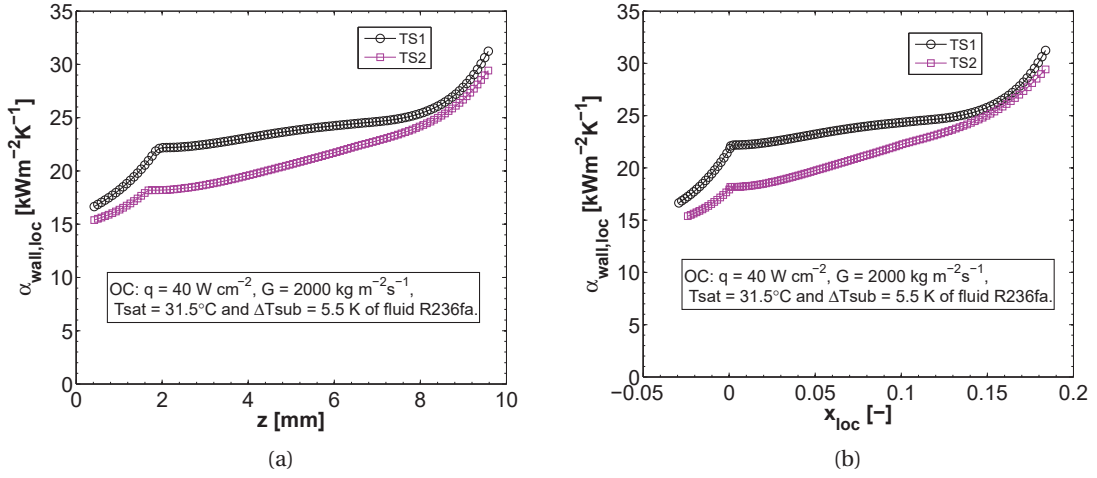


Figure 4.8 – Effect of test section inlet orifice on new R236fa widthwise averaged local heat transfer coefficients for $q = 40 \text{ W cm}^{-2}$, $G = 2000 \text{ kg m}^{-2} \text{ s}^{-1}$, $T_{sat} = 31.5^\circ \text{C}$ and $\Delta T_{sub} = 5.5 \text{ K}$: (a) versus local length and (b) versus local vapor quality.

4.5 Local heat transfer predictions

4.5.1 Comparison with existing models

The mean absolute error (MAE) was used to assess the prediction accuracy from the models, which is defined as:

$$MAE = \frac{1}{M} \sum \frac{|\alpha_{Pred} - \alpha_{Exp}|}{\alpha_{Exp}} \times 100\% \quad (4.19)$$

Saturated flow boiling region

The saturated flow boiling data ($x_{loc} > 0$) were compared with six leading heat transfer models, and the results are shown in Fig. 4.9. It is found that the flow pattern based model Costa-Patry and Thome (2013) provided the best prediction against the local experimental data (1,503,732 data points that refers to all the relevant pixels) with a MAE of 17.2 and 85.5% of the data within $\pm 30\%$, as shown in Fig. 4.9e. Otherwise, all the models except the Cooper pool boiling model Cooper (1984) tend to over-predict the data in the very low vapor quality region.

Subcooled flow boiling region

In the literature, the availability of subcooled flow boiling data, especially local data, are limited due to the difficulty in their measurement. So far, there have been only a few mean empirical

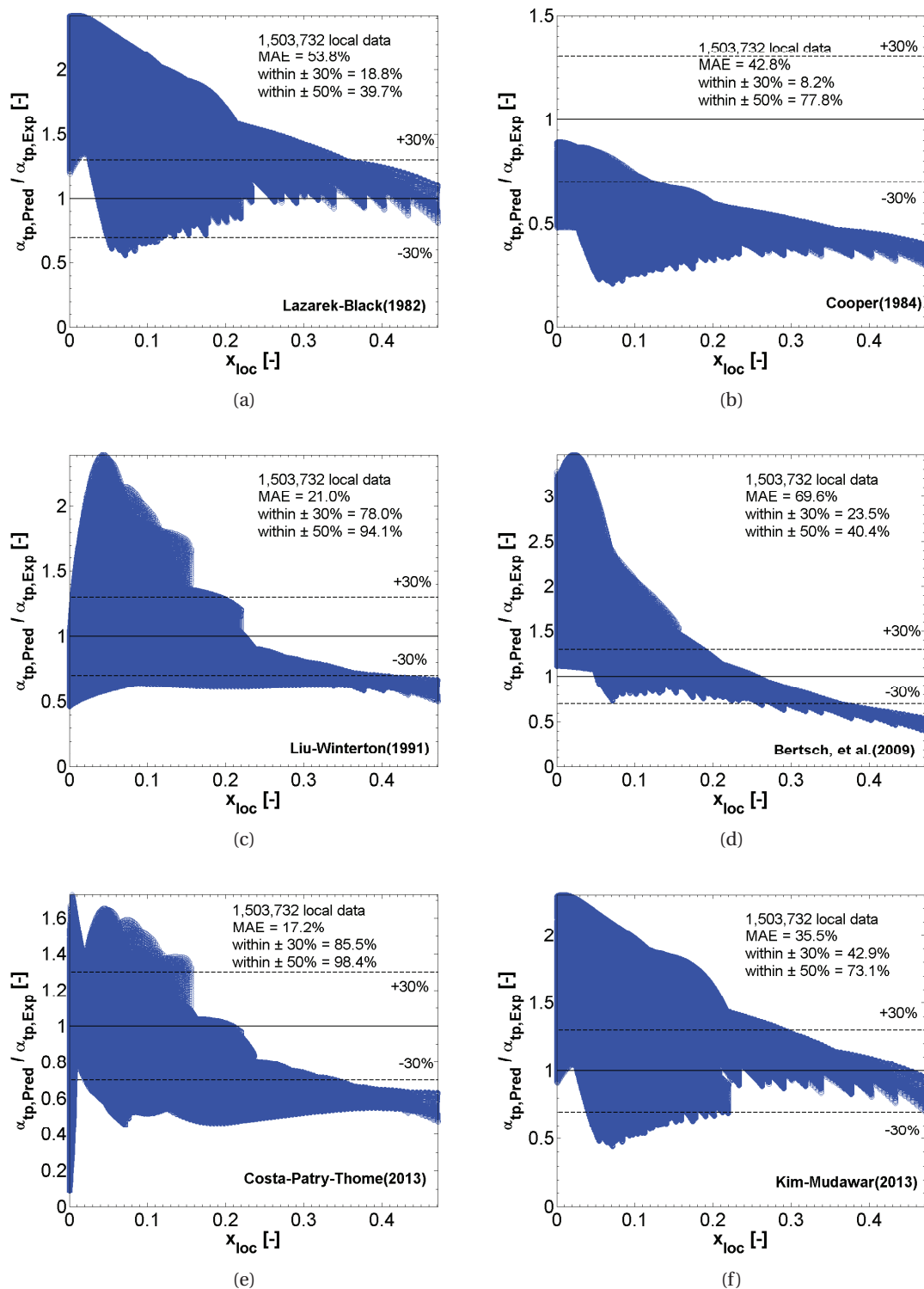


Figure 4.9 – Comparison of experimental saturated flow boiling heat transfer coefficients with two-phase heat transfer models of (a) Lazarek and Black (1982), (b) Cooper (1984), (c) Liu and Winterton (1991), (d) Bertsch et al. (2009), (e) Costa-Patry and Thome (2013) and (f) Kim and Mudawar (2013a).

subcooled flow boiling heat transfer models reported, which are listed in Table 4.2. Their comparison to the present results are presented in Fig. 4.10. It is shown that none of the three existing subcooled flow boiling models were able to predict the local data with a good accuracy. Note, however, that these other methods were based on other test fluids than in the present study.

Table 4.2 – Correlations from subcooled flow boiling heat transfer.

References	Correlations
Papell (1963)	$\frac{Nu_{sub}}{Nu_{spMY}} = 90Bo^{0.7} Ja^{*-0.84} \left(\frac{\rho_v}{\rho_l}\right)^{0.756}$
Moles and Shaw (1972)	$\frac{Nu_{sub}}{Nu_{spMY}} = 78.5Bo^{0.67} Ja^{*-0.50} \left(\frac{\rho_v}{\rho_l}\right)^{-0.03} Pr_l^{0.45}$
Lee and Mudawar (2008)	$\frac{Nu_{sub}}{Nu_{spMY}} = 90Bo^{0.9} Ja^{*-0.98} We^{*0.15} ar^{-0.42},$ $Bo = \frac{q_{wall}}{GH_{lv}}, Ja^* = \frac{c_{p,l}\Delta T_{sub,inlet}}{H_{lv}}, We^* = \frac{G^2 D_h}{(\rho_l - \rho_v)\sigma}$
Present work	$Nu_{sub} = \frac{\alpha_{sub,loc} D_h}{k_l},$ $\alpha_{sub,loc} = \alpha_{sp,loc} \left(\frac{\Delta T_{sub,loc}}{\Delta T_{sub,inlet}}\right) + \alpha_{xlow}^0 \left(1 - \frac{\Delta T_{sub,loc}}{\Delta T_{sub,inlet}}\right),$ $\alpha_{sp,loc}$ and α_{xlow}^0 are given in Table 4.4

Single-phase thermal developing region

Based on the local heat transfer trend in the subcooled region, the database for the single-phase thermal developing region was collected from the previous tests of R1233zd(E) in Huang et al. (2016b) and the present tests of R245fa and R236fa in test section 1 having an inlet orifice width of 50 μm . The reason why no single-phase data were obtained with test section 2 with an inlet orifice width of 25 μm is due to the relatively larger pressure drop in the inlet orifice compared to that of test section 1. The best performing single-phase thermal developing heat transfer model of Muzychka and Yovanovich (2004) (see Table A.1) is compared to the data in Fig. 4.11a which were under-predicted. This is due to the influence from the inlet micro-orifice since no method in literature as mentioned above can handle this geometry.

In summary, the comparison of these results indicate shortcomings in the present heat transfer models: (1) the existing flow pattern based model provided a over-prediction for the saturated very low vapor quality region near x_{local} approaching 0.0; (2) the few existing mean subcooled flow boiling models were not capable of predicting the experimental data.

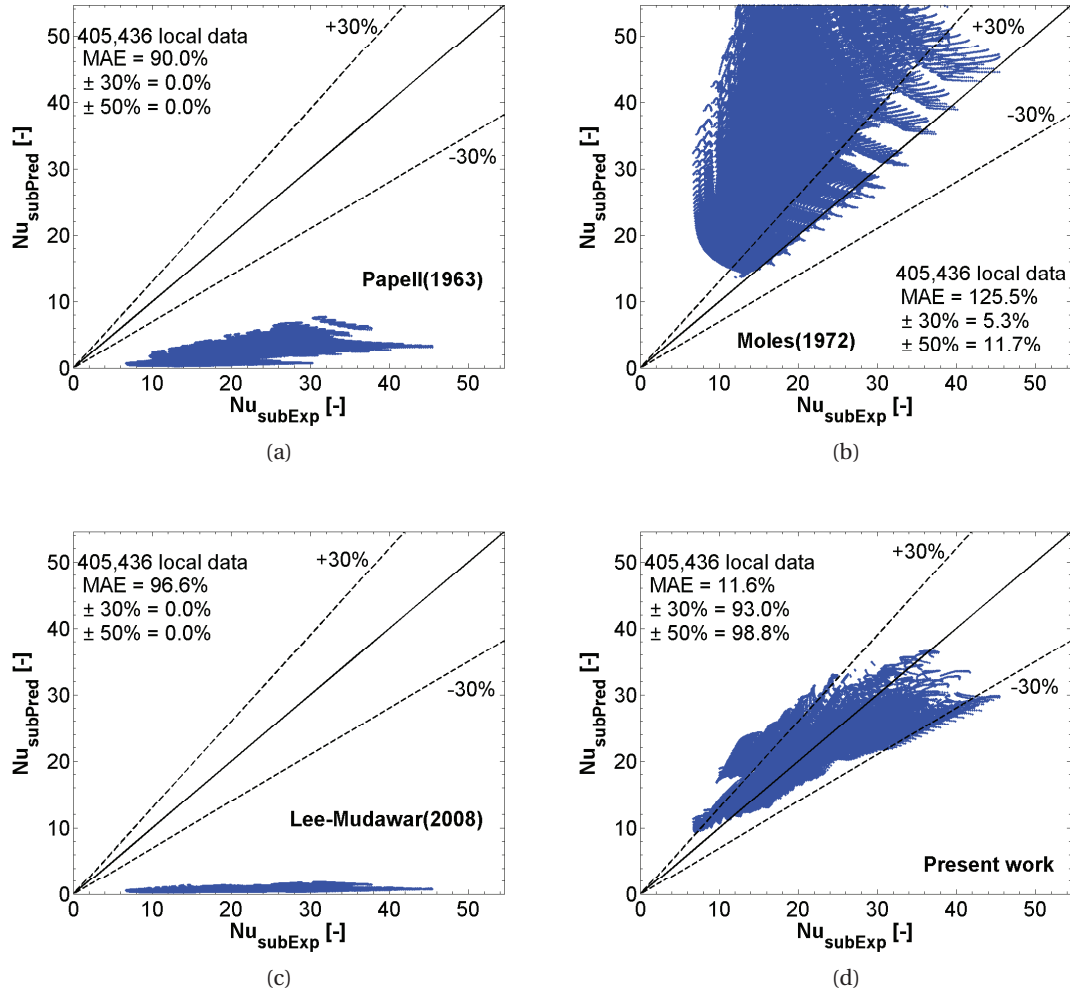


Figure 4.10 – Comparison of experimental subcooled flow boiling heat transfer data with models of (a) Papell (1963), (b) Moles and Shaw (1972), (c) Lee and Mudawar (2008) and (d) present work.

4.5.2 New local heat transfer models development

Based on the above observations, it is necessary to develop a new local heat transfer model, covering subcooled and saturated flow boiling, to better predict the local heat transfer data and ensure that the method gives a transition from one region to another without a non-physical jump in the predicted local heat transfer coefficient.

Table 4.3 – Correlations from literature for single-phase local Nusselt number in channels.

Muzychka and Yovanovich (2004)	
$Nu_{spMY} = \left[\left(\frac{C_4 f(Pr)}{\sqrt{z^*}} \right)^m + \left\{ C_2 C_3 \left(\frac{f Re_{\sqrt{A}}}{z^*} \right)^{1/3} \right\}^5 + \left\{ C_1 \left(\frac{f Re_{\sqrt{A}}}{8\sqrt{\pi} ar^\gamma} \right) \right\}^5 \right]^{1/m}$	
$f Re_{\sqrt{A}} = \frac{12}{\sqrt{ar}(1+ar) \left[1 - \frac{192ar}{\pi^5} \tanh\left(\frac{\pi}{2ar}\right) \right]}$	
$\left\{ \begin{array}{ll} m = 2.27 + 1.65 Pr^{1/3}, & Pr = \frac{c_p \mu}{k} \\ z^* = \frac{z}{\sqrt{A} Re_{\sqrt{A}} Pr}, & Re_{\sqrt{A}} = \frac{G \sqrt{A}}{\mu}, A = W_{ch} H_{ch} \\ C_3 = 0.409, C_1 = 3.24, & f(Pr) = \frac{0.564}{[1 + (1.664 Pr^{1/6})^{9/2}]^{2/9}}, \text{ UWF} \\ C_3 = 0.501, C_1 = 3.86, & f(Pr) = \frac{0.886}{[1 + (1.909 Pr^{1/6})^{9/2}]^{2/9}}, \text{ UWT} \\ C_2 = 1, C_4 = 1, & \text{Local} \\ C_2 = 3/2, C_4 = 2, & \text{Average, } Nu = \frac{1}{z} \int_0^z Nu(z^*) dz \\ \gamma = 1/10, \text{Upper bound, } & \gamma = -3/10, \text{Lower bound} \\ ar \approx \frac{\ell_{short}}{\ell_{long}} \end{array} \right.$	
Present work	
$Nu_{sp} = \left(\frac{41.9}{Re^{0.17} Pr^{1.43}} \right) Nu_{spMY}; 438 \leq Re \leq 980, 4.5 \leq Pr \leq 6.2$	

Single-phase thermal developing flow

Since the correlation of Muzychka and Yovanovich (2004) tends to under-predict the local data of the three fluids (R1233zd(E), R245fa and R236fa) in test section 1 (see Fig. 4.11a), a modified heat transfer model for single-phase thermal developing flow was proposed below by adding a correction factor as follows:

$$Nu_{sp} = \left(\frac{41.9}{Re^{0.17} Pr^{1.43}} \right) Nu_{spMY} \quad (4.20)$$

where Nu_{spMY} refers to the prediction from Muzychka and Yovanovich (2004) for the uniform wall heat flux boundary condition. The leading coefficient and the exponents were determined based on a least square curve fitting with the local experimental data.

Fig. 4.11b presents the comparison between the prediction of Eq. 4.20 and the experimental heat transfer data of the three fluids. A good prediction accuracy can be found with a MAE of

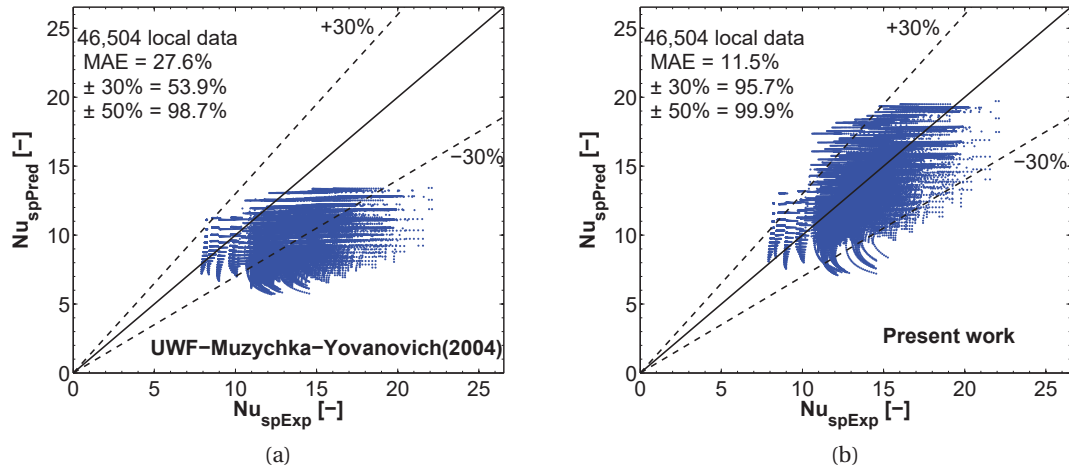


Figure 4.11 – Validation of single-phase thermal developing heat transfer models: (a) Muzychka and Yovanovich (2004) for UWF and (b) present work.

10.8%. Physically speaking, one can interpret this correction to empirically account for the influence of the inlet micro-orifices. Data for only one size of orifice was obtained experimentally, and hence there is no size effect in this method, so this is an issue requiring more future study.

Saturated flow boiling

As mentioned before, the flow pattern based model Costa-Patry and Thome (2013) was shown to over-predict the local heat transfer coefficients in the very low vapor quality region, essentially the short bubbly flow region before slug flow. To improve this prediction, an empirical correlation is proposed that adds a correction to the three-zone model of Thome et al. (2004) using the local Boiling number:

$$\alpha_{xlow} = 10^5 \alpha_{3Z}^{0.12} Bo^{0.39} \quad (4.21)$$

This model was built empirically according to the least square curve fitting of the experimental data. The experimental heat transfer data at the very low vapor quality region were selected according to the transition criterion (from slug flow to annular flow regime) adopted in the flow pattern based model of Costa-Patry and Thome (2013), which is given as follows

$$x_{CB-AF} = 425 \left(\frac{\rho_v}{\rho_l} \right)^{0.1} \frac{Bo^{1.1}}{Co^{0.5}} \quad (4.22)$$

The original coefficients in Eq. 4.22 were modified according to the present data set, thus the new transition criterion became

$$x'_{CB-AF} = 89.5 \left(\frac{\rho_v}{\rho_l} \right)^{0.06} Bo^{2.03} Co^{3.36} \quad (4.23)$$

The results are shown in Fig. 4.12 for this region. A good prediction with a MAE of 10.9% can be found.

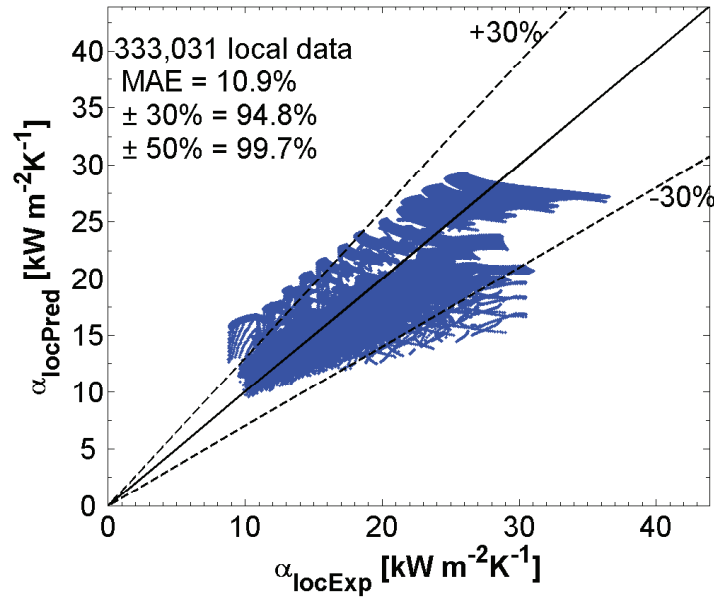


Figure 4.12 – Validation of saturated flow boiling heat transfer model at very low vapor quality.

Subcooled flow boiling

The transition from the single-phase flow to subcooled flow boiling, i.e. the onset of the subcooled flow boiling, is very complex to model. To avoid such difficulty, a new local heat transfer correlation was developed for the subcooled flow region, involving the single-phase thermal developing flow model and the saturated flow boiling model at very low vapor quality. Applying the “proration” approach, the local subcooled flow boiling region heat transfer coefficient can be predicted as:

$$\alpha_{sub,loc} = \alpha_{sp,loc} \left(\frac{\Delta T_{sub,loc}}{\Delta T_{sub,inlet}} \right) + \alpha_{xlow}^0 \left(1 - \frac{\Delta T_{sub,loc}}{\Delta T_{sub,inlet}} \right) \quad (4.24)$$

$$\alpha_{sp,loc} = Nu_{sp} \frac{k_l}{D_h}, \quad \alpha_{xlow}^0 = \alpha_{xlow}(x = 0.005) \quad (4.25)$$

where α_{xlow} is calculated at $x = 0.005$ as the method in Eq. (4.21) does not work at $x = 0.0$. This new model was validated against the present local subcooled flow boiling data in Fig. 4.10d. It predicted 93.0% of the local data (405,436 points) to be within $\pm 30\%$ and showed a good prediction accuracy with a MAE of 11.6%. Furthermore, this new model is able to ensure a continuous transition from the single-phase flow (if encountered) to subcooled boiling and from subcooled boiling to saturated flow boiling, as witnessed in Fig. 4.13 (to be discussed in the next section).

Table 4.4 – A new flow pattern based model including subcooled flow.

For saturated flow boiling, $x \geq 0.005$:

$$\alpha_{sat,loc} = \begin{cases} \alpha_{xlow}, & x \leq x'_{CB-AF}; \\ \alpha_{CB-AF}, & x'_{CB-AF} < x \leq x'_{CB-AF} + 0.02; \\ \alpha_{AF}, & x > x'_{CB-AF} + 0.02; \end{cases}$$

$$\alpha_{xlow} = 10^5 \alpha_{3Z}^{0.12} Bo^{0.39}, x'_{CB-AF} = 89.5 \left(\frac{\rho_v}{\rho_l} \right)^{0.06} Bo^{2.03} Co^{3.36}$$

$$r = \frac{x - x'_{CB-AF}}{0.02}, \alpha_{CB-AF} = (1 - r)\alpha_{xlow} + r\alpha_{AF}, Co = \sqrt{\frac{\sigma}{g(\rho_l - \rho_v)D_h^2}}$$

α_{3Z} based on the three-zone model of Thome et al. (2004)

α_{AF} from the annular flow model of Cioncolini and Thome (2011).

For subcooled flow, $x < 0.005$:

$$\alpha_{sub,loc} = \alpha_{sp,loc} \left(\frac{\Delta T_{sub,loc}}{\Delta T_{sub,inlet}} \right) + \alpha_{xlow}^0 \left(1 - \frac{\Delta T_{sub,loc}}{\Delta T_{sub,inlet}} \right)$$

$$Nu_{sp,loc} = \left(\frac{41.9}{Re^{0.17} Pr^{1.43}} \right) Nu_{spMY}, \alpha_{sp,loc} = Nu_{sp,loc} \frac{k_l}{D_h}$$

$$\alpha_{xlow}^0 = \alpha_{xlow}(x = 0.005)$$

4.5.3 Global prediction from the new flow pattern based model

A new flow pattern based model including the subcooled flow region has been formulated after combining all the above-proposed methods for each local flow regime. The new model is summarized in Table 4.4. This new flow pattern based model was compared with all the local heat transfer data, including the single-phase thermal developing, subcooled and saturated flow boiling regions. Fig. 4.13 shows two examples for the comparison of the local wall heat transfer coefficient versus the local vapor quality. Local heat transfer predictions from the three-zone model Thome et al. (2004), annular flow model Cioncolini and Thome (2011) and flow pattern based model Costa-Patry and Thome (2013) are also depicted. Compared

with the existing models, the new flow pattern based model exhibited the best prediction for subcooled flow (SPL and SCFB) and saturated very low quality (SVLQ) regions. It is worthwhile to highlight that the present subcooled flow boiling model (Eqs. (4.24) to (4.25)) fills in the void of the prediction of the local subcooled heat transfer data, which was missing in the micro-scale heat transfer literature.

In Fig. 4.13a, for R1233zd(e) in TS1 four flow regimes (subcooled flow boiling, saturated very low quality, transition to annular flow and annular flow) without the single-phase liquid (thermal developing) flow were found. After increasing the mass flux to $2500 \text{ kg m}^{-2}\text{s}^{-1}$, as shown in Fig. 4.13b, a very small portion of the single-phase liquid flow regime appeared, which was predicted by Eqs. (4.24) to (4.25). As stated previously, no non-physical jump in the local heat transfer coefficient was found at the transition from the single-phase liquid flow (SPL) to the subcooled flow boiling (SCFB) region, nor to the saturated very low quality (SVLQ) region.

The global detailed comparison is presented in Fig. 4.14. It can be seen that the new flow pattern based model predicted the local data very well with a MAE of 14.2% and it captured 90.1% of the data to within $\pm 30\%$. The under prediction at the high vapor quality region close to the channel end was probably due to the extrapolation of the annular flow model Cioncolini and Thome (2011) from the original macro- and mini-scale circular channel geometry to the micro-scale rectangular channel shape, since the assumption of uniform circumferential liquid film thickness in circular channels does not suit the case of rectangular microchannels in which more liquid tends to be trapped in the rectangular corners.

In Table 4.5, the local heat transfer data are sorted into four categories with respect to the local flow patterns, fluids, outlet saturation temperatures and inlet subcoolings. Fig. 4.15 describes the ratio of predicted to experimental data versus local vapor quality for the four categories, where the prediction accuracy for each condition in each category can be evaluated locally. For example, in the category of the flow patterns, the prediction performance (MAE) of the new flow pattern based model was assessed individually according to each local flow regime. The statistical results are listed in Table 4.5. Nearly a quarter of the local data (23.2%) fell in the subcooled flow region and almost half (46.7%) in the annular flow regime. The relatively high MAE (17.0%) for annular flow was because of the under-prediction from the annular flow model Cioncolini and Thome (2011) at higher vapor qualities, as discussed above.

4.6 Conclusions

Local heat transfer coefficients during flow boiling of two refrigerants (R245fa and R236fa) in two multi-microchannel evaporators have been measured under a wide range of operating conditions. A three-dimensional inverse heat conduction problem was solved to obtain the local heat transfer coefficients on a pixel-by-pixel basis. The experimental results revealed that

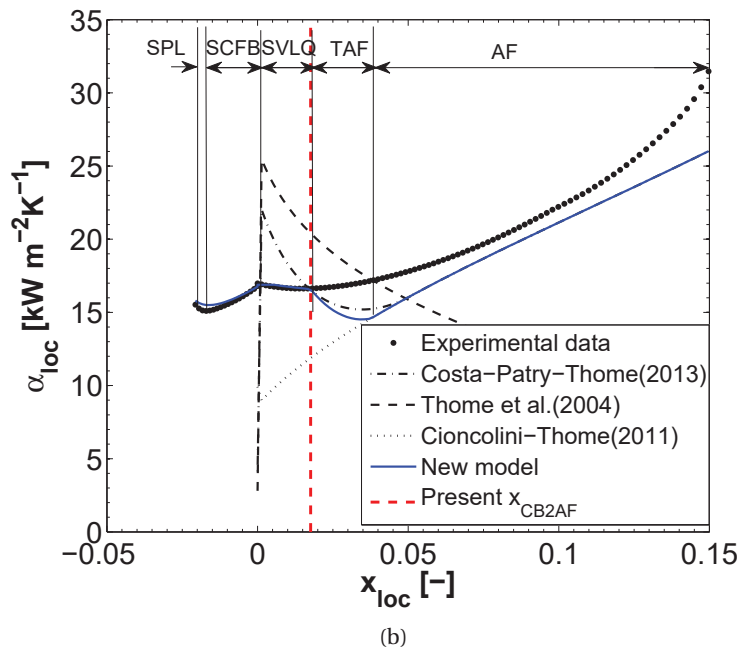
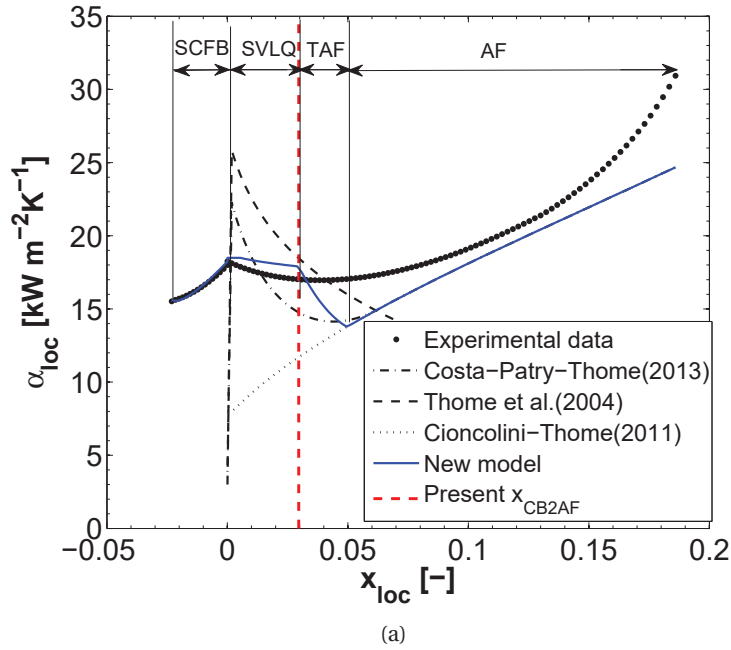


Figure 4.13 – Comparison of the local heat transfer coefficient versus local vapor quality between the prediction from the new flow pattern based model and the experimental data: (a) for fluid R1233zd(E) Huang et al. (2016b) in TS1 at $y = 7.5$ mm under $G = 2000$ kg m⁻²s⁻¹, $q = 48$ W cm⁻², $T_{sat} = 35$ °C and $\Delta T_{sub} = 5.5$ K; (b) for fluid R1233zd(E) Huang et al. (2016b) in TS1 at $y = 7.5$ mm under $G = 2500$ kg m⁻²s⁻¹, $q = 48$ W cm⁻², $T_{sat} = 35$ °C and $\Delta T_{sub} = 5.5$ K (SPL: single-phase liquid, SCFB: subcooled flow boiling, SVLQ: saturated very low quality, TAF: transition to annular flow and AF: annular flow).

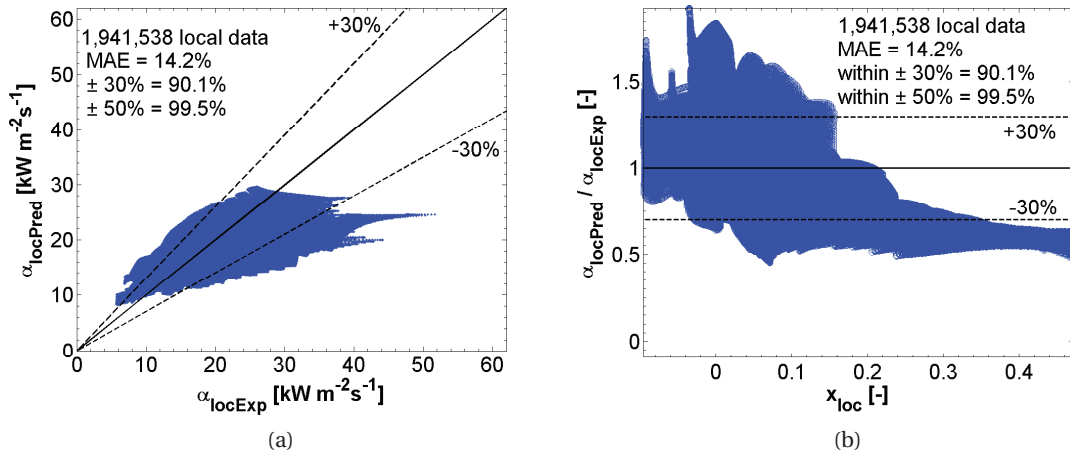


Figure 4.14 – The new flow pattern based model validation against the total experimental data bank: (a) absolute value, (b) ratio of prediction to measured data versus local vapor quality.

the local heat transfer coefficient decreased with the inlet subcooling, increased with the saturation temperature and with the size of the inlet orifice width. Furthermore, R1233zd(E) tested in Huang et al. (2016b) exhibited the lowest heat transfer coefficient while R236fa showed the highest value.

For saturated flow boiling, it was concluded that the flow pattern based model Costa-Patry and Thome (2013) provided the best agreement with a MAE of 17.2%. The original flow pattern based model Costa-Patry and Thome (2013) was modified here to improve its prediction accuracy at the very low vapor quality region.

The single-phase thermal developing heat transfer data of R1233zd(E) from Huang et al. (2016b), R245fa and R236fa in test section 1 were selected based on their local trend. In order to better predict the local data, the heat transfer model of Muzychka and Yovanovich (2004) for single-phase thermal developing flow with uniform wall flux (UWF) was modified to consider the impact from the inlet micro-orifice.

The new single-phase heat transfer method (Eq. (4.20)) and the new one for the saturated very low quality region (Eq. (4.21)) were prorated together to form a new local heat transfer model for subcooled flow boiling. This new subcooled local heat transfer model provided the best agreement against the local subcooled boiling data (405,436 points) with a MAE of 11.6% compared to the other mean empirical correlations.

Combining the models described above, a new flow pattern based model starting from subcooled liquid flow all the way through to annular flow was proposed in this paper. It presented a good prediction for the local heat transfer data (1,941,538 points) with a MAE of 14.2% and 90.1% of the data were predicted to be within $\pm 30\%$.

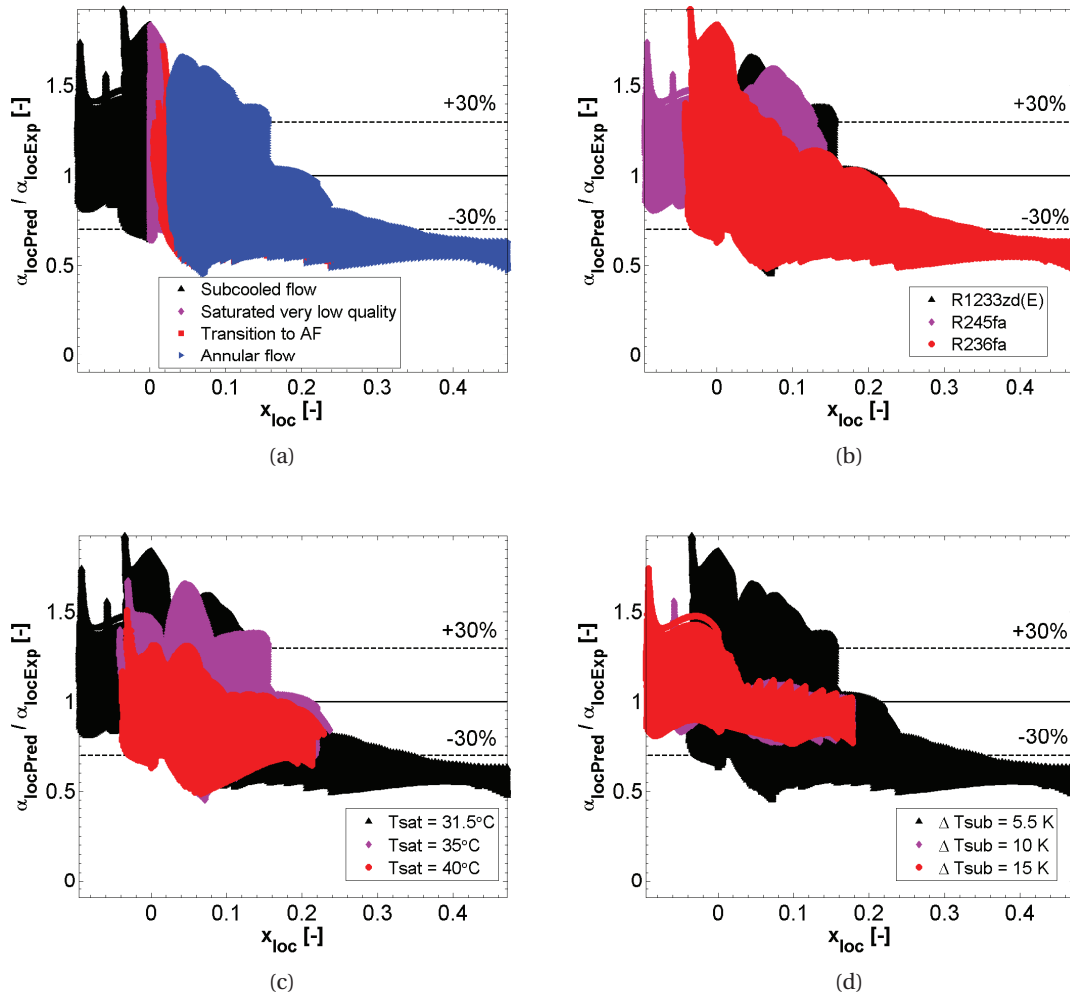


Figure 4.15 – The new model comparison with experimental data sorted into four categories: (a) flow regime, (b) fluid, (c) outlet saturation temperature and (d) inlet subcooling.

Table 4.5 – Statistical comparison between new model prediction and experimental data sorted into different categories.

Category	Ratio in total (%)	MAE (%)	$\pm 30\%$	$\pm 50\%$
Flow patterns				
Subcooled flow ^a	23.2	11.6	93.2	98.9
Saturated very low quality	17.0	11.4	94.2	99.3
Transition to AF	13.1	12.3	93.6	100
Annular flow	46.7	17.0	86.0	99.8
Fluids				
R1233zd(E)	31.2	11.6	96.0	99.8
R245fa	25.8	10.4	97.5	99.9
R236fa	43.0	18.5	81.3	99.2
T_{sat} (°C)	$(T_{sub} = 5.5 \text{ K})$			
31.5	46.3	15.9	85.9	99.2
35	43.1	11.9	95.3	99.8
40	10.6	16.2	87.4	100
ΔT_{sub} (K)	$(T_{sat} = 31.5 \text{ °C})$			
5.5	90.4	14.4	89.4	99.5
10	4.4	10.4	99.3	100
15	5.2	12.8	94.1	99.8

a: Subcooled flow includes the single-phase flow taking a share of only 2% of the total data and the subcooled flow boiling region.

5 Transient base temperature response

This chapter is from the paper below by Huang et al. (2016c):

H. Huang, N. Borhani, J.R. Thome, Thermal Response of Multi-microchannel Evaporators During Flow Boiling of Refrigerants under Transient Heat Loads with Flow Visualization, *Journal of Electronics Packaging* 138 (2016) 031004.

Abstract

Multi-microchannel evaporators with flow boiling, used for cooling high heat flux devices, usually experience transient heat loads in practical applications. These transient processes may cause failure of devices due to a thermal excursion or poor local cooling or dryout. However, experimental studies on such transient thermal behavior of multi-microchannel evaporators during flow boiling are few. Thus, an extensive experimental study was conducted to investigate the base temperature response of multi-microchannel evaporators under transient heat loads, including cold startups and periodic step variations in heat flux using two different test sections and two coolants (R236fa and R245fa) for a wide variety of flow conditions. The effects on the base temperature behavior of the test section, heat flux magnitude, mass flux, inlet subcooling, outlet saturation temperature and fluid were investigated. The transient base temperature response, monitored by an IR camera, was recorded simultaneously with the flow regime acquired by a high-speed video camera. For cold startups, it was found that reducing the inlet orifice width, heat flux magnitude, inlet subcooling and outlet saturation temperature but, increasing the mass flux decreased the maximum base temperature. Meanwhile, the time required to initiate boiling increased with the inlet orifice width, mass flux, inlet subcooling and outlet saturation temperature but, decreased with the heat flux magnitude. For periodic variations in heat flux, the resulting base temperature was found to oscillate and then damp out along the flow direction. Furthermore, the effects of mass flux and heat flux pulsation

period were insignificant.

5.1 Introduction

Flow boiling in multi-microchannel evaporators has proved to be a promising means of addressing the increasing demands for heat dissipation in high heat flux electronic devices, such as high performance CPUs, IGBTs of power electronics and the new 12.5 Giga-pixel high energy physics particle detector for ALICE at CERN Thome (2004); Thome et al. (2004); Thome (2006); Wang et al. (2008); Marzoa et al. (2013). As a result of this, a considerable number of studies have been conducted to investigate the hydraulic and thermal performance of microchannel evaporators with different fluids under steady operating conditions of heat flux and mass flux Qu and Mudawar (2003a); Agostini et al. (2008); Costa-Patry (2011); Szczukiewicz et al. (2013); Kim and Mudawar (2014); Huang et al. (2016b). For example, recently in Huang et al. (2016b) the steady state flow boiling pressure drop and heat transfer of a new fluid R1233zd(E) have been investigated experimentally by reducing the local IR camera data through solving a 3D inverse heat conduction problem Huang et al. (2016a).

Steady state flow boiling is an ideal solution for the operation of micro-evaporators. However, in practical applications, the heat dissipation through micro-evaporators changes with time due to the variation in cooling tasks demanded by electronic devices. One typical example occurs on the cold startup of electronic devices, during which the heat generation changes suddenly from zero to the first load level. This requires micro-evaporators to respond to the sudden heat load rapidly while maintaining a relatively low base temperature to protect the devices from being burned out, i.e. avoid a too severe temperature overshoot.

Currently, only a few recent experimental studies are available in the literature to investigate the thermal response of a single microchannel evaporator Chen and Cheng (2009); Chen et al. (2010); Basu et al. (2015a,b) and a micro-pin evaporator David et al. (2014) during flow boiling under transient heat loads. Their transient processes were initiated by a step change or pulse change in heat flux. For a step change, the heat flux is changed from one value to another and maintained at the later level. A pulse change implies alternating the heat flux from one value to another.

For a single microchannel, a series of rectangular heat flux pulses were applied in Chen and Cheng (2009); Chen et al. (2010) to study the transient wall temperature recorded by RTDs with the resulting flow regime evolutions acquired by a high-speed CCD in a single microchannel. The effects of mass flux and heat flux magnitude on the transient flow boiling process were thus obtained and also analyzed. Furthermore, four flow regimes including single-phase, nucleate boiling, film boiling and dry out were identified.

The temperature response of a micro-gap etched on a silicon wafer under a step change and a rectangular pulse change in heat flux was studied experimentally in Basu et al. (2015a,b).

Fluid property, mass flux, heat flux magnitude in a step change, and heat flux pulse width in a pulse change were their control variables. The wall superheat, time required to trigger boiling, and bubble dynamics were the objective parameters. The transient wall temperature was measured by a RTD, which also functioned as a micro-heater. Two main flow regimes of vigorous boiling and discrete bubble flow, depending on the operating conditions, were identified through a high-speed video camera.

Compared to single microchannel evaporators, from the perspective of practical applications in the electronics industry, multi-microchannel evaporators are needed to cool electronic devices due to their larger heat transfer surface areas. However, experimental studies on the thermal response of multi-microchannel evaporators during flow boiling under transient heat loads are few in the literature. So far, there has been only one experimental study on this aspect reported by Costa-Patry (2011), where a copper multi-microchannel evaporator was tested. This test section had a size of $17.8 \times 13.2 \text{ mm}^2$, a channel height of $1560 \text{ }\mu\text{m}$, a channel width of $163 \text{ }\mu\text{m}$, a fin thickness of $178 \text{ }\mu\text{m}$ and a channel number of 52. The test section base temperature responses, recorded by a 7×5 array of RTDs, during the heat flux disturbance and cold start-ups were analyzed. It was found that the temperature changed nearly instantaneously towards the change in heat flux and the temperature overshoot during a cold start-up was only about $2 \text{ }^\circ\text{C}$ when increasing the heat flux to 58.2 W cm^{-2} at a mass flux of $462 \text{ kg m}^{-2}\text{s}^{-1}$. However, the testing conditions in this study were very limited. For example, for cold start-ups only two heat fluxes at one mass flux under one saturation temperature were tested.

In fact, the temperature response to transient heat loads evolves very fast in both spatial and temporal domain, thus indicating that the main challenge faced by such studies is to accurately measure the spatio-temporal base temperature variation. Therefore, the traditional techniques of using RTDs Costa-Patry (2011); Chen and Cheng (2009); Chen et al. (2010); Basu et al. (2015a,b); Bigham and Moghaddam (2015) or thermistors Rao et al. (2014) are not sufficient in this regard. Infrared thermography using cameras, having high spatial resolution, low response times and non-intrusive detectors, can meet this requirement to accurately capture the transient temperature response in the spatiotemporal domains. This approach has already been widely used in experimental studies of flow boiling in multi-microchannel evaporators Hetsroni et al. (2002); Xu et al. (2005); Ribatski et al. (2007); Szczukiewicz et al. (2013); Huang et al. (2016a,b).

In the present study, the base temperature response of multi-microchannel evaporators during flow boiling of refrigerants under various transient heat loads were investigated. Two types of transient heat loads are tested here. The first is named as the cold startup by imposing a step change in heat flux from zero. The second is defined as the periodic variation in heat flux, which means varying the heat flux between two fixed values during flow boiling.

For cold startups, the effects on the micro-evaporator's base temperature response in terms of the operating conditions, such as the micro-evaporator inlet orifice width, heat flux magni-

tude, mass flux, inlet subcooling, outlet saturation temperature and fluid were systematically investigated. The maximum base temperature and time required to trigger boiling after imposing a sudden heat load were objective parameters of interest. For periodic variations in heat flux, the effects of heat flux pulse period, distance downstream of micro-evaporator, and mass flux on the base temperature response were studied. During the transient process, the base temperature variation recorded by a fine-resolution IR camera were correlated with the corresponding flow regime acquired by a high-speed video camera.

5.2 Experimental Setup

5.2.1 Facility and test section

The facility used for transient flow boiling tests of refrigerants in multi-microchannel evaporators is shown in Fig. 5.1. The fluid circulation in the system was driven by an oil-free gear pump. The mass flow rate was measured with a Coriolis mass flowmeter. As described in our previous steady-state work Huang et al. (2016b), the test section (see Fig. 5.2) was made of silicon with a finned area of $10 \times 10 \text{ mm}^2$ on the base plate. It had 67 channels with a height of $100 \text{ }\mu\text{m}$, a width of $100 \text{ }\mu\text{m}$, and a fin thickness between channels of $50 \text{ }\mu\text{m}$. A micro-orifice was fabricated into the entrance of each channel to obtain good flow distribution and to stabilize the flow by inhibiting flow reversal. Two types of inlet orifices with different widths were fabricated. As listed in Table 5.1, test section 1 (TS1) had a width of $50 \text{ }\mu\text{m}$ and test section 2 (TS2) had a width of $25 \text{ }\mu\text{m}$. The silicon micro-evaporator base was bonded to a transparent pyrex top plate for making flow visualizations. Two micro-heaters sputtered on the bottom of the test section were connected to a DC power supply (Sorensen DLM32–95E) to provide the required transient heat loads.

The fluid temperature and pressure were measured individually by the K-type thermocouples and pressure transducers placed at the inlet and outlet manifolds, as shown in Fig. 5.1. The base temperature, referring to the temperature on the test section's backside (covered by a piece of thin high-emissivity matt tape Xu et al. (2005); Szczukiewicz et al. (2013)), was monitored and recorded by an IR camera (FLIR ThermaCAM SC3000) with a spatial resolution of 120×120 pixels in an area of $10 \times 10 \text{ mm}^2$. The response time of this IR camera is 1.1 ms , which is more than adequate for the present transient temperature measurement. The flow visualization were realized by a high speed camera (Photron Fastcam-Ultima APX) coupled with a microscope (Nikon 800). The fluid temperature and pressure signals were acquired by a NI-DAQ instrument. A LabView program was employed to control the facility and acquire the data by synchronizing the high-speed video camera and IR camera.

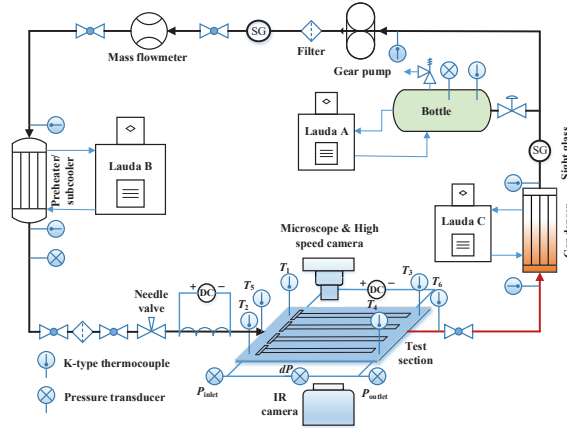
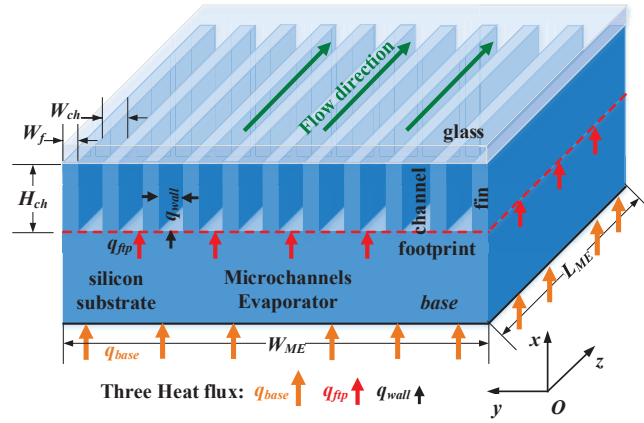
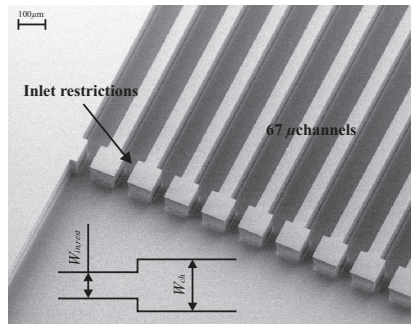


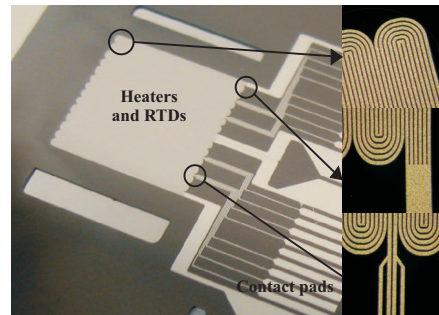
Figure 5.1 – Schematic diagram of the facility.



(a)



(b)



(c)

Figure 5.2 – Test section: (a) schematic of the microchannel evaporator, (b) photo of the microchannels with inlet orifices Szczukiewicz et al. (2013) and (c) photo of the micro-heaters Szczukiewicz et al. (2013).

5.2.2 Operating conditions and measurement uncertainties

The transient flow boiling tests were conducted for the two test sections using two refrigerants (R236fa and R245fa) under three mass fluxes ($G = 1000, 1500$ and $2000 \text{ kg m}^{-2}\text{s}^{-1}$), three inlet subcoolings ($\Delta T_{sub} = 2, 5$ and 10 K) and three outlet saturation temperatures ($T_{sat} = 31.5, 35$ and $40 \text{ }^\circ\text{C}$). Two types of transient heat loads were applied: cold startups (from 0 to q_{max}) and heat flux periodic variations (from q_{min} to q_{max} with different pulse periods). The test matrix was listed in Table 5.1. Here, q_{max} of 30 W cm^{-2} was kept comfortably below the highest value previously tested in steady-state tests (50 W cm^{-2}) to avoid surpassing critical conditions that would damage the test section.

The response of the maximum base temperature and the time required to trigger boiling due to a sudden heat load under various operating conditions were the main parameters of interest. Before applying the sudden heat load, the facility was operating at a steady state to allow some steady state data to be recorded as a reference for the transient results. The fluid temperature, pressure and mass flow rate were saved at a frequency of 1 kHz and, the test sections base temperature was recorded by an IR camera at a frequency of 60 Hz. The overall recording time for pressure and thermal information by the NI (National Instrument) and IR camera was 60 seconds. The transient flow regime was recored by a high speed camera at a frequency of 500 Hz, and the recording time was approximately 12.28 seconds limited by the memory capacity of the camera. Therefore, the temporal resolution of the transient tests was determined by the IR camera's frequency which was 60 Hz. The IR camera was self-calibrated in-situ on a pixel by pixel basis Szczukiewicz et al. (2013); Huang et al. (2016b). After calibration, the error of the IR camera was reduced to $\pm 0.2 \text{ }^\circ\text{C}$ from the standard value by $\pm 2 \text{ }^\circ\text{C}$ of the manufacturer.

5.3 Results for cold startups

In this section, the base temperature response due to cold startups under various operating conditions will be presented in the sections below.

5.3.1 Thermal and flow visualization during a cold startup

Prior to the discussion on the effects of the various imposed operating conditions on the thermal response of the micro-evaporators during cold startups, a simultaneous thermal and flow visualization of the TS1 microchannel evaporator under a typical operating condition is presented and discussed here to reveal the transient flow dynamics.

Fig. 5.3 describes the TS1's backside temperature variation versus time at the location $y = 5.0, z = 7.5 \text{ mm}$ (as marked in Fig. 5.5a with a black cross) during the sudden increase of the heat flux from 0 to 30 W cm^{-2} . The mass flux before the sudden heat load was set to $1500 \text{ kg m}^{-2}\text{s}^{-1}$, and the inlet subcooling and outlet saturation temperature were 5.5 K and $31.5 \text{ }^\circ\text{C}$,

Table 5.1 – Transient tests matrix.

	Test section 1 (TS1)	Test section 2 (TS2)
Inlet orifice width (μm)	50	25
Cold startup		
q_{max} (W cm^{-2})	14, 20 and 30	14, 20 and 30
G ($\text{kg m}^{-2}\text{s}^{-1}$)	–	1000, 1500 and 2000
ΔT_{sub} (K)	–	2, 5.5 and 10
T_{sat} ($^{\circ}\text{C}$)	–	31.5, 35 and 40
Fluid	R236fa	R236fa and R245fa
Heat flux		
periodic variation		
τ (s)	–	2, 4 and 8
G ($\text{kg m}^{-2}\text{s}^{-1}$)	–	1500 and 2000

respectively.

Eight typical moments according to the base temperature response are selected and marked

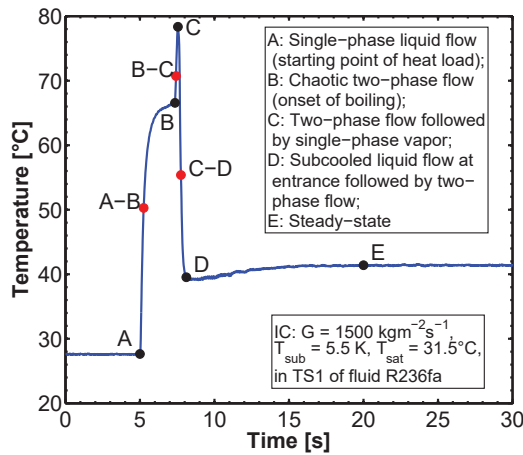


Figure 5.3 – Wall temperature variation versus time at $y = 5.0$ and $z = 7.5$ mm of test section 1 with heat load from 0 to 30 W cm^{-2} at an initial mass flux of $1500 \text{ kg m}^{-2}\text{s}^{-1}$.

in Fig. 5.3 from points A to E. The instantaneous flow regime and thermal map were recorded by the high-speed video camera and IR camera individually. By combining the thermal and flow visualization, six flow scenarios at the six typical moments (from A-B to D) were identified, as demonstrated in Fig. 5.4 and Fig. 5.5.

Point A indicates the time when the sudden heat load was imposed to the previously steady



Figure 5.4 – Transient flow regime response in test section 1 after the heat load is suddenly increased from 0 to 30 W cm^{-2} at initial mass flux of $1500 \text{ kg m}^{-2}\text{s}^{-1}$, inlet subcooling of 5.5 K, and outlet saturation temperature of 31.5°C : (a) $t = 5.250$ s (moment A-B), superheated single-phase liquid, (b) $t = 7.350$ s (moment B), chaotic two-phase flow, (c) $t = 7.417$ s (moment B-C), pure vapor phase in channels and two-phase in inlet and outlet slits, (d) $t = 7.550$ s (moment C), two-phase flow followed by vapor phase, (e) $t = 7.750$ s (moment C-D), the vapor phase nearly replaced by the two-phase, and (f) $t = 8.117$ s (moment D), subcooled liquid at channel inlet followed by the two-phase flow (The time datum is 0 s, as shown in Fig. 5.3. The net flow direction is from left to right, same to all the figures in this paper.).

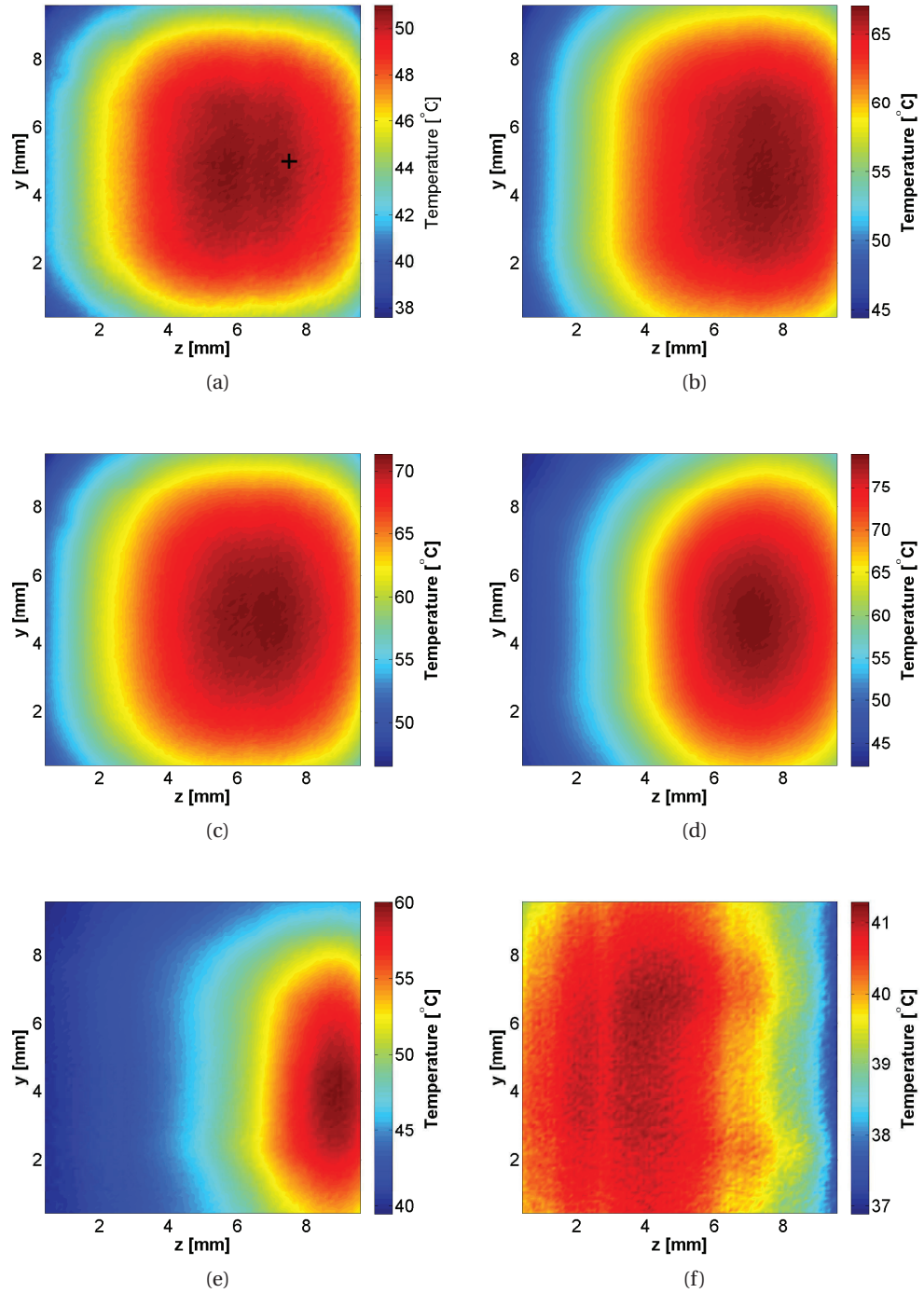


Figure 5.5 – Thermal maps of test section 1 after the heat load is suddenly increased from 0 to 30 W cm^{-2} , at $G = 1500 \text{ kg m}^{-2}\text{s}^{-1}$, $\Delta T_{\text{sub}} = 5.5 \text{ K}$, and $T_{\text{sat}} = 31.5^\circ\text{C}$ for six times : (a) $t = 5.250 \text{ s}$ (moment A-B), (b) $t = 7.350 \text{ s}$ (moment B), (c) $t = 7.417 \text{ s}$ (moment B-C), (d) $t = 7.550 \text{ s}$ (moment C), (e) $t = 7.750 \text{ s}$ (moment C-D) and (f) $t = 8.117 \text{ s}$ (moment D).

conditions, corresponding to an adiabatic single-phase liquid flow. After imposing the sudden

heat load, the base temperature first rose from 27.7 to 66.6 °C (point B) within 2.35 seconds. Point B is the onset of boiling (see Fig. 5.4b and Fig. 5.5b). Next, the vapor expanded towards the channel inlet and outlet (in Fig. 5.4b) due to a considerable sudden increase in fluid volume, thus making vapor prevalent in most of the microchannels by pushing away the liquid. This instant marked as point B-C is demonstrated in Fig. 5.4c and Fig. 5.5c (One might note that the base temperature still kept increasing after this point). Meanwhile, the pumping power was gradually increased by the flow controller to maintain the original mass flux. As a result of this, when the channel inlet pressure was increased to a level high enough to push the two-phase flow back into the channels, a flow regime of two-phase flow followed by the vapor phase appeared, as shown in Fig. 5.4d. At the beginning of this re-wetting process by the two-phase flow, a large part of the microchannels was still occupied by the vapor phase or dryout with inefficient heat transfer. Hence, the maximum base temperature increased to 78.6 °C (point C shown in Fig. 5.4d and Fig. 5.5d). As more and more two-phase flow was pushed back into the channels, two-phase flow boiling took over with more efficient heat transfer through its thin liquid film evaporation. This resulted in a significant drop in the base temperature from 78.6 °C (point C) to 39.5 °C (point D) within 0.56 seconds, and then steady-state was finally reached at 41.5 °C at point E.

To demonstrate a comparative investigation of the evolution of the micro-evaporator base

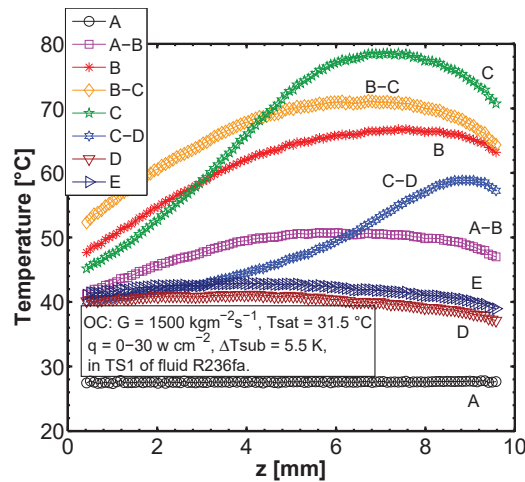


Figure 5.6 – Evolution of centerline base temperature along the flow direction at seven typical moments versus time for test section 1 with heat load from 0 to 30 W cm⁻² at G = 1500 kg m⁻² s⁻¹.

temperature during the cold startup, the base temperature at the centerline along the flow direction for eight instants (points A to E, as marked in Fig. 5.3) are plotted in Fig. 5.6. It is shown that after imposing the sudden heat load the centerline base temperature profile rose globally until instant B-C, at which most of the microchannels were temporarily occupied by the vapor phase, as shown in Fig. 5.4c. Afterwards (from B-C to C), the two-phase flow was

pushed back into the channels, resulting in a drop in the local base temperature. However, the base temperature at the area close to the channel outlet, where the vapor phase was still prevalent, kept increasing until the arrival of the two-phase flow (i.e. from C-D to C). Finally, the base temperature appeared to be moderate and more uniform at moment D, presenting a flow regime of subcooled liquid followed by two-phase flow, as seen in Fig. 5.4f, and the steady state soon at time E.

Through the process of cold startup, the micro-evaporator experienced very large temporal and spatial temperature differences. The base temperature increased to 78.6 °C from 27.5 °C, while the largest spatial temperature difference reached 33.4 K at time C. These large spatial and temporal temperature differences will inevitably induce local thermal stress and probably burn out the micro-evaporator, thus causing severe safety problems for operation. Thus, avoiding or limiting the temporal and spatial temperature differences by reducing the micro-evaporator maximum base temperature during cold startups is of paramount practical importance. The influential operating parameters on the maximum base temperature during cold startups are now presented and discussed in the following sections, including how to greatly reduce the temperature overshoot.

5.3.2 Effect of test section

Two test sections with different inlet orifice widths were tested to characterize their effect on the base temperature response during cold startups. Their base temperature variations versus time are compared in Fig. 5.7. At the current operating condition ($G = 1500 \text{ kg m}^{-2}\text{s}^{-1}$, $\Delta T_{sub} = 5.5 \text{ K}$, $T_{sat} = 31.5 \text{ °C}$, $q = 0\text{-}30 \text{ W cm}^{-2}$), the base temperature of test section 1 (TS1) spiked to 78.6 °C after the onset of boiling. This was not observed in test section 2 (TS2), for which the maximum base temperature was 66.8 °C. This is due to the smaller inlet orifice width which prevents or limits the flow reversal from forming a temporary vapor phase zone or dryout in the microchannels. Hence, the maximum base temperature during the cold startup can be reduced by reducing the inlet orifice width.

Furthermore, it took less time for test section 2 to reach two-phase flow than test section 1 after applying the sudden heat load. This is due to different ways of initiating two-phase flow. For test section 1 the two-phase flow was triggered by some nucleate bubbles inside the microchannels (see Fig. 5.4b), thus requiring a large wall superheat for the onset of boiling. Instead, for test section 2 the two-phase flow in the microchannels was triggered by the bubbles starting from the manifold outlet, which then traveled back to the channel outlet plenum and then spread to the channel inlet, as presented in Fig. 5.8.

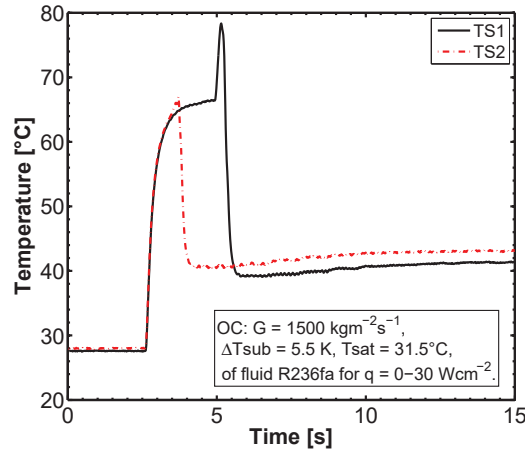


Figure 5.7 – Effect of test section inlet orifice ratio on the thermal response of test section 2 with heat load from 0 to 30 W cm⁻².

5.3.3 Effect of pulse magnitude

To study the effect of the magnitude of the heat flux pulse on the thermal response of micro-evaporators, three heat flux magnitudes were tested for each of the two test sections and the results are shown in Fig. 5.9. It is found that the maximum base temperature increases with the increase in heat flux magnitude. As shown in Fig. 5.9a, for test section 1, the maximum base temperature jumped from 47.7 to 78.6 °C when increasing the heat flux magnitude from 14 to 30 W cm⁻². Furthermore, the onset of flow boiling occurred earlier for higher heat flux magnitude. However, the time required to trigger boiling seems to be similar when increasing the heat flux magnitude from 20 to 30 W cm⁻². The similar results are found for test section 2 (as shown in Fig. 5.9b) except for the heat flux magnitude of 14 W cm⁻², for which the flow boiling was not triggered within the time period investigated.

5.3.4 Effect of mass flux

Fig. 5.10 presents the effect of mass flux on the base temperature response of test section 2. It is found that the time required to trigger boiling increases with mass flux, and the base temperature for $G = 1000 \text{ kg m}^{-2} \text{ s}^{-1}$ reached its highest value of 73.1 °C. For $G = 1500 \text{ kg m}^{-2} \text{ s}^{-1}$ the onset of boiling has been discussed in Fig. 5.8. On the other hand, for $G = 1000 \text{ kg m}^{-2} \text{ s}^{-1}$, the high-speed video indicates that the two-phase flow was triggered by a vapor jet from one microchannel, as shown in Fig. 5.11a. This jet then started to expand upstream and downstream from the channel outlet, as shown in Figs. 5.11b to 5.11d.

To better demonstrate the flow regime evolution in spatial-temporal domain during the cold

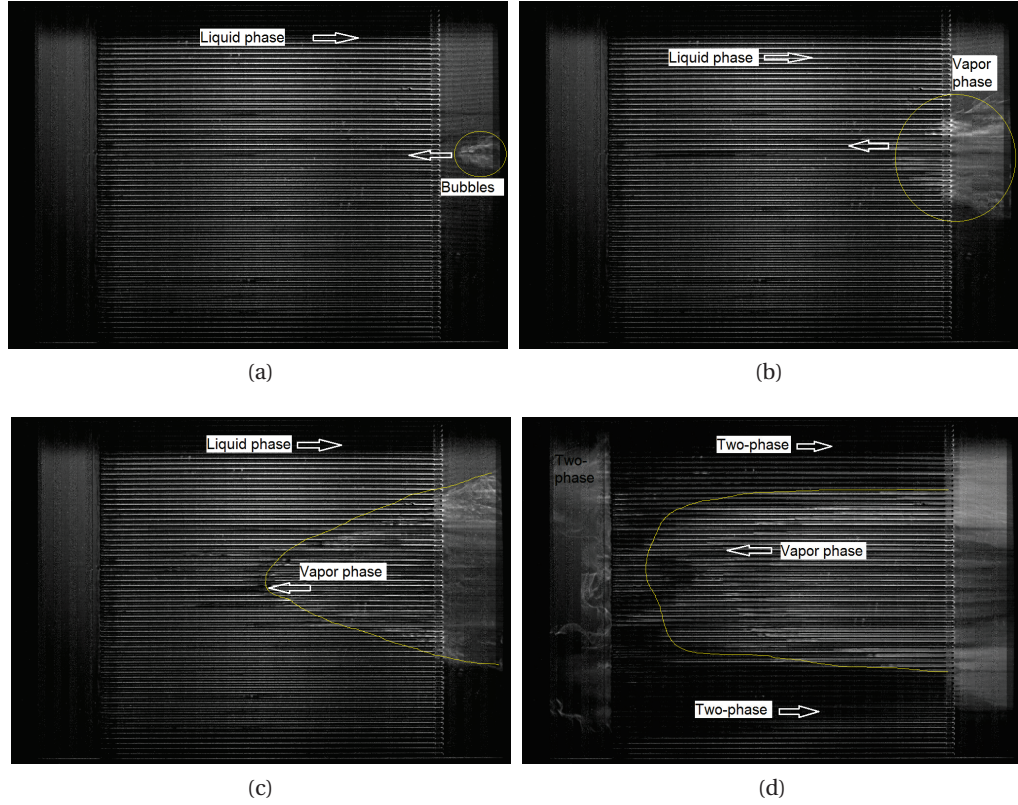


Figure 5.8 – Process of triggering two-phase flow during a cold startup in test section 2 for $G = 1500 \text{ kg m}^{-2}\text{s}^{-1}$, $\Delta T_{sub} = 5.5 \text{ K}$, $T_{sat} = 31.5 \text{ }^{\circ}\text{C}$, $q = 0\text{-}30 \text{ W cm}^{-2}$: (a) $t = t_0 \text{ s}$, bubbles traveling back to the outlet plenum, (b) $t = t_0 + 0.008 \text{ s}$, small stream of vapor phase starting moving upstream from the channel exit, (c) $t = t_0 + 0.016 \text{ s}$, vapor phase arriving at the channel middle with large part of channels occupied by the liquid phase and (d) $t = t_0 + 0.030 \text{ s}$, vapor phase arriving at the channel entrance with two-phase flow between the vapor phase and the two test section boundaries moving downstream (the net flow direction is from left to right).

startup, the time-strip method proposed by Borhani and Thome (2010) was applied to the case of $G = 1000 \text{ kg m}^{-2}\text{s}^{-1}$ to post-process the recorded high-speed movie at three locations along the flow direction, as marked by three yellow lines in Fig. 5.11d. The time-strip method is a way to evaluate two-phase flow dynamics from flow visualization videos by looking at fields of interest of the recorded video images and plotting these versus time. This method is based on the fact that the different phases show different reflections towards the same light source. The time-strip results are presented in Fig. 5.12. The time frame for the high-speed video processed by the time-strip method is 2.488 s, starting at the moment of 0.012 s before the onset of the vapor jet (see Fig. 5.11a).

By analyzing the time-strip plots, a qualitative and quantitative detail of two-phase flow dynamics the during cold startup were obtained. As mentioned before, the light regions in Fig. 5.12 indicate either liquid or vapor phase, while the dark ones represent the two-phase

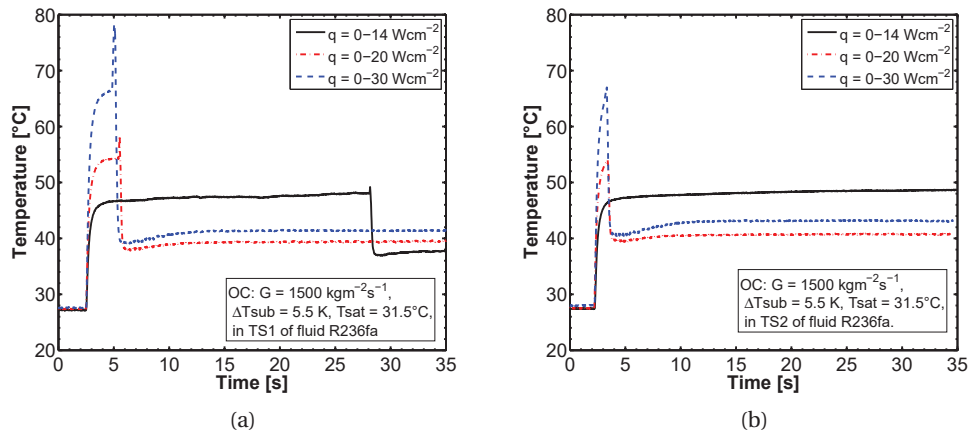


Figure 5.9 – Effect of heat flux magnitudes on the thermal response of micro-evaporators: (a) test section 1 and (b) test section 2.

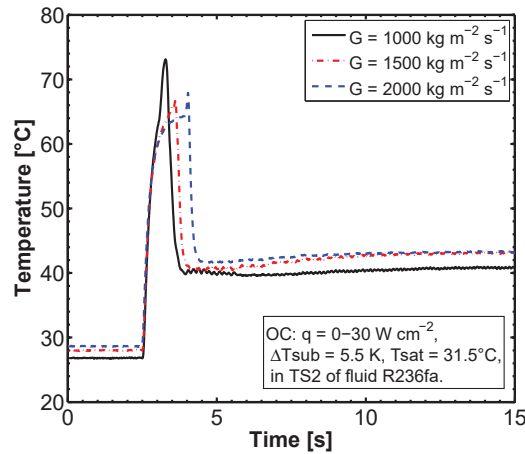


Figure 5.10 – Effect of mass flux on the thermal response of test section 2 with heat load from 0 to 30 W cm⁻².

mixture, due to their differences in light reflection. The first vertical dark streak appearing in Fig. 5.12c at $t = 0.016$ s (pointed by the yellow arrow) represents the trace of back flow of the two-phase mixture when it passed by the location of $z = 9$ mm. Therefore, the light areas on the left side of this streak indicated the liquid phase, while the vapor phase was on its right side. The velocity of the back flow can be quantitatively characterized by tracking the first dark line in the three time-strip plots. For example, the first vertical dark streak occurred at 0.022 s at the location of $z = 5$ mm in Fig. 5.12b and it appeared at 0.028 s when it moved to the location of $z = 1$ mm, as shown in Fig. 5.12a. Hence, the velocity of two-phase back flow was obtained to be 0.67 m s^{-1} . Furthermore, it is also shown that the time frame during which the location of $z = 9$ mm was occupied by the vapor phase after the first passage of the

two-phase back flow is 0.288 s, which is obviously longer than the other two locations, thus indicating a higher base temperature. Finally, an periodic alternative between light and dark lines in Fig. 5.12a implies the flow boiling instability, which is also witnessed by a moderate fluctuation of base temperature for $G = 1000 \text{ kg m}^{-2}\text{s}^{-1}$ in Fig. 5.10.

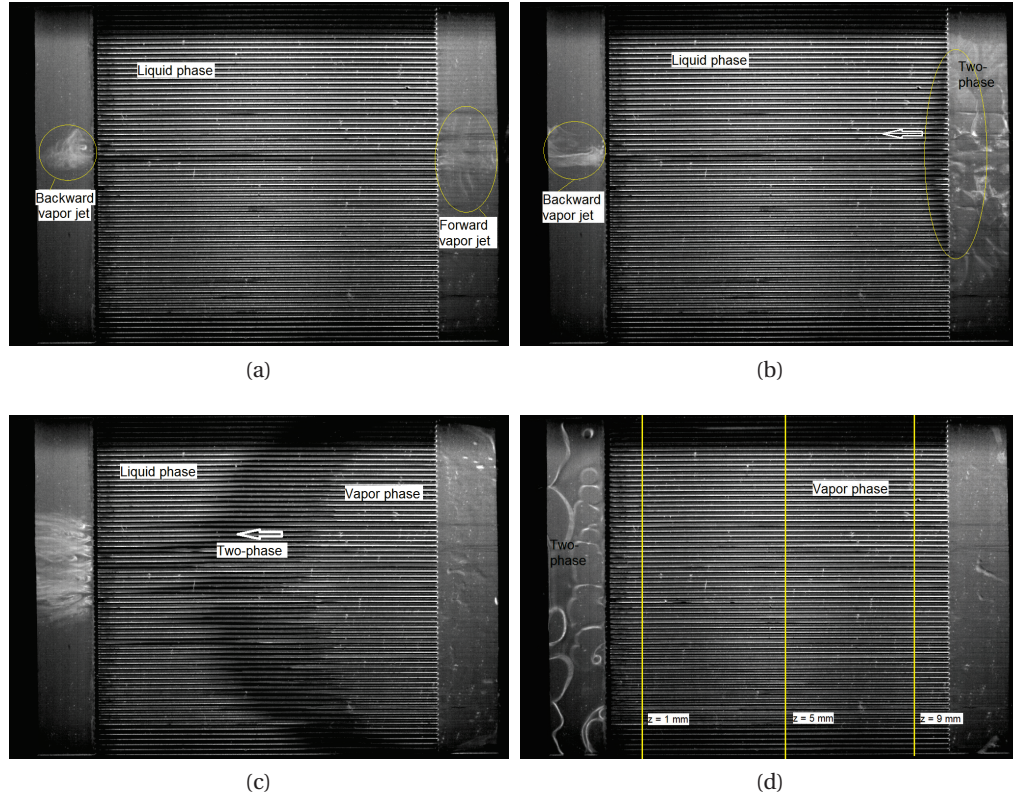


Figure 5.11 – Process of triggering two-phase flow during cold startup in test section 2 at $G = 1000 \text{ kg m}^{-2}\text{s}^{-1}$: (a) $t = t_0$ s, onset of boiling by a vapor jet with liquid phase in microchannels, (b) $t = t_0 + 0.002$ s, starting to explode from the channel exist upstream and downstream with still liquid phase in microchannels, (c) $t = t_0 + 0.008$ s, liquid was pushed back by the two-phase mixture creating a vapor phase behind, and (d) $t = t_0 + 0.024$ s, two-phase in the inlet plenum with vapor phase in channels (The net flow direction is from left to right).

5.3.5 Effect of inlet subcooling

The inlet subcooling is an important parameter for the onset of boiling since it indicates the amount of heat energy or enthalpy needed to reach saturation. The inlet subcooling here was determined by the difference between the fluid saturation temperature at the inlet pressure and the measured fluid temperature. The effect of inlet subcooling on the base temperature response of test section 2 during cold startups is presented in Fig. 5.13. It is shown that the time needed to trigger boiling increases when increasing ΔT_{sub} from 5.5 to 10 K whilst

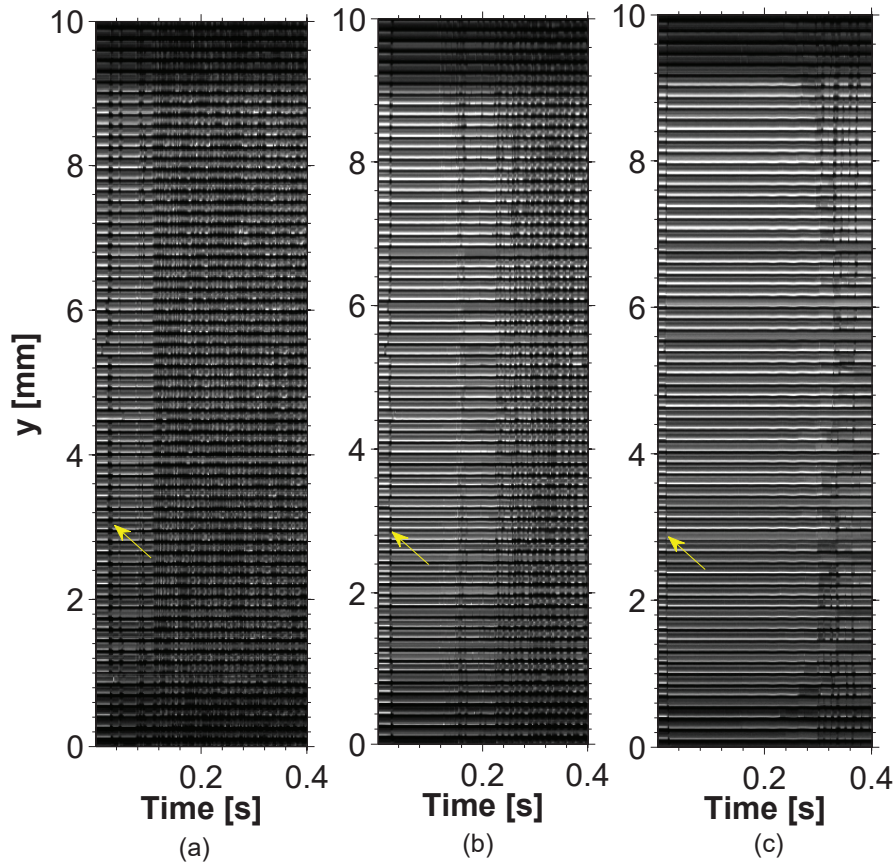


Figure 5.12 – Time strips at three stream-wise locations during a cold startup at $G = 1000 \text{ kg m}^{-2}\text{s}^{-1}$ in test section 2: (a) $z = 1.0 \text{ mm}$, (b) $z = 5.0 \text{ mm}$ and (c) $z = 9.0 \text{ mm}$ (position z was marked with yellow lines in Fig. 5.11d).

their base temperature profiles present similar trends. However, a different base temperature profile is found for $\Delta T_{sub} = 2 \text{ K}$, for which the maximum base temperature was only 48.1°C , obviously smaller than other two cases. Notably, inlet subcooling are found to be $\leq 1 \text{ K}$ in mini-thermosyphon tests by Ong et al. (2016) for a CPU prototype cooling system.

In the current experimental setup, the inlet subcooling was decreased by increasing the inlet fluid temperature through the electrical preheater placed at the upstream of the test section. Consequently, the initial base temperature for $\Delta T_{sub} = 2 \text{ K}$ was the highest one among the three cases, as shown in Fig. 5.13. In fact, when reducing the inlet subcooling to 2 K , some slug bubbles appeared at the beginning of each channel due to the flash effect caused by the inlet orifices. This flow scenario was recorded by the high-speed video camera and presented in Fig. 5.14. Some small flash bubbles were condensed back into the liquid downstream when no heat flux was applied. As a result of this, when imposing a sudden heat load, the two-phase flow in the whole microchannels was easily to initiate by the inlet flashing, without the need for high wall superheat. Therefore, reducing the inlet subcooling to initiate some bubbles by

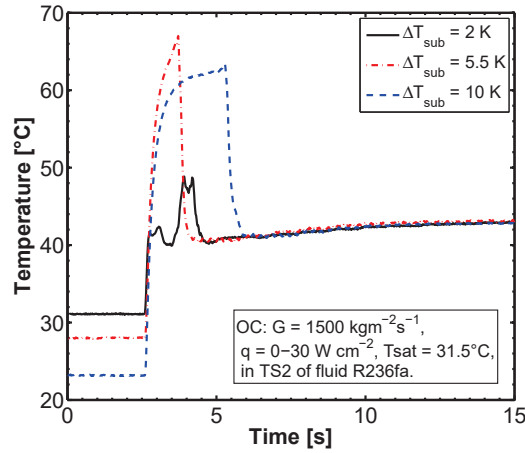


Figure 5.13 – Effect of inlet subcooling on the thermal response of test section 2 with heat load from 0 to 30 W cm^{-2} .

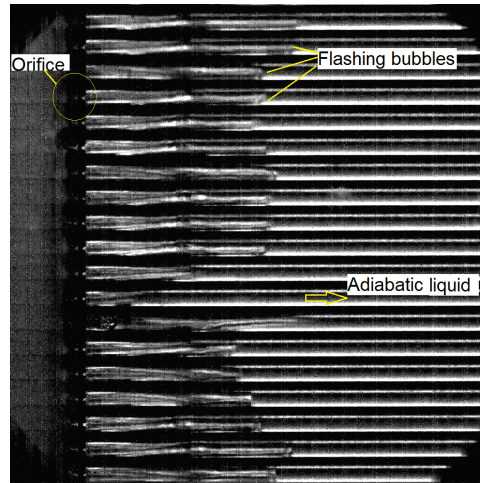


Figure 5.14 – Photo of slug bubbles due to flash after the inlet orifices for test section 2 at $\Delta T_{sub} = 2 \text{ K}$ for $G = 1500 \text{ kg m}^{-2} \text{ s}^{-1}$, $T_{sat} = 31.5^\circ \text{C}$ under adiabatic condition.

flashing is very helpful for limiting the maximum base temperature peak during cold startups.

5.3.6 Effect of outlet saturation temperature

Three outlet saturation temperatures were tested to investigate the effect on the base temperature response of test section 2 during cold startups and the results are shown in Fig. 5.15. It is found that increasing the saturation temperature increased the maximum base temperature and the time needed to trigger boiling. It is also shown that the wall superheat for the onset of boiling decreased from 34.5 to 31.8 K when increasing the saturation temperature from 31.5 to 40°C . This is because the increase in saturation temperature leads to a decrease in the fluid

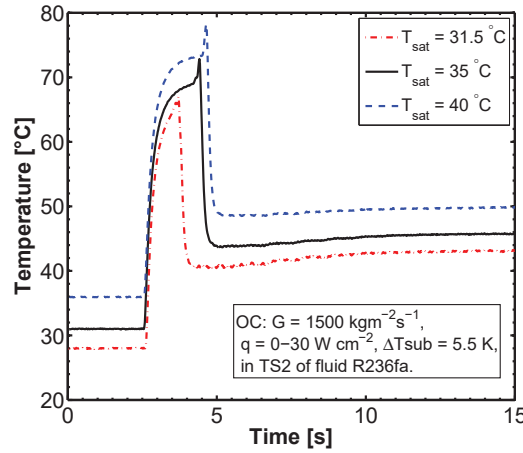


Figure 5.15 – Effect of outlet saturation temperature on the thermal response of test section 2 with heat load from 0 to 30 W cm^{-2} .

surface tension, thus decreasing the required wall superheat for the onset of boiling Kandlikar (2004).

For $T_{sat} = 31.5$ and 35 °C at $G = 1500 \text{ kg m}^{-2}\text{s}^{-1}$, it was observed that the two-phase flow in the microchannels was initiated by bubbles (in the manifold outlet) traveling back to channel outlet plenum, and then spread to the channel inlet, similarly as shown in Fig. 5.8. For $T_{sat} = 40 \text{ °C}$, the two-phase flow in the microchannels was triggered by a vapor jet similar to that described in Fig. 5.11. Furthermore, a short moment of vapor phase in the microchannels was generated for $T_{sat} = 35$ and 40 °C , while this was not observed for the case of $T_{sat} = 31.5 \text{ °C}$. Therefore, the base temperature for $T_{sat} = 31.5 \text{ °C}$ dropped immediately after the onset of boiling rather than spike up like the other two cases.

5.3.7 Effect of fluid

Fig. 5.16 plots the effect of the two fluid on the base temperature response of test section 2 during cold startups ($G = 1500 \text{ kg m}^{-2}\text{s}^{-1}$, $\Delta T_{sub} = 5.5 \text{ K}$, $T_{sat} = 31.5 \text{ °C}$, $q = 0-30 \text{ W cm}^{-2}$). It is shown that, different from the fluid R236fa, the onset of boiling for the fluid R245fa was not observed during the time period investigated, thus the base temperature stayed high due to only having the single-phase liquid cooling. This is because the surface tension of R245fa (0.013 Nm^{-1}) is 42% higher compared to R236fa (0.0093 Nm^{-1}), and therefore it requires a higher wall superheat to reach the bubble departure diameter for initiating boiling Kandlikar (2004). Hence, using a fluid with a low surface tension is helpful to prevent micro-evaporators from being highly superheated for a long time period before the onset of boiling.

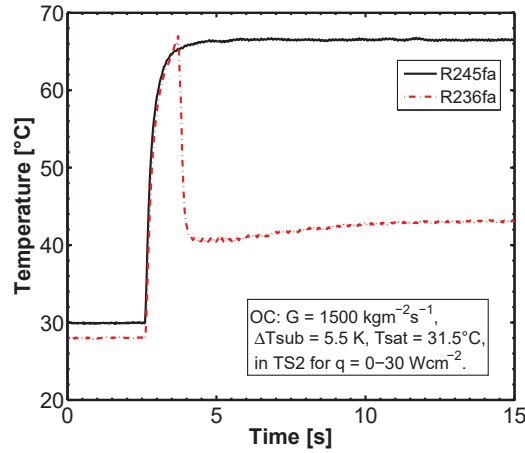


Figure 5.16 – Effect of fluid property on the thermal response of test section 2 with heat load from 0 to 30 W cm^{-2} .

5.3.8 Effect of surface roughness

While the effect of surface roughness is not able to be investigated here, the roughness of the surface is perceived to create nucleate sites in its cavities. The size of the nucleate sites available in the channel (if inlet flashing is not triggered) is an important factor in the onset of boiling. Therefore, less wall superheat is required for the onset of boiling to occur on a rough channel surface than on a relatively smooth surface. Since the present silicon multi-microchannel evaporators had an average surface roughness of only 90 nm, which is significantly smaller than that of copper microchannel evaporators tested by Costa-Patry (2011) (460 nm), the current temperature overshoot during cold startups found in the silicon microchannel evaporators was not observed by Costa-Patry (2011) in the copper test section. This is because the latter requires less wall superheat for the onset of boiling due to the numerous cavities on the channel surface. Therefore, properly increasing the channel surface roughness is expected to decrease the maximum base temperature during cold startups.

5.4 Heat flux periodic variation

After the onset of boiling during the cold startup, the heat generation from the electronics equipment will vary according to the operational tasks performed. This results in a variation in heat load for micro-evaporators. To investigate the thermal response of the micro-evaporators during such processes, a series of tests with periodic variations in heat fluxes were conducted. The effects of heat flux pulse period and mass flux on the thermal response of micro-evaporators were investigated, and the results are presented and discussed below.

5.4.1 Effect of pulse period

The base temperature responses at five distances downstream along the centerline for changing the heat flux from 20 to 30 W cm^{-2} periodically with three pulse periods are plotted in Fig. 5.17. The same temperature scale was used in Fig. 5.17 to better demonstrate the temperature evolution over the distance downstream. It is shown that the base temperature first increased but then decreased along the distance downstream, and the oscillation in base temperature caused by the periodic variation in heat flux was damped with the distance downstream. This is due to the local flow regime. As reported in Huang et al. (2016b) for flow boiling in multi-microchannel evaporators, in the channel entrance the single-phase or subcooled flow boiling usually prevailed, while moving further downstream the two-phase flow, typically annular flow, began to dominate. Since the transfer of heat in the annular flow regime through thin liquid film convection evaporation is more efficient than that in the single-phase or subcooled flow boiling regime, thus along the flow direction the base temperature became less sensitive to the periodic variation in heat flux. As a result, the channel entrance regions of micro-evaporators are more subject to base temperature oscillations during the periodic variation in heat load.

Furthermore, the effect of heat flux pulse period on the base temperature response is shown to be negligible within the test range, with a maximum temperature difference of less than 1 K .

5.4.2 Effect of mass flux

Fig. 5.18 represents the effect of mass flux on the variation of base temperature during the periodic variation in heat flux. The results at five distances downstream along the centerline are presented. It is shown that the base temperature of $G = 2000 \text{ kg m}^{-2}\text{s}^{-1}$ is always higher than that of $G = 1500 \text{ kg m}^{-2}\text{s}^{-1}$. This is due to the difference in the inlet fluid temperature, which was increased to maintain the same inlet subcooling when increasing the mass flux.

5.5 Conclusions

The thermal response of multi-microchannel evaporators under cold startups and periodic variations in heat fluxes during flow boiling of refrigerants were investigated experimentally. During cold startups, the maximum base temperature and time required to trigger boiling were comparatively studied with a large range of operating conditions, including the test section geometry (inlet orifice width), heat flux magnitude, mass flux, inlet subcooling and outlet saturation temperature for two fluids. The base temperatures measured by a fine-resolution IR camera in spatial-temporal domain were correlated with the observations of flow regime acquired by a high-speed video camera. It is found that the maximum base temperature was limited by lowering the inlet orifice width, the heat flux magnitude (no less than the minimum

value required to initiate two-phase flow), inlet subcooling and outlet saturation temperature, but increased when decreasing the mass flux. Besides, the time required to initiate boiling increases when increasing the inlet orifice width, mass flux, inlet subcooling, outlet saturation temperature, and fluid surface tension, but decreases with the increase in heat flux magnitude. Furthermore, three flow scenarios leading to the onset of boiling were observed. The first was caused by nucleation sites occurring inside multiple microchannels, the second was initiated by the bubbles starting from the manifold outlet (a flashing of superheated liquid as it emerged from the microchannels) and the last one was referred to the vapor jet inside one microchannel.

For transient cases with a periodic variation in heat flux, the effects of mass flux and heat flux pulse period on the base temperature response are shown to be insignificant within the current testing range. Independent of the mass flux and heat flux pulse width, the temperature variation resulted from the periodic change in heat flux was damped along the distance downstream.

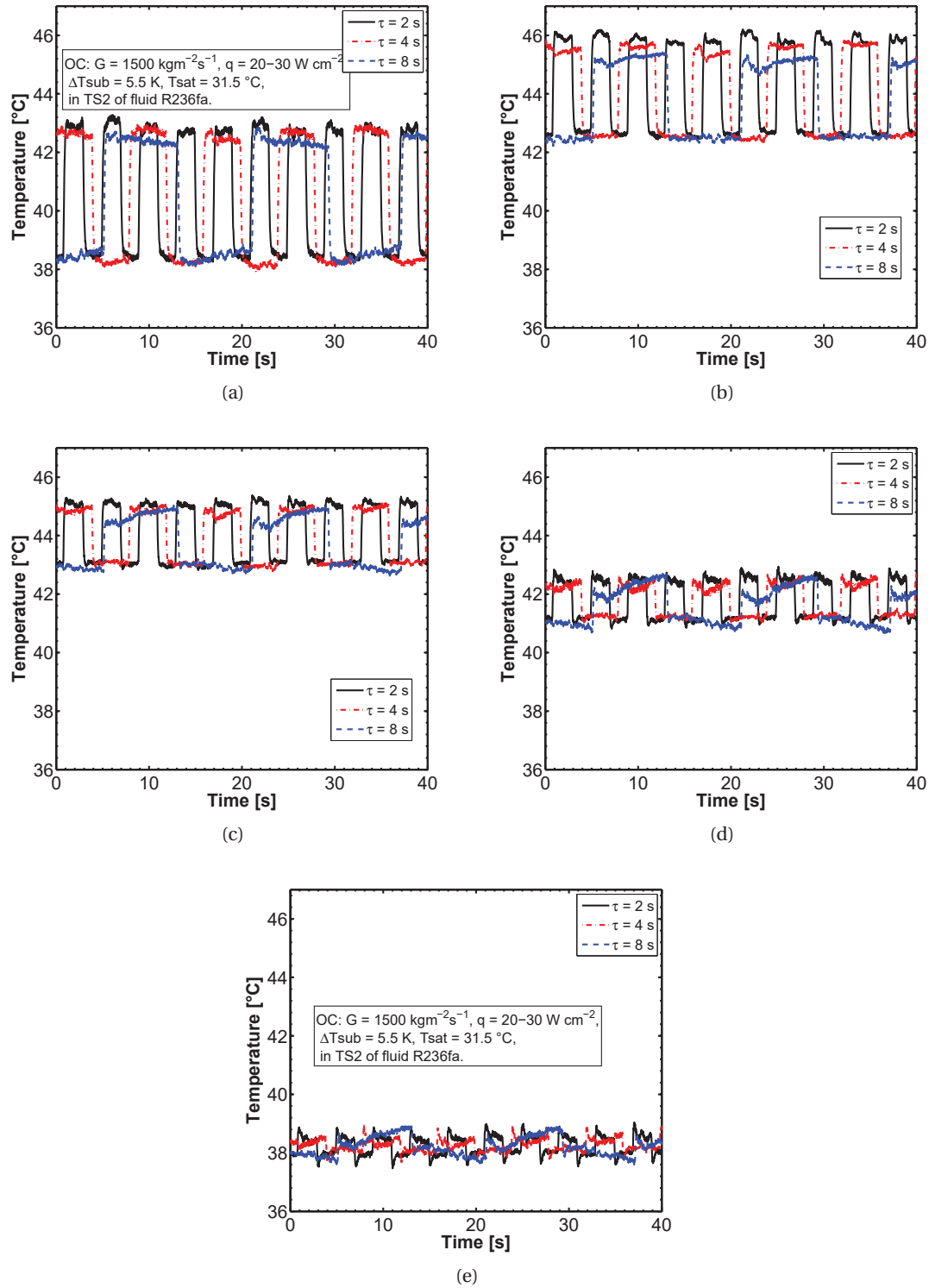


Figure 5.17 – Effects of heat flux pulse period and distance downstream on the base temperature response of test section 2 under periodic variations in heat flux: (a) $y = 5.0$, $z = 0.25$ mm, (b) $y = 5.0$, $z = 2.5$ mm, (c) $y = 5.0$, $z = 5.0$ mm, (d) $y = 5.0$, $z = 7.5$ mm and (e) $y = 5.0$, $z = 9.5$ mm.

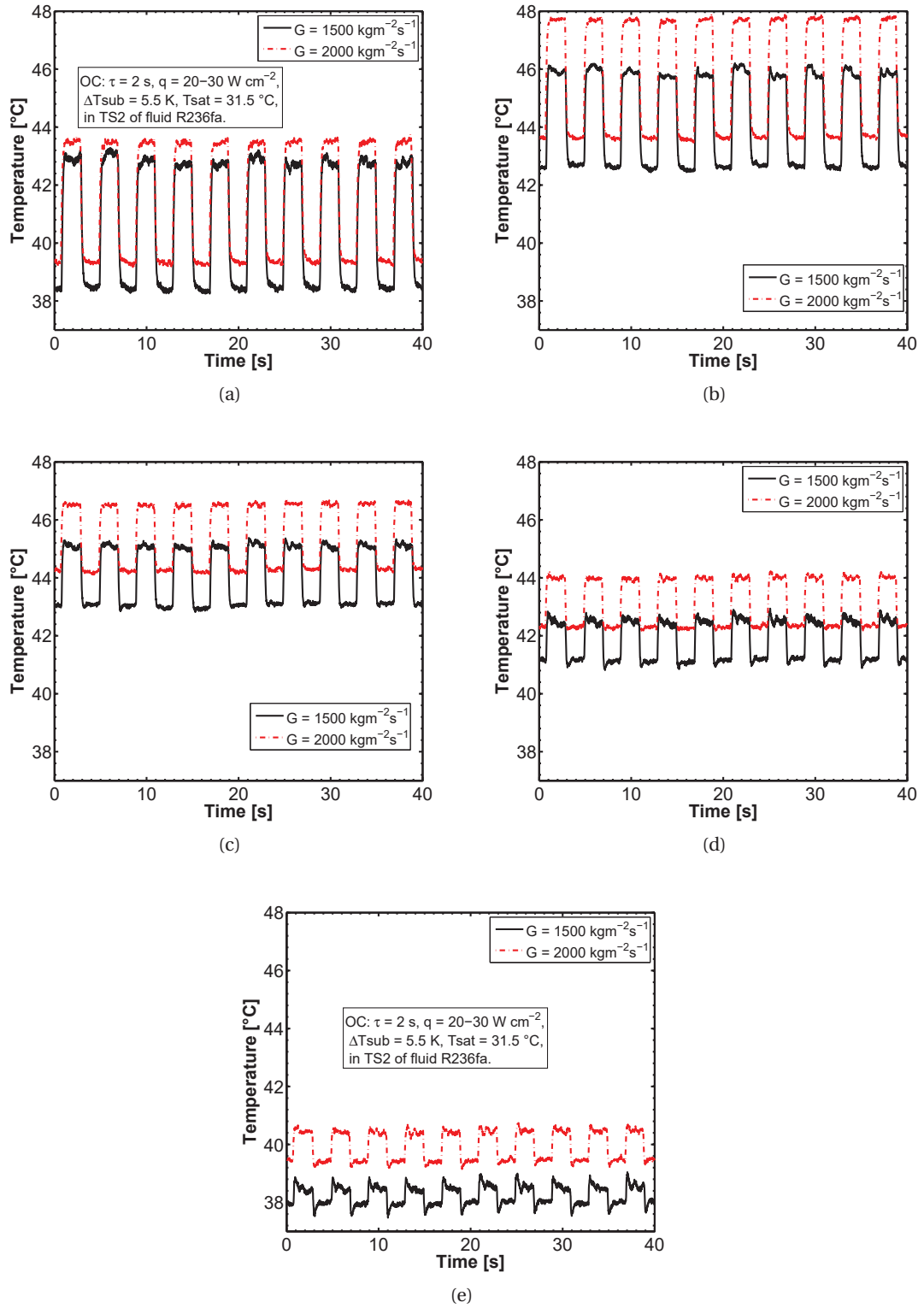


Figure 5.18 – Effects of mass flux on the base temperature response for periodic variations in heat flux: (a) $y = 5.0$, $z = 0.25 \text{ mm}$, (b) $y = 5.0$, $z = 2.5 \text{ mm}$, (c) $y = 5.0$, $z = 5.0 \text{ mm}$, (d) $y = 5.0$, $z = 7.5 \text{ mm}$, and (e) $y = 5.0$, $z = 9.5 \text{ mm}$.

6 Transient heat transfer coefficient

This chapter is from the paper below by Huang et al. (2016d):

H. Huang, N. Lamaison, J.R. Thome, Transient data processing of flow boiling local heat transfer in a multi-microchannel evaporator under a heat flux disturbance, under review by *Journal of Electronic Packaging*, 2016.

Abstract

Multi-microchannel evaporators are often used to cool down electronic devices subjected to continuous heat load variations. However, so far, rare studies have addressed the transient flow boiling local heat transfer data occurring in such applications. The present paper introduces and compares two different data reduction methods for transient flow boiling data in a multi-microchannel evaporator. A transient test of heat disturbance from 20 to 30 W cm⁻² was conducted in a multi-microchannel evaporator using R236fa as the test fluid. The test section was 1 × 1 cm² in size and had 67 channels, each having a cross-sectional area of 100 × 100 μm². The micro-evaporator backside temperature was obtained with a fine-resolution infrared camera. The first data reduction method (referred to 3D-TDMA) consists in solving a transient 3D inverse heat conduction problem by using a TDMA (Tri-Digonal Matrix Algorithm), a Newton-Raphson iteration and a local energy balance method. The second method (referred to 2D-controlled) considers only 2D conduction in the substrate of the micro-evaporator and solves at each time step the well-posed 2D conduction problem using a semi-implicit solver. It is shown that the first method is more accurate, while the second one reduces significantly the computational time but led to an approximated solution. This is mainly due to the 2D assumption used in the second method without considering heat conduction in the widthwise direction of the micro-evaporator.

6.1 Introduction

Multi-microchannel evaporators with two-phase flow boiling provide a promising potential for cooling of high heat flux devices, such as top end central processing units (CPUs), graphics processing units (GPUs), and advanced military avionics. The multi-microchannel evaporators thus experience heat load disturbances in time during operation due to the variation in the heat generation from the cooled devices. This requires the two-phase cooling system to respond swiftly while avoiding or limiting an adverse variation in the evaporator wall temperature, which will be inevitably passed on to the electronics. Under a heat load disturbance, the local micro-evaporator wall temperatures depend on the local flow boiling heat transfer coefficients, and therefore the study of transient flow boiling heat transfer during the heat load disturbance is of scientific and practical importance for implementing the two-phase cooling system with multi-microchannel evaporators. However, the study of transient flow boiling heat transfer in multi-microchannel evaporators under such conditions is currently very limited in the open literature.

So far, steady state flow boiling heat transfer and pressure drop of various fluids in multi-microchannel evaporators have been studied comprehensively Qu and Mudawar (2003a); Lee and Garimella (2008); Agostini et al. (2008); Costa-Patry (2011); Szczukiewicz et al. (2013); Kim and Mudawar (2014); Huang et al. (2016b), while the transient flow boiling heat transfer of a single microchannel evaporator under constant heat flux has been investigated in only a few recent studies Rao et al. (2014); Bigham and Moghaddam (2015).

Rao et al. (2014) reported the transient flow boiling heat transfer of de-ionized water in a single channel microdevice ($D_h = 230 \mu\text{m}$). The temperature responses were measured by several titanium thermistors. In order to resolve the thermal response of the thermistor during boiling, a 3D conjugate heat transfer model was formulated and solved using ANSYS software. In their model, the boiling process regarding the bubble nucleation and growth was modeled by varying the guessed heat transfer coefficients (named as Robin boundary condition) by either a linear increase in the heat transfer coefficient to a maximum value then a linear decrease back to the previous value, or a linear increase to a constant high value. A constant heat flux evaluated from the energy balance was used in their study without mentioning the non-uniformity of heat flux distribution at the solid-fluid interface.

Later, Rao and Peles (2015) measured the spatio-temporally resolved flow boiling heat transfer of HFE 7000 in a single microchannel ($D_h = 370 \mu\text{m}$). A dimensionless slip coefficient (S) representing the fraction of the real variation in the local heat transfer quantity that can be captured by a sensor was proposed to consider the conjugate conduction effects in the substrate. With a *priori* knowledge of $S(t)$, the transient data processing procedure was simplified from a 3D conjugate heat conduction model used by the authors previously in Rao et al. (2014) to a 1D model, and the time varying local convective heat flux was also obtained, eliminating the assumption of constant heat flux used in Rao et al. (2014). However, it is not straightforward to

obtain a comprehensive $S(t)$ since it requires a 3D finite element model to be solved under a range of operating conditions.

Bigham and Moghaddam (2015) studied the transient heat transfer of FC-72 during flow boiling in a single microchannel evaporator under a constant heat flux boundary condition. The bottom part of the test section was composed by a silicon substrate with a thickness of 500 μm and a coated SU8 layer with a thickness of 9.8 μm . Their thin film heaters were deposited at the SU8-silicon interface. There were 53 platinum resistance temperature detectors (RTDs) sputtered onto the fluid-SU8 interface and the SU8-silicon interface were used to measure the temperature during boiling. With the temperatures measured by the RTDs at the top and bottom of the SU8 layer, a 2D transient heat conduction model was built and solved by ANSYS Fluent to resolve the transient heat flux distribution at the fluid-SU8 interface, which was used for calculating the transient heat transfer coefficients. By correlating the temperature and heat transfer data with the synchronized images of flow regimes, four types of mechanisms of heat transfer during boiling process were observed: (1) microlayer evaporation, (2) interline evaporation, (3) transient conduction, and (4) micro-convection.

In general, there are two main challenges faced when dealing with the transient flow boiling heat transfer in multi-microchannel evaporators under heat load disturbances. The first is to measure the spatial-temporally resolved micro-evaporators' base temperature with a fine-resolution. Hence, the traditional techniques using a few RTDs Chen and Cheng (2009); Chen et al. (2010); Basu et al. (2015a,b); Bigham and Moghaddam (2015), or thermistors Rao et al. (2014), are not sufficient even though providing a high frequency of data acquisition. In comparison, an infrared (IR) camera having a high span resolution, a low response time, and a non-intrusive measurement, is able to precisely capture the transient temperature response in spatial and temporal domain. This approach has been widely used in experimental studies of steady state flow boiling in multi-microchannel evaporators Hetsroni et al. (2002); Xu et al. (2005); Szczukiewicz et al. (2013); Huang et al. (2016a,b). An IR camera was also used by Huang et al. (2016c) to track and measure the transient temperature response of multi-microchannel evaporators during cold startups and periodic variations in heat flux.

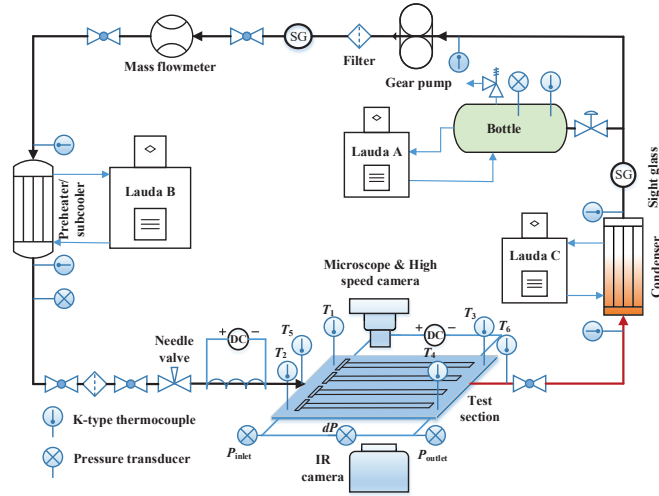
The second challenge is to obtain the transient heat flux distribution at the micro-evaporator footprint, or solid-fluid interface, when changing the heat flux at the base. It was shown in Huang et al. (2016b) that the steady-state heat flux distribution at the multi-microchannel evaporator's footprint was not uniform even when a uniform heat flux was applied at the base. This is because the local footprint heat flux is related to the local heat transfer which depends on the local flow regime, that varies locally according to the local boundary condition and with vapor quality. Using a two dimensional heat conduction model to reduce the transient heat transfer data along the flow direction, which has been used for a single microchannel evaporator Rao et al. (2014); Bigham and Moghaddam (2015), is not sufficient to account for the widthwise variation of local heat transfer coefficients in multi-microchannel evaporators. As a result of this, a new method extended from the 3D inverse data processing of Huang et al.

(2016a) will be presented here to obtain the transient heat flux/heat transfer coefficient distribution at the micro-evaporator footprint. Additionally, for simplicity, a second new method using 2D heat conduction model adapted from the transient model of Lamaison et al. (2013) will be also presented, and the results will be compared with the 3D-TDMA method in order to see how necessary is the third dimension.

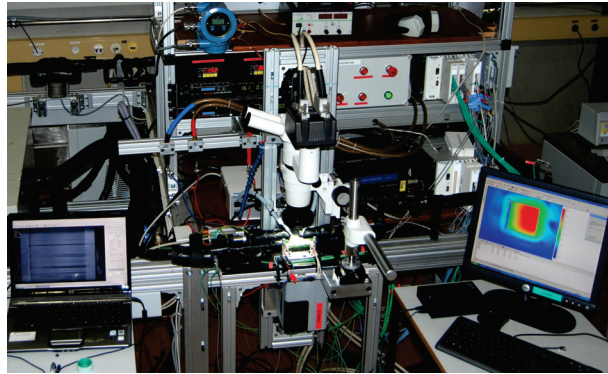
In the present work, the experimental facility used to perform the heat flux disturbance test is first presented with a fine-resolution IR camera measuring the micro-evaporator's base temperature. Then, the procedure employed to reduce the local fluid temperature through pressure drop measurement is described. Using the base temperature from IR measurements and fluid temperature profile at each time step, two different heat transfer coefficient data reduction methods are described. The first one considers a 3D inverse problem with a Newton-Raphson iteration at each time step on the heat transfer coefficient boundary condition while the second one solves a 2D well posed conduction problem at each time step with only a temporal correction of the heat transfer coefficient boundary condition using a numerical PI controller. Finally, the data processed with both methods are presented and compared in terms of mean and local transient heat transfer coefficients along the widthwise centerline of the micro-evaporator.

6.2 Experimental setup

Fig. 6.1 depicts the facility used for the transient flow boiling tests. The fluid was circulated by an oil-free gear pump and its mass flow rate was monitored by a Coriolis mass flowmeter. As described in our previous work Huang et al. (2016b), the test section (see Fig. 6.2) was made of silicon with a finned area of $10 \times 10 \text{ mm}^2$ on the base plate. In the test section, there were 67 parallel channels with a height of $100 \text{ }\mu\text{m}$, a width of $100 \text{ }\mu\text{m}$, and a fin thickness between channels of $50 \text{ }\mu\text{m}$. The transient heat load was realized through two micro-heaters sputtered on the backside of the test section, each connected to a DC power supply (Sorensen DLM32–95E). K-type thermocouples and pressure transducers placed at the inlet and outlet manifolds, as shown in Fig. 6.2d, were used to measure the fluid temperature and pressure, individually. The fluid temperature and pressure signals were acquired by a NI-DAQ instrument. The temperature of test section backside (covered by a piece of thin high-emissivity matt tape Xu et al. (2005); Szczukiewicz et al. (2013)) was monitored and recorded by an IR camera (FLIR ThermoCAM SC3000 with $83 \text{ }\mu\text{m}$ pixel resolution), which was synchronized by a LabVIEW program with the data acquisition system.



(a)



(b)

Figure 6.1 – Layout of the facility: (a) schematic diagram and (b) photo.

6.3 Data reduction

6.3.1 Pressure drop

The total experimentally measured pressure drop is the sum of those of the inlet restriction, channel and outlet restriction pressure drops. The inlet and outlet restriction pressure drop are processed as presented in Huang et al. (2016b). The channel pressure drop is then deduced from the total pressure drop measurement by subtracting these inlet and outlet singularities. In order to obtain the local fluid pressure in the channels, the single-phase region pressure drop is first calculated using the model of Shah and London (1978). Then, once the energy balance indicates the onset of the saturated flow boiling, a parabolic fit between the pressure at the end point of the single-phase region and that at the channel outlet is performed. Effectively, since state-of-the-art two-phase pressure drop models are not accurate enough to predict the

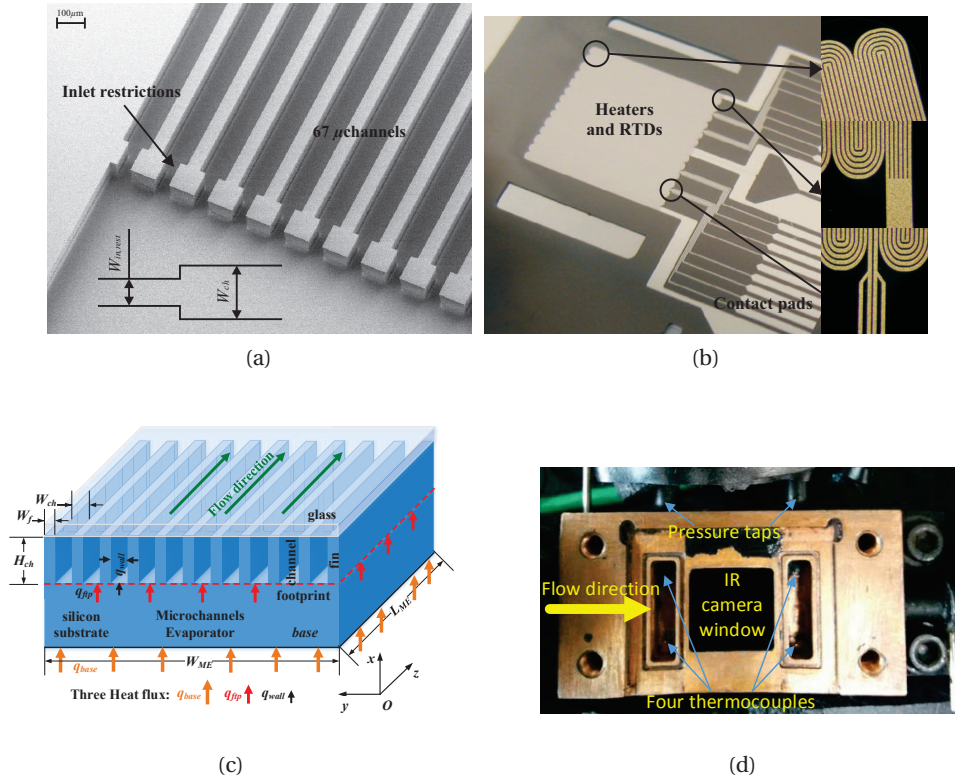


Figure 6.2 – Test section: (a) schematic of the microchannel evaporator, (b) photo of the microchannels with inlet orifices Szczukiewicz et al. (2013), (c) photo of the micro-heaters Szczukiewicz et al. (2013), (d) photo of the manifold bottom.

experimental channel outlet absolute pressure, this parabolic fit is chosen instead in order to reproduce the pressure drop gradient increase with vapor quality while respecting the experimental data. An example of the local fluid pressure in the microchannels is shown in Fig. 6.3.

The main interest in obtaining the local fluid pressure is to deduce the local fluid temperature (also shown in Fig. 6.3). Indeed, the fluid temperature in the single-phase/subcooled flow region is obtained based on an energy balance, while in the saturated flow boiling region, the local fluid temperature is the saturation temperature at the local fluid pressure. The local fluid temperature $T_{fl,loc}$ is then used as an input for the data processing of the local heat transfer coefficient.

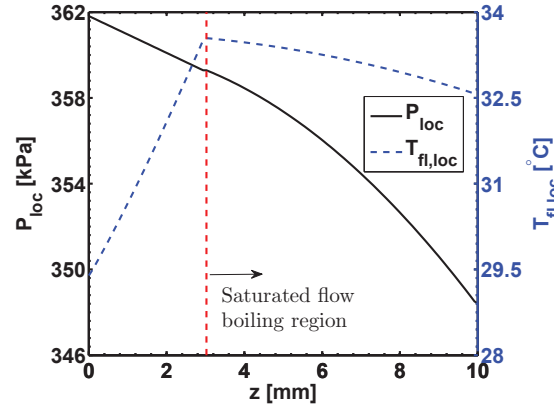


Figure 6.3 – Initial local pressure and temperature profile.

6.3.2 Data reduction method 1 - 3D-TDMA

The transient local channel wall heat transfer coefficients were calculated through the transient local footprint heat transfer coefficients based on the fin equation Incropera (2006) as follows:

$$\alpha_{ftp}(y, z, t) = \frac{q_{ftp}(y, z, t)}{T_{ftp}(y, z, t) - T_{fl}(y, z, t)} \quad (6.1)$$

$$\alpha_{wall}(y, z, t) = \frac{\alpha_{ftp}(y, z, t) W_{ME} L_{ME}}{N_{ch} [W_{ch} L_{ME} + 2(L_{ME} + W_f/2) H_{ch} \eta_f(y, z, t)]} \quad (6.2)$$

$$\eta_f(y, z, t) = \frac{\tanh[m(y, z, t) H_{ch}]}{m(y, z, t) H_{ch}} \quad (6.3)$$

$$m(y, z, t) = \sqrt{\frac{2\alpha_{wall}(y, z, t)(L_{ME} + W_f)}{k_{Si}(y, z)(W_f L_{ME})}} \quad (6.4)$$

where k_{Si} is the thermal conductivity of silicon, depending on the temperature Costa-Patry (2011):

$$k_{Si} = 0.0007T^2 - 0.5416T + 157.39 \quad (6.5)$$

$q_{ftp}(y, z, t)$ is the transient local footprint heat flux, which is essential for the transient local channel wall heat transfer coefficients and can be obtained by solving a 3D transient inverse heat conduction problem. This is an extension of our previous work Huang et al. (2016a), where the 2D steady state local footprint heat flux was obtained by solving a 3D steady state inverse heat conduction problem.

Turning now to the transient 3D heat conduction problem, the present experimental case is

governed by the following equations:

$$\frac{\partial}{\partial x}(k \frac{\partial T}{\partial x}) + \frac{\partial}{\partial y}(k \frac{\partial T}{\partial y}) + \frac{\partial}{\partial z}(k \frac{\partial T}{\partial z}) = \rho c_p \frac{\partial T}{\partial t}; \quad (6.6)$$

$$t = 0, T = T^0(x, y, z); \quad (6.7)$$

$$t > 0,$$

$$T(0, y, z, t) = T_{IR}(t), q(0, y, z, t) = q_b(t) \quad (6.8)$$

$$q(x, 0, z, t) = q_s(t), q(x, W_{ME}, z, t) = q_n(t) \quad (6.9)$$

$$q(x, y, 0, t) = q_w(t), q(x, y, L_{ME}, t) = q_e(t) \quad (6.10)$$

where x, y, z indicate the thickness x , widthwise y and lengthwise z (flow) directions, as shown in Fig. 6.4. T_0 is the initial temperature field before the heat flux disturbance obtained by solving a 3D steady state inverse heat conduction problem, which was documented by Huang et al. (2016a). The heat fluxes q_w, q_e, q_n and q_s are at the four lateral sides of the substrate evaluated by the local transient base temperature from the IR camera. The principle for this is to calculate the temperature gradient at two neighboring pixels at each of the four lateral sides to approximately determine the individual Neumann boundary condition. The thickness of the micro-heater ($1.5 \mu\text{m}$) was neglected. The details regarding the determination of boundary condition and the process for solving the 3D steady state inverse heat conduction problem were presented in Huang et al. (2016a).

The finite volume method integrating Eq. (6.6) on a control volume basis Patankar (1980) was

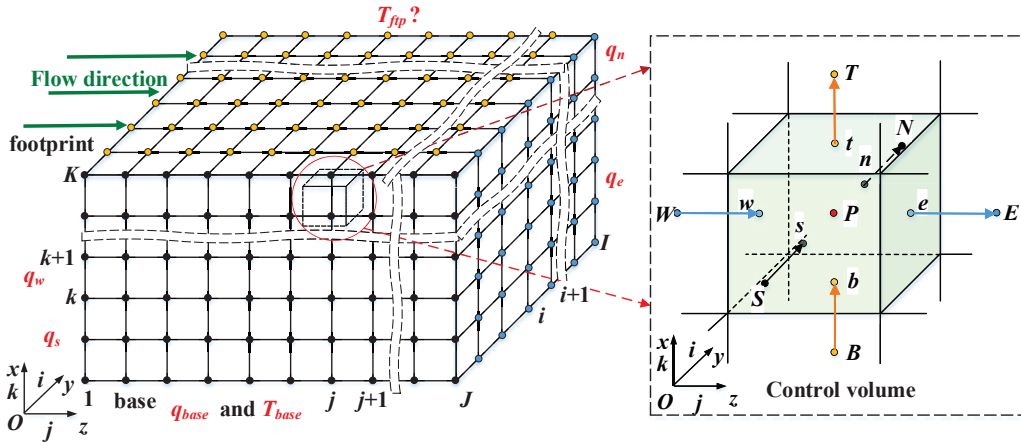


Figure 6.4 – Mesh types used in the 3D-TDMA model.

used to discretize the transient 3D heat conduction equation. Through this method the local energy balance at each control volume can be easily monitored. During discretization, the temporal item was approximated by the first order backward difference, and the diffusion

items were addressed by the central difference. The vertex-centered grid type was implemented in the discretization of the silicon substrate, as demonstrated in Fig. 6.4, since this grid type allows the base temperature map to be used directly as the investigator. The harmonic average thermal conductivity between the two neighboring nodes was used to maintain the energy balance at the interface of the two neighboring control volumes. Both the Dirichlet and Neumann boundary conditions were addressed as source items. A fully implicit format was adopted here to make the calculation converge without any constraint condition. After rearrangement, the original non-linear heat conduction equation becomes an algebraic one and its generalized format is expressed as follows:

$$a_P T_P = \sum a_{nb} T_{nb} + a_P^0 T_P^0 + S_u \quad (6.11)$$

$$a_P = \sum a_{nb} + a_P^0 - S_P \quad (6.12)$$

$$a_P^0 = \rho c_p \frac{\Delta x \Delta y \Delta z}{\Delta t} \quad (6.13)$$

where the subscript nb in the 3D model represents the node of W , E , N , S , T , or B (see the control volume in Fig. 6.4). T_P^0 is the initial temperature field or the calculated one from the last time step. The time step of 1/60 s determined by the IR camera frequency (60 Hz) was used in the transient calculation.

The flowchart for solving the transient 3D inverse heat conduction problem is shown in Fig. 6.5 and the main steps are as follows:

1. Obtain the initial 3D temperature field $T_0(x, y, z)$ by solving the 3D steady state inverse heat conduction problem;
2. Solve the transient 3D inverse heat conduction problem by combining the finite volume method using a 3D TDMA solver, the Newton-Raphson method, and the local transient energy balance method to get $q_{f, tp}$, $T_{f, tp}$, and $T(x, y, z, t)$;
3. Use the pressure drop model to predict the local fluid temperature $T_{f, l}$;
4. Calculate the local footprint heat transfer coefficients by Eq. (6.1);
5. Iterate Eqs. (6.2) to (6.4) to obtain the local wall heat transfer coefficients;
6. Move further to the next time step $(t + 1)$ with $T(x, y, z, t)$ known from last time step, and repeat steps (2) to (5) until the ending time.

6.3.3 Method 2 - 2D-Controlled

The second data reduction method considers only 2D conduction from the test section base to the footprint and along the lengthwise or flow direction, i.e. x and z direction in Fig. 6.2c. Eq. (6.14) presents the heat diffusion equation solved in the silicon substrate of the test section. The east, west, top and bottom boundary conditions, necessary for solving the well-posed conduction problem are listed in Eqs. (6.15) to (6.18). The east and west boundary conditions

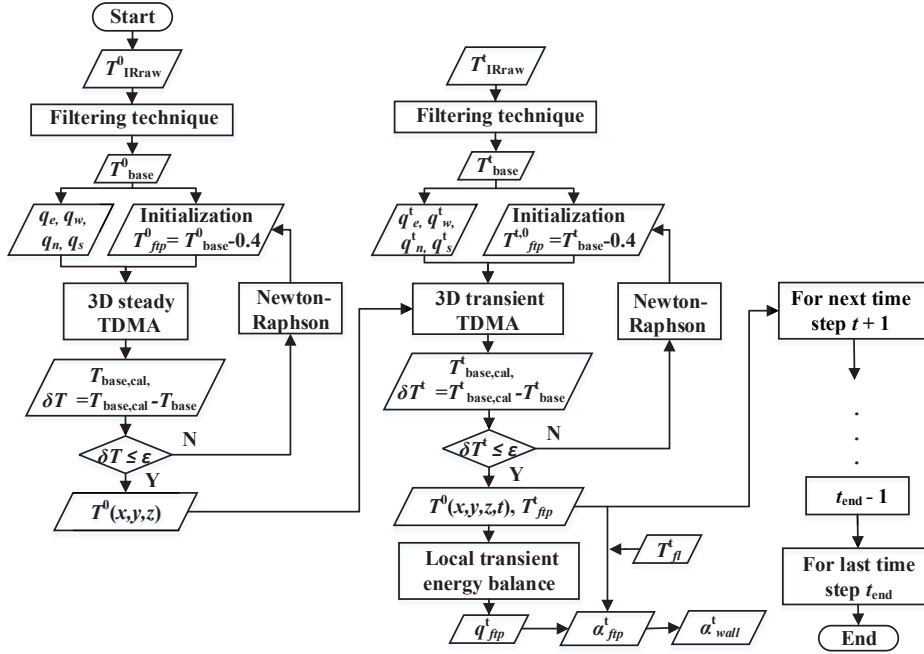


Figure 6.5 – Flow chart for obtaining transient wall heat transfer coefficients with the 3D-TDMA method.

$q_{loss,w}$ and $q_{loss,e}$ were obtained in the same manner as described in the previous Section, i.e. using the local experimental base temperature gradients. The bottom boundary condition $q_{base}(z, t)$ was obtained using experimental measurement of the input electrical heat load at each time step. Finally, for the top boundary condition, the fluid temperature $T_{fl}(z, t)$ was obtained as explained in the pressure drop data processing section, i.e. using the pressure drop measurement and a parabolic fit at each time step. Thus, the goal will be to obtain the correct $\alpha_{ftp,calc}(z, t)$ boundary condition at each time step during the temporal resolution of Eq. (6.14) below. In order to do so, Eq. (6.19) was used to correct this top boundary condition at each time step. The temporal correction took the form of a PI controller using the error between the calculated local base temperature $T_{base,calc}(z, t)$, i.e. from the resolution of Eq. (6.14), and the experimentally measured local base temperature $T_{base,exp}(z, t)$.

$$\frac{dT_p(x, z, t)}{dt} = \frac{1}{\rho_p c_{p,p}} \left[\lambda_z(x, z, t) \frac{\partial^2 T_p(x, z, t)}{\partial z^2} + \lambda_x(x, z, t) \frac{\partial^2 T_p(x, z, t)}{\partial x^2} \right] \quad (6.14)$$

$$\dot{q}(x, t)_{(z=0)} = q_{loss,w} \quad (6.15)$$

$$\dot{q}(x, t)_{(z=L_{ME})} = q_{loss,e} \quad (6.16)$$

$$\dot{q}(z, t)_{(x=0)} = q_{base}(z, t) \quad (6.17)$$

$$\dot{q}(z, t)_{(x=th_{Si})} = \alpha_{ftp,calc}(z, t) [T_p(z, t) - T_{fl}(z, t)] \quad (6.18)$$

In Eq. (6.19), the integral and proportional gains K_i and K_p were determined from a system identification, for which the 2D conduction was initially solved for the steady-state case before the heat flux disturbance (see next section for the operating conditions) and with $\alpha_{ftp,calc}(z, t)$ first set equal to a constant value of $20 \text{ kW m}^{-2} \text{ K}^{-1}$. Once converged, $\alpha_{ftp,calc}(z, t)$ was suddenly set to a constant value of $30 \text{ kW m}^{-2} \text{ K}^{-1}$ and the calculated base mean temperature was tracked with time. Fig. 6.6 shows the results of this system identification in terms of $\alpha_{ftp,calc,mean}$ and associated $T_{base,calc,mean}$ variations with time.

$$\frac{\partial \alpha_{ftp,calc}(z, t)}{\partial t} = K_i [T_{base,calc}(z, t) - T_{base,exp}(z, t)] + K_p \frac{\partial T_{base,simu}(z, t)}{\partial t} \quad (6.19)$$

A first order model without dead time, also shown in Fig. 6.6 and was fitted to this identification

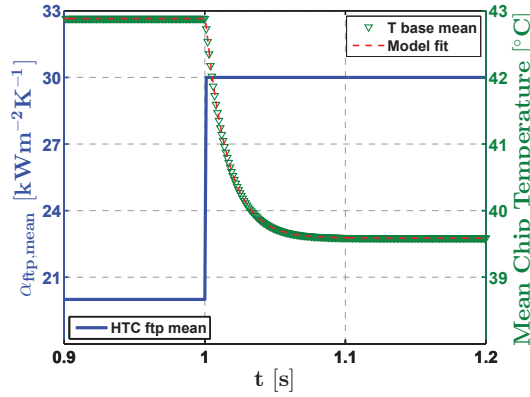


Figure 6.6 – System identification for K_i and K_p determination

test:

$$\tau_p \frac{\partial T_{base,mean}(t)}{\partial t} + T_{base,mean}(t) = K \alpha_{ftp,mean}(t) \quad (6.20)$$

The time constant τ_p and process gain K are respectively equal to 0.0157 s and $-0.0003 \text{ K}^2 \text{ m}^2 \text{ W}^{-1}$. Using this first order model, the method of Karimi et al. (2007) based on linear programming was used to calculate the proportional and integral gains of Eq. (6.19). The latter were found to be equal to $18,537 \text{ W K}^2 \text{ m}^{-2}$ and $1,158,563 \text{ W K}^2 \text{ m}^{-2} \text{ s}^{-1}$ (respectively K_p and K_i). It is worth mentioning that these gains can also be calculated as a function of heat flux using the gain schedule method presented in Karimi et al. (2007) and applied for example in the work of Lamaison (2014). The latter allows a more robust controller model for processing the data when the test conditions vary.

For the resolution, the Partial Differential Equation (PDE) of Eq. (6.14) was discretized in space using the finite difference method with a centered scheme. The resulting set of Ordinary Differential Equations (ODEs) and Eq. (6.19) were solved simultaneously using a semi-implicit solver called the Livermore Solver of Ordinary Differential Equation (LSODE) Hindmarsh (1980). It

employed a predictor-corrector scheme and a variable time step all along the integration, in which the first prediction was based on an explicit formula. This guess was then corrected by an iteration using a modified Newton-Raphson technique with internally generated numerical Jacobian.

Once the set of equations converged at each time step (residual error of 10^{-9}), the wall heat transfer coefficient α_{wall} was calculated by iteration using the converged $\alpha_{ftp,calc}$ profile and the fin equations already presented in Eqs. (6.1) to (A.11). The time resolution of this second method is better than the 60 Hz of the IR camera. In general, a new $\alpha_{ftp,calc}$ profile is obtained at a frequency of 1 kHz. In this case, the input boundary conditions $T_{fl}(z, t)$ and $q_{base}(z, t)$ which were experimentally obtained at the 60 Hz frequency are updated only after about 17 simulated time steps. Also, since the present method considers only the two dimensions x and z , the experimental widthwise centerline profiles were used for $T_{fl}(z, t)$ and $T_{base,exp}(z, t)$. Fig. 6.7 presents the flowchart of this second data processing method, referred to as 2D-controlled, and the different steps explained beforehand are highlighted in this figure.

Finally, it is worth mentioning that the present method has been obtained by modifying the simulation code presented in Lamaison et al. (2013) for which the wall heat transfer coefficient was calculated using correlations and then used as an input for the 2D conduction simulation of the micro-evaporator. In the latter case, the authors were interested in obtaining the chip base temperature for design purposes while the present interest is to process experimental data to obtain the transient local wall heat transfer coefficient.

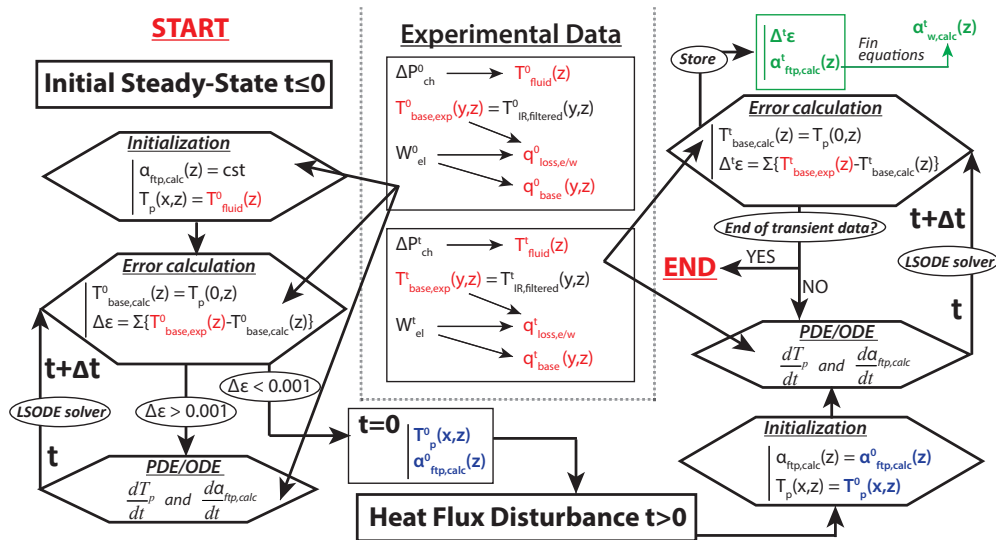


Figure 6.7 – Flow chart for obtaining transient wall heat transfer coefficients with the 2D-controlled method.

6.4 Results and discussions

6.4.1 Case study presentation

The present transient flow boiling test was conducted in a test section with an inlet orifice width of $25\ \mu\text{m}$ using refrigerant R236fa. Prior to the heat flux disturbance, the facility operated at a stable flow boiling regime. The initial operating conditions were: i) heat flux $q_0 = 20\ \text{W cm}^{-2}$, ii) mass flux $G = 1500\ \text{kg m}^{-2}\text{s}^{-1}$, iii) inlet subcooling ($\Delta T_{sub} = 5\ \text{K}$), and iv) outlet saturation temperature $T_{sat} = 31.5\ ^\circ\text{C}$. At a given instant ($t = 0.5\ \text{s}$), the input heat flux was suddenly increased to $30\ \text{W cm}^{-2}$. The test matrix is summarized in Table 6.1.

The mass flux was controlled by a PI controller implemented in the Labview program. The

Table 6.1 – Heat flux disturbance test condition.

Inlet orifice width (μm)	25
$q^0\ (\text{W cm}^{-2})$	20
$q^t\ (\text{W cm}^{-2})$	30
$G^0\ (\text{kg m}^{-2}\text{s}^{-1})$	1500
$\Delta T_{sub}^0\ (\text{K})$	5.5
$T_{sat}^0\ (^{\circ}\text{C})$	31.5
Fluid	R236fa

fluid temperature, pressure and mass flow rate were saved at a frequency of 1 kHz, and the test section base temperature was recorded by an IR camera at a frequency of 60 Hz. The overall recording time for pressure and thermal information by the NI (National Instrument) and IR camera was 60 seconds. The transient flow regime was recorded by a high speed camera at a frequency of 500 Hz, and the recording time was approximately 12.28 seconds limited by its capacity. Therefore, the temporal resolution of the transient tests was determined by the IR camera frequency, which was 60 Hz. The IR camera was self-calibrated in-situ on a pixel by pixel basis Huang et al. (2016a,b). After calibration, the error of IR camera was reduced to $\pm 0.2\ ^\circ\text{C}$ from the default value of $\pm 2\ ^\circ\text{C}$ of the manufacturer.

6.4.2 Pressure drop

The analysis of the dynamic pressure drop variation following the heat flux disturbance is of great interest to understand the variations of the fluid temperature, necessary to the determination of the heat transfer coefficient. When increasing the heat flux from 20 to 30 W cm^{-2} , the pressure drop along the micro-evaporator will increase due to the increased

vapor quality, thus resulting in a decrease in the mass flux. However, since the mass flux was controlled by an experimental PI controller, the mass flux will be gradually dragged up to the previous set point. This whole process is described in Fig. 6.8. The transient total and channel

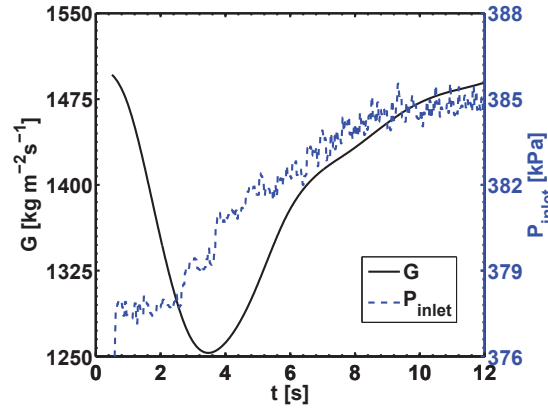


Figure 6.8 – Mass flux and inlet pressure response to the sudden heat load disturbance at 0.5 s.

pressure drop are described in Fig. 6.9. As mentioned before, the mass flux was increased gradually by the flow controller after the heat flux disturbance, thus leading to an increase of the total pressure drop. The relatively large increase of the channel pressure drop just after the heat flux disturbance is explained by the reduction of inlet and outlet restrictions pressure drop due to the decrease of mass flux, while the total pressure drop increased because of the larger vapor quality. Finally, the local fluid pressure and temperature at four locations at the

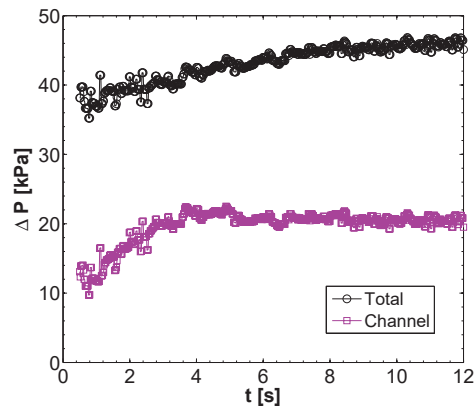


Figure 6.9 – Transient pressure drop.

widthwise centerline along the flow direction are shown in Fig. 6.10. The main results to draw from these graphs are: (i) the fluid temperature at $z = 1.5$ mm follows the variation of the mass flow rate underlining the presence of single-phase flow at this location, (ii) the two-phase flow was triggered after/close to $z = 2.5$ mm since the fluid temperature started to decrease

after this location and the pressure drop between 1.5 and 2.5 mm was very small (underlining the presence of single-phase flow between these two locations), and (iii) the pressure drop gradient in the two-phase region increases along the flow direction, as can be seen with the pressure drop difference in Fig. 6.10 between 2.5 and 5 mm and between 5 and 9 mm, due to the increasing local vapor quality.

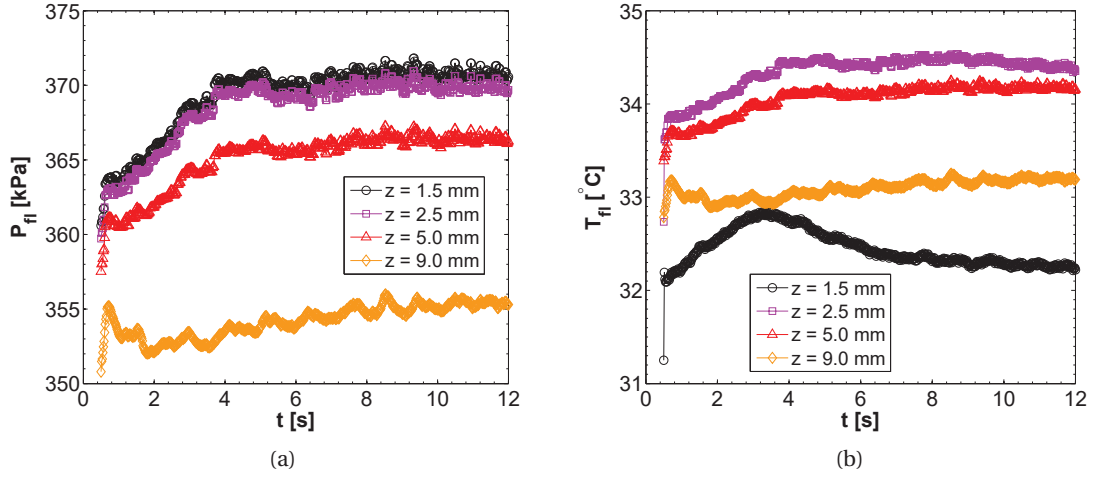


Figure 6.10 – Transient local pressure and temperature at four locations at the widthwise centerline: (a) local pressure and (b) local fluid temperature.

6.4.3 Heat transfer

The present section is dedicated to the comparison of the performance of both data reduction methods, referred as 3D-TDMA and 2D-controlled, to reduce the local $\alpha_{wall,loc}$ and mean wall heat transfer coefficient $\alpha_{wall,mean}$ at the widthwise centerline of the microevaporator, i.e. $y = 5$ mm and $x = th_{Si}$ for the 3D method, and for $x = th_{Si}$ for the 2D method. The local mean wall heat transfer coefficient $\alpha_{wall,mean}$ was obtained by averaging the local pixel heat transfer coefficients along the widthwise centerline at each time frame.

Local/Mean heat transfer coefficient transient variations

Fig. 6.11a presents the variation of the mean wall heat transfer coefficient along the widthwise centerline after the heat flux disturbance at $t = 0.5$ s for both methods. It can be seen that the mean wall heat transfer coefficient changed significantly within the first 1 second after applying the sudden heat load disturbance. Hence, in order to reveal more details about the transient mean heat transfer coefficient, a zoom in the first 1.5 s is also provided in Fig. 6.11a. It is seen that both methods predict a sudden sharp significant increase of the wall heat

transfer coefficient followed by a slightly less sharp and less significant decrease. Then, the wall heat transfer coefficient increases less significantly again and finally slowly decreases to its new steady-state value, higher than for the previous steady-state (as expected since the heat flux is higher). The mean absolute error between both methods is less than 1%. Since these two methods are completely independent, the latter statement reinforces the validity of both methods applied when obtaining the mean transient heat transfer coefficients.

The heat transfer coefficient peak is due to the coupled conduction and convection heat transfer mechanisms following a sudden heat load disturbance. After increasing suddenly the heat flux, both the wall and fluid temperatures increased, while the latter increased faster just after the disturbance. This is related to the way of obtaining the fluid temperature for which the single-phase energy balance and the saturation pressure profile were used according to the local flow regime. This explains the heat transfer coefficient peak in Fig. 6.11a considering Newton's law of cooling. The delayed increase of $T_{wall,loc}$ would then lead to the reduction of the heat transfer coefficient.

Fig. 6.11b presents the maximum error of both methods at each time step. This error was set as the maximum local difference between the calculated and experimental base temperature. Over the entire 12 s of the test, the mean and maximum of the previous variable were calculated. It is seen that the maximum of the 2D-controlled method, i.e. 0.087 K (0.95%), is higher than for the 3D-TDMA method (0.05 K, i.e. 0.12%) and was obtained just after the heat flux disturbance. However, for the mean error, the 2D-controlled method is better (0.004 K vs. 0.05 K). In terms of computational time, the 3D-TDMA method is drastically longer, i.e. 22 hours, compared to the 2D-controlled method, which took about 25 minutes. Moreover, the former considered only 5 elements in the x -direction while the latter had 20. It is worth mentioning that for the 2D-controlled method, 2520 ordinary differential equations were solved at each time step (120×20 for the 2D conduction and 120 for the controller equation).

Fig. 6.12 presents the time evolution of the local wall heat transfer coefficient at four different locations along the widthwise centerline after the heat flux disturbance for both methods. For the four locations, a similar analysis as the one performed for the mean heat transfer coefficient can be done, i.e. both methods give similar results and a sharp increase of the heat transfer coefficient is noticed just after the disturbance. The additional information to draw from this graph is the increase of the heat transfer coefficient downstream along the channel length. The next section below gives additional details regarding the spatial shape of the heat transfer coefficient profiles during the heat flux disturbance test.

Heat transfer coefficient profile variations

Fig. 6.13 presents the local wall heat transfer coefficient profiles along the widthwise centerline at five different instants in time. The profile plotted at $t = 0.5$ s is the one just before the

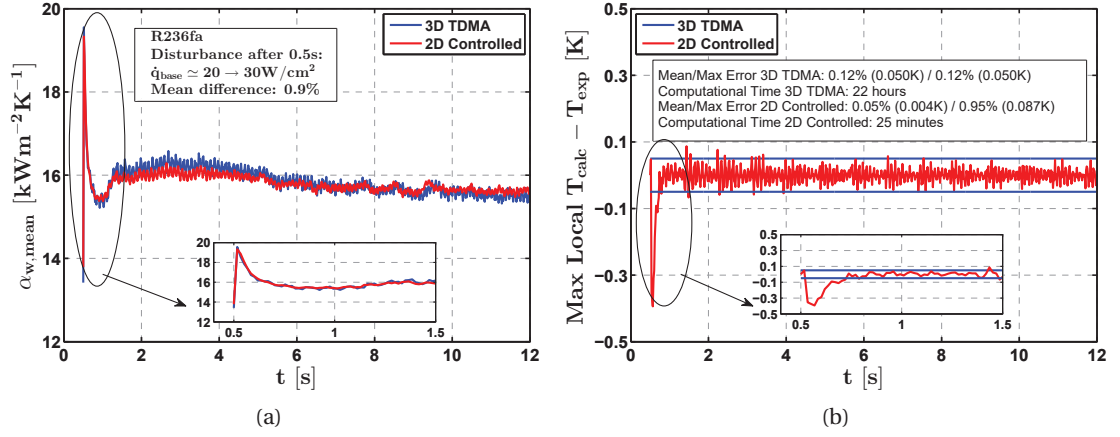


Figure 6.11 – Time evolution along the widthwise centerline after the heat flux disturbance at 0.5s for both methods.: (a) mean heat transfer coefficient, (b) maximum error on the calculated temperature compared to the experimental data.

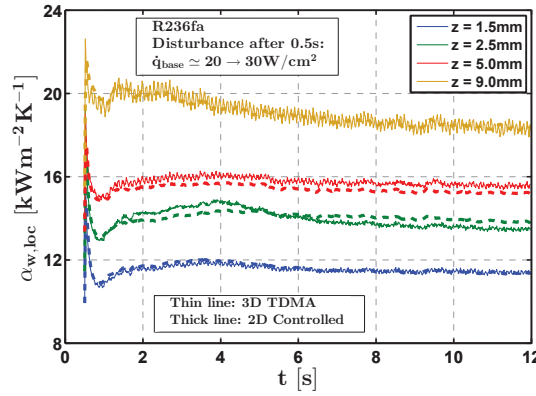


Figure 6.12 – Time evolution of the local wall heat transfer coefficient at four different locations along the widthwise centerline after the heat flux disturbance at 0.5s for both methods.

disturbance, i.e. the wall heat transfer coefficient for steady-state when the heat flux is $20 \text{ kW m}^{-2} \text{K}^{-1}$. All the other profiles plotted consider instants in time after the heat flux disturbance, i.e. when the heat flux is now $30 \text{ kW m}^{-2} \text{K}^{-1}$. After increasing the base heat flux suddenly to 30 W cm^{-2} , the local heat transfer coefficients rose up globally to a new value which was approximately 1.5 times the steady-state value. Meanwhile, during this process the onset of saturated flow boiling advanced towards the channel inlet due to the increased heat flux. Afterwards, the local heat transfer coefficient dropped gradually. This is because of a faster increase in the footprint temperature than the fluid temperature resulting in an increase in their temperature difference.

Generally, the 3D-TDMA method yielded more accurate results (shown by symbols in Fig. 6.13) compared to those from 2D-controlled method (described by lines in Fig. 6.13), especially

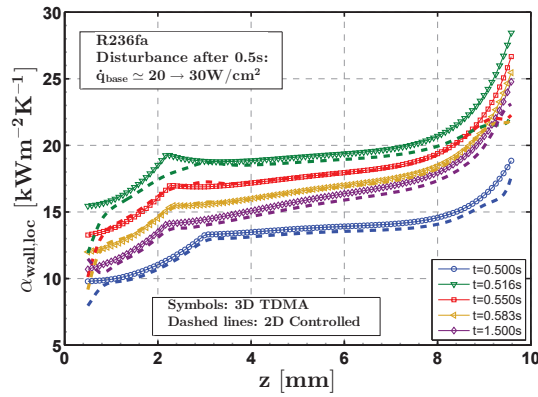


Figure 6.13 – Local wall heat transfer coefficient profiles along the widthwise centerline at five different instants of time.

at the channel inlet and outlet boundaries, and at the instant right after the disturbance where the 3D-TDMA method successfully captured the onset of saturated flow boiling (see $t = 0.516$ in Fig. 6.13). The deviation from the 2D-controlled method is mainly resulted from its pertinent 2D assumption for simplicity without considering the heat conduction in the widthwise direction of the test section. This also leads to a less accurate estimation of the heat flux boundary conditions, i.e. heat loss, at the channel inlet and outlet, which could explain the deviation between the two methods in the local heat transfer coefficients at the boundaries. Regarding the intrinsic variation of the wall heat transfer coefficient profile during the test, it is observed that the onset of saturated flow boiling moved towards the channel inlet due to the increased heat flux. The latter is located at about $z = 3$ mm before the disturbance and moved to about $z = 2.2$ mm after the disturbance, confirming that the location of $z = 2.5$ mm is already in the flow boiling region after the disturbance as discussed in the pressure drop results section (see Fig. 6.10). Again, the 2D-controlled method was not able to track the displacement of the onset of saturated flow boiling towards the entrance of the channels for the profile at $t = 0.516$ s.

As already discussed in Huang et al. (2016b), the local heat transfer trend is closely related to the local flow regimes, which are composed of a single-phase/subcooled flow boiling region until the onset of saturated flow boiling, a very short isolated to coalescing bubble region, and a large annular flow region. The annular flow regime is noticeable with the increase of the heat transfer coefficient towards the end of the channel as the liquid film gets thinner.

6.5 Conclusion

The present paper addressed the data processing of dynamic heat transfer coefficients in a multi-microchannel evaporator subjected to a heat flux disturbance. An experimental test bench comprising an IR camera with fine spatial (120×120 pixels) and temporal (60 Hz) reso-

lutions to measure the base temperature of the evaporator was presented.

Two different data reduction methods were then presented for the calculation of the local heat transfer coefficient at each time step. The first one dealt with the resolution of a 3D transient inverse heat conduction problem. The second method solved at each time step a well-posed 2D conduction problem with a guessed heat transfer boundary condition. The latter was corrected upon a temporal iteration with a numerical PI controller used to reduce the local error between the calculated and measured base temperature. The proportional and integral gains of the controller were obtained with a system identification.

As a summary, the 3D-TDMA method by solving a transient 3D inverse heat conduction problem provided full local data but it required a longer calculation time which was about 22 hours for the present 699 frames of transient temperature measurements. On the other hand, the 2D-controlled method capturing only the centerline data consumed much less time, i.e. only 25 minutes for the present case. However, the 2D-controlled method has a lower accuracy, especially at the boundaries and at the instant right after the heat flux disturbance. The latter is noticeable by: (i) the maximum error obtained on the local base temperature of 0.09 K, (ii) the distorted heat transfer coefficient profiles close to the entrance and outlet of the channels due to the less accurate heat loss accountability, and (iii) the incapability of the 2D-controlled method to track the displacement of the two-phase front upstream just after the disturbance. For the future work, it is planned to update the 2D-controlled method to be 3D to resolve the issues with the distorted profiles close to the entrance and outlet without drastically increasing the computational time. Also, it is worth mentioning that the dynamic 2D-controlled method has already been tested to solve hot-spot configurations and that the latter will also be further extended in the future.

7 Conclusions and recommendations

7.1 Conclusions

An extensive experimental study was carried out to investigate the flow boiling pressure drop and heat transfer of refrigerants in multi-microchannel evaporators under various test conditions. The single-phase flow tests of the flow friction factor and Nusselt number were validated by the leading single-phase correlations. The applicability of seventeen leading two-phase pressure drop models and six leading heat transfer models were assessed by the present data base. The research results have been documented in six papers which are published or under review by the peer-reviewed journals. Each of the six papers was made into a main chapter of this manuscript. The main achievements of this thesis are summarized as below:

1. A new method (algorithm) for obtaining the local heat transfer coefficients by solving the 3D inverse heat conduction problem was proposed. The method involves a polynomial surface fitting, a finite volume method, a Newton-Raphson iteration and a local energy balance method. It was shown to be more accurate for reducing the local heat transfer data in multi-microchannel evaporators, especially for cases using IR measurements, since such flows exhibit very large and sharp variations in the local heat transfer coefficient as a function of two-phase flow regime transitions.
2. Stable flow boiling pressure drops were measured under various test conditions. The contributions of the inlet and outlet restriction pressure drops at high mass flux are significant (from 8.4% to 29.4% and 25.9% to 51.3% respectively of the evaporator's total). The channel pressure drop was calculated by subtracting the inlet and outlet restriction pressure drops from the total pressure drop measured by a differential pressure transducer. A total of 184 points of stable flow boiling data acquired here were used to evaluate the existing models and to develop a new empirical channel pressure drop model, which provided the fluid temperature for calculating the local heat transfer coefficients. This pressure drop was built by fitting the Chisholm parameter C with

the vapor and liquid only Reynolds numbers. The new frictional pressure drop model provided agreement with the experimental data to a MAE of 27.8%.

3. Fine-resolution local heat transfer coefficients of R1233zd(E), R245fa and R236fa were measured in two multi-microchannel evaporators under various test conditions. The effects of inlet subcooling, outlet saturation temperature, inlet orifice width, fluid, mass flux and heat flux on the local heat transfer coefficients were investigated.
4. For saturated flow boiling, it was concluded that the flow pattern based model of Costa-Patry and Thome (2013) provided the best agreement with a MAE of 17.2%. The original flow pattern based model of Costa-Patry and Thome (2013) was modified here to improve its prediction accuracy at the very low vapor quality region.
5. A new flow pattern based model, starting from subcooled liquid flow all the way through to annular flow, was then proposed in this thesis. It presented a good prediction for the local heat transfer data (1,941,538 points) with a MAE of 14.2% and 90.1% of the data predicted within $\pm 30\%$.
6. For cold startups, the maximum base temperature was limited by lowering the inlet orifice width, the heat flux magnitude (no less than the minimum value required to initiate two-phase flow), inlet subcooling and outlet saturation temperature, but increased when decreasing the mass flux. Besides, the time required to initiate boiling increases when increasing the inlet orifice width, mass flux, inlet subcooling, outlet saturation temperature, and fluid surface tension, but decreases with the increase in heat flux magnitude. Furthermore, three flow scenarios leading to the onset of boiling were observed.
7. The transient flow boiling local heat transfer coefficient during a heat flux disturbance was obtained by a new method of solving a transient 3D inverse heat conduction problem, which is an upgrade from the method (item 1 above) proposed here for steady-state conditions.

7.2 Future recommendations

Based on the forgoing achievements, future efforts on this topic are recommended as following:

1. Try to use a standard way, i.e. iterative regularization, to solve the 3D inverse heat conduction problem and compare the results with the present method.
2. Extend the present data base by testing a higher pressure fluid, i.e. R134a to include the stable flow boiling data at relatively low mass flux, thus enlarging the suitability of the present models.
3. Improve the methodology of pressure drop measurement to obtain individual channel pressure drops and local pressure profile, which will provide more precise local fluid

temperature profiles for calculating the local heat transfer coefficients.

4. Upgrade the present flow visualization system with a high-resolution, high-speed video camera and a suitable light source to acquire more information on the flow boiling process, such as the bubble frequency and the thin liquid film thickness along the channel wall, which can be used to update the existing heat transfer models, such as the three-zone model of Thome (2004).
5. Make more studies to obtain transient local heat transfer coefficients with the high-resolution, high-speed flow visualization to reveal more insight into the heat transfer mechanism of flow boiling in multi-microchannels during these transients.

A An appendix

This part is extracted from the paper below by Huang et al. (2016b):

H. Huang, N. Borhani, J. R. Thome, Experimental investigation on flow boiling pressure drop and heat transfer of R1233zd(E) in a multi-microchannel evaporator, *International Journal of Heat Mass Transfer* 98 (2016) 596-610.

A.1 Detailed data reduction

A.1.1 Single-phase flow

Energy balance

The main objective of single-phase flow energy balance analysis is to help evaluate the energy loss in two-phase flow. The single-phase energy balance is given as follows:

$$Q_{total} = Q_{eff} + Q_{amb} + Q_{wire} \quad (A.1)$$

$$Q_{eff} = \dot{m}c_p(T_6 - T_5) \quad (A.2)$$

$$Q_{total} = VI \quad (A.3)$$

where Q_{eff} is the effective heat absorbed by the single-phase flow, Q_{amb} is the heat loss to the ambient through natural convection and radiation, which are characterized by empirical correlations Incropera (2006), and Q_{wire} is the heat loss through the Joule heating in the electrical power wires. Noting that the fluid is heated by flowing through the manifold inlet before entering the channel due to some heat conducted to the cooper manifold, the thermocouples of T_5 and T_6 placed ahead and after the manifold were employed to calculate the effective heat absorbed by the fluid. With the rest three values known in Eq. A.2, the value of Q_{wire} can be identified and is used in the two-phase energy balance analysis.

Appendix A. An appendix

Local Nusselt number

The single-phase local Nusselt number is given by:

$$Nu(y, z) = \frac{\alpha_{wall}(y, z) D_h}{k_{fl}(y, z)} \quad (A.4)$$

where $\alpha_{wall}(y, z)$ is the local wall heat transfer coefficient. The fluid temperature is evaluated locally with the local heat flux at the footprint obtained by using the 3D heat conduction model to reduce the data, instead of assuming a linear variation in temperature along the flow direction. A detailed description of the 3D iterative heat conduction model used to solve the heat equations was documented in our previous work Huang et al. (2016a).

A.1.2 Two-phase flow

Energy balance

The purpose of the two-phase energy balance analysis is to identify the net heat absorbed by the fluid during evaporation. The two-phase flow energy balance can be expressed as:

$$Q_{total} = Q_{eff} + Q_{loss} \quad (A.5)$$

$$Q_{loss} = Q_{mf} + Q_{amb} + Q_{wire} \quad (A.6)$$

$$Q_{mf} = \dot{m} c_p \left(\frac{T_1 + T_2}{2} - T_5 \right) \quad (A.7)$$

where Q_{total} is the electrical power measured by the NI data acquisition system (DAQ); Q_{loss} is the total heat loss; Q_{eff} is the effective heat absorbed by the fluid at the test section part; Q_{mf} is the heat loss through conduction to the manifold, determined from the single-phase energy balance measured by the two thermocouples placed ahead the manifold (see T_5 in Fig. 6.1a) and in the manifold inlet (see T_1 and T_2 in Fig. 6.1a); Q_{amb} is the heat loss to the ambient, evaluated by empirical correlations; $Q_{lossWire}$ is assumed to be the same as that in the single-phase flow test, which was estimated during the single-phase energy balance analysis.

Local heat transfer coefficients

The local channel wall heat transfer coefficients were calculated through the local footprint heat transfer coefficients based on the fin equation Incropera (2006) as follows:

$$\alpha_{wall}(y, z) = \frac{\alpha_{ftp}(y, z) W_{ME} L_{ME}}{N_{ch} [W_{ch} L_{ME} + 2(L_{ME} + W_f/2) H_{ch} \eta_f(y, z)]} \quad (A.8)$$

$$\alpha_{ftp}(y, z) = \frac{q_{ftp}(y, z)}{T_{ftp}(y, z) - T_{fl}(y, z)} \quad (A.9)$$

$$\eta_f(y, z) = \frac{\tanh[m(y, z) H_{ch}]}{m(y, z) H_{ch}} \quad (A.10)$$

$$m(y, z) = \sqrt{\frac{2\alpha_{wall}(y, z)(L_{ME} + W_f)}{k_{Si}(y, z)(W_f L_{ME})}} \quad (A.11)$$

where k_{Si} is the thermal conductivity of silicon, depending on the temperature Costa-Patry (2011):

$$k_{Si} = 0.0007 T^2 - 0.5416 T + 157.39 \quad (A.12)$$

The two-phase local fluid temperature was predicted by the two-phase pressure drop model proposed in this paper by Huang et al. (2016b)

$$-\left(\frac{dp}{dz}\right)_{fr} = \frac{2f_l G^2 (1-x)^2 v_l}{D_h} \phi_l^2 \quad (A.13)$$

$$\phi_l^2 = 1 + \frac{C}{X} + \frac{1}{X^2}, \quad X = \sqrt{\frac{(dP/dz)_l}{(dP/dz)_v}} \quad (A.14)$$

$$f_l = \begin{cases} \frac{8.058}{Re_l}, & Re_l \leq 2000, \\ \frac{0.079}{Re_l^{0.25}}, & Re_l > 2000 \end{cases} \quad (A.15)$$

$$C = \begin{cases} 0.0034 Re_v^{2.01} Re_{lo}^{-1.15}, & Re_l \leq 2000, Re_v \leq 2000 \\ 0.51 Re_v^{0.01} Re_{lo}^{0.34}, & Re_l \leq 2000, Re_v > 2000 \end{cases} \quad (A.16)$$

$$Re_v = \frac{G x D_h}{\mu_v}, \quad Re_l = \frac{G(1-x) D_h}{\mu_l}, \quad Re_{lo} = \frac{G D_h}{\mu_l} \quad (A.17)$$

The local footprint heat flux $q_{ftp}(y, z)$ and temperature $T_{ftp}(y, z)$ were obtained by solving a steady state 3D inverse heat conduction problem. The main steps for solving the steady state 3D inverse heat conduction problem are: (1) solving direct steady state 3D heat conduction equations with a guessed footprint temperature; (2) using the Newton-Raphson method to optimize the new footprint temperature; (3) employing the local energy balance method to get the footprint heat flux. The detailed procedure for doing this has been described in our

previous work Huang et al. (2016a), where the equations to solve are:

$$\frac{\partial}{\partial x}(k \frac{\partial T}{\partial x}) + \frac{\partial}{\partial y}(k \frac{\partial T}{\partial y}) + \frac{\partial}{\partial z}(k \frac{\partial T}{\partial z}) = 0; \quad (\text{A.18})$$

$$T(0, y, z) = T_{IR}, q(0, y, z) = q_b \quad (\text{A.19})$$

$$q(x, y, 0) = q_w, q(x, y, L_{ME}) = q_e \quad (\text{A.20})$$

$$q(x, 0, z) = q_s, q(x, W_{ME}, z) = q_n \quad (\text{A.21})$$

where x , y , and z individually indicates the thickness, the widthwise and the lengthwise directions of the microchannel evaporator. q_w , q_e , q_n and q_s are the heat flux at the four lateral sides of the substrate. Currently, in most of the literature, the lateral side heat fluxes are assumed to be zero, i.e. no heat loss through the lateral sides. In this case, the local footprint heat flux at the beginning and ending part of the evaporator would be obviously higher than the rest, which is not true in reality. Therefore, a new method to determine the boundary condition at the lateral sides was proposed based on the test section base IR temperature map. Here we have to assume each of the four heat fluxes were constant, while q_b was the heat flux at the base of the substrate, which was adjusted from the nominal base heat flux q_{base} combining the total heat loss and that at the lateral sides:

$$q_b A_b = Q_{total} - (Q_{loss} - Q_{axial}) \quad (\text{A.22})$$

$$Q_{axial} = q_w A_w + q_e A_e + q_s A_s + q_n A_n \quad (\text{A.23})$$

After the local footprint heat flux was obtained, the local vapor quality can be calculated from the local energy balance in each control volume ignoring the kinetic energy variation:

$$x(y, z) = \frac{\int_0^z q_{ftp}(y, z) \Delta y dz}{\dot{m}_0} + H_{inlet} - H_l(P(y, z)) \quad (\text{A.24})$$

A.2 Analysis of results and discussion

In this section, the experimental results of heat transfer for single- and two-phase flow in test section 1 (TS1) are presented and discussed.

A.2.1 Single-phase flow validation

Energy balance

For the single-phase flow energy balance tests, the manifold outlet saturation temperature was set to 60°C. As mentioned before, the main objective of the single-phase flow energy balance

analysis is to determine the energy loss on the electrical wires, which is needed to define the energy loss in the two-phase flow tests. The results of energy loss for single-phase flow are plotted in Fig. A.1. For the same heat flux, the energy loss decreases with the increase in mass flux, as shown in Fig. A.1a. This is associated with the increase in convective heat transfer coefficients. The energy loss on the electrical wires is plotted in Fig. A.1b.

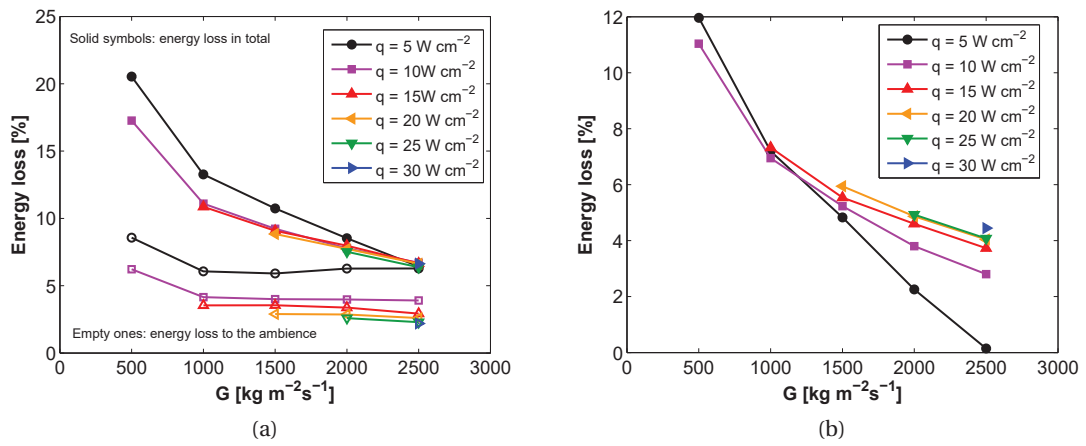


Figure A.1 – Energy loss for single-phase flow of R1233zd(E): (a) energy loss in total and to the ambience and (b) energy loss to the electrical wire.

Local Nusselt number

For the local single-phase Nusselt number, two methods, as listed in Table A.1 were employed to validate the experimental results. One example of the experimental results at $G = 1500 \text{ kg m}^{-2}\text{s}^{-1}$ and $q = 5 \text{ W cm}^{-2}$ is presented in Fig. A.2. It shows good agreement with the correlation of Muzychka and Yovanovich (2004) for the uniform wall heat flux boundary condition. The discrepancies in the experimental data at the entrance to the microchannels is due to the influence of the inlet orifices. The same conclusion can be found from the global comparison between the local experimental data and prediction from the correlations, as represented in Fig. A.3. The total number of the local data is counted according to the pixel numbers in the IR temperature map. In the global comparison, five pixels at each lateral side of the test section were cut to reduce the impact from the heat spreading to the manifold.

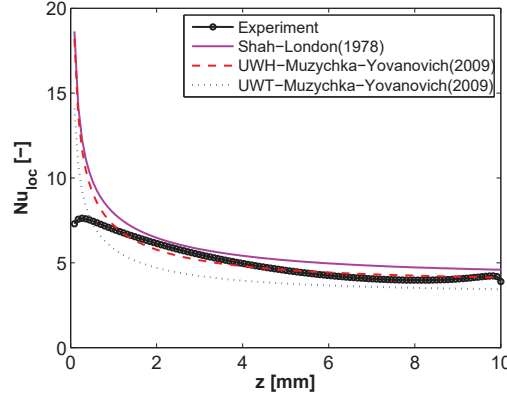


Figure A.2 – Single-phase local Nusselt number validation for R1233zd(E) at $G = 1500 \text{ kg m}^{-2} \text{ s}^{-1}$ and $q = 5 \text{ W cm}^{-2}$.

Table A.1 – Correlations from literature for single-phase local Nusselt number in channels.

Muzychka and Yovanovich (2004)

$$Nu_{spMY} = \left[\left(\frac{C_4 f(Pr)}{\sqrt{z^*}} \right)^m + \left\{ C_2 C_3 \left(\frac{f Re_{\sqrt{A}}}{z^*} \right)^{1/3} \right\}^5 + \left\{ C_1 \left(\frac{f Re_{\sqrt{A}}}{8\sqrt{\pi} ar^\gamma} \right) \right\}^5 \right]^{1/m}$$

$$f Re_{\sqrt{A}} = \frac{12}{\sqrt{ar}(1+ar) \left[1 - \frac{192ar}{\pi^5} \tanh\left(\frac{\pi}{2ar}\right) \right]}$$

$$\left\{ \begin{array}{ll} m = 2.27 + 1.65 Pr^{1/3}, & Pr = \frac{c_p \mu}{k} \\ z^* = \frac{z}{\sqrt{A} Re_{\sqrt{A}} Pr}, & Re_{\sqrt{A}} = \frac{G \sqrt{A}}{\mu}, A = W_{ch} H_{ch} \\ C_3 = 0.409, C_1 = 3.24, & f(Pr) = \frac{0.564}{[1 + (1.664 Pr^{1/6})^{9/2}]^{2/9}}, \text{UWF} \\ C_3 = 0.501, C_1 = 3.86, & f(Pr) = \frac{0.886}{[1 + (1.909 Pr^{1/6})^{9/2}]^{2/9}}, \text{UWT} \\ C_2 = 1, C_4 = 1, & \text{Local} \\ C_2 = 3/2, C_4 = 2, & \text{Average, } Nu = \frac{1}{z} \int_0^z Nu(z^*) dz \\ \gamma = 1/10, \text{Upper bound, } & \gamma = -3/10, \text{Lower bound} \\ ar \approx \frac{\ell_{short}}{\ell_{long}} \end{array} \right.$$

Shah and London (1978)

$$Nu(z^0) = \begin{cases} 1.302 z^{0-1/3} - 1, & z^0 \leq 0.00005 \\ 1.302 z^{0-1/3} - 0.5, & 0.00005 \leq z^0 \leq 0.0015 \\ 4.364 + 8.68(1000 z^0)^{-0.506} e^{-41 z^0}, & z^0 \geq 0.0015 \end{cases}$$

$$z^0 = \frac{\pi z}{4 Re Pr D_h}, Pr = \frac{c_p \mu}{k}, Re = \frac{G D_h}{\mu}$$

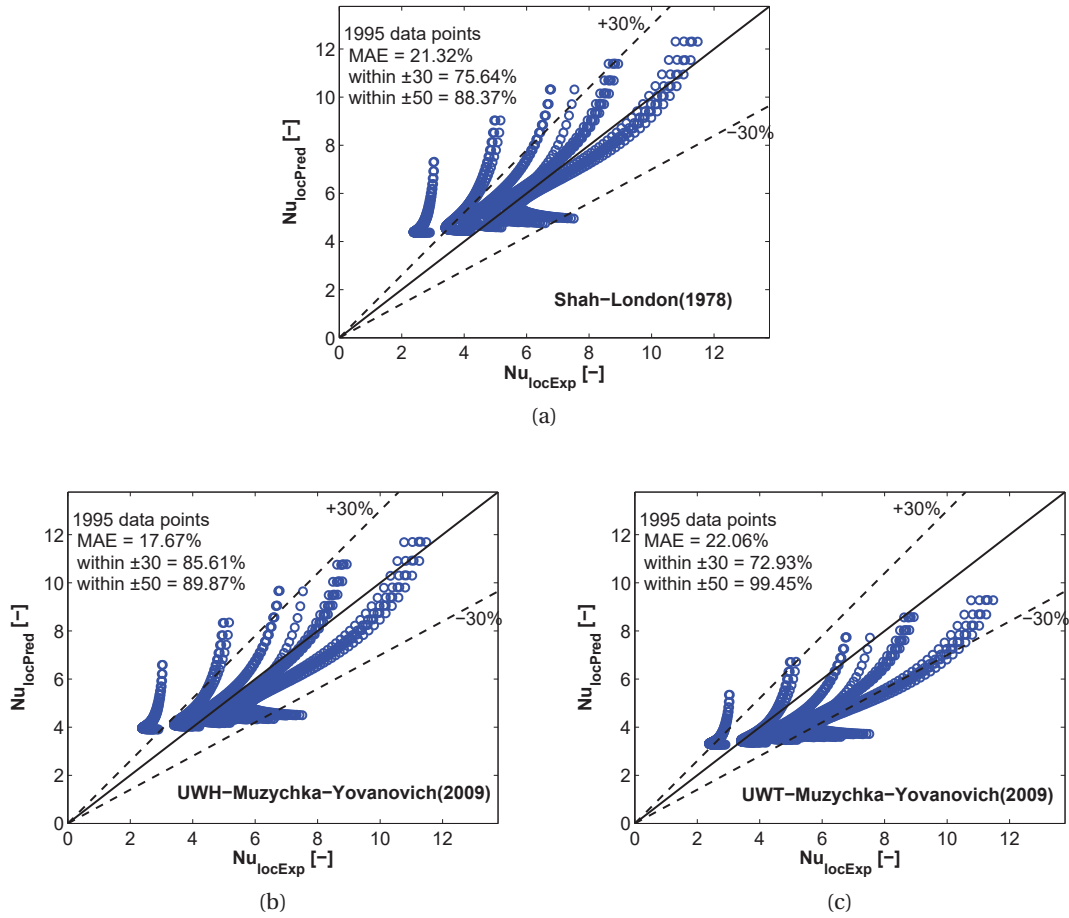


Figure A.3 – Assessment of single-phase local Nusselt number correlations with experimental data of R1233zd(E) in the test section with inlet orifice of $50\ \mu\text{m}$: (a) Shah and London (1978), (b) Muzychka and Yovanovich (2004) for uniform wall heat flux, and (c) Muzychka and Yovanovich (2004) for uniform wall temperature (five pixels at each lateral side were cut).

A.2.2 Two-phase flow heat transfer

Energy balance

During the stable flow boiling tests, the lowest heat flux tested was $24\ \text{W cm}^{-2}$; thus the heat loss through the wire for most cases fell in the range between 4% and 6%, as shown in Fig. A.1b (assuming the energy loss on the electrical wires in the two-phase flow test was the same as that in the single-phase flow test). Therefore, an average value of 5% was estimated as the heat loss out through the electrical power wires. The two-phase flow energy loss was characterized for each test condition, as shown in Fig. A.4, where the energy loss generally increases with outlet vapor quality and mass flux. This is due to the increase in heat loss to the ambience from the higher wall temperature encountered at high outlet vapor quality and mass flux.

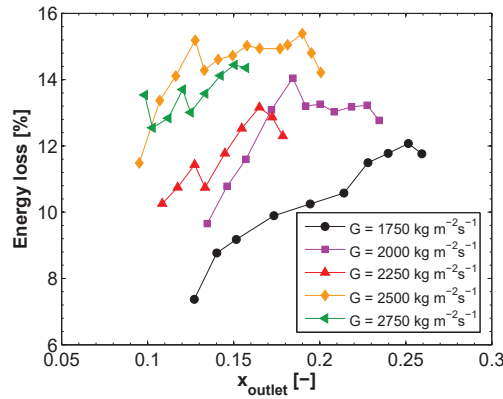


Figure A.4 – Energy loss for two-phase flow boiling tests of R1233zd(E).

Local heat transfer coefficients

In experimental studies using traditional temperature measurements (thermocouples or RTDs) Qu and Mudawar (2003a); Wang et al. (2008); Agostini et al. (2008), the local heat transfer coefficients usually end up as a limited number of points along the channel length. However, in this present experimental work, high-resolution of local heat transfer coefficients were obtained by using the IR camera measurements. Fig. A.5 demonstrates the contour maps of the footprint temperature, two-phase fluid temperature, temperature difference between the footprint and fluid, footprint heat flux, footprint heat transfer coefficients, and wall heat transfer coefficients. The highest footprint temperature, as shown in Fig. A.5a, exists at the bottom, because this side is close to the micro-heater electrodes integrated in a PCB board. The footprint heat flux (see Fig. A.5b) is not uniform even though the uniform base heat flux is provided by the micro-heater. As expected, the highest heat flux happens at the inner area when considering the Neumann boundary conditions at the lateral sides. In Fig. A.5c to A.5f, a demarcation at approximately $z = 2 \text{ mm}$ can be found. This is the transition curve from the single-phase or subcooled flow boiling region to the saturated flow boiling region. Along the widthwise direction, the onset of saturated flow boiling gradually moves to the channel inlet, appearing to be a parabolic curve. This is due to the local variation of the footprint heat flux (see Fig. A.5b).

Saturated flow boiling heat transfer models

Six leading heat transfer models compared in this thesis with the present experimental results are listed in Table A.2.

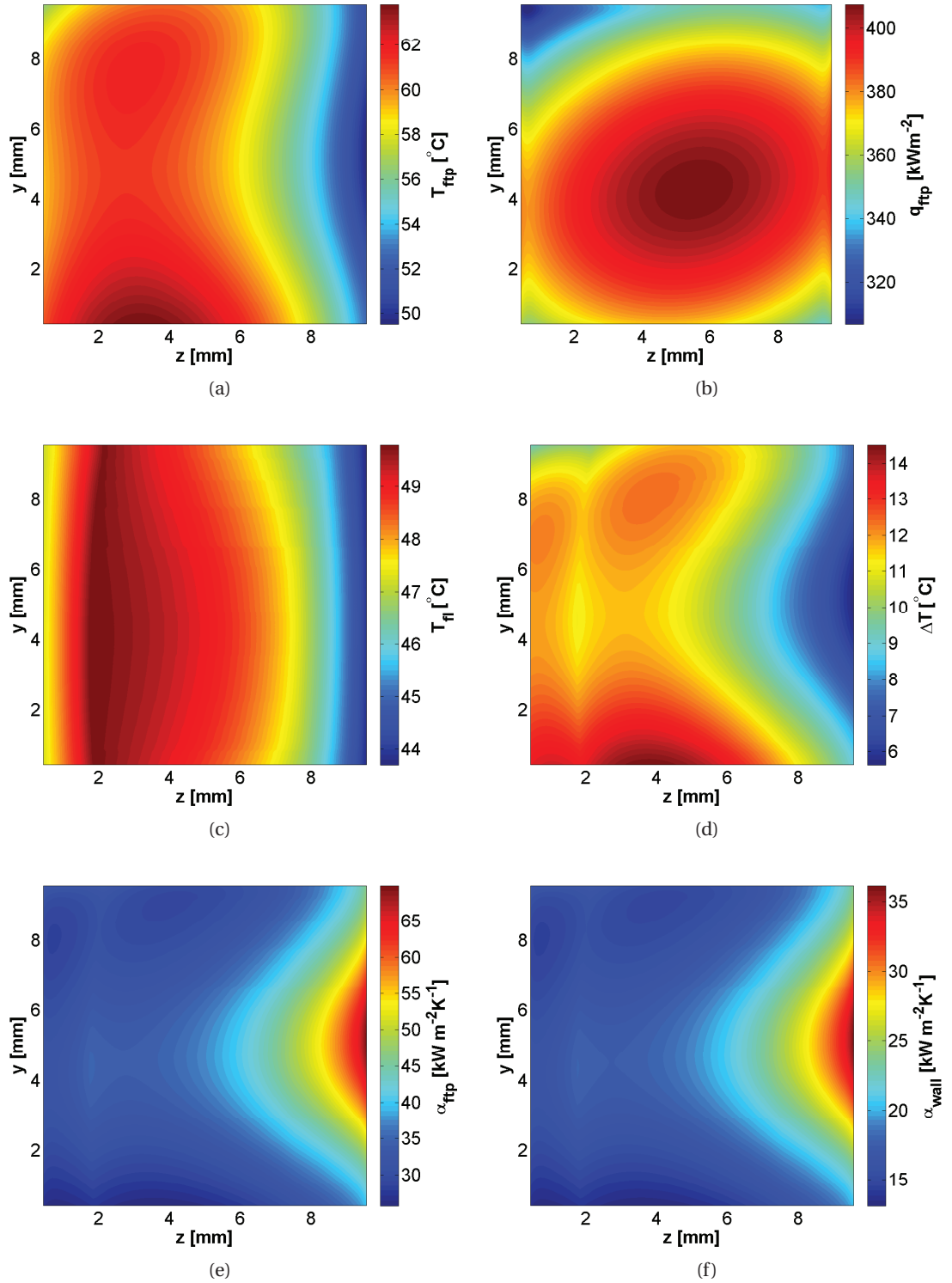


Figure A.5 – Thermal maps of two-phase flow at $G = 2500 \text{ kg m}^{-2}\text{s}^{-1}$, $q = 44 \text{ W cm}^{-2}$: (a) footprint temperature T_{ftp} , (b) footprint heat flux q_{ftp} , (c) fluid temperature T_f , (d) temperature difference between footprint and fluid, (e) footprint heat transfer coefficients α_{ftp} and, and (f) wall heat transfer coefficients α_{wall} (The flow direction is from left to right side).

Table A.2 – Saturated flow boiling heat transfer models.

Reference	Correlation
Cooper (1984) (pool boiling)	$\alpha_{tp} = 55 P_R^{0.12-0.2 \log_{10} R_P} [-\log_{10}(P_R)]^{-0.55} M^{-0.5} q_{wall}^{0.67}$
Lazarek and Black (1982)	$\alpha_{tp} = (30 Re_{lo}^{0.857} Bo^{0.714}) \frac{k_l}{D_h}$ $Re_{lo} = \frac{GD_h}{\mu_l}, Bo = \frac{q_{wall}}{GH_{lv}}$
Liu and Winterton (1991)	$\alpha_{tp} = [(E\alpha_{sp})^2 + (S\alpha_{NB})^2]^{0.5}, \alpha_{sp} = 0.023 Re_{lo}^{0.8} Pr_l^{0.4} \frac{k_l}{D_h}$ $E = \left[1 + x Pr_l \left(\frac{\rho_l}{\rho_v} - 1\right)\right]^{0.35}, \alpha_{NB} = \alpha_{tp, Cooper}$ $S = \frac{1}{1 + 0.055 E^{0.1} Re_{lo}^{0.16}}$ for horizontal tube with $Fr_l \leq 0.05$, E and S are corrected with $E Fr_l^{(0.1-2Fr_l)}$ and $S Fr_l^{0.5}$, respectively
Bertsch et al. (2009)	$\alpha_{tp} = F\alpha_{FC} + S\alpha_{NB}$ $F = 1 + 80(x^2 - x^6)e^{-0.6Co}, S = 1 - x$ $\alpha_{FC} = \alpha_{FC, lo}(1 - x) + \alpha_{FC, vo}x, \alpha_{NB} = \alpha_{tp, Cooper}$ $\alpha_{FC, lo} = \left(3.66 + \frac{0.0668 Re_{lo} Pr_l \frac{D_h}{L}}{1 + 0.04 \left[Re_{lo} Pr_l \frac{D_h}{L}\right]^{2/3}}\right) \frac{k_l}{D_h}$ $\alpha_{FC, vo} = \left(3.66 + \frac{0.0668 Re_{vo} Pr_v \frac{D_h}{L}}{1 + 0.04 \left[Re_{vo} Pr_v \frac{D_h}{L}\right]^{2/3}}\right) \frac{k_v}{D_h}$ $Co = \sqrt{\frac{\sigma}{g(\rho_l - \rho_v)D_h^2}}, Re_{lo} = \frac{GD_h}{\mu_l}, Re_{vo} = \frac{GD_h}{\mu_v}$
Costa-Patry and Thome (2013)	$\alpha_{tp} = \begin{cases} \alpha_{3Z}, & x \leq x_{CB-AF} - \frac{x_{exit}}{5} \\ \alpha_{CB-AF}, & x_{CB-AF} - \frac{x_{exit}}{5} < x < x_{CB-AF} + \frac{x_{exit}}{5} \\ \alpha_{AF}, & x \geq x_{CB-AF} + \frac{x_{exit}}{5} \end{cases}$ $x_{CB-AF} = 425 \left(\frac{\rho_v}{\rho_l}\right)^{0.1} \frac{Bo^{1.1}}{Co^{0.5}}$ $Bo = \frac{q_{wall}}{GH_{lv}}, Co = \sqrt{\frac{\sigma}{g(\rho_l - \rho_v)D_h^2}}$ $\alpha_{CB-AF} = (1 - r)\alpha_{3Z} + \frac{r\alpha_{AF}[r\alpha_{AF} - (1-r)\alpha_{3Z}]}{(1-r)\alpha_{3Z} + \alpha_{AF}}$ $r = \frac{x - x_{CB-AF}}{0.4x_{exit}} + 0.5$ α_{3Z} based on three-zone model of Thome et al. (2004) α_{AF} from annular flow model of Cioncolini and Thome (2011).
Kim and Mudawar (2013a)	$\alpha_{tp} = (\alpha_{NB}^2 + \alpha_{FC}^2)^{0.5}$ $\alpha_{NB} = \alpha_{sp} \left[2345 \left(Bo \frac{P_H}{P_F}\right)^{0.70} P_R^{0.38} (1 - x)^{-0.51}\right]$ $\alpha_{FC} = \alpha_{sp} \left[5.2 \left(Bo \frac{P_H}{P_F}\right)^{0.08} We_{lo}^{-0.54} + 3.5 \left(\frac{1}{x_{ft}}\right)^{0.94} \left(\frac{\rho_v}{\rho_l}\right)^{0.25}\right]$ $\alpha_{sp} = 0.023 Re_l^{0.8} Pr_l^{0.4} \frac{k_l}{D_h}$

Continued on next page

Table A.2 – *Continued from previous page*

Reference	Correlation
	$Bo = \frac{q_{wall}}{GH_{lv}}, P_R = \frac{P}{P_{crit}}, Re_l = \frac{G(1-x)D_h}{\mu_l}, We_{lo} = \frac{G^2 D_h}{\rho_l \sigma}$
	$X_{tt} = \left(\frac{\mu_l}{\mu_v}\right)^{0.1} \left(\frac{1-x}{x}\right)^{0.9} \left(\frac{\rho_v}{\rho_l}\right)^{0.5}$

Bibliography

- B. Agostini, R. Revellin, J. R. Thome, M. Fabbri, B. Michel, D. Calmi, and U. Kloter. High heat flux flow boiling in silicon multi-microchannels - Part III: Saturated critical heat flux of R236fa and two-phase pressure drops. *Int. J. Heat Mass Transf.*, 51:5426–5442, 2008.
- W. W. Akers, H. A. Deans, and O. K. Crosser. Condensing heat transfer within horizontal tubes. *Chem. Eng. Progr.*, 54(10):171–176, 1958.
- O.M. Alifanov. Inverse Heat Transfer Problems. *Springer-Verlag, New York*, 1994.
- S. Basu, B. Werneke, Y. Peles, and M. K. Jensen. Thermal behavior of a microdevice under transient heat loads. *Int. J. Heat Mass Transf.*, 91:1078–1087, 2015a.
- S. Basu, B. Werneke, Y. Peles, and M. K. Jensen. Transient microscale flow boiling heat transfer characteristics of HFE-7000. *Int. J. Heat Mass Transf.*, 90:396–405, 2015b.
- D. R. H. Beattie and P. B. Whalley. A simple two-phase frictional pressure drop calculation method. *Int. J. Multiph. Flow*, 8(1):83–87, 1982.
- J.V. Beck, B. Blackwell, and C.R. St. Clair. Inverse Heat Conduction Problem: Ill Posed Problems. *Wiley-Interscience: New York*, 1985, 1985.
- S. S. Bertsch, E. A. Groll, and S. V. Garimella. A composite heat transfer correlation for saturated flow boiling in small channels. *Int. J. Heat Mass Transf.*, 52(7-8):2110–2118, 2009.
- S. Bigam and S. Moghaddam. Microscale study of mechanisms of heat transfer during flow boiling in a microchannel. *Int. J. Heat Mass Transf.*, 88:111–121, 2015.
- N. Borhani and J.R. Thome. A novel time strip flow visualisation technique for investigation of intermittent dewetting and dryout in elongated bubble flow in a microchannel evaporator. *Int. J. Heat Mass Transf.*, 53(21-22):4809–4818, 2010.
- M. B. Bowers and I. Mudawar. Two-Phase electronic cooling using mini-channel and micro-channel heat sinks: Part 2-Flow rate and pressure drop constraints. *J. Electron. Packag.*, 116(4):298–305, 1994.

Bibliography

- F. Bozzoli and S. Rainieri. Comparative application of CGM and Wiener filtering techniques for the estimation of heat flux distribution. *Inverse Probl. Sci. Eng.*, 19(4):551–573, June 2011.
- F. Bozzoli, G. Pagliarini, and S. Rainieri. Experimental validation of the filtering technique approach applied to the restoration of the heat source field. *Exp. Therm. Fluid Sci.*, 44: 858–867, January 2013.
- G. M. Carlomagno and G. Cardone. Infrared thermography for convective heat transfer measurements. *Exp. Fluids*, 49(6):1187–1218, August 2010.
- G. Chen and P. Cheng. Nucleate and film boiling on a microheater under pulse heating in a microchannel. *Int. Commun. Heat Mass Transf.*, 36(5):391–396, 2009.
- G. Chen, X. Quan, and P. Cheng. Effects of surfactant additive on flow boiling over a microheater under pulse heating. *Int. J. Heat Mass Transf.*, 53(7-8):1586–1590, 2010.
- D. Chisholm. A theoretical basis for the Lockhart-Martinelli correlation for two-phase flow. *Int. J. Heat Mass Transf.*, 10(18):1767–1778, 1967.
- D. Chisholm. Pressure gradients due to friction during the flow of evaporating two-phase mixtures in smooth tubes and channels. *Int. J. Heat Mass Transf.*, 16(29):347–358, 1973.
- A. Cicchitti, C. Lombardi, M. Silvestri, G. Soldaini, and R. Zavattarelli. Two-phase cooling experiments: pressure drop, heat transfer and burnout measurements. *Energ. Nucl.*, 7: 407–425, 1960.
- A. Cioncolini and J. R. Thome. Algebraic turbulence modeling in adiabatic and evaporating annular two-phase flow. *Int. J. Heat Fluid Flow*, 32(4):805–817, 2011.
- A. Cioncolini, J. R. Thome, and C. Lombardi. Unified macro-to-microscale method to predict two-phase frictional pressure drops of annular flows. *Int. J. Multiph. Flow*, 35(12):1138–1148, 2009.
- J. G. Collier and J. R. Thome. *Convective Boiling and Condensation*. Clarendon Press, Oxford, 1994.
- M.G. Cooper. Heat flow rates in saturated nucleate pool boiling - a wide ranging examination using reduced properties. *Adv. Heat Transfer*, 16:157–239, 1984.
- E. Costa-Patry. *Cooling high heat flux micro-electronic systems using refrigerants in high aspect ratio multi-microchannel evaporators*. PhD thesis, École Polytechnique Fédéral de Lausanne, 2011.
- E. Costa-Patry and J. R. Thome. Flow pattern-based flow boiling heat transfer model for microchannels. *Int. J. Refrig.*, 36(2):414–420, 2013.

- E. Costa-patry, S. Nebuloni, J. Olivier, and J. R. Thome. On-Chip Two-Phase Cooling with Refrigerant Under Hot-Spot Conditions. 2(2):311–320, 2012.
- P. Craven and G. Wahba. Smoothing noisy data with spline functions. *Numerische Mathematik*, (3):377–403, 1979.
- T. David, D. Mendler, a. Mosyak, a. Bar-Cohen, and G. Hetsroni. Thermal Management of Time-Varying High Heat Flux Electronic Devices. *J. Electron. Packag.*, 136(2):021003, 2014.
- D. Delpueyo, X. Balandraud, and M. Grédiac. Heat source reconstruction from noisy temperature fields using an optimised derivative Gaussian filter. *Infrared Phys. Technol.*, 60:312–322, September 2013.
- P. Dierckx. An algorithm for surface-fitting with spline functions. *IMA J Numer Anal*, 3(1): 267–283, 1981.
- A. E. Dukler, M. Wicks, and R. G. Cleveland. Frictional pressure drop in two-phase flow: B. An approach through similarity analysis. *AIChE J.*, 10:44–51, 1964.
- T. El Abbass, C. Jallouli, Y. Albouy, and M. Diamant. A comparison of surface fitting algorithms for geophysical data. *Terra Nov.*, 2(5):467–475, September 1990.
- L. Friedel. Improved friction pressure drop correlations for horizontal and vertical two-phase pipe flow. *Two-Phase Flow Group Meeting, Paper E2, Ispra, Italy, June*, 1979.
- G.E. Geiger. Sudden contraction losses in single and two-phase flow, Ph.D. thesis, University of Pittsburgh, USA, 1964.
- R. Grönnerud. Investigation of liquid hold-up, flow-resistance and heat transfer in circulation type evaporators, part IV: two-phase flow resistance in boiling refrigerants. *Annexe 1972-I, Bull. de l'Inst. du Froid*, 1979.
- W. M. Haynes. *CRC Handbook of Chemistry and Physics. 91st Edition*. Taylor and Francis Group, 2010.
- G. Hetsroni, A. Mosyak, Z. Segal, and G. Ziskind. A uniform temperature heat sink for cooling of electronic devices. *Int. J. Heat Mass Transf.*, 45(16):3275–3286, July 2002.
- G. Hetsroni, A. Mosyak, E. Pogrebnyak, and L.P. Yarin. Heat transfer in micro-channels: Comparison of experiments with theory and numerical results. *Int. J. Heat Mass Transf.*, 48 (25-26):5580–5601, December 2005.
- G. Hetsroni, A. Mosyak, E. Pogrebnyak, and R. Rozenblit. Infrared temperature measurements in micro-channels and micro-fluid systems. *Int. J. Therm. Sci.*, 50(6):853–868, June 2011.

Bibliography

- A.C. Hindmarsh. LSODE and LSODI, Two New Initial Value Ordinary Differential Equation Solvers. *ACM SIGNUM Newsletter*, 15(4):10–11, 1980.
- S. Hozejowska, M. Piasecka, and M. E. Poniewski. Boiling heat transfer in vertical minichannels. Liquid crystal experiments and numerical investigations. *Int. J. Therm. Sci.*, 48(6):1049–1059, 2009.
- H. Huang and J. R. Thome. Local measurements and a new flow pattern based model for subcooled and saturated flow boiling heat transfer in multi-microchannel evaporators. *Int. J. Heat Mass Transf.*, 98:596–610, 2016.
- H. Huang and J. R. Thome. An experimental study on flow boiling pressure drop in multi-microchannel evaporators with different refrigerants. *Exp. Therm. Fluid Sci.*, 80:391–407, 2017.
- H. Huang, N. Borhani, N. Lamaison, and J. R. Thome. Local experimental heat transfer in multi-microchannel evaporators. *Under review by Int. J. Therm. Sci.*, 2016a.
- H. Huang, N. Borhani, and J. R. Thome. Experimental investigation on flow boiling pressure drop and heat transfer of R1233zd(E) in a multi-microchannel evaporator. *Int. J. Heat Mass Transf.*, 98:596–610, 2016b.
- H. Huang, N. Borhani, and J.R. Thome. Thermal Response of Multi-microchannel Evaporators during Flow Boiling of refrigerants under transient heat loads with flow visualization. *Journal of Electronics Packaging*, 138:031004, 2016c.
- H. Huang, N. Lamaison, and J.R. Thome. Transient Data Processing of Flow Boiling Local Heat Transfer in a Multi-Microchannel Evaporator under a Heat Flux Disturbance. *Under review by Journal of Electronics Packaging*, 2016d.
- R. J. Hulse, R. S. Basu, R. R. Singh, and R. H. P. Thomas. Physical properties of HCFO-1233zd(E). *J. Chem. Eng. Data*, 57:3581–3586, 2012.
- I. E. Idel'chik. *Handbook of Hydraulic Resistance, 4th ed. rev. and augmented*. Redding, CT: Begell House, 2007.
- F. P. Incropera. *Fundamentals of Heat and Mass Transfer*. John Wiley & Sons, 2006.
- S. G. Kandlikar. Two-phase flow patterns, pressure drop, and heat transfer during boiling in minichannel flow passages of compact evaporators. *Heat Transf. Eng.*, 23(1):5–23, 2002.
- S. G. Kandlikar. Heat Transfer Mechanisms During Flow Boiling in Microchannels. *Trans. ASME*, 126(February):8–16, 2004.

- A. Karimi, M. Kunze, and R. Longchamp. Robust controller design by linear programming with application to a double-axis positioning system. *Control Eng. Pract.*, 15(2):197–208, 2007.
- W. M. Kays. Loss coefficients for abrupt changes in flow cross section with low Reynolds number flow in single and multiple-tube systems. *Trans. ASME*, 72:1067–1074, 1950.
- S. M. Kim and I. Mudawar. Universal approach to predicting two-phase frictional pressure drop for adiabatic and condensing mini/micro-channel flows. *Int. J. Heat Mass Transf.*, 55(11-12):3246–3261, 2012a.
- S. M. Kim and I. Mudawar. Consolidated method to predicting pressure drop and heat transfer coefficient for both subcooled and saturated flow boiling in micro-channel heat sinks. *Int. J. Heat Mass Transf.*, 55(13-14):3720–3731, 2012b.
- S. M. Kim and I. Mudawar. Universal approach to predicting saturated flow boiling heat transfer in mini/micro-channels - Part II. Two-phase heat transfer coefficient. *Int. J. Heat Mass Transf.*, 64:1239–1256, 2013a.
- S. M. Kim and I. Mudawar. Universal approach to predicting two-phase frictional pressure drop for mini/micro-channel saturated flow boiling. *Int. J. Heat Mass Transf.*, 58(1-2):718–734, 2013b.
- S. M. Kim and I. Mudawar. Review of databases and predictive methods for heat transfer in condensing and boiling mini/micro-channel flows. *Int. J. Heat Mass Transf.*, 77:627–652, 2014.
- S. J. Kline and F. A. McClintock. Describing uncertainties in single-sample experiments. *ASME Mechanical Engineering*, 75(1):3–8, 1953.
- D. Krebs, V. Narayanan, J. Liburdy, and D. Pence. Spatially resolved wall temperature measurements during flow boiling in microchannels. *Exp. Therm. Fluid Sci.*, 34(4):434–445, 2010.
- N. Lamaison. *Dynamic modeling and experimental evaluation of a controlled two-phase on-chip cooling system designed for high efficiency datacenter*. phdthesis, Ecole Polytechnique Fédérale de Lausanne (EPFL), Switzerland, 2014.
- Nicolas Lamaison, Jackson Braz Marcinichen, and John Richard Thome. Two-phase flow control of electronics cooling with pseudo-CPU's in parallel flow circuits: dynamic modeling and experimental evaluation. *J. Electron. Packag.*, 135(3):030908, July 2013.
- G.M. Lazarek and S.H. Black. Evaporative heat transfer, pressure drop and critical heat flux in a small vertical tube with R-113. *Int. J. Heat Mass Transf.*, 25(7):945–960, 1982.

Bibliography

- J. Lee and I. Mudawar. Two-phase flow in high-heat-flux micro-channel heat sink for refrigeration cooling applications: Part I - Pressure drop characteristics. *Int. J. Heat Mass Transf.*, 48: 928–940, 2005.
- J. Lee and I. Mudawar. Fluid flow and heat transfer characteristics of low temperature two-phase micro-channel heat sinks – Part 2. Subcooled boiling pressure drop and heat transfer. *Int. J. Heat Mass Transf.*, 51(9):4327–4341, 2008.
- P.-S. Lee and S. V. Garimella. Saturated flow boiling heat transfer and pressure drop in silicon microchannel arrays. *Int. J. Heat Mass Transf.*, 51:789–806, 2008.
- J. Li and P. Cheng. Bubble cavitation in a microchannel. *Int. J. Heat Mass Transf.*, 47(12-13): 2689–2698, 2004.
- S. Lin, C. C. K. Kwok, R.-Y. Li, Z.-H. Chen, and Z.-Y. Chen. Local frictional pressure drop during vaporization of R-12 through capillary tubes. *Power*, 17(1):95–102, 1991.
- D. Liu and S.V. Garimella. Flow boiling heat transfer with models in microchannels. *Journal of Heat Transfer*, 129(10):1321–1332, 2007.
- D. Liu, P. S. Lee, and S. V. Garimella. Prediction of the onset of nucleate boiling in microchannel flow. *Int. J. Heat Mass Transf.*, 48(25-26):5134–5149, 2005.
- Z. Liu and R.H.S. Winterton. A general correlation for saturated and subcooled flow boiling in tubes and annuli, based on a nucleate pool boiling equation. *Int. J. Heat Mass Transf.*, 34(11):2759–2766, 1991.
- R. W. Lockhart and R. C. Martinelli. Proposed correlation of data for isothermal two-phase two-component flow in pipes. *Chem Eng Progr.*, 45(1):39–48, 1949.
- S. Luciani, D. Brutin, C. Le Niliot, O. Rahli, and L. Tadrist. Flow boiling in minichannels under normal, hyper-, and microgravity: local heat transfer analysis using inverse methods. *J. Heat Transfer*, 130(10):101502, 2008.
- M. Gómez Marzoa, M. Battistin, C. Bortolin, and et al. Thermal studies of an ultra-low-mass cooling system for the ALICE ITS Upgrade project at CERN. *In Proceedings, 8th World Conference on Experimental Heat Transfer Fluid Mechanics and Thermodynamics, ExHFT-8*, Lisbon, Portugal, 2013.
- W. H. McAdams, W. K. Woods, and L.C. Heroman. Vaporization inside horizontal tubes-II-benzene-oil mixtures. *Trans. ASME*, 64:193–200, 1942.
- K. Mishima and T. Hibiki. Some characteristics of air-water two-phase flow in small diameter vertical tubes. *Int. J. Multiph. Flow*, 22:703–712, 1996.

- F. D. Moles and J.F.G. Shaw. Boiling heat transfer to subcooled liquids under condition of forced convection. *Trans. Inst. Chem. Eng.*, 50:76–84, 1972.
- H. Müller-Steinhagen and K. Heck. A simple friction pressure drop correlation for two-phase flow in pipes. *Chem. Eng. Process. Process Intensif.*, 20(1):297–308, 1986.
- Y. S. Muzychka and M. M. Yovanovich. Laminar forced convection heat transfer in the combined entry region of non-circular ducts. *J. Heat Transfer*, 126(1):54, 2004.
- Y. S. Muzychka and M. M. Yovanovich. Pressure drop in laminar developing flow in noncircular ducts: a scaling and modeling approach. *J. Fluids Eng.*, 131(11):111105–1–11, 2009.
- C. L. Ong, N. Lamaison, J. B. Marcinichen, and J. R. Thome. Two-Phase Mini-Thermosyphon Electronics Cooling , Part 1 : Experimental Investigation. *Accepted by IThERM 2016*, pages xxx–xxx, 2016.
- H. R.B. Orlande, O. Fudym, D. Maillet, and R. M. Cotta. *Thermal Measurements and Inverse Techniques*. 2011.
- M.N. Ozisik. Heat Conduction - 2nd ed. *Wiley-Interscience*, 1993.
- S. S. Papell. Subcooled boiling heat transfer under forced convection in a heated tube, NASA Technical Note D-1583, Lewis Resarch Center, Cleveland, OH. 1963.
- S.V. Patankar. Numerical Heat Transfer and Fluid Flow. *McGraw-Hill, New York*, 1980, 1980.
- M. Piasecka, S. Hozejowska, and M. E. Poniewski. Experimental evaluation of flow boiling incipience of subcooled fluid in a narrow channel. *Int. J. Heat Fluid Flow*, 25(2):159–172, 2004.
- W. Qu and I. Mudawar. Prediction and measurement of incipient boiling heat flux in micro-channel heat sinks. *Int. J. Heat Mass Transf.*, (4):3933–3945, 2002.
- W. Qu and I. Mudawar. Measurement and prediction of pressure drop in two-phase micro-channel heat sinks. *Int. J. Heat Mass Transf.*, 46:2737–2753, 2003a.
- W. Qu and I. Mudawar. Flow boiling heat transfer in two-phase micro-channel heat sinks-I. Experimental investigation and assessment of correlation methods. *Int. J. Heat Mass Transf.*, 46:2755–2771, 2003b.
- S. Rainieri and G. Pagliarini. Data filtering applied to infrared thermographic measurements intended for the estimation of local heat transfer coefficient. *Exp. Therm. Fluid Sci.*, 26(2-4): 109–114, June 2002.

Bibliography

- S. Rainieri, F. Bozzoli, and G. Pagliarini. Wiener filtering technique applied to thermographic data reduction intended for the estimation of plate fins performance. *Exp. Therm. Fluid Sci.*, 28(2-3):179–183, January 2004.
- S. R. Rao and Y. Peles. Spatiotemporally resolved heat transfer measurements for flow boiling in microchannels. *Int. J. Heat Mass Transf.*, pages 482–493, 2015.
- S. R. Rao, F. Houshmand, and Y. Peles. Transient flow boiling heat-transfer measurements in microdomains. *Int. J. Heat Mass Transf.*, 76:317–329, 2014.
- G. Ribatski, W. Zhang, L. Consolini, J. Xu, and J.R. Thome. On the Prediction of Heat Transfer in Micro-Scale Flow Boiling. *Heat Transf. Eng.*, 28(10):842–851, 2007.
- Susan N. Ritchey, Justin A. Weibel, and Suresh V. Garimella. Local measurement of flow boiling heat transfer in an array of non-uniformly heated microchannels. *Int. J. Heat Mass Transf.*, 71:206–216, April 2014.
- Y. Rouizi, D. Maillet, and Y. Jannot. Fluid temperature distribution inside a flat mini-channel: Semi-analytical wall transfer functions and estimation from temperatures of external faces. *Int. J. Heat Mass Transf.*, 64:331–342, 2013.
- Y. Rouizi, W. Al Hadad, D. Maillet, and Y. Jannot. Experimental assessment of the fluid bulk temperature profile in a mini channel through inversion of external surface temperature measurements. *Int. J. Heat Mass Transf.*, 83:522–535, 2015.
- T. Sannen. *Modeling a two-phase microchannel electronics cooling system*. phdthesis, Katholieke Universiteit Leuven, Belgium, 2013.
- M.M. Shah. A general correlation for heat transfer during subcooled boiling in pipes and annuli. *ASHRAE Trans.*, 83:202–217, 1977.
- R.K. Shah and A.L. London. *Laminar Flow Forced Convection in Ducts: A Source Book for Compact Heat Exchanger Analytical Data*. Academic Press, New York, 1978.
- S. Szczukiewicz. *Thermal and visual operational characteristics of multi-microchannel evaporators using refrigerants*. phdthesis, École Polytechnique Fédérale de Lausanne (EPFL), Switzerland, 2012.
- S. Szczukiewicz, N. Borhani, and J. R. Thome. Fine-resolution two-phase flow heat transfer coefficient measurements of refrigerants in multi-microchannel evaporators. *Int. J. Heat Mass Transf.*, 67:913–929, December 2013.
- C. Teodosiu, G. Rusaouën, and R. Hohotă. Influence of boundary conditions uncertainties on the simulation of ventilated enclosures. *Numerical Heat Transfer*, 44(January):483–504, 2003.

- J. R. Thome. Boiling in microchannels: a review of experiment and theory. *Int. J. Heat Fluid Flow*, 25(2):128–139, April 2004.
- J. R. Thome. State-of-the-Art Overview of Boiling and Two-Phase Flows in Microchannels. *Heat Transf. Eng.*, 27(9):4–19, 2006.
- J. R. Thome and J. Kim. *Encyclopedia of Two-Phase Heat Transfer and Flow*. World Scientific, 2015.
- J. R. Thome, V. Dupont, and A. M. Jacobi. Heat transfer model for evaporation in microchannels. Part I: Presentation of the model. *Int. J. Heat Mass Transf.*, 47:3375–3385, 2004.
- A.N. Tikhonov and V.Y. Arsenin. Solution of Ill Posed Problems. *Winston-Sons, Washington, DC*, 1977.
- T. N. Tran, M. C. Chyu, M. W. Wambsganss, and D. M. France. Two-phase pressure drop of refrigerants during flow boiling in small channels: An experimental investigation and correlation development. *Int. J. Multiph. Flow*, 26:1739–1754, 2000.
- D.B. Tuckerman and R.F.W. Pease. High-performance heat sinking for VLSI. *IEEE Electron Device Lett.*, 2(5):126–129, May 1981.
- G. Wang, P. Cheng, and A. E. Bergles. Effects of inlet/outlet configurations on flow boiling instability in parallel microchannels. *Int. J. Heat Mass Transf.*, 51:2267–2281, 2008.
- M. A. Woldesemayat and A. J. Ghajar. Comparison of void fraction correlations for different flow patterns in horizontal and upward inclined pipes. *Int. J. Multiph. Flow*, 33:347–370, 2007.
- J.L. Xu, Y.H. Gan, D.C. Zhang, and X.H. Li. Microscale heat transfer enhancement using thermal boundary layer redeveloping concept. *Int. J. Heat Mass Transf.*, 48(9):1662–1674, April 2005.
- Y. Xu and X. Fang. Correlations of void fraction for two-phase refrigerant flow in pipes. *Appl. Therm. Eng.*, 64:242–251, 2014.
- S. M. Zivi. Estimation of steady-state steam void-fraction by means of the principle of minimum entropy production. *J. Heat Transfer*, 86:247–252, 1964.

Personal information

Name	Houxue Huang
Date of birth	October 24 th , 1986
Place of birth	Jiangsu Province, China
Nationality	Chinese

Education

11.2012–10.2016	Currently pursuing a Ph.D degree in Energy, Laboratory of Heat and Mass Transfer, Swiss Federal Institute of Technology Lausanne (EPFL), Switzerland
09.2008-03.2012	Master in Engineering Thermo-physics, Shanghai Jiao Tong University (SJTU), China
09.2004-06.2008	Bachelor in Thermal and Power Engineering, Nanjing Normal University (NNU), China

Professional experience

2012–2016	Swiss Federal Institute of Technology at Lausanne (EPFL), Laboratory of Heat and Mass Transfer, doctoral assistant, teaching assistant, and laboratory research and development.
2008–2012	Shanghai Jiao Tong University (SJTU), China, research assistant and teaching assistant

Journal publications

1. **Houxue Huang**, Navid Borhani, John R. Thome. Experimental investigation on flow boiling pressure drop and heat transfer of R1233zd(E) in a multi-microchannel evaporator, *International Journal of Heat and Mass Transfer* 98(2016) 596-610;
2. **Houxue Huang**, Navid Borhani, John R. Thome. Thermal response of multi-microchannel evaporators during flow boiling of refrigerants under transient heat loads with flow visualization, *Journal of Electronic Packaging*, 2016(138) 031004;.
3. **Houxue Huang**, John .R. Thome, Local measurements and a new flow pattern based model for subcooled and saturated flow boiling heat transfer in multi-microchannel evaporators, *International Journal of Heat and Mass Transfer*, 103(2016) 701-714.
4. **Houxue Huang**, John R. Thome, An experimental study on flow boiling pressure drop in multi-microchannel evaporators with different refrigerants, *Experimental Fluid and Thermal Science*, 80(2017) 391-407;
5. **Houxue Huang**, Navid Borhani, Nicolas Lamaison, John R. Thome. Local heat transfer data reduction in multi-microchannel evaporators using inverse approach, under third-round review

by *International Journal of Thermal Sciences*, 2016);

6. **Houxue Huang**, Nicolas Lamaison, John R. Thome, Transient Data Processing of Flow Boiling Local Heat Transfer in a Multi-Microchannel Evaporator under a Heat Flux Disturbance, under review by *Journal of Electronic Packaging*, 2016.

Conference abstract

1. **Houxue Huang**, Nicolas Lamaison, John R. Thome. Transient flow boiling local heat transfer in a multi-microchannel evaporator under a heat flux disturbance. Accepted by 5th Micro and Nano Flows Conference, Milan, Italy, September, 2016;

